Numerical Simulation of Wet Biomass Carbonization in Tubular Reactors

Zur Erlangung des akademischen Grades eines
DOKTORS DER INGENIEURWISSENSCHAFTEN (Dr.-Ing.)

von der KIT-Fakultät für Chemieingenieurwesen und Verfahrenstechnik
des Karlsruher Instituts für Technologie (KIT)

genehmigte

Dissertation

von

Salar Tavakkol, M.Sc.

Erster Gutachter: Prof. Dr.-Ing. Henning Bockhorn
Zweiter Gutachter: Prof. Dr.-Ing. Nicolaus Dahmen

Tag der mündlichen Prüfung: 24.06.2021

IV

Acknowledgment

Table of Contents

Abbreviations

CFD   Computational fluid dynamics

DEM   Distinct/discrete element method

DOM   Discrete ordinates model

DPM   Discrete particle model

FVM   Finite volume method

HTC   Hydrothermal carbonization

htc   heat transfer coefficient

MRT   Mean residence time

MP-PIC   Multiphase particle in cell

MS   Moisture content

PSD   Particle size distribution

RET   Radiative transport equation

RPS   Reduced particle stiffness

Symbols

Latin Letters

$\mathbf{a}_\mathrm{p}$	Particle acceleration	$\mathrm{m\,s^{-2}}$
A_p	Particle's projected area	$\mathrm{m^2}$
A_pc	Projected area of the cell	$\mathrm{m^2}$
A_s	Particle's surface area	$\mathrm{m^2}$
c_i	Mass fraction of the main components of biomass	-
C_d	Drag coefficient	-
C_{p_i}	Vapor concentration at the particle surface	$\mathrm{mol\,m^{-3}}$
C_∞	Vapor concentration in the bulk gas	$\mathrm{mol\,m^{-3}}$
c_p	Specific heat capacity	$\mathrm{J\,kg^{-1}K^{-1}}$
D	Mass diffusivity	$\mathrm{m^2\,s^{-1}}$
D_{ax}	Axial dispersion coefficient	$\mathrm{m^2\,s^{-1}}$
$D_{i\,,m}$	Diffusion coefficient of vapor in the gas phase	$\mathrm{m^2\,s^{-1}}$
d_p	Particle's diameter	m
d_R	Inner diameter of the reactor	m
$\mathrm{d}t$	Timestep	s
e	Restitution coefficient of particles	-
E_a	Activation energy of Arrhenius equation	$\mathrm{J\,mol^{-1}}$
E	Young's modulus	$\mathrm{kg\,m^{-1}\,s^{-2}}$
E^*	Effective Young's modulus	$\mathrm{kg\,m^{-1}\,s^{-2}}$
E_disperse	Emitted radiation by particles in a control volume	$\mathrm{W\,m^{-3}}$
$\mathbf{F}_\mathrm{c}$	Collision force	$\mathrm{kg\,m\,s^{-2}}$
$\mathbf{F}_\mathrm{d}$	Drag force	$\mathrm{kg\,m\,s^{-2}}$
$\boldsymbol{F}_\mathrm{external}$	Resultant of forces on a particle	$\mathrm{kg\,m\,s^{-2}}$
$\mathbf{F}_g$	Gravity and Bouyancy fource	$\mathrm{kg\,m\,s^{-2}}$
$\mathbf{F}_\mathrm{v}$	Virtual mass force	$\mathrm{kg\,m\,s^{-2}}$
$\mathbf{F}_\mathrm{N}$	Normal force in particle collision	$\mathrm{kg\,m\,s^{-2}}$
$\mathbf{F}_\mathrm{T}$	Tangential force in particle collision	$\mathrm{kg\,m\,s^{-2}}$

f	Probability function	-
f_p	Measure of the frequency of particle collisions	s^{-1}
$\boldsymbol{g}$	Gravitational acceleration	$m\,s^{-2}$
g_0	Radial distribution function	-
G	Incident radiation	$W\,m^{-2}$
h_{fg}	Enthalpy of water phase-change	$J\,kg^{-1}$
h_p	Heat transfer coefficient of particle	$W\,m^{-2}K^{-1}$
h_s	Sensible enthalpy	$J\,kg^{-1}$
h_{tot}	Total enthalpy	$J\,kg^{-1}$
I_b	Radiation intensity of black body	$W\,m^{-2}$
I_{abs}	Absorbed radiation intensity in a cell	$W\,m^{-2}$
k_0	Frequency factor of Arrhenius equation	s^{-1}
k_C	Mass transfer coefficient	$m\,s^{-1}$
k_{rxn}	Reaction rate coefficient	s^{-1}
k_N	Normal stiffness	$N\,m^{-1}$
k_T	Tangential stiffness	$N\,m^{-1}$
l	Characteristic length	m
m	Mass	kg
$\widetilde{M}_{H_2O}$	Molar weight of water	$kg\,mol^{-1}$
M_{fsp}	Moisture content at the fiber saturation point	-
M_p	Particle's moisture content (dry basis)	-
n	Order of the reaction	-
n_p	Number of parcels per control volume	m^{-3}
n_{pcell}	Number of parcels in a specified computational cell	-
N_p	Molar flux of vapor	$mol\,m^{-2}\,s^{-1}$
N_{pp}	Number of particles per parcel	-
p	Gas pressure	Pa
p_{sat}	Saturation pressure	Pa
P_s	Solid pressure coefficient	Pa
Q	Heat	J
$\dot{Q}$	Heat flow	W
$\dot{q}$	Delivered heat flux density	$W\,m^{-2}$

$\dot{Q}_{\mathrm{R,g}}$	Volumetric heat flux to the gas in a control volume	$\mathrm{W\,m^{-3}}$
$\dot{Q}_{\mathrm{R,p}}$	Delivered heat flow to a particle	W
R	Universal gas constant	$\mathrm{J\,kg^{-1}\,K^{-1}}$
$S_{i,j}$	Location variable in direction $\widehat{S}$	-
$S_{\mathrm{p},h}$	Interphase exchange source term for enthalpy	$\mathrm{W\,m^{-3}}$
$S_{\mathrm{p},m}$	Interphase exchange source term for mass	$\mathrm{kg\,m^{-3}s^{-1}}$
$\boldsymbol{S}_{\mathrm{p},mom}$	Interphase exchange source term for momentum	$\mathrm{N\,m^{-3}}$
S_{rad}	Interphase exchange source term for radiation	$\mathrm{W\,m^{-3}}$
S_{p,Y_i}	Interphase exchange source term for species	$\mathrm{kg\,m^{-3}s^{-1}}$
T	Temperature	K
t	Residence time	s
$\boldsymbol{u}_{\mathrm{g}}$	Gas velocity	$\mathrm{m\,s^{-1}}$
$\boldsymbol{U}_{\mathrm{rel,N}}$	Relative velocity in the normal direction	$\mathrm{m\,s^{-1}}$
V_{c}	Volume of a computational cell	$\mathrm{m^3}$
$\mathbf{v}_{\mathrm{N}}$	Normal velocity	$\mathrm{m\,s^{-1}}$
$\mathbf{v}_{\mathrm{p}}$	Particle's velocity	$\mathrm{m\,s^{-1}}$
$\mathbf{v}_{\mathrm{p}}^{\mathrm{corr}}$	Corrected velocity for a particle (in packing model)	$\mathrm{m\,s^{-1}}$
$\mathbf{v}_{\mathrm{p}}^{\mathrm{ref}}$	Reference velocity for a particle	$\mathrm{m\,s^{-1}}$
$\mathbf{v}_{\mathrm{p}}^{\mathrm{orig}}$	Original velocity for a particle	$\mathrm{m\,s^{-1}}$
$\mathbf{v}_{\mathrm{p}}^{\mathrm{new}}$	Recalculation particle velocity (isotropy model)	$\mathrm{m\,s^{-1}}$
$\overline{\mathbf{v}_i}$	Average local velocity of particles	$\mathrm{m\,s^{-1}}$
$\mathbf{v}_{\mathrm{p}}^{\mathrm{temp}}$	Temporary velocity (isotropy model)	$\mathrm{m\,s^{-1}}$
$\mathbf{v}_{\mathrm{T}}$	Tangential velocity	$\mathrm{m\,s^{-1}}$
V_{p_i}	Particle's volume	$\mathrm{m^3}$
$\boldsymbol{x}_{\mathrm{p}}$	Location of particle	m
$X_{\mathrm{H_2O}}$	Local bulk mole fraction of water	-
Y_{char}	Mass fraction of char within a particle	-
$Y_{\mathrm{moist.}}$	Mass fraction of moisture within a particle	-
$Y_{\mathrm{vol.}}$	Mass fraction of volatiles within a particle	-
y_{max}	Maximum bed height	m

Dimensionless Numbers

Bi	Biot number
Fr	Froude number
Nu	Nusselt number
Pe	Peclet number
Pr	Prandtl number
Py	Pyrolysis number
Re	Reynolds number
Sc	Schmidt Number
Sh	Sherwood number

Greek letters

$\alpha_{(\text{eff})}$	(Effective) thermal diffusivity	$\text{kg m}^{-1}s^{-1}$
α_{pvf}	Particle volume fraction of a computational cell	-
α_{cp}	Particle volume fraction at the close-packing limit	-
α_{rxn}	Overall degree of conversion	-
$\boldsymbol{\delta}_{\text{N}}$	Displacement of the surface of the particle	m
ΔH_{rxn}	Enthalpy of reaction	J kg^{-1}
Δh_{sorp}	Heat of sorption	J kg^{-1}
Δh_{vap}	Heat of vaporization	J kg^{-1}
ϵ_{p}	Emissivity of the particle	-
ϵ_w	Emissivity of the Wall	-
η	Damping coefficient	N s m^{-1}
θ	Dynamic angle of repose	$^\circ$
κ	Absorption coefficient	m^{-1}
κ^*	Modified absorption coefficient	m^{-1}
λ	Thermal conductivity	$\text{W m}^{-1}\text{K}^{-1}$
μ	Sliding friction coefficient	-
ν_{g}	Kinematic viscosity	m^2s^{-1}
μ_{g}	Dynamic viscosity	Pa s
ρ	Density	kg m^{-3}

σ	Stefan-Boltzmann constant	W m^{-2} K^{-4}
$\sigma_{s,p}$	Scattering coefficient of disperse phase	m^{-1}
σ_p	Scalar and random variation of particles' velocities	m s^{-1}
σ_Θ^2	Dimensionless variance	-
τ_G	Time constant for particle collision	s
τ_p	Solid stress	Pa
Φ	Probability function for scattered beams	sr^{-1}
Ω_i	Discrete directions with solid angles	sr

Indices

0	Initial state
∞	Infinity (time/space)
corr	Corrected
conv	Convection
devol	Devolatilization
dry	Drying
final	Final state
fsp	Fiber saturated point
g	Gas
mom	Momentum
p	Particle / disperse phase
pp	Particles per parcel
pvf	Particle volume fraction
rad , R	Radiation
rxn	Reaction
s	Surface
sorp	Sorption
temp	Temporary

1 Introduction

The development of alternative methods for using clean energy resources has become increasingly urgent due to environmental concerns. Lignocellulosic biomass and biogenic wastes are important renewable sources for energy because of their abundant supply and low life-cycle carbon emissions [1]. Their usage not only avoids any competition with food production but also helps developing an ecological solution for waste disposal [2]. However, the demand for localizing energy densification processes, i.e., biomass carbonization, is inevitable to make renewable resources for energy economically feasible. Thermally pretreated biomass can sustainably improve soil fertility and can be used to produce activated charcoal [3], [4] and constitutes the basis for coal chemistry.

Current technologies for converting biomass to energy-densified products still face many challenges. One of them is the complex nature of the various physical processes during, for instance, wet biomass carbonization [5]–[8] which is hard to assess experimentally [9]. Additionally, the fluctuating parameters of the feedstock, e.g., moisture content, volatile fraction, size distribution, etc. give rise to large uncertainties for designing and operating a specifically defined process on an industrial scale.

A well-known thermochemical conversion that upgrades the low-energy density and wet organic feedstock in the absence of oxygen is steam-assisted carbonization [10]. It is a kind of slow pyrolysis in which biomass is treated for 30 to 90 min at 250 - 400 °C in a superheated steam atmosphere [11]–[14]. This steam must either be supplied externally or fed back directly from the wet biomass. Compared to the virgin feedstock, the solid product has an increased carbon content as well as an increased calorific value and its properties are similar to brown coal. Unlike hydrothermal carbonization, the reaction time is relatively short, the process operates at atmospheric pressure [15]–[11] and, therefore, can be easily performed continuously. The purpose of utilizing steam-assisted carbonization is to maximize the yield of solid products, i.e. biochar, and its carbon content.

Steam-assisted carbonization is a thermochemical process that promotes the energy density of wet organic materials in the absence of oxygen. Besides energetic promotion, this process is a promising approach to convert unstable wastes before their biological degradation into stable and high-energy-density biochar and byproducts [16]–[18]. The process is suitable for recycling different organic waste streams with a wide range of water contents and it can convert them into a carbon-enriched

solid product. Indeed, an optimum conversion requires a well-designed and optimized process corresponding to wet biomass input and reaction conditions.

The thermochemical conversion of biomass is governed by a large number of concurrent physical and chemical processes including the motion of the pieces of biomass (from here on referred to as particles) into a suitable reactor, such as heating-up, drying, particle shrinkage and the primary pyrolysis involving countless chemical reactions and therefore it is complex to investigate. Radiative and convective heat transfer within the reactor, as well as the mass transfer under transient flow regimes, have also an additional impact on uncertainties. Experimental techniques developed in laboratory scales are difficult to scale up and the upscaling process is often based on empirical correlations.

Scale-up calculations can be supported by numerical simulations and the development of models that reproduce the interplay of the aforementioned complex phenomena. The present thesis gives an insight into the phenomena inside an indirectly heated rotary kiln loaded with a continuous flow of wet biomass. Numerical simulations and experimental studies are applied in order to improve the operation of these reactors for efficient carbonization with a higher yield of char production. The present work investigates the product properties under different circumstances due to the changes in the kiln operating conditions.

1.1 Motivation and objectives of this research

Environmental and sociopolitical motivations stand behind sustainable methods of utilizing virgin biomass and agricultural leftovers as well as municipal and biogenic waste for many industrial investors in the sector of biomass conversion. Ecological and economical interests for biomass conversion via low-temperature methods persuade the further development and improvement of the related process design. In the case of handling high moisture content feedstock, the process is remarkably energy-intensive and thus, there is a demand for any possible optimization. This is especially due to the low energy density of the feedstock and the restricted economical margin. Even in the case of environment-friendly waste disposal strategies, it is not easy to keep the process cost-effective [1]. Thus, process optimization is a key step to settle a perspective for the low-temperature conversion as a sustainable solution. Numerical simulations are important tools for the design of thermochemical processes of multi-phase flow concerning time and cost reduction.

The particles must leave the reactor when the reaction is completed. The earlier discharge causes a drop in product quality – measured by carbon recovery or calorific value – and the longer retention

is redundant and waste of energy. Thus, detailed modeling and simulation of the reactor coping with the dominant mechanisms in every reactor zone are necessary to predict the overall performance of the process precisely. The main objective of the current research is to develop a computational model for low-temperature thermal conversion of biomass in rotary kiln reactors and to find the suitable operating conditions of producing fully converted biochar through intuitive parameter variation at a minimal energy expense. Regarding the characteristics of input, this model should analyze the conversion of solid biomass and offer the best possible operating parameters for the reactor.

The study of such a complex physical system requires either oversimplifying assumptions or a comprehensive model. For the former, the assumptions limit the ability to predict process performance. For the latter, it is computationally too expensive and consequently impossible to apply for large-scale purposes. Therefore, a meaningful compromise is necessary to cover the main aspects of the physical system. The designed model in this work is thought for large-scale applications such as industrial size rotary drum reactors.

In this work[1], a transient, two-phase, multi-dimensional model is developed which is capable of handling the thermal conversion of high-moisture discrete phase in contact with the gas phase in the reactor. Biomass particles are represented by Lagrangian particles that collide and form a moving bed. The gas phase is treated as an Eulerian phase. Computational methods are based on finite volume discretization of the reactor space with a structured grid for the continuum and its interaction with the solid phase. The model includes conservation of mass, momentum, energy and species for each biomass particle (discrete phase) as well as for the continuous phase. Both phases are fully coupled with the exchange of momentum, energy, and mass of chemical species.

To carry out the detailed simulation including all modules, the geometries of a laboratory-scale and industrial-scale reactor are given. The numerical model including various submodels is implemented, further developed and verified on the laboratory-scale geometry. Thereafter, the results are validated against experimental data. The verified model consequently is applied to a large-scale reactor. Then the final solid conversion is studied at various reactor temperatures to find an optimum temperature at a constant mass flow. The results suggest a practical resolved method

for the simulation of solid conversion in industrial-scale reactors which evaluates whether the setup is optimized and cost-effective for the given operating and input conditions.

1.2 Challenges

The main challenges for slow thermal conversion processes with multi-phase reacting flows can be categorized into three sequential groups. First, the characterization of the input biomass that is used in the conversion. The determination of the biomass properties restricts the decisions for the second concern which is the design of the reactor. Based on the assumed input characteristics and the chosen reactor design, the dominant process steps that occur during the overall process can be specified. Furthermore, modeling and optimization of physical and chemical processes related to these steps can proceed.

1.2.1 Characterization of the input materials

The multiphase flow in the reactor is highly complex and the optimization of the operating conditions for desired product yields is difficult. The varying characteristics of the wet input, e.g., moisture content, volatile fraction, etc., which influence the thermophysical and physical properties of the particles, additionally escalate the complexity. In addition, because of the multi-scale nature of the biomass feedstock, which is due to the existence of various components, the performance of the reactor depends significantly on the geometrical and material characteristics of the biomass particles [19]. Therefore, it is almost impossible to predict the process performance without consideration of a well-defined range for feedstock characteristics. Hence, a deeper understanding of the conversion process and its milestones are necessary by means of numerical modeling and simulation a well as experimental investigations.

Particle size and its distribution have a decisive role in specifying the type of reactor and consequently mixing and residence time. During the transport of the bulk in the reactor, different particle sizes may result in widespread residence times. On the other hand, the interaction between heat and mass transport, due to particle shrinkage, can lead to different temperatures and residence times for the diverse sizes of the bulk material. The influence of the shrinkage on size distribution has a direct impact on the bed motion, mixing and back mixing behavior within the reactor. This is particularly important in this context since the average residence time has to be defined by the completed thermochemical conversion.

So, every small variation in the input has a direct effect on the overall thermochemical conversion and consequently the properties of the product. Numerical simulation can help to identify the operational conditions, regarding the arbitrary properties of the input biomass to ensure a uniform consistency of the produced biochar.

1.2.2 Design of the reactor

Besides the mentioned restricting parameters, other characteristics of the input and product such as material sensitivity or operational hazards have also a crucial influence on the type of reactor. The method of heat transfer to the reactants is an essential key step for the design of the reactor. For instance, a low rate of heat transport to biomass in low-temperature thermochemical conversions is a significant challenge for reactor design. It is because of the temperature sensitivity of the reactant on one hand and the demand for a long reaction time on the other hand.

Depending on the requirements of the thermal processes, reactors can be heated directly, e.g., flames in the tube or indirectly by means of the heated wall. The industrial process studied in this work requires the use of indirectly heated reactors to fulfill the requirements for the sensitivity of the material against extremely high temperatures and the presence of oxygen.

Among different applicable types of reactors, tubular reactors with indirectly heated walls are chosen for the thermal treatment of biomass utilizing the steam-assisted carbonization in this study. Tubular reactors are apparatuses utilized in many industries for the thermochemical treatment of bulk materials generally at high temperatures. They are often constructed including rotary tubes with or without internal flights or including rotating screws.

1.2.3 Modeling and optimization of processes inside the reactor

With known input properties and the reactor design, it is possible to specify the dominant phenomena inside the reactor. Generally, there are mechanical and thermal process steps that have the most effect on the overall process. The main challenge of this study is to model the specified processes, couple them and apply appropriate optimization.

Mechanical processes involve the physical movement taking place due to the collision of single particles and thereupon the general motion of the bulk. By a valid model for the mechanical process in the reactor, bed motion, residence time and mixing can be studied and simulated. This needs a straightforward experimental verification for a resolved solid phase model because of the complex particle interaction and physical movement within the reactor.

Thermal processes are phenomena related to heat and mass transfer between the reactor, gas phase and solid phase. These processes connect both phases tightly and thus a proper coupling is needed. It includes the heating of the initial gas and injected particles in the first step via diverse mechanisms of heat transfer. In the next step, the drying of moist particles as the most energy-intensive part of the process occurs followed by the release of the relatively colder vapor to its surrounding gas. After the drying process, a further increase in temperature of the bulk is followed to the critical temperature in which the thermal decomposition of the biomass begins. The release of volatiles from biomass referred to devolatilization proceeds through a kinetic law of the carbonization reaction. Depending on the reactor design, the drying can occur in a separate step or together with the carbonization reaction in a single-step process. For steam-assisted conversions, it is common to have a single step process which is the case here.

In the complex processes involved in the wet-biomass carbonization, the influence of the mechanical and thermal processes is twisted mutually and they affect each other. For instance, the local bulk density has an influence on the transverse mixing behavior of the solid. In the case of polydisperse feedstock or feedstock under chemical reactions resulting in shrinkage of particles (which shifts the particle size distribution), the local bulk density is varying. This can cause a different bed motion along the reactor depending on the state of the solid phase. Therefore, it is important to assess the regime of transversal movement of bulk in the reactor to ensure an efficient mixing behavior.

Only a comprehensive model with resolved and coupled modules can overcome these challenges and deliver reliable results, which can lead to cost-effective process design and practical implementation. This study is going to suggest a multiphase resolved three dimensional model for the thermochemical conversion of biomass in rotary kiln reactors.

2 Physical and Mathematical Model of Rotary Kilns

2.1 Rotary kiln reactor

Tubular reactors are devices used in many industries for the thermochemical treatment of granular bulk materials generally at high temperatures. They usually consist of at least one rotary part and are often provided with rotating internals for the treatment of solids or as rotary tubes with or without internals flights. The axial bulk transport is maintained by means of the continuous rotation around the horizontal axis where the reactor is set in a slightly tilted position. A rotary kiln is a long rotating horizontal cylinder with a certain inclination with respect to its axis [20].

Depending on the design specifications and the characteristics of the process, a rotary kiln can be designed and operated by direct or indirect heating conditions. Material within the kiln is heated directly through hot flue gas in the freeboard gas or indirectly (externally) via the heated wall to high temperatures so that physical processes and chemical reactions can take place. Thus, rotary kilns are fundamentally a tube heat exchanger in which energy is transferred from the hot gas or heated wall to the solid bulk undergoing chemical reaction [21].

Indirectly heated kilns are designed for applications where the material is temperature-sensitive or only specific ambient composition, e.g. an inert gas, is desired for the contact with material under the reaction. As an example, for the pyrolysis of biomass, both of the aforementioned statements are required. So, generally, indirectly heated kilns are utilized instead of direct-fired kilns when direct contact between the providing gas and the material should be limited or avoided. On the other hand, due to the lower thermal efficiency, indirectly heated kilns are built usually below 1.3 m in diameter [21].

Due to the multiple and compartmentalized heating zones, indirect-fired kilns have a particular advantage in controlling and setting temperature zones individually (see Figure 2.1). Thus, a gradual and well-defined heating rate is easily achievable in the reactor. Historically, rotating kilns for pyrolysis have been developed for the treatment of municipal solid waste several decades ago in Japan and Europe [3]. There are several operational advantages of a rotating drum reactor over traditional reactors (such as Lambiotte reactor, operating on a packed and moving bed). One of the highlighted ones is that any arbitrary size of the particles could be processed without the risk of disproportionate

pressure drop or considerable segregation. This explains the reason behind the application of thermal treatment of municipal solid waste and agricultural residue in rotary kilns. Disadvantages can be the occurrence of back mixing and extensive attrition, which may give rise to large quantities of fines and flying particles [18].
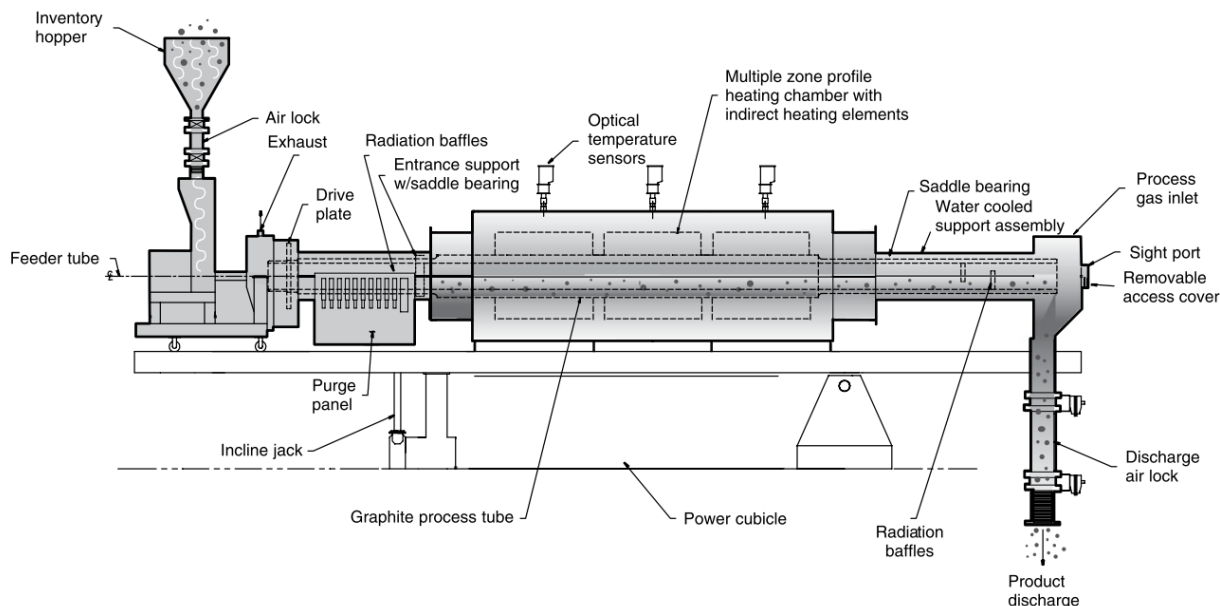
Figure 2.1 Scheme of a typical indirectly (externally) heated rotary kiln and its axillary units, from [21].

2.2 Steam-assisted carbonization of biomass

Conversion of biologically unstable biomass to an energy-densified form of stable fuel is a major motivation for the shift from fossil fuels to biomass. Among the wide field of biomass conversion including both biochemical and thermal conversion routes, rotary kiln devices are only suitable for the operation of the pyrolysis conversion family, namely torrefaction, carbonization and quasi-fast pyrolysis. The type of thermal conversion is bonded to the necessary pre-treatment steps, biomass characterizations and most importantly the definition of the desired product which has been discussed in previous studies [22]. Carbonization is a low temperature and low heating rate slow pyrolysis [2] in which the biomass undergoes an accelerated coalification reaction. Unlike natural coalification which can take up to millions of years, the carbonization process can occur within hours. Steam-assisted carbonization is proven to be an improved reaction mechanism of carbonization regarding enhanced heat and mass transfer, reaction mechanism and char yield [11]–[13], [23], [24].
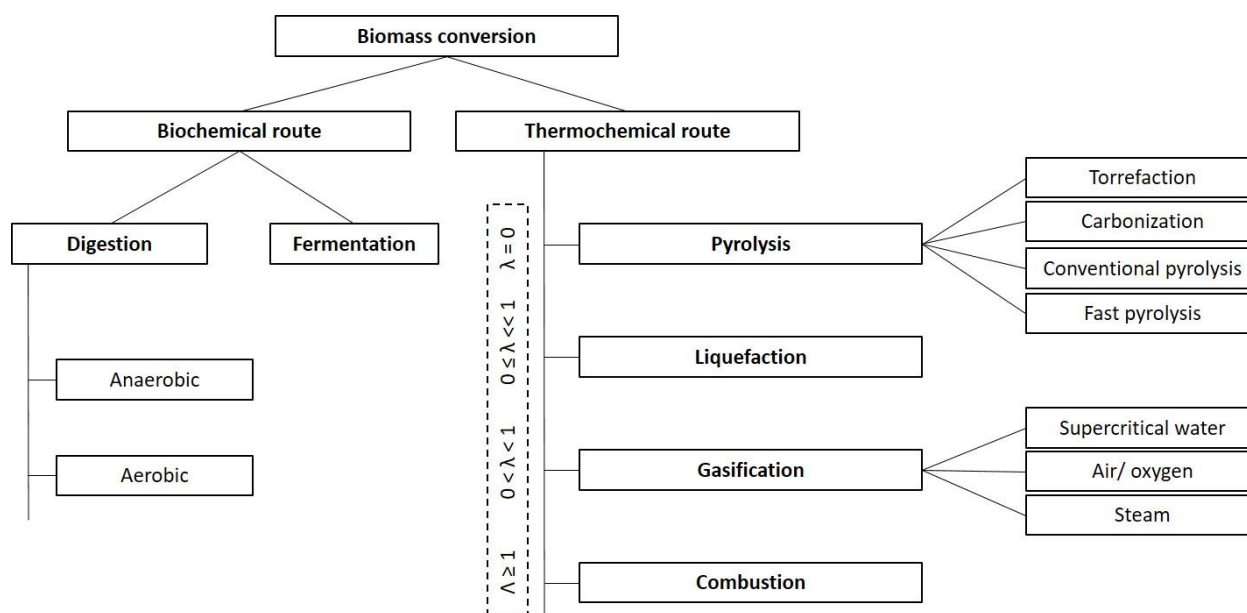
Figure 2.2 Routes of conversion of biomass into fuel, gases, or chemicals; with modification from [2].

In steam-assisted carbonization, the biomass is heated slowly in the absence of oxygen to a relatively low temperature e.g., 300 – 400 °C, over an extended period [24]. Unlike the conventional and fast pyrolysis, in steam-assisted carbonization, there is no need for drying and any other kinds of pre-treatment. Therefore, a single-stage reactor can be designed for the entire process from wet biomass to char. For biomass with above 30 wt.% moisture, the process is self-sustainable regarding steam production and there is no need to inject superheated steam additionally. Remarkable features of steam-assisted carbonization can be summarized by maximizing the char yield, enhancing the product quality in terms of carbon content and optimization of the energy consumption of the process. Additionally, from the operational point of view, the excess amount of steam in the process prevents the tar condensation and blockage of pipelines which is a usual problem in ordinary pyrolysis plants.

2.3 Aspects of selecting carbonization reactors

Ecological friendliness as a crucial factor of sustainable design requires modern plants to integrate afterburner units to oxidize pyrolysis gases [18]. Additionally, from an economical point of view, it is very important to combine the afterburner unit with a heat recovery system to gain back a part of the process energy after oxidizing and inertizing the hazardous organic substances by the combustion. The heating model and schematic process flow diagram of the steam-assisted carbonization via an indirectly heated rotary drum is shown in Figure 2.3.
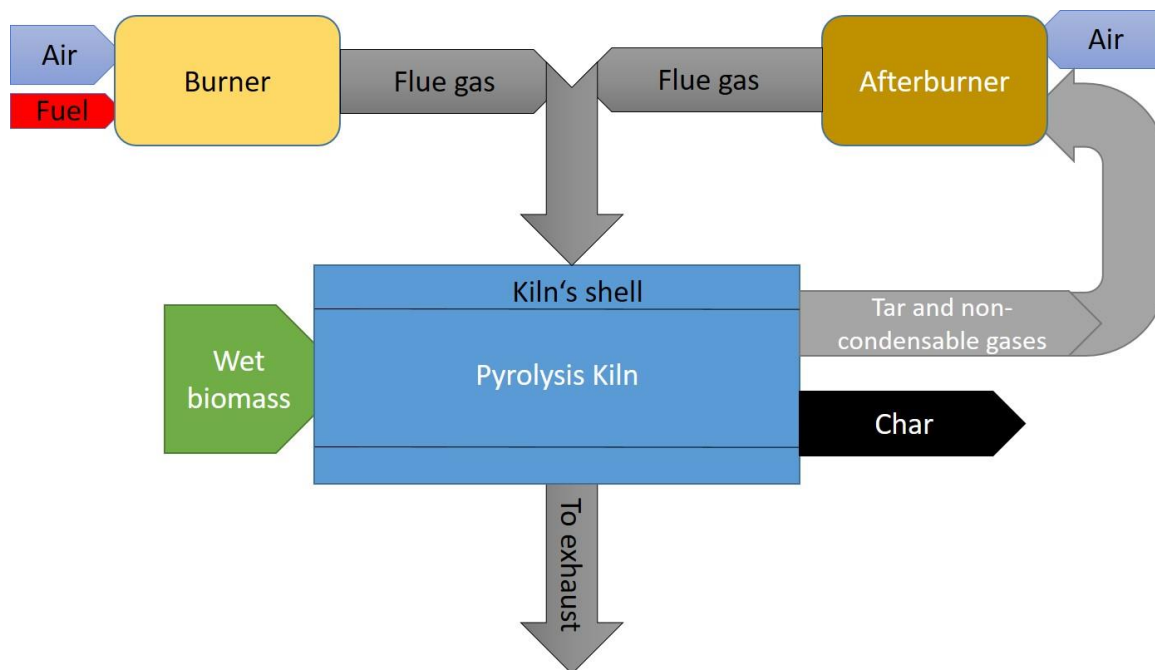
Figure 2.3 Schematic process flow diagram of the carbonization via indirectly heated rotary drum.

A decisive aspect of the carbonization process is the certain flexibility concerning the feedstock characteristics. The advantage of rotary kilns is that they allow fine and fast tuning of the process conditions regardless of the plant size. The quality of the input can be changed day to day due to countless factors such as seasonal and composition fluctuations. Current technologies that meet the aforementioned criteria for carbonization are screw (auger) reactors and rotary kilns [18]. Despite the advantages regarding narrow residence time distribution (close to ideal plug flow reactors) and almost no back mixing, screw reactors are not preferred for industrial-scale plants. Highlighted reasons can be due to less radial mixing and consequently even lower thermal efficiency, construc-tional difficulty and less flexibility concerning the size of the input. The practical experience of the author's research group proves higher maintenance cost and the probability of shut down especially in case of operating wet and sludgy biomass due to constant blockage and damage of the long screw. For higher operational temperatures, the maintenance requirements of screw reactors are even higher due to the thermal stress on the axial shaft of the screw by facing a large temperature differ-ence which can cause deformation.

Rotary kilns, besides their widely known applications in the cement industry, are employed to carry out a wide range of operations such as the reduction of ore, the calcination of petroleum coke, the recycling of hazardous waste and last but not the last the thermal conversions of biomass [20]. With the growing interest in biochar, there is increased demand for continuous carbonization units with capacities ranging above one ton per day of charcoal production. Rotary kilns are already adopted

and redesigned successfully for various biomass treatments. A Simplified layout of an indirectly heated rotary drum for charcoal production is shown in Figure 2.4.
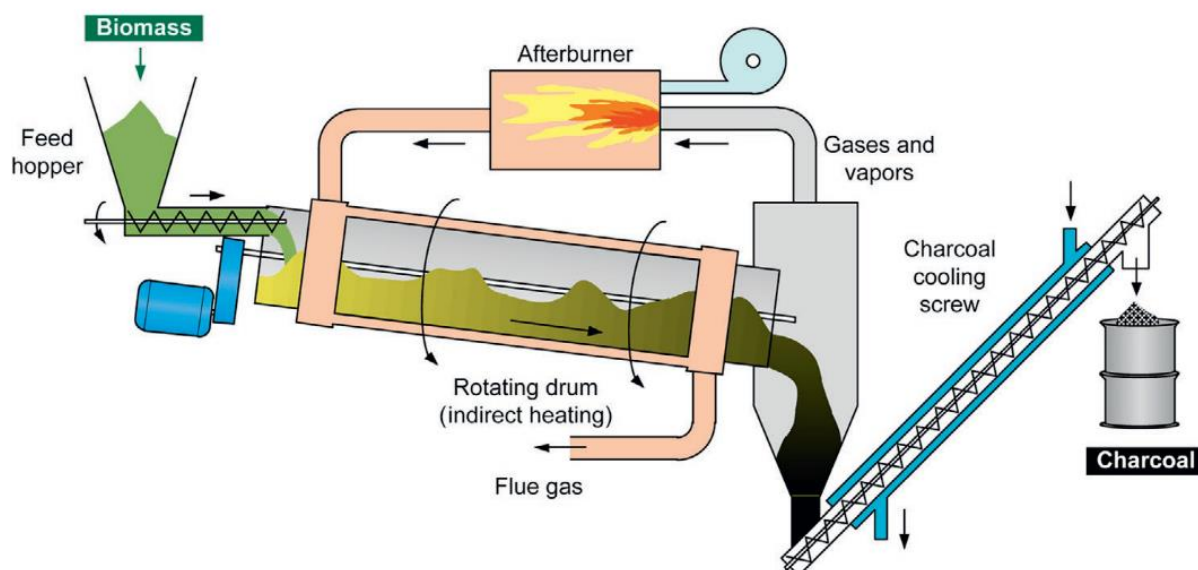
Figure 2.4 Simplified layout of an indirectly heated rotary drum for charcoal production from [18].

2.4 Demand for detailed modeling

The interactions between reactor- and process-related variables like heat and mass transfer and chemical reactions are determined by a large number of parameters. On the other hand, material-related properties play an important role in the reactor design. Generally, the experimental determination of the influences of these parameters is not reasonable, because of the dramatically expensive procedure to obtain results in terms of cost and time. This increases the investment risks and therefore endangers the industry-originated projects.

Recently, several numerical methods are developed based on related physical models in which these interactions are coupled and interpreted for the design of such reactor systems. However, it is often the case that very strong simplifications are introduced into these models [16], [20], [25]–[31].

In contrast, the suggested approach in this work covers more details and it is computationally time-intensive due to the comprehensive physical and chemical processes which take place in each phase and between them. Nevertheless, the numerical simulation seems promising regarding the competence for a detailed comparison to the experimental investigation of such systems.

In this work, a detailed multiphase numerical model has been further developed, utilized and proposed for applications of scale-up and comprehensive studies of multiphase and reacting flows and their interaction in the reactor. Finally, the model is compared with conventional steady-state mass and energy calculations based on non-differential equations. In the further sections fundamental physical and mathematical models which are necessary for the numerical approach will be covered.

2.5 Governing Equations for the discrete phase

Governing equations of the discrete phase are different and separated from the continuous phase. Governing equations will be solved for each particle, which in this study represents a moist piece of biomass. Law of mass conservation as the first governing equation for discrete phase is

$$-\frac{\mathrm{d}m_{\mathrm{p}}}{\mathrm{d}t} = \frac{\mathrm{d}m_{\mathrm{drying}}}{\mathrm{d}t} + \frac{\mathrm{d}m_{\mathrm{devolatilization}}}{\mathrm{d}t}, \qquad (2.1)$$

where the left-hand side of Equation 2.1 is the overall change of mass of a particle over time and the right-hand side shows the mass change due to drying and devolatilization from the particle, respectively. A biomass particle in this equation initially contains char, ash, moisture and volatiles. During the drying, the moisture will be transferred to the gas and dried biomass remains. Devolatilization releases the volatiles from the particle and the final product, containing char and ash, stays unchanged in this study, e.g., no further reactions at the char surface occur.

The calculated mass release from each particle is summed and coupled to the continuity equation of the continuous phase (written in section 2.6) as a source term. For this purpose, the species source terms are defined to transport the exact amount of every component between phases. Therefore, the conservation of species is considered separately from the mass conservation equation for both phases (section 2.6).

The particle shrinkage influences the particle interaction forces and consequently, it reduces the precision of the particle trajectory, if not considered [32]. Additionally, it has a direct impact on heat transfer to particles, thus unrealistic sizes lead to inaccuracy in the model. For larger particles, the effect of particle shrinkage is more important because of the critical diameter of particles during the reaction (will be discussed in section 2.12.1). Thus, a suitable shrinkage model is an essential prerequisite for an accurate simulation. The constant-density shrinkage is used in this study, where it is assumed that the volume reduction of the particle occurs during the drying and devolatilization process proportional to the mass of volatile products [33]. In this shrinkage model, the diameter of each particle is calculated through a mass-proportional equation by

$$d_{\mathrm{p}} = \left(\frac{6\,m_{\mathrm{p}}}{\pi\,\rho_p}\right)^{1/3}, \tag{2.2}$$

where m_p and ρ_p depict mass and density of the particle and d_p is the diameter.

In order to obtain the temperature of particles, an energy balance has to be written for each particle. Equation 2.3 is the energy conservation equation for each particle based on the different considered processes.

$$m_{\mathrm{p}}c_{p_{\mathrm{p}}}\frac{\mathrm{d}T_{\mathrm{p}}}{\mathrm{d}t} = h_p \cdot A_{\mathrm{s}}\left(T_{\mathrm{g}} - T_{\mathrm{p}}\right) + \epsilon_{\mathrm{p}}\left(A_{\mathrm{p}}G_{p} - \sigma A_{\mathrm{s}}T_{\mathrm{p}}^{4}\right) - \dot{Q}_{\mathrm{dry.}} - \dot{Q}_{\mathrm{devol.}} \tag{2.3}$$

T_p is the temperature of the particle, and on the right-hand side terms are the heat transfer due to convection, radiation (first and second term respectively) and source terms $\dot{Q}_{\mathrm{dry(ing)}}$ and $\dot{Q}_{\mathrm{devol(atilization)}}$ representing the latent heat of phase change of moisture and the endothermic devolatilization processes, respectively. The model is known for an assumption, in which the physical properties of the particle are considered to be uniform within the particle. Here $c_{p_{\mathrm{p}}}$ is the instantaneous isobaric specific heat capacity. h_p represents the local convective heat transfer coefficient obtained from the Ranz-Marshall correlation (section 2.9.1) [34]. A_{p} and A_{s} are the projected and surface areas of the particle and T_{g} is the local gas temperature, ϵ_{p} the particle emissivity, G_p the incident radiation and σ indicates the Stefan-Boltzmann constant.

The governing equation for the momentum of each particle follows Newton's second law. Equation 2.4 shows the results of the kinematic forces. The location of each particle can then be calculated according to

$$m_p \frac{\mathrm{d}\mathbf{v}_{\mathrm{p}}}{\mathrm{d}t} = \sum \boldsymbol{F}_{\mathrm{external}} = \mathbf{F}_{\mathrm{c}} + \mathbf{F}_{\mathrm{g}} + \mathbf{F}_{\mathrm{d}} + \mathbf{F}_{\mathrm{p}} + \mathbf{F}_{\mathrm{v}}, \tag{2.4}$$

$$\frac{\mathrm{d}\boldsymbol{x}_{\mathrm{p}}}{\mathrm{d}t} = \mathbf{v}_{\mathrm{p}}, \tag{2.5}$$

where $\boldsymbol{x}_{\mathrm{p}}$ and $\mathbf{v}_{\mathrm{p}}$ represent the location and velocity of the particle respectively. $\mathbf{F}_{\mathrm{c}}$ is the force from collisions with other particles and the wall of the reactor (to be considered in more detail in section 2.8), $\mathbf{F}_{g}$ shown in Equation 2.6 is the result of gravity and buoyancy force and $\mathbf{F}_{\mathrm{d}}$ from Equation 2.7 is the drag force, based on the solid-sphere drag model. $\mathbf{F}_{\mathrm{p}}$ and $\boldsymbol{F}_{\mathrm{v}}$ are the pressure gradient and virtual mass forces, respectively and they are neglected due to their insignificant influence in this study [35].

$$\mathbf{F}_{\mathrm{g}} = m_{\mathrm{p}} \, \boldsymbol{g} \left(1 - \frac{\rho_{\mathrm{g}}}{\rho_{\mathrm{p}}} \right), \tag{2.6}$$

$$\mathbf{F}_{\mathrm{d}} = \frac{3 \, m_{\mathrm{p}} \, C_{\mathrm{d}} \, Re_{\mathrm{p}} \, \mu_{\mathrm{g}}}{4 \, \rho_{\mathrm{p}} \, d_{\mathrm{p}}^2} \left(\mathbf{v}_{\mathrm{p}} - \boldsymbol{u}_{\mathrm{g}} \right), \tag{2.7}$$

ρ_g and μ_g are the gas density and dynamic viscosity, $\mathbf{u}_{\mathrm{g}}$ is the gas velocity. Drag coefficient C_d is calculated depending on the particle Reynolds number Re_p (Equation 2.8) in Equation 2.9 [35]

$$Re_{\mathrm{p}} = \frac{|\boldsymbol{u}_{\mathrm{g}} - \mathbf{v}_{\mathrm{p}}| \, \rho_{\mathrm{g}} \, d_{\mathrm{p}}}{\mu_{\mathrm{g}}}, \tag{2.8}$$

$$C_{\mathrm{d}} = \begin{cases} \dfrac{24}{Re_{\mathrm{p}}} \left(1 + \dfrac{1}{6} \, Re_{\mathrm{p}}^{2/3} \right), & Re_{\mathrm{p}} \leq 1000 \\ 0.424 \, Re_{\mathrm{p}} \quad , & Re_{\mathrm{p}} \geq 1000 \end{cases}. \tag{2.9}$$

In order to calculate the velocity of each particle from Equation 2.4, dominant forces are gravity $\mathbf{F}_{\mathrm{g}}$ and collision including inter-particle and particle-wall interactions collected in the term $\mathbf{F}_{\mathrm{c}}$. The physical model and related mathematical equations regarding the collision will be presented in section 2.8.

2.6 Governing equations for the continuous phase

In most of the thermal conversion processes without combustion, the gas velocity does not approach the speed of sound ($Ma \ll 1$; the ratio of gas velocity to the speed of sound) and consequently, compressibility effects are negligible. The gas density, on the other hand, does vary due to the significant temperature and composition changes. For this, equations in the solver for the continuous phase are fully compressible and in addition, the buoyancy force is considered in the model.

The gas phase is observed as a density-varying continuum and the flow is assumed laminar or turbulent depending on the gas velocity within the reactor. Its interaction with the solid phase is taken into account by source terms in the governing equations, due to the exchange of mass, momentum, and energy between two phases. In general, the velocity of the continuous phase is very low in the entire domain because there is no additional gas introduced to the reactor. In larger scales, due to the higher Reynolds numbers and disturbance between the solid and gas phase, turbulence needs to be considered.

For the continuous phase, conventional governing equations for mass, momentum, energy, and species are represented respectively by the following equations

$$\frac{\partial \rho_{\mathrm{g}}}{\partial t} + \nabla \cdot \left(\rho_{\mathrm{g}} \boldsymbol{u}_{\mathrm{g}}\right) = S_{\mathrm{p},m} \, , \tag{2.10}$$

$$\frac{\partial \left(\rho_{\mathrm{g}} \boldsymbol{u}_{\mathrm{g}}\right)}{\partial t} + \nabla \cdot \left(\rho_{\mathrm{g}} \boldsymbol{u}_{\mathrm{g}} \boldsymbol{u}_{\mathrm{g}}\right) = -\nabla p + \nabla \cdot \boldsymbol{\tau}_{\mathrm{eff}} + \rho_{\mathrm{g}} \boldsymbol{g} + \boldsymbol{S}_{\mathrm{p},mom} \, , \tag{2.11}$$

$$\frac{\partial}{\partial t}\left(\rho_{\mathrm{g}} h_{tot}\right) + \nabla \cdot \left(\boldsymbol{u}_{\mathrm{g}} \rho_{\mathrm{g}} h_{tot}\right) = \frac{\partial p}{\partial t} + \nabla \cdot \left(\alpha_{\mathrm{eff}} \nabla h_{\mathrm{s}}\right) + S_{\mathrm{p},h} + S_{\mathrm{rad}} \, , \tag{2.12}$$

$$\frac{\partial \rho_{\mathrm{g}} Y_i}{\partial t} + \nabla \cdot \left(\rho_{\mathrm{g}} \boldsymbol{u}_{\mathrm{g}} Y_i\right) = \nabla \cdot \left(\rho_{\mathrm{g}} D_{i,\mathrm{eff}} \nabla Y_i\right) + S_{\mathrm{p},Y_i}, \tag{2.13}$$

where $\boldsymbol{u}_g$ is the gas velocity, ρ_g the density, p the static gas pressure, $\boldsymbol{g}$ the gravitational acceleration. The energy equation is defined here in the enthalpy form, where h_{tot} is the total enthalpy, h_{s} the sensible enthalpy of the gas phase and $\alpha_{\mathrm{eff}} = \frac{\lambda_g}{c_{p_g}}$ the thermal diffusivity. $S_{\mathrm{p,m}}$, $\boldsymbol{S}_{\mathrm{p},mom}$, $S_{\mathrm{p,h}}$ and S_{p,Y_i} are the source terms that describe interphase exchange terms for mass, momentum, enthalpy, and species between gas and particles, respectively. S_{rad} is the radiation source term from the heated wall or the discrete phase, i.e., what is absorbed by the gas in the control volume. The $\boldsymbol{\tau}_{\mathrm{eff}}$ is an effective stress tensor for the calculation of effective shear viscosity of the gas, allowing for contributions from both the laminar and the turbulent viscosities. α_{eff} is the effective thermal diffusivity and $D_{i,\mathrm{eff}}$ is the effective mass diffusivity.

In principle, Equation 2.13 has to be solved for any chemical species being released from the solid phase during devolatilization and drying. In this work, a simplified reaction mechanism representing devolatilization with the help of a multi-species one-step reaction is used. Therefore, the reaction rates of the different species are coupled with the decomposition rate of the solid and mass balances for only a limited number of species have to be calculated. Details are given in section 2.11.

In this section, a very brief overview of the governing equations for the continuous phase has been given. This study will focus more on the investigation of the discrete phase and the modeling of related processes in the rotary drums. More information for the well-studied continuous phase can be found vastly in the literature including [21], [31], [36].

2.7 Transverse motion of particles in the rotary kiln

Mixing and motion of solid materials in rotary kilns are highly dependent on the transversal type of movement of the solid bed. Although it decisively affects the temperature of the bed and its con-

version, in most of the research the bed is modeled as a transversely well-mixed plane, e.g., continuous stirred tank models, that is, the bed material is isothermal over any transverse section of the kiln. However, many kiln operations suffer from considerable difficulty in achieving a uniform product composition as it is the case in lime production and biomass conversion, where grain size differences exist. Thus, often the ability to simulate the freeboard conditions tends to exceed the ability to determine conditions within the bed [21].

To establish the type of movement of the particles in the rotary kiln for experimental work and the simulations, it is essential to define criteria comparable to literature. As Henein et al. suggested, based on simple physical models, transition criteria can be derived in the form of critical wall friction coefficients and critical rotational Froude numbers in terms of the filling degree which can be reflected on the bed behavior diagram [37].

Table 2.1 Forms of transverse motion of solids in rotating cylinders from [38]

Basic form	Slipping motion		Cascading ("tumbling") motion			Cataracting motion	
Subtype	Sliding	Surging	Slumping	Rolling	Cascading	Cataracting	Centrifuging
Schematic							
Physical process	Slipping		Mixing			Crushing	Centrifuging
Froude number Fr [-]	$0 < Fr < 10^{-4}$		$10^{-5} < Fr < 10^{-3}$	$10^{-4} < Fr < 10^{-2}$	$10^{-3} < Fr < 10^{-1}$	$0.1 < Fr < 1$	$Fr \geq 1$
Filling degree f [-]	$f < 0.1$	$f > 0.1$	$f < 0.1$	$f > 0.1$		$f > 0.2$	
Wall friction coeff. μ_w [-]	$\mu_w < \mu_{w,c}$	$\mu_w \geq \mu_{w,c}$	$\mu_w > \mu_{w,c}$			$\mu_w > \mu_{w,c}$	
Application	no use		Rotary kilns and reactors; rotary dryers and coolers; mixing drums			Ball mills	no use
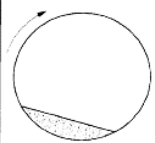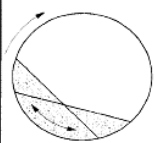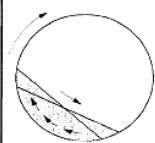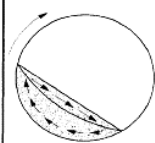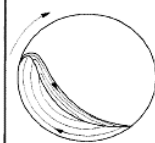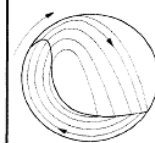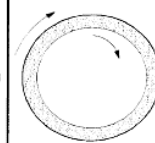
Table 2.1 summarizes the basic forms and various types of transverse bed motion in rotating cylinders where the rotational Froude number $Fr = \dfrac{\omega^2 R}{g}$ is a dimensionless criterion for measuring the ratio of the inertial forces to the gravitational forces, by ω as the angular speed of the cylinder, R its radius and g the acceleration due to gravity in SI units. Regarding the application of any device, it has to be designed in a way that the bed motion and the mixing meet the related criteria shown in the table.

The bed motion is the result of the movement of all particles and their collisions with each other and the rotating wall. A resolved particle-particle and particle-wall collision should lead to a corresponding bed motion. Therefore, available particle collision models that can be applied to this work are introduced and discussed next.

2.8 Particle Collision Model

2.8.1 Soft sphere model

The soft-sphere collision model, usually known as the discrete element method (DEM), is the resolved calculation of granular particles. The soft-sphere collision model has been reintroduced and validated by Cundall and Strack [39]. In order to formulate the contact forces between two particles or particle-wall, the suggested spring-dashpot-slider from Cundall et al. has been used. This particle collision model assumes that the contact maintains for a period of time [40]. During the collision process, a slight overlap exists between the particles to represent the deformation at the contacting surface. Figure 2.5 schematically presents how particle-particle interaction occurs and how neighboring particles collide with each other.
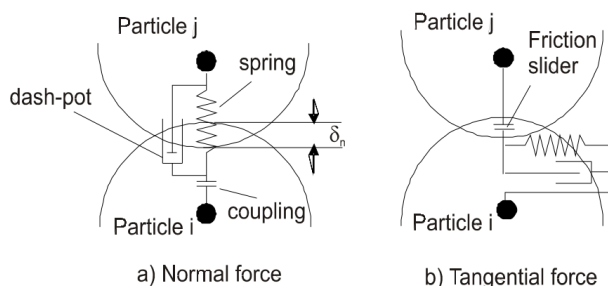
Figure 2.5 Soft sphere models used in DEM a) spring-dashpot model used for normal force.
b) spring-friction slider model used for tangential force; from [35].

Efforts and developments of Tsuji et al. finally completed the model considering the effect of fluid on the movement of granular particles in a horizontal pipe [41]. In this model, inter-particle forces were expressed by using the Hertzian contact theory as done by Cundall et al. [39] and additionally the Ergun drag model was applied to give the fluid force acting on particles in a moving or stationary bed [41].

The formulation of the soft sphere model used in DEM is described comprehensively in [35], [39], [41], [42]. For the sake of brevity, only the main equations are written here,

$$\mathbf{F_c} = \mathbf{F_N} + \mathbf{F_T}, \tag{2.14}$$

$$\mathbf{F_N} = k_N \, \boldsymbol{\delta}_N^{\frac{3}{2}} - \eta \, \boldsymbol{U}_{rel,N}, \tag{2.15}$$

Equation 2.14 shows the collision force $\mathbf{F_c}$, which is a dominating term from Equation 2.4 in the case of a dense phase system. $\mathbf{F_c}$ is a resultant of normal $\mathbf{F_N}$ and tangential $\mathbf{F_T}$ forces for each collision. Equation 2.15 calculates the normal force $\mathbf{F_N}$ based on Hertzian contact theory where $\boldsymbol{U}_{rel,N}$ is the relative velocity between contacting particles in the normal direction. Normal stiffness $k_N = 4/3 \, \sqrt{R} \, E^*$ will be computed regarding effective Young's modulus $E^* = E/2 \, (1 - v^2)^*$ by known Poisson's ratio v and equivalent radius $R = 0.5 \, d_A \, d_B/(d_A + d_B)$. The damping coefficient $\eta = \xi \, \sqrt{M \, k_N} \, \sqrt[4]{|\delta_N|}$ is evaluated from [41], where ξ is an empirical coefficient related to the restitution coefficient, M is the effective mass and $\boldsymbol{\delta}_N$ is the displacement of the surface of the particles in the normal direction.

Tangential force $\mathbf{F_T}$ (Equation 2.16) is calculated from the same methodology as $\mathbf{F_N}$ in the case that the tangential force is smaller than the sliding friction force, meaning that the particle does not slip,

$$\mathbf{F_T} = -k_T \, \boldsymbol{\delta}_T - \eta \, \boldsymbol{U}_{slip}, \tag{2.16}$$

with tangential stiffness as $k_T = 8 \, \sqrt{R \, |\boldsymbol{\delta}_T|} \, G^*$. The damping coefficient in tangential directions equals the one in the normal direction according to Tsuji et al. [42]. Tangential stiffness k_T will be computed regarding effective shear modulus $G^* = G/2 \, (2 - v)$ by shear modulus $G = E/2 \, (1 - v)$ which is related to Young's modulus.

If the tangential force is greater than the sliding friction force, the particle slips and the tangential force is calculated by Coulomb's friction law

$$\mathbf{F_T} = \mu \cdot \mathbf{F_N} \tag{2.17}$$

In the particle collision model, for the calculation of particle-wall interaction, all of the above-mentioned equations for particle-particle collision are valid. The only difference is instead of the second particle, the wall is assumed as a hard surface.

2.8.2 Hard sphere model

As the soft-sphere approach can be employed to collisions with various kinds of discrete and continuous regimes, the hard-sphere model is restricted to applications where the collision can be treated as an instantaneous collision of two particles. Thus, the possible occurrence of multiple collisions at the same instant is a huge challenge for this model [40]. However, the hard-sphere

model is mathematically simplified and suitable to apply in case of studying large numbers of particles. The hard-sphere model decomposes the particle velocity vector to its normal and tangential components when a particle encounters a wall

$$\mathbf{v}_\text{p} = \mathbf{v}_\text{N} + \mathbf{v}_\text{T} \,, \tag{2.18}$$

$$\mathbf{v}_\text{N}^{(t+1)} = -e \cdot \mathbf{v}_\text{N}^{(t)} \,, \tag{22.18a}$$

$$\mathbf{v}_\text{T}^{(t+1)} = (1 - \mu) \cdot \mathbf{v}_\text{T}^{(t)} \,, \tag{22.18b}$$

where $\mathbf{v}_\text{N}^{(t)}$ and $\mathbf{v}_\text{T}^{(t)}$ show the impact velocity (before the collision) and $\mathbf{v}_\text{N}^{(t+1)}$ and $\mathbf{v}_\text{T}^{(t+1)}$ represent the normal and tangential velocities after the rebound. In Equations 2.18 the particle velocity is calculated relative to the wall. Therefore, it is assumed that the wall is relatively motionless. For inter-particle collision, the same assumption has to be taken consequently. The restitution coefficient e for the direction normal to the wall indicates how elastic or plastic the collision effect is. A fully elastic impact is described by $e = 1$ and an inelastic impact by $e = 0$ and in between, the impact is partially elastic. μ functions analogously for the tangential component of the velocity and it can be interpreted physically as the tangential friction coefficient. However, it is defined vice versa, so that $\mu = 0$ describes a fully frictionless impact and $\mu = 1$ describes a sticking-like behavior of particle to the surface. Both e and μ are user input properties.

In this section, two different physical models of particle collision are discussed. In the next chapter, their implementation in numerical models will be explained. Additionally, the pros, cons and restrictions in numerical applications will be reviewed thoroughly.

2.9 Heat transfer in the rotary kiln

The heat flux through hot walls is required to drive several phenomena in the reactor during the thermal conversion. First, sensible heat is required to increase the temperature of the gas and particles. Consequently, the latent heat is taken up to dry and further to remove bound water from the biomass particle. Next, again sensible heat brings the hot and dried particle to the point at which decomposition and devolatilization occur. The major part of the heat transfer to the solid-phase is assumed to take place over two mechanisms of convection and radiation, if a heat carrier, e.g. sand in fast pyrolysis, is not involved in the process [18]. Energy coupling between the continuum and discrete phase is expressed by Equations 2.3 and 2.12. Gray gas assumption is taken for the radiative heat transfer to the continuous phase.

Convective heat transfer deals with particles and their surrounding gas. The influence of radiation in the operating temperature of this work is neither negligible nor substitutable with other parameters, for instance, by using the assumption of effective conductive heat [43]. It is also not accurate to use the modified (e.g., external) heat transfer coefficient to account for radiant heat in case of high temperature moving bed with decomposition [44]. The radiative heat transport to the discrete phase is to be calculated based on the temperature of particles, their surrounding gas and the heated walls.

The particles are assumed to be perfectly shaped spheres. It means that the contact surface between neighboring particles is zero and therefore, the contact heat transfer between particles cannot be calculated. Consequently, the heat flux from the hotter particles to the colder ones has to occur through the surrounding gas. In other words, convective heat transfer between neighboring particles and the surrounding gas compensates for the absence of the contact heat transfer. Besides, the radiative heat is assumed for the bulk of the particles and apportioned to each of them based on their surface areas (see section 2.9.2).

Neglecting the contact heat transfer is a conventional assumption, where the temperature difference between the phases is dominant over the temperature difference within the bulk, for instance in well-mixed beds. Based on the report of Zhong et al., the contribution of the contact heat transfer for the bulk in high-temperature moving beds during the coal combustion is less than 2% of the total heat transfer [40]. Additionally, McCarthy et al. studied the ratio of convective to contact heat transfer in rotary drums with similar parameters as applied in this study [45]. For conditions of low convective heat transfer coefficients and particles with low thermal conductivity, e.g. biomass, the ratio of convective and conductive heat transfer is above 30 at 10 rpm. This holds even in the case of neglecting radiation in the rotary drum as reported, whereas in the case of bed mixing the temperature distribution in the bed is more uniform. Therefore, the negligible influence of contact heat transfer in the well-mixed and high-temperature rotary drum can be assumed. For this study, specifically due to the mixing behavior and radiation model for the dense particulate flow, the heat transport via convection and radiation is a reasonable compensation of the overall heat transport to the discrete phase.

In the following sections, the formulation of convective heat transfer will be discussed firstly and a detailed description of the radiative heat transfer will be given.

2.9.1 Convective heat transfer

Despite the complexity of convection, the rate of the convective heat transfer is proportional to temperature difference and it is expressed by Newton's cooling law $\dot{Q}_{conv} = h_p\,A_s(T_s - T_\infty)$ [46]. The rate of transferred heat obtained from Newton's cooling law can be determined by the heat transfer coefficient or "htc" known as the rate of heat transfer between a solid surface A_s and fluid per unit surface area, per unit temperature difference of them.

Convective heat transfer to the discrete phase is calculated for every particle based on their (thermo)physical properties and the local parameters of the surrounding gas. Important variables for the particle are the temperature, diameter and velocity and for the local gas the temperature, thermal conductivity, velocity, density and viscosity. The equation of convective heat transfer for particles can be rewritten from the first term of the right-hand side of Equation 2.3 as

$$\dot{Q}_{conv} = Nu \cdot \pi \cdot \lambda_\mathrm{g} \cdot d_\mathrm{p} \cdot (T_\mathrm{g} - T_\mathrm{p}), \qquad (2.19)$$

using the definition of the Nusselt number Nu

$$Nu = \frac{h_\mathrm{p} \cdot d_\mathrm{p}}{\lambda_\mathrm{g}}, \qquad (2.20)$$

where λ_g is the gas thermal conductivity and h_p is the particle heat transfer coefficient.

Wakao et al. studied the effect of the particle-to-fluid htc in packed beds where all of the particles are moving and the number of layers is more than two [47]. They compared the numerous experimental data on htc published in the literature over a wide range of Reynolds numbers where transfer coefficients are expressed in terms of the Nusselt number. For higher Reynolds numbers they found consistency, however at low flow rates an abnormal decrease in the Nusselt number is reported. They concluded that based on the analogy to heat transfer around a single sphere particle, a limiting Nusselt number should exist at zero flow rate. Moreover, models based on different assumptions often predict differently and contradicting Nusselt numbers so that two completely divergent conclusions have been drawn based on different assumptions [34]. Kunii et al. pointed out that fluid flowing in channels in the bed was the reason for this anomaly [48]. On the contrary, it is claimed that the anomaly could be explained by a renewal of the fluid element surrounding each particle [47]. Based on the observations of Wakao et al. [47], the Nusselt number for packed beds approaches the same limiting value from the Ranz-Marshall correlation for lower Reynolds numbers. In this study, the Reynolds number is generally low. Therefore, the Ranz-Marshall correlation is applied to both setups of single particles and particles in the bed.

The Ranz-Marshall correlation for calculation of the Nusselt number for particulate flow with the Reynolds numbers less than 5×10^4 [47] is written as

$$Nu = 2 + 0.6 \cdot Re_{\mathrm{p}}^{\frac{1}{2}} \cdot Pr^{\frac{1}{3}}, \tag{2.21}$$

where the rate of convective heat transfer increases with the relative particle-flow velocity with regard to the local Reynolds number Re_{p} from Equation 2.8 and the Prandtl number. Pr is defined as

$$Pr = \frac{\mu_{\mathrm{g}} \, C_{p_{\mathrm{g}}}}{\lambda_{\mathrm{g}}}. \tag{2.22}$$

The model accounts for increased htc through increased Reynolds numbers of particles in the packed bed due to transversal bed motion. However, it is reported that the Nusselt numbers for packed beds are generally higher than those predicted from Equation 2.21 for single spheres, but the difference diminishes at lower Reynolds numbers [34]. In this study, the Ranz-Marshall model is chosen for the motion with low Reynolds number to avoid any overestimation of the htc.

In contrast to general models (including Eulerian-Eulerian) where an effective heat transfer coefficient is estimated empirically for the entire bed, here h_{p} is obtained for every single particle regarding its properties and thermophysical values of the surroundings within the bed. An overall solid-phase htc then can be averaged from all individual data for comparison.

2.9.2 Radiative heat transfer

By the range of operating temperature of the system in this study, the heat transfer due to radiation has to be considered. The proportion of thermal radiation is especially highlighted due to the low convective heat transport, which comes from the low particle Reynolds number in the reactor. The Radiative Transport Equation (RTE) describes the propagation of the thermal radiation in radiation-active media. The RTE integrated over the wavelength is written as

$$\frac{\mathrm{d}I}{\mathrm{d}s} = \kappa I_{\mathrm{b}} - \kappa I - \sigma_s I + \frac{\sigma_s}{4\pi} \int_{4\pi} I \, \Phi \, \mathrm{d}\Omega. \tag{2.23}$$

Equation 2.23 defines the change of radiation intensity I over an infinitesimal path length $\mathrm{d}s$. The first term on the right hand side is the intensity gain through absorption with the absorption coefficient κ related to the medium existing along $\mathrm{d}s$ where I_{b} stands for black body intensity. The

second and the third terms are attenuation through emission[1] and scattering from the path length to other directions with the scattering coefficient σ_s. The fourth term is amplification by scattering from other directions to the path length ds.

The difficulty in solving this integrodifferential equation lies in the fact that the radiation intensity is not only dependent on location and time but also the direction. Several common simplifications are undertaken to solve the mentioned equation. In the following, they are noted and discussed briefly.

The RTE can be seen both as a wavelength-dependent equation or integrated over the entire wavelength range. For the former, the full resolution of the wavelength spectrum aims at reproducing the fundamental physical processes called "Line-by-line calculation". In this case, the computational effort to solve the RTE makes it unfeasible for engineering applications [49]. On the contrary, the latter approach summarizes the spectral absorption/emission properties in a single average value which is known as the standard approach for thermal radiation for industrial applications. The "gray gas assumption" is one of the simplified models that treat all radiative properties independent of the wavelength. Equation 2.23 shows the integrated form over the entire wavelength range and thus the intensities have no indices corresponding to the wavelengths.

In a gas-solid two-phase system, both phases interact by radiation. Particles, the same as the gas phase, can absorb, emit and scatter. To solve the RTE, absorption/emission and scattering coefficients of both phases in addition to their temperatures have to be known. On the other hand, the radiation source terms are required to solve the energy equations, i.e., to find the temperature. For this purpose, RTE and energy conservation equations should be solved iteratively.

To obtain the radiation heat flux to the particle, the difference between absorbed and emitted radiation has to be formulated. The solution of Equation 2.24 can be implemented in Equation 2.3 as the radiation source term for the discrete phase energy equation

$$\dot{Q}_{R_p} = \epsilon_p\big(A_p G - \sigma A_s T_p^4\big) = \epsilon_p A_s \left(\frac{G}{4} - \sigma T_p^4\right), \tag{2.24}$$

$$G = \int\limits_{4\pi} I \, d\Omega \,, \tag{2.25}$$

---

[1] According to Kirchhoff's radiation law, the emissivities of diffuse radiators always correspond to the absorption coefficient, therefore, for simplicity in the equations, the absorption coefficient κ is used also for emission.

where $A_{\mathrm{p}_i} = \frac{\pi d_{\mathrm{p}_i}^2}{4}$ represents the projected area of one spherical particle. ϵ_{p_i} is the emissivity of one particle, where it is assumed that all particles have the same emissivity. For spherical particles, the correlation of the projected and surface areas is $A_{\mathrm{p}} = A_{\mathrm{s}}/4$. Mathematically, G sums up the arriving radiation rays at a point in space from all directions.

The calculation of absorption/emission coefficients in the continuous phase has been performed through

$$\kappa_{\mathrm{g}} = \sum_i \frac{p_i}{p} \kappa_{\mathrm{g},i}(T), \qquad (2.26)$$

where $\kappa_{\mathrm{g},i}$ is a temperature-dependent polynomial of fifth-order for the specie i in the gas phase. These coefficients for CO_2 and H_2O as the main radiation-active gas-phase components are obtained from the experimental correlations of Chmielewski et al. [50]. In their work, they fitted their data for the grey gas at the temperature range between 300 K to 2500 K to obtain an absorption coefficient function. In this work, to increase the precision of the fitted curves, their data from the range between 300 K to 1000 K is used which passes to the operating temperature range of the kiln reactor. The coefficients are finally calculated as a weighted sum by partial pressures p_i.

Similar to the discrete phase, the radiation-related source term for the energy equation of the continuous phase can be calculated as the difference between absorbed and emitted radiation

$$\dot{Q}_{\mathrm{R,g}} = \kappa_{\mathrm{g}} G - 4\left(\kappa_{\mathrm{g}} \sigma T_{\mathrm{g}}^4\right), \qquad (2.27)$$

in which $\dot{Q}_{\mathrm{R,g}}$ is the volumetric heat flux with the unit $\frac{\mathrm{W}}{\mathrm{m}^3}$. The final quantity of Equation 2.27 can be implemented in the energy equation 2.12 of the continuous phase as the radiation source term S_{rad}. The interaction of radiation energy between particles and their surrounding gas will be discussed in the next chapter in the numerical solutions.

2.10 Drying of biomass

Experimental observations in the laboratory of the Engler-Bunte Institute show that the water content of wet biomass can be 5% (wet basis) for naturally dried biomass, 30% for green wood, 50% for grass clippings and even more than 80% for the freshly cut banana trunk. The range of water content in a mixture of different biomasses can widely depend on the type, region and other conditions of the operation, e.g., the harvest season and time. Biological wastes usually have high water

content, for instance, a mixture of grass clipping and municipal biological wastes can have a water content between 40% to 60% according to our measurements.

The high moisture content of input material in the rotary kiln leads to gradually filling of the drying zone of the reactor with saturated/superheated steam. This phenomenon has different outcomes. Firstly, the phase-change temperature increases to the boiling temperature and no evaporation occurs. Secondly, during the heating-up and vaporization, c_{p_g} increases dominantly which leads to a higher Prandtl number. On the other hand, a slight increase in kinematic viscosity, ν_g results in a higher Reynolds number. Based on Equation 2.21, these lead to an elevation in the Nusselt number, i.e., raise in particle heat transfer coefficient, h_p as well as wall-gas heat transfer coefficient $h_{wall-gas}$. Additionally, this fulfills the conditions required for the steam-assisted carbonization reaction without any further injection of steam. Moreover, the steam flow in the reactor and outlet streams will alleviate the process design from the manufacturers point of view. This causes that the produced tar in the reaction zone will be diluted and flows smoother, i.e., lower viscosity and less stickiness and consequently less deposition and solidification occur in the outlet streams.

The drying model used in this work considers the evaporation below $T_{\text{boil.}}$ based on diffusion. The moisture removal rate from the particle is written as

$$\frac{\mathrm{d}m_{\text{drying}}}{\mathrm{d}t} = N_p\, A_s\, \widetilde{M}_{\text{H}_2\text{O}}\,, \qquad T_p < T_{\text{boil.}}\,, \tag{2.28}$$

which is used in the mass governing equation for the discrete phase (Equation 2.1). A_s is the particle surface area; $\widetilde{M}_{\text{H}_2\text{O}}$ is the molar weight of evaporated species (water) and N_p denotes the molar flux density of vapor, which is calculated for each particle by

$$N_{p_i} = k_C\big(C_{p_i} - C_\infty\big), \tag{2.29}$$

where k_C is the mass transfer coefficient, C_{p_i} vapor concentration at the particle surface and C_∞ the vapor concentration in the bulk gas. They can be calculated using the following equations

$$k_C = \frac{D}{d_p}Sh = \frac{D}{d_p}\left(2 + 0.6\cdot Re_p^{\frac{1}{2}}\cdot Sc^{\frac{1}{3}}\right), \tag{2.30}$$

$$C_{p_i} = \frac{p_{\text{sat}}}{RT_p}, \tag{2.31}$$

$$C_\infty = X_{H_2O}\frac{p_g}{RT_g}, \tag{2.32}$$

where D presents the diffusion coefficient of vapor in the gas phase, Sh is the Sherwood number and calculates the mass transfer analogous to Equation 2.21 for the Nusselt number in the convective heat transfer. Sc is the Schmidt number v_g/D. The saturation pressure at the particle temperature is denoted by p_{sat} and X_{H_2O} the bulk mole fraction of water vapor and R is the universal gas constant and p_g the absolute pressure in the surrounding gas.

Employing Equation 2.28, the heat transferred due to the moisture evaporation $\dot{Q}_{dry.}$ in the right-hand side of Equation 2.3 is calculated as

$$\dot{Q}_{dry.} = \frac{dm_{drying}}{dt} \cdot h_{fg} , \qquad (2.33)$$

where h_{fg} represents the latent heat of the liquid required for the phase change.

For the saturated environment, the above evaporation model is not valid. In this situation, constant-temperature boiling occurs in which the total delivered heat to the particle vaporizes the moisture. This model is commonly called the thermal model in the literature and it is valid when there is no concentration difference between the particle surface and surrounding ambient [51] with

$$\frac{dm_{drying}}{dt} = \frac{\dot{Q}_p}{h_{fg}} . \qquad (2.34)$$

Furthermore, in the drying model, the hygroscopicity of biomass is taken into account. If the moisture content is below the fiber saturation point, besides the heat of vaporization, the heat of sorption has to be provided, i.e., the effect of hygroscopicity should be considered. The fiber saturation point depends on the type of biomass and for the wooden texture, it is around 30% (dry basis) of moisture content [28].

The hygroscopicity is due to hydrogen bonding within the wood fibers, which produces a strong attraction for bound water molecules and cellulosic polymers [52]. The strength of this adsorption increases as the amount of moisture decreases inside the fiber texture [53]. For this, the model of Stanish et al. was implemented during this study in the modified model by using the following correlation [53]

$$\Delta h_{sorp} = 0.4 \, \Delta h_{vap} \left(1 - \frac{M_p}{M_{fsp}}\right)^2 \qquad M_p < M_{fsp} , \qquad (2.35)$$

where Δh_{sorp} is the heat of sorption, Δh_{vap} the heat of vaporization, M_{p} the moisture content (dry basis) and M_{fsp} depicts the moisture content at the fiber saturation point. Considering the additional heat of sorption, the heat required for the phase change can be now written as $h_{\text{fg}} = \Delta h_{\text{vap}} + \Delta h_{\text{sorp}}$.

The implementation of the drying model and limitations in the numerical models will be discussed in the next chapter.

The phase change continues as long as moisture exists within the particles. When a particle becomes fully dry, its temperature increases while there is no heat sink within the particle. This physical process continues until the temperature reaches the value that biomass decomposition, i.e. thermochemical conversion, starts.

2.11 Devolatilization of biomass

The thermochemical reaction within biomass particles is assumed in this study as a carbonization process. In thermochemical conversion, chemical bonds of organic molecules are broken and the lighter molecules including water, so-called volatile matter, are released as gases. Slow thermochemical conversions include the charring of the solid and the microscopic change of the structure [2]. The actual decomposition reactions, especially the primary devolatilization, are endothermic. However, at a higher temperature in the direction of pyrolysis and fast pyrolysis, the secondary tar and char cracking and tar condensations shift the overall enthalpy of the reaction toward exothermic conditions. This explains the wide variation of reaction enthalpy recorded for pyrolysis and carbonization. A more detailed explanation of biomass thermal degradation and the influence of char yield on the endothermicity and exothermicity of the carbonization reaction can be found in [22]. In this context for the reaction modeling, the devolatilization and carbonization processes are used in an identical meaning.

The rate of devolatilizing of particles is modeled using a multi-species one-step chemical reaction with an Arrhenius-like temperature dependency (see Equation 2.36 and 2.38). The microscopic structure and alteration during the chemical process are not considered in this study and a homogenous thermochemical conversion without mass transport limitation is considered inside the particles. The experimental data implemented in the model are from low-temperature carbonization evaluations.

2.11.1 Experimental background and physical model

Bockhorn et al. performed kinetic measurements and modeling of pyrolysis using online thermo-gravimetry/mass spectrometry (TG/MS) [54], isothermal measurements [29] and experimentally measured weight-loss rates using thermogravimetric analysis at low heating rates [30]. They measured degradation rates of the main components of the lignocellulosic biomass species, namely cellulose, hemicelluloses, and lignin [56]. The devolatilization rates of these main components of biomasses were modeled according to Equations 2.36 to 2.38 and the over all devolatilization rate of biomasses was assembled according to Equation 2.39.

$$\frac{d\alpha_{\mathrm{rxn}_i}}{dt} = k_{\mathrm{rxn}_i}\big(1 - \alpha_{\mathrm{rxn}_i}\big)^{n_i}, \tag{2.36}$$

$$\alpha_{\mathrm{rxn}} = \frac{m_0 - m_{\mathrm{p}}}{m_0 - m_\infty}, \tag{2.37}$$

with α_{rxn} as the degree of conversion of the main components i, k_{rxn} as reaction rate coefficient (devolatilization rate) and n as the order of the reaction. m_0 defines the initial mass, m_{p} the actual mass and m_∞ the final mass. The devolatilization rate coefficient is approximated by an Arrhenius approach

$$k_{\mathrm{rxn}} = k_0\, e^{\frac{-E_{\mathrm{a}}}{RT}}, \tag{2.38}$$

where k_0 is the frequency factor with the unit of 1/s (for n $\neq$1, k_0 contains $(m_0 - m_\infty)^{(n-1)}$), E_{a} the apparent activation energy in J/mol, T the temperature in K. The devolatilization rate for biomass with the main components cellulose, hemicelluloses and lignin is given by the sum of the respective devolatilization rates of the main components [56],[57]

$$\frac{d\alpha_{\mathrm{rxn}}}{dt} = \sum_i c_i \cdot k_{\mathrm{rxn}_i}\big(1 - \alpha_{\mathrm{rxn}_i}\big)^{n_i}, \tag{2.39}$$

where c_i is the mass fraction of the main components of biomass. Equation 2.39 is an important conclusion to define an overall single reaction rate for a specific type of biomass using c_i, where the kinetic rate of each component is measured individually in separate experiments.

Table 2.2 gives the corresponding rate parameters for lignocellulosic biomasses.

Table 2.2 formal kinetic parameters calculated from dynamic experiments at slow heating rate [14], [56].

Component	c_i Wt.%	$\log k_0$ (1/min)	E_a (kJ/mol)	n
Cellulose	50	14.5 ($\pm$0.2)	181 ($\pm$ 8)	0.9 ($\pm$0.1)
Hemicelluloses	30	14.6 ($\pm$0.7)	163($\pm$ 2)	1.7 ($\pm$0.1)
Lignin	20	7.8 ($\pm$0.1)	99 ($\pm$ 2)	1.3 ($\pm$0.1)

The results are compared and verified additionally with the results from [16]. The achievement of this approach is a comprehensive and transferable formal kinetic model so that an overall reaction rate based on the main components of biomass is accessible. Bockhorn et al. performed also a series of experiments for variable educts and could evaluate the formal kinetic parameters for different types of biomasses [14].

This approach permits to define the devolatilization kinetics of biomasses from each main contributor by considering its respective kinetic rate. However, considering of other components is inevitable. Therefore, Di Blasi [33] suggested using the term ''pseudo-component'' that could be more appropriate as it is impossible to avoid overlap between the different components in the measured weight loss curves. Additionally, the results from [14] for comparison of virgin and acid-washed biomass species bring about that ash constituents, especially potassium, sodium, and calcium act as catalysts for the decomposition process. In the model applied in this work, the focus is to keep the simplified single-step reaction applicable to the biomass thermal conversion. Therefore, the approach from [14],[56] is used and implemented in the devolatilization model of this thesis.

2.11.2 Devolatilization model

The above approach describes the devolatilization rate in terms of the conversion of the solid phase. This does not include the formation rates of single gaseous products. To include this, a reaction mechanism is modeled based on a multi-species single-step global reaction of primary pyrolysis according to a globalized form of a reaction mechanism from Shafizade et al. [58] as shown in Figure 2.6.
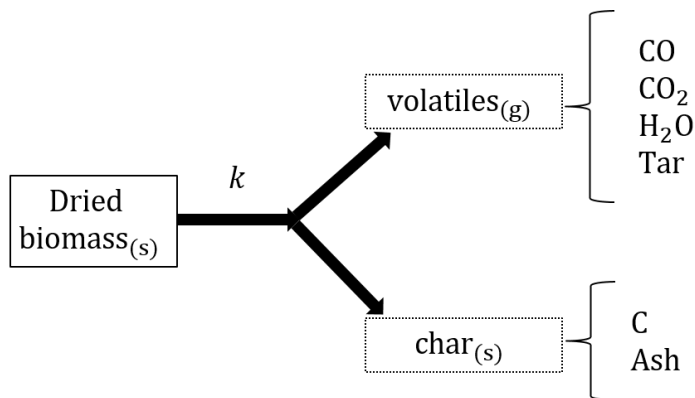
Figure 2.6 Globalized form of overall reaction mechanism in the discrete phase.

Figure 2.6 illustrates four gaseous species and two solid substances representing the products of the thermal conversion. Based on experiments, the formal conversion equation

$$C_{6.0}H_{9.9}O_{4.4} \rightarrow 0.7\ C_{5.7}H_{7.85}\ O_{2.6} + 1.3H_2O + 0.2\ CO_2 + 0.3\ C_6H_6O_3 \qquad (2.40)$$
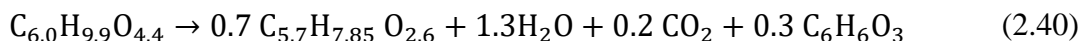
and traces of CO as well can be derived from this ash-free basis reaction scheme [24]. The formed char is described by $C_{5.7}H_{7.85}O_{2.6}$ and the volatiles evolving during carbonization H_2O, CO_2, and tar are released to the gas phase. The component "tar" represents an organic species with average thermophysical properties of various higher molecular weight components [11], [12]. Levoglucosan and Hydroxymethylfurfural (HMF) have often been chosen as a compound for tar in primary products of biomass pyrolysis [33]. In this study, a virtual species with the same molecular weight and thermophysical properties as HMF ($C_6H_6O_3$) has been considered to model the tar in the gas phase.

Since the model is rearranged based on proximate and ultimate analysis tailored to the biomass carbonization reaction, the mass fraction of moisture, volatiles and fixed char has to be specified initially. These values vary slightly from the formal conversion Equation 2.40 due to consideration of ash content and other model specifications and they can be implemented in the model based on the aforementioned experimental results. Table 2.3 summarizes the important values.

Table 2.3 Parameter inputs from the experiment for biomass and converted products.

Parameter input based on proximate analysis from the experiment for biomass (mass fraction)		Reformed parameter input based on the product analysis (mass fraction)		
Moisture content	0.50		Tar	0.381
Volatiles	0.25	Volatiles	Reaction moisture	0.432
Fixed char	0.25	0.5	Carbon dioxide	0.177
Ash content*	0.035		Carbon monoxide	0.010
* Ash content is based on the organic content		Fixed char	Organic content	0.93
		0.5	Ash content	0.07

Applying the stoichiometry of the above formal conversion Equation 2.40, the formation rate of the gaseous and solid products are coupled to the devolatilization rate of the biomass and can be calculated corresponding to their share in the total amount of volatiles or mass fractions within the particles, respectively. The fractions of CH_4 and H_2 are neglected in low-temperature conversions. These formation rates are fed into the mass balances of the species, see section 2.6.

Lumping the sum in Equation 2.39 into a single expression of the same form effective rate parameters appear: $k_0 = 2.58 \times 10^{11} \frac{1}{s}$ is the effective pre-exponential factor, likewise, the activation energy $E_a = 159.2 \times 10^3 \frac{J}{mol}$ and the reaction order $n = 1.22$ represent effective parameters in this study. The reaction order amounts close to 1, so that the dependency of k_0 on the initial mass may be neglected.

2.11.3 Enthalpy of reaction

The enthalpy of the reaction can be calculated for the implementation in the conservation equation for energy of the discrete phase (Equation 2.3) as

$$\dot{Q}_{devol.} = \frac{dm_{\text{devol.}}}{dt} \Delta H_{\text{rxn}} , \qquad (2.41)$$

where ΔH_{rxn} is the enthalpy of reaction (kJ/kg) of volatile matter and it is assumed to be negative because the reaction is slightly endothermic [22].

The devolatilization model in this study represents the important phenomenon of the evolution of volatile substances from biomass. A single-step n[th] order reaction is applied to volatiles consisting of different components simultaneously, see Equation 2.40. Due to the operation at relatively low temperatures, the effect of secondary cracking can be neglected. The total released mass from a particle is called total volatile mass m_{v_0} and it is measured experimentally.

The composition of released volatiles is an input parameter to the model. Another user-specified parameter is the reaction enthalpy that can be considered as endothermic, exothermic or neutral. The reaction is considered to be endothermic and ΔH_{rxn} is given as 200 kJ/kg$_{\text{Feedstock}}$ in this study.

2.12 Process characterization

2.12.1 Biot number

The overall rate of biomass conversion in carbonization depends on which heat transfer step is rate-limiting. Additionally, to determine the final rate-limiting key factor of the carbonization process, heat transfer rates and reaction rates have to be evaluated and compared separately. If the interphase heat transfer determines the heat transfer regime, the solid phase is referred to as "thermally thin". In such a regime, the temperature gradient within the particle is negligible in comparison to the temperature gradient between the gas phase and the boundary layer surrounding the biomass particle. This is a usual case for particles with high thermal conductivity or weak interphase heat transfer with a low heat transfer coefficient. On the other hand, if the heat transfer within the particles is rate-limiting, the solid phase is designated as "thermally thick". In such a case, the temperature gradients in the gas phase are negligible, whereas temperature gradients within the particles become significant [59].

The dimensionless Biot number quantifies the ratio of the rate of external heat transfer to the rate of internal heat transfer or characterizes the solid phase as thermally thin or thick.

$$Bi = \frac{h_{ex} \ L_c}{2 \ \lambda} \tag{2.42}$$

Where h_{ex} is the external heat transfer coefficient in W/(m^{2}K), L_c is the characteristic length for a particle being heated from every direction d_p [60] and λ is the thermal conductivity of the particle in W/(m.K) [46]. Since the heat transfer coefficient in this study is evaluated directly from the experimental operating conditions, where the overall heat transfer balance can be calculated, the term h_{ex} is determined. The above definition of the Biot number follows Bryden et al. [44] which is used also by [60] because it accounts for a correction of the surface temperature due to the contribution of radiation. This is applied by the factor 2 in the denominator of Equation 2.42. By $Bi > 1$ thermally thick assumption within the particle is dominant and by $Bi < 1$ thermally thin assumption drives the process.

Using the dimensionless Biot number, the critical diameter of particles for utilizing the developed model with the thermally thin assumption for the particles can be determined. Due to the large variation of thermophysical properties of particles during the process, two critical diameters have to be calculated separately for two various scenarios of drying and reaction. An overall external

heat transfer coefficient for a typical pilot-scale biomass carbonization unit is evaluated and assumed to be about 35 W/(m^{2}K) from own experimental data. The value represents a typical overall heat transfer coefficient of indirectly heated rotary kilns without externally introduced flow in similar operating conditions regardless of their scales which is concluded in [30] as well. Based on this value and evaluated thermophysical properties of wet biomass particles from literature, the critical diameter for drying can be estimated by 1.4 cm. This means, particles injected into the reactor can be up to 1.4 cm in diameter. In this study, the largest particles injected into the reactor would be 0.9 cm.

For the reaction zone, because of lower thermal conductivity, the critical diameter of particles entering the zone is different and smaller than that of the drying zone. However, since the particle shrinkage is considered, the critical diameter of 0.85 cm is guaranteed for the largest particles in the solid phase.

2.12.2 Pyrolysis number

The Biot number is a good indicator of the process characterization of inert particles. However, in the case of reacting particles, it is not enough to have a comprehensive assessment. Therefore, another dimensionless indicator the so-called pyrolysis number, (Py) [61] can be applied. The pyrolysis number indicates whether the process is kinetically controlled or is controlled and limited by the overall rate of the heat transfer. The pyrolysis number determines the ratio of internal heat transfer rate and rate of the carbonization reaction and it is calculated as

$$Py = \frac{\lambda}{k_{\mathrm{rxn}} \, \rho_p \, c_p \, L_c^{\,2}} \tag{2.43}$$

Where k_{rxn} is already introduced as the reaction rate coefficient in 1/s, ρ_p, c_p and L_c are the particle density, the specific heat and particle diameter, respectively. For cases with $Py \gg 1$, the process is under kinetic control and therefore heat transfer rate is fast as compared with the reaction rate. On the opposite, for $Py \ll 1$, the process is under heat transfer control which means the reaction proceeds fast comparing to the heat transfer inside the particle. The pyrolysis number for the steam-assisted carbonization is around 13.4 from experimental reaction rates at 623 K. The large pyrolysis number emphasizes the applicability of the thermally thin assumption that the temperature resolved model for particles does not influence the end time of the reaction, therefore the temperature resolved model does not improve the model considerably. The calculated values are in qualitative and

quantitative agreement with the literature [16], [18], [61]–[63]. Figure 2.7 summarizes the phenomena that can dominate in controlling the overall process in the reactor.
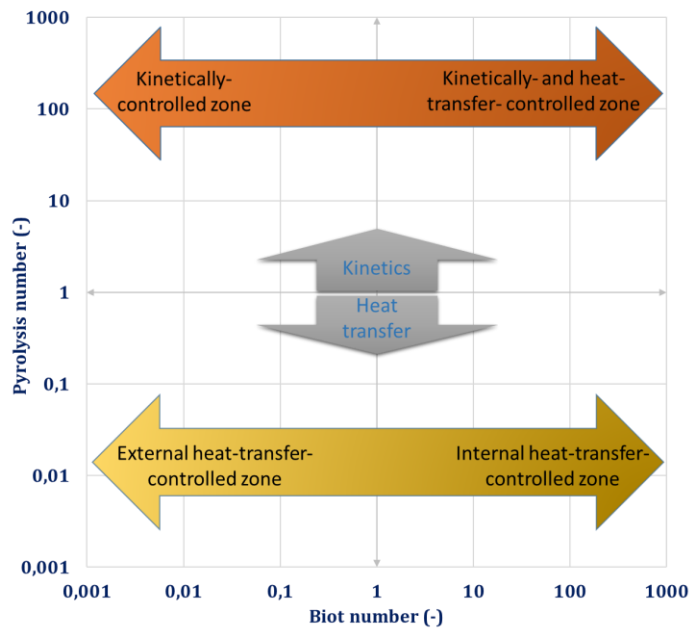
Figure 2.7 Reaction-transport map for biomass pyrolysis with modification from [61], [63].

3 Numerical Modeling and Implementation

A reacting dense particulate system can be defined as a system that contains high particle concentration with occurring chemical reaction at the same time [40]. In this chapter, the core of the numerical modeling and simulation related to the dense particulate reaction system will be explained. The presented physical and mathematical models from the previous chapter regarding thermophysical and thermochemical processes, as well as mechanical interactions, are reintroduced in this chapter and further discussed from their numerical aspects. In each section, connections between the physical and numerical models are briefly discussed. Implementation and modification of developed models are presented in detail and adopted models are linked to their physical models in the former sections.

A solver is developed that integrates the modeling of the most important physical processes required for the simulation of three dimensional, time-resolved biomass conversion of moving particle beds in a single application. This is realized by combining OpenFOAM®'s particle collision models for dense inert particle flows with OpenFOAM®'s models for heat and mass transport and chemical kinetics. Firstly, possible approaches to analyze these processes will be introduced. Then the definition of numerical concepts and solvers will be followed by designing an appropriate model. Thereafter, all of the modules and submodels that are used, developed or adjusted will be discussed in detail.

Due to the physical complexity of the occurring processes in the rotating reactors including their simultaneous interactions, no standard solver exists in the library of the open-source software OpenFOAM® to model the entire phenomena. To overcome this deficiency, a solver has been developed combining existing discrete phase models with a CFD code. The solver is a comprehensive model for solid-gas phase interaction of carbonization of wet biomass in the dense particulate flow. The open-source software OpenFOAM® version 6.0 is used in this study.

3.1 Numerical approach

For the modeling of a two-phase case study with the interaction of solid and gas, there are different techniques developed up to now. Eulerian-Eulerian and Eulerian-Lagrangian approaches are amongst the most known methods [64]. These two approaches are principally different from each other in the methodology of the computational aspects such as describing the motion of solid

particles and therefore completely different approaches have been set up for solving the governing equations [65].

In the Eulerian-Eulerian method [65], both the particulate and the fluid phase are regarded as inter-penetrating continua. For both phases, the governing equations of fluid dynamics are solved. Trajectories of solid particles are not monitored in this method which makes it an affordable modeling approach for industrial-scale simulations. All processes at particle scale such as heterogeneous reactions are required to be solved in an Eulerian numerical grid (fixed location-based mesh). Therefore, the continuum balances and phase interaction terms of the phases are coupled by including source terms into the Eulerian governing equations [35]. The spaces occupied by each phase are distinguished by the concept of phase volume fraction.

This approach is mainly used for systems with a high and homogenous particle volume fraction, as they represent a computationally efficient method. Nevertheless, the (thermo)physical characteristics of the solid particles such as shape and size cannot be recognized discretely and are included in the continuum description through empirical correlations [40]. Hence, this approach is not suitable for the present study because the particles are large compared with the reactor size and they have a wide size distribution. In general, the Eulerian-Eulerian method has underlined drawbacks especially for studies related to the fundamental research of particle physics where particle-particle interaction is dominant. In the recent decade, there are many numerical researches focused on circulating fluidized bed combustors and gasifiers as well as blast furnaces, but there are no comprehensive studies known for rotary kiln reactors [40].

In the Eulerian-Lagrangian approach [39], [42] however, only the fluid phase is considered as a continuum and the particles are considered discretely. This allows an independent treatment of finite numbers of particles (solid phase) where equations for mass, momentum, and energy conservations can be solved for each particle. Explicit consideration of interphase exchanges between solid and fluid is possible via source terms.

The method offers the advantage that particles, especially with different properties (e.g. size distributions, compositions temperature, etc.), can be mapped more precisely [64]. The method can provide information about the trajectories and transient forces acting on individual particles by solving the governing equation for the momentum of each particle (described in section 2.5) for the entire discrete domain based on Newtons's equations of motion [40]. Higher accuracy makes this approach popular and preferable to simulate a system containing a finite number of particles with a high probability of collisions.

In this study, the Eulerian-Lagrangian approach will be used for the simulation of the thermochemical conversion of biomass particles in an indirectly heated rotary drum reactor where the interaction of particle-gas phase plays an important role. The approach will be discussed in the following section in detail.

3.2 Eulerian-Lagrangian approach

The Eulerian-Lagrangian approach is a common and suitable method for dispersed multiphase flow, where particles are represented in a Lagrangian reference frame and the governing equations for the discrete phase from section 2.5 can be directly solved. The carrier-phase flow is represented in an Eulerian frame where the spatially discretized forms of the governing equations from section 2.6 are solved straightforwardly. There are generally three different methods of coupling the discrete and continuous phases.

3.2.1 Classification map of particle-laden flows

One-way coupling implies that the fluid phase influences the solid particles but not vice versa. This assumption can be taken for systems with sufficiently small particle volume fraction. It is accepted that for the volume fraction below 10^{-6}, the influence of the particles on the fluid phase would be negligible [66].

In contrast, two-way coupling considers mutual interaction between the two phases. This method is suitable for non-dense flows where the fluid dynamics forces play a major role in particle motion [35]. In this model, the exchange of heat and momentum between the gas phase and solid phase is included. For particle volume fractions up to 10^{-3}, generally, this model is common [66]. Particle-particle collisions and the resulting momentum transfer are generally not included in the two-way coupling approach.

For large particles present with volume fractions larger than 10^{-3}, an additional coupling between particles is necessary since inter-particle interactions are important. Four-way coupling, the third method, considers particle-particle interaction additionally, which is a capable method for modeling of dense particulate flows used for this study.

However, there is no suitable standard solver in open-source packages to consider the entire physics of the case study. Therefore, a solver tuned for drying and carbonization of dense particulate flow

in rotary drum reactors has been developed. This is done by the coupling of different existing solvers as well as by creating new submodels to present a meaningful modeling approach.

3.2.2 Resolved and unresolved approaches in Eulerian-Lagrangian method

The Eulerian-Lagrangian computational approach can be classified into two different categories regarding the particle sizes and quantities, namely resolved and unresolved categories.

Resolved approach

In the resolved Eulerian-Lagrangian method, the particles are remarkably larger than the fluid cells, which means a particle covers several cells of mesh at once (see Figure 3.1a). The particle resolved approach offers a high level of detailed information within the particles including their surface and the fluid around them. This approach reduces the usage of empirical correlations and consequently makes the approach less dependent on particular experimental conditions. If the focus is to investigate the exact behavior of only few relatively large particles, the resolved method allows for obtaining more precise conclusions.

This approach is also useful for cases with only small amounts of particles [67]. Due to computing efforts, it is not advisable to use this method for a large amount of moving particles. The approach has been commonly used in Direct Numerical Simulations – Discrete Element Method (DNS-DEM) [64], [67], but the application is not only limited to DNS simulations [68], [69]. The main drawback is that the simulation becomes quickly very expensive by increasing the number of particles and refining the computational domain. Figure 3.1a represents a graphical scheme for the resolved method.

Unresolved approach

This method is for handling a large number of particles and it assumes that particles are significantly smaller than the mesh cells. Therefore, as shown in Figure 3.1b, each cell can contain more than one particle at one moment. Usually in this method, the focus of computational power is on the Lagrangian part. Using the unresolved method, a computation domain including several millions of particles can be handled, depending on the available computational resources [35]. If the behavior of a large amount of non-uniform objects is of interest, the unresolved method seems to be a reasonable choice [67].

Due to dealing with a large number of particles in this study, the unresolved method is used. An important precondition for applying this approach is that the cells have to be larger than particles to

guarantee an accurate discrete phase interaction as well as numerically stable interphase heat and mass transfer.
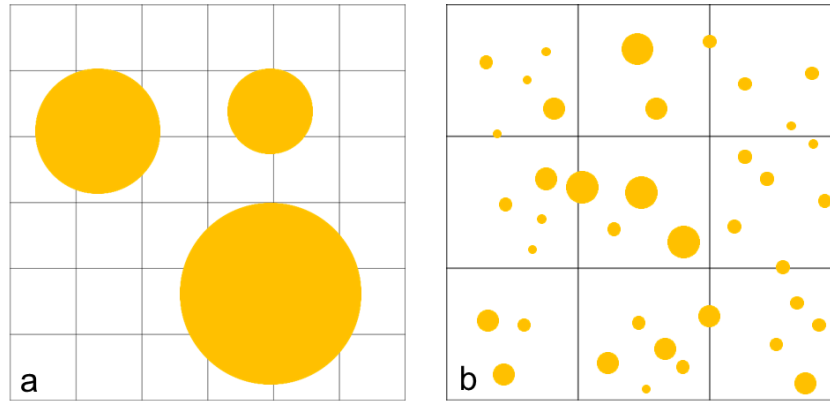
Figure 3.1 Eulerian-Lagrangian computational methods compared to the grid size. Figure a) represents the resolved method and b) the unresolved method.

A restriction related to the unresolved approach is that the grid size limits the particle size. This, however, helps to keep the solver more stable especially during the solving of the energy equation. Contrary, larger computational cells allow a larger range of timesteps. This, especially for larger geometries, is helpful for instance in the modeling of industrial applications. The *CFL* number (after Courant-Friedrichs-Lewy) determines the relation between timestep and cell size

$$CFL = \frac{|\mathbf{u}_g| \cdot \Delta t}{\Delta x} \tag{3.1}$$

where $|\mathbf{u}_g|$ is the magnitude of gas velocity, Δt and Δx are time and space resolution, respectively. Although the *CFL* number can be large for large-scale simulations, for the stability of the calculation it must not exceed a user-defined value. Numerical researches suggest the maximum value of $CFL < 1$ [36].

3.2.3 Implementation of the new solver

The solution of the Lagrangian phase requires high computing performance, as properties need to be determined for every single particle. In practical cases and industrial-size geometries, particle numbers could be in the range of several millions to several hundred millions. The concept of clustering is developed to calculate the properties of one particle and transfer to a user-specified number of particles that are aggregated in a group defined as one numerical particle or "Parcel". This method is largely used to reduce the computational expenses by several orders of magnitude and therefore make the simulation of large geometries possible, particularly in the conventional two-way coupled

systems. Nowadays, utilizing parcels is a common approach in CFD solvers, e.g., Barracuda® [70], Star-CCM [71], Ansys-CFX [72], Ansys-Fluent[73] and OpenFOAM® [74].

OpenFOAM® provides several different classes for defining parcels by means of their functionality. For instance, `CollidingParcel` and `MPPICParcel` are suitable for parcel collisions (inter-parcel interaction). `KinematicParcel` is a class for the movement of parcels by means of summing up all internal and external forces. The `ThermoParcel` considers the energy equation and consequently heat transfer and thermal properties added to the previous class. Further classes have more capabilities, which are in addition to what they inherited from the previous classes unless they are contradictory to them [75]. Table 3.1 expresses the highlighted features of the main particle classes in OpenFOAM®.

Table 3.1 Features of different particle classes in OpenFOAM®.

Class \ Feature	Kinematic Colliding-/MPPIC Parcel	Kinematic-Parcel	Thermo-Parcel	Reacting-Parcel	Multiphase-Reacting-Parcel	Coal-Parcel
Inter-particle-collisions	Yes	No	No	No	No	No
Coupled Forces	Yes	Yes	*Kinematic-Parcel*	*Thermo-Parcel*	*Reacting-Parcel*	*Multiphase-Reacting-Parcel*
Wall interaction	Yes	Yes				
Heat transfer			Yes			
Phase change				Yes		
Mass transfer				Yes		
Multiphase component					Yes	
Devolatilization					Yes	
Surface reaction						Yes

It is important to use the proper class in order to have a consistent solution. As can be seen in Table 3.1, none of the parcel classes has the thermal feature and inter-particle collision simultaneously. This means that four-way coupled solvers in OpenFOAM® are isothermal and there are no further features considered, i.e., inter-particle collision. On the other hand, the solvers, which solve the energy equation cannot consider the inter-particle interaction model. This is the motivation to create a new single solver to combine collision and thermal features.

The modified solver

The more inclusive definition for "solver" can be given as a pre-defined and consecutive series of code that takes a computational domain[1], the governing equations including their state[2], the initial and boundary conditions, appropriate values of physical constants, the solution conditions[3] and appropriate discretization parameters[4] as input [76]. Algorithms and submodels that are called to be solved by a solver use an identical specified parcel class to capture the physics of the discrete phase in the reactor.

The solver `CoalChemistryFoam` uses the `CoalParcel` class and it is by default a two-way coupled solver originally programmed for gasifiers and combustors where pulverized particles are injected into a large chamber. The `CoalParcel` class has no inter-particle collision. Therefore, to maintain a solver with the ability of modeling four-way coupled considering heat and mass transfer and reactions one needs to develop a new solver.

Theoretically, there could be two ways to perform this operation: starting from `KinematicMPPICParcel/KinematicCollidingParcel` and upgrade the parcel class with thermo-, reacting- and multiphase-class or considering the `CoalParcel` as a base and couple it with `MPPICParcel/CollidingParcel`. In both cases, not only a new solver with new equations needs to be programmed but also the entire library needs to be updated in a way that the hierarchy of OpenFOAM® could consider the coupled modules.

In this project, the second approach has been applied while the structure of `MPPICParcel/CollidingParcel` is more compact and thus, it is easier to be merged in the solver `CoalChemistryFoam`. The final layout of the developed Eulerian-Lagrangian solver in OpenFOAM® is sketched in Figure 3.2.

---

[1] usually referred to as the mesh
[2] Steady/unsteady, incompressible/compressible, laminar/turbulent for Navier-Stokes equation, for example.
[3] E.g. timestep size, variables to be saved
[4] First/second order, upwind/central-differencing, implicit/explicit time-stepping
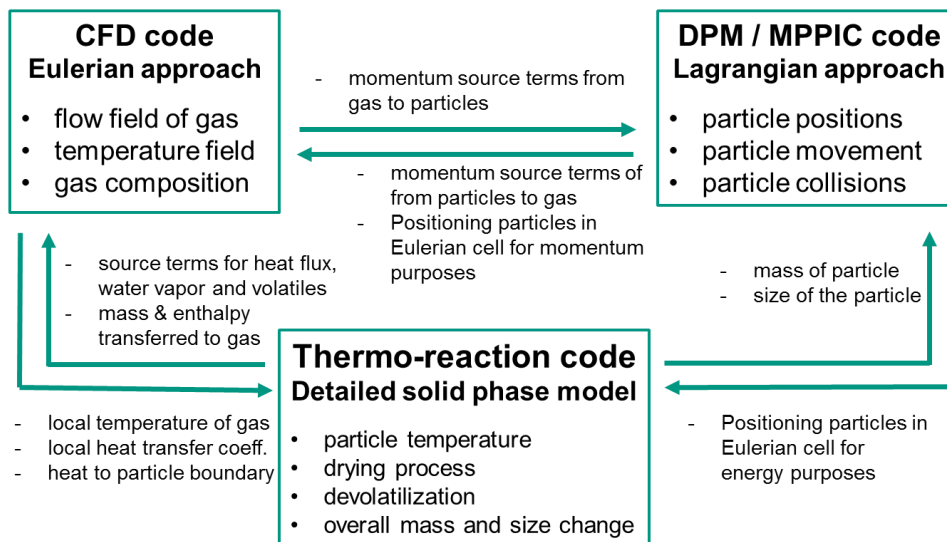
Figure 3.2 Final layout of the developed Eulerian-Lagrangian solver consisting of different codes so-called `coalMPPICChemistryBuoyancyFoam/coalCollidingChemistryBuoyancyFoam`.

The original existing solvers have coupled only two of the three modules from Figure 3.2. In other words, the existing infrastructure is not enough to cover the entire physics of this modeling. The developed solvers are called `coalMPPICChemistryBuoyancyFoam` and `coalCollidingChemistryBuoyancyFoam`. They are using different collision models (MP-PIC/DPM) to solve a problem with similar considerations as mentioned in the scheme from Figure 3.2.

The two mentioned numerical collision models are introduced in the next following sections for calculating the collision of particles in a moving bed. These numerical models are connected to the physical models discussed in the previous chapter as well. Both methods will be utilized and compared to each other and the efficient method will be chosen for this study.

3.3 Discrete Particle Method (DPM) in OpenFOAM®

The Discrete Element Method (DEM) is the physical model for particle collisions using the soft-sphere model (expressed in section 2.8.1) and the Discrete Particle Method (DPM) is a particle-based numerical model based on DEM. The numerical model was first derived by physical laws and mathematical work from [77].

Because different numerical methods have been used and developed by researchers with the same name, it is not possible to find a unique terminology in Lagrangian approaches. In open-source software OpenFOAM®, DPM is the numerical model that uses the DEM methodology with the ability to assume particles as parcels. However, in commercial packages, these terms are used for

other physical/mathematical concepts. Hence, these terms have to be interpreted carefully depending on the context and the applied tools. In this thesis, the term DEM is utilized for the physical modeling and the mathematical meaning of the particle collision and DPM points to the specific numerical solver in OpenFOAM® with DEM background.

The DPM model is known as the Lagrangian explicit numerical scheme for the resolved calculation of granular particles. The parcel class is called `collidingParcel` from the previous section. The DPM method for the study of particles is analog to the Direct numerical simulations (DNS) method in computational fluid dynamics. The DPM provides an algorithm to list all of the particles in order to search for neighboring particles or the ones that have the potential for collision. The concept of parcel might not be useful for this model since the particle interactions have to be considered for every individual particle. Thus, clustering particles is not physically meaningful but numerically reasonable, so that it is implemented in the DPM solver in OpenFOAM®.

Detailed data on flow properties and fully coupling between the two phases have been performed in Tsuji et al. [41]. They considered a collision force between only two neighboring particles and similar to Cundall et al. [39], they neglected the propagation of collision force to further particles (see section 2.8.1). To fulfill this, the timestep has to be chosen sufficiently small. This assumption reduces the memory requirements and prevents unnecessary complications. Additionally, a small timestep guarantees only one collision for a certain particle and this enables equations of the contact force to be solved analytically. Therefore, the motion of each particle can be acquired by the sum of all forces in each time step, allowing for the calculation of contact forces between the particle and its direct neighbor [41].

DPM model is precise but a very small timestep is required to calculate the motion during collision [35]. On the other hand, besides memory limitation for calculation of stiffness for every particle, the restriction on the timestep is a disadvantage for long-time simulations. This drawback will be more highlighted for the case of packed-bed or dense gasifier calculations and when a big fraction of particles are in contact with each other. Washino et al. in [78] suggested a model named Reduced Particle Stiffness (RPS) to increase the time step and decrease the calculation cost, in which the stiffness of particles is reduced from the real material property. It is reported that this approach is widely accepted for cases that contact forces are dominant specifically for dry and relatively coarse particles, however, the model cannot prevent the drastic changes of the powder behavior when cohesion forces are applied to the particles [79]. The Author proved that for the mentioned

appropriate applications, the simulations using the RPS model show identical bulk velocity, sticking and rebounding behavior compared with the original model [78].

Moreover, due to the memory limit and computation time, an empirical correlation is inevitable for the calculation of overall particle stiffness and damping coefficient in the case of a high number of particles. To overcome these limitations, an equivalent particle size should be taken into account as the representing particle. Therefore, a compromise between precision and efficiency is decisive in large-scale simulations.

To give an idea for the very high computational demand of the DPM method some highlighted works from the literature are given. Independent works of [17] and [18] on 2D lab-scale geometry for non-reacting flows show that the computing effort required to perform the CFD-DPM simulation is 2–4 orders of magnitude higher than that of in the Eulerian–Eulerian simulation. Løvås et al. reported that 2D simulation of a small laboratory-size reactor with 40.000 reacting particles in non-reacting flows with CFD-DPM model using OpenFOAM® lasted 14 days for just 20 s of physical time on a 16-core intel node [32]. Zhong et al. [40] concluded that using this model is not acceptable for a simplified industrial-scale geometry with 8,000,000 cells and 600,000 particles where it would take 7000 days to calculate 30 s of physical time on a single CPU.

To recapitulate, the DPM model is not suitable for the simulation of industrial-size units. However, in this thesis for the laboratory-scale reactor, this model is validated using experimental evaluations and is also compared with other numerical models.

3.4 Multiphase Particle in Cell (MP-PIC)

A computationally improved stochastic[5] Eulerian-Lagrangian model called Multiphase Particle In Cell (MP-PIC) was developed by Andrews and O'Rourke and published in 1996 [82]. But the original idea is from the numerical calculation of two-phase flows [83]. The model was firstly developed for dilute phase interactions with the two-way coupled method, but then later on extended to the four-way coupled model. Similar to other Lagrangian models, Equation 2.4 is solved and interactions between particles are considered. In contrast to the DPM model, not every particle-particle impact is calculated individually but considered using stochastic models based on the

---

[5] Having a random probability distribution or pattern that may be analysed statistically but may not be predicted precisely [Oxford dictionary]

kinetic gas theory. The related parcel class is called `MPPICParcel` and it is defined in Table 3.1 and Figure 3.2.

The promising feature of MP-PIC in computational affordability is one of the main reasons that many researchers during the recent decade developed 2D and 3D dense particulate reaction simulations based on this approach [40]. Zhong et al. reported that the computation time for simulating the reacting flow via MP-PIC is only about twice the Eulerian–Eulerian simulations and for a case study in their work, MP-PIC was at least 50 times faster than the DPM model [40].

While DPM tracks every single particle-particle collision separately, the MP-PIC uses collective particle properties to obtain the value for the inter-particle forces within each control volume. In the MP-PIC model, the effect of particle-particle interaction is considered by introducing grid-based properties [84]. Based on the position of discrete particles, the algorithm first determines which particle belongs to which computational cell. Consequently, in each control volume, the particle properties such as mass, temperature, velocity and density, etc. are mapped. Using these properties, specifically mass and density, the volume of particles located in a specific cell and consequently the particle volume fraction α_{pvf} can be determined. Correspondingly the inter-particle force of each cell in the form of particle pressure is calculated and applied to all particles within the particular control volume, which reflects the influence of collisions. Further details of the inter-particle force model are given in section 3.4.1.

The dynamics of the dispersed phase and the state of the particle field in principle can be described using a distribution function $f(\ )$ and its time evolution. The functional $f(\ )$ can be written for any arbitrary vector or scalar properties of a particle that are important in a particular application, for instance, $f(\mathbf{x}_{\text{p}}, \mathbf{v}_{\text{p}}, m_{\text{p}}, T_{\text{p}}, t)$, where terms in the bracket are the position, velocity, mass, the temperature of the particles and time, respectively [85]. This is a multi-dimensional distribution function which dimension can be reduced by integration over one or several variables. Then $\iiint f(\mathbf{x}_{\text{p}}, \mathbf{v}_{\text{p}}, m_{\text{p}}, T_{\text{p}}, t)\, d\mathbf{x}_{\text{p}} dm_{\text{p}} dT_{\text{p}} = f(\mathbf{v}_p, t)$ would be the velocity distribution of the particles at a certain time for particles with any mass, position and temperature (marginal distribution). The distribution function $f(\mathbf{v}_p, t)$ describes the number of particles at a certain time with a velocity between $\mathbf{v}_p$ and $\mathbf{v}_p + d\mathbf{v}_p$. The distribution function in discretized form is written as e.g.

$$f(\mathbf{v}_{\text{p}}, t) = \frac{dn_p(\mathbf{v}_{\text{p}}, t)}{d\mathbf{v}_{\text{p}}} = \frac{n_{\text{pi}}(\mathbf{v}_{\text{p}i}, t)}{\Delta \mathbf{v}_{\text{p}}}, \mathbf{v}_{\text{p}i} = \mathbf{v}_{\text{p}(i-1)} + \Delta \mathbf{v}_{\text{p}}, i = 1 \ldots \tag{3.2}$$

meaning the number of particles at any position of any mass or temperature with a particle velocity within the velocity interval $\mathbf{v}_{\mathrm{p}i} + \Delta\mathbf{v}_{\mathrm{p}}$.

The distribution function for the position of the particles is a kind of Liouville equation [82], [86]. The Liouville equation can be used for finding particle positions and also ensures that the general conservation of variables of the disperse phase such as mass and momentum will be kept [84]. The Liouville equation for particle positions is

$$\frac{\partial f(\mathbf{x}_{\mathrm{p}}, t)}{\partial t} + \nabla \cdot \left(f(\mathbf{x}_{\mathrm{p}}, t)\mathbf{v}_{\mathrm{p}}\right) + \nabla_{\mathbf{v}_{\mathrm{p}}} \cdot \left(f(\mathbf{x}_{\mathrm{p}}, t)\mathbf{a}_{\mathrm{p}}\right) = \frac{df(\mathbf{x}_{\mathrm{p}}, t)}{dt}\bigg|_{\mathrm{collision}}, \quad (3.3)$$

where $\mathbf{a}_{\mathrm{p}}$ is the change in particle velocity $\mathbf{v}_{\mathrm{p}}$ over time and $\nabla_{\mathbf{v}_{\mathrm{p}}}$ is the divergence operator with respect to particle velocity, i.e., $\nabla_{\mathbf{v}_{\mathrm{p}}} = \left(\frac{\partial}{\partial\mathbf{v}_{\mathrm{p},x}}, \frac{\partial}{\partial\mathbf{v}_{\mathrm{p},y}}, \frac{\partial}{\partial\mathbf{v}_{\mathrm{p},z}}\right)$. For applications where the collision is not considered, i.e. two-way coupled simulations, the right-hand side of the equation is set to zero. The Liouville equation theoretically calculates the positions of the particles in terms of a distribution function including all processes that affect the movement of the particles. This avoids in contrast to DPM-models the book-keeping of calculating collision forces for every single particle and interactions of neighboring particles. In this work, however, the Liouville equation for the distribution function of particle positions is not solved directly but the discretized representation is used, see Equation 3.2, taking the results of the solutions of motion of the Lagrangian particles. This is done also for other particle properties.

The number density of particles in a specific control volume and at a certain time with solid mass in the interval $(m_{\mathrm{p}}, m_{\mathrm{p}}+dm_{\mathrm{p}})$, the Cartesian velocity in the interval $(\mathbf{v}_{\mathrm{p}}, \mathbf{v}_{\mathrm{p}}+d\mathbf{v}_{\mathrm{p}})$ and particle temperature in the interval $(T_{\mathrm{p}}, T_{\mathrm{p}}+dT_{\mathrm{p}})$ is obtained by the integration of the distribution function over velocity, mass and temperature

$$n_p = \iiint f(\mathbf{x}_{\mathrm{p}}, \mathbf{v}_{\mathrm{p}}, m_{\mathrm{p}}, T_{\mathrm{p}}, t) \, dm_{\mathrm{p}} d\mathbf{v}_{\mathrm{p}} dT_{\mathrm{p}} . \quad (3.4)$$

In reality, in the algorithm of the MP-PIC model, each particle is tracked during the entire time of their residence within the domain. Similar to the DPM model, the book-keeping of every single particle and its properties is performed for each timestep. Therefore, n_p is calculated directly from the properties of particles available in the domain. This can be done deterministically but analogous to the discretized representation of the Liouville equation.

The following equation can be performed for every control volume of the entire computational domain to calculate the number of particles in that specific control volume

$$n_{\text{pcell}} = n_p \cdot V_{\text{cell}} .\qquad(3.5)$$

Further, $\frac{1}{V_{\text{cell}}}\sum_{i}^{n_{\text{pcell}}} V_{\text{p}_i}$ (summation is over all particles in the cell) defines the volume fraction of particles in a specific control volume which is a critical parameter for the calculation of the collision forces [87]. This method is considerably faster for a large number of particles due to saving a considerable effort by means of bypassing the neighbor algorithm detection. This accelerates the simulation performance despite inter-particle collisions are a contributing factor. Moreover, the MP-PIC method uses the concept of parcels (numerical particles, explained in section 3.2.3) to reduce the number of particles involved in the computations. Further, the particle phase is divided into a finite number of parcels that each represent a number of real particles at the accumulated position of one with identical mass, temperature, velocity and location.

The calculation of particle movements using the MP-PIC method in OpenFOAM® is divided into three sequential submodels to numerically represent the physical motion of all particles in the bulk. These submodels are the damping model, the packing model and the isotropy model. Each of these submodels has also its submodels in OpenFOAM®, which provides various possibilities to study the particle movement. This allows adapting the MP-PIC method to the respective application, but also makes it more complicated to choose the appropriate settings.

The calculation of the particle motion using the MP-PIC method is performed in a way that all particles are first moved without considering interactions between them. With this, the movement of each particle is calculated iteratively, so that the particle position is corrected. The particle velocity is then recalculated with the substituted parameters. The movement process of particles is shown schematically in Figure 3.3. Submodels in the calculation process are sequential but independent from each other so in the case of deactivation of each submodel, the algorithm continues by calculation of the next submodel.

Movement of particles without considering collision	←	Next time-step	←	Listing the speeds and positions at the end of time-step

Damping modell		**Packing modell**		**Isotropy modell**
Calculation of the corrected speeds $\mathbf{v}_p^{corr}$		Calculation of the corrected speed $\mathbf{v}_p^{corr}$		Random selection of the particles whose velocity is changed
Correction of particles' positions with the corrected speeds	→	Correction of particles' position with the corrected speed	→	Correction of the corresponding particle velocities
Calculation of the new particle velocities $\mathbf{v}_p^{new}$ with the corrected velocities		Calculation of the new particles' velocities $\mathbf{v}_p^{new}$ with the corrected velocities		Correction of all velocities to maintain variance

Figure 3.3 Overview of the position and velocity calculation process using the MP-PIC method.

The damping model represents the numerical effect of the collisional model by considering the effect of physical mean loss in kinetic energy in fast collisions. This model reproduces physically realistic scattering behavior but can have destructive effects on the packing behavior of particles. The model is specifically suitable for high-velocity interaction where collisions have a significant influence on kinetic energy loss [74]. In this investigation, the damping model is deactivated in the simulations due to the negligible effect on the behavior of rolling/slumping particles in the bed and also due to saving computational effort.

Observations and test cases in this study declare that by relatively larger timesteps, which are optimal for the performance of the long simulations, the damping model has no considerable influence. On the contrary, the packing model and the isotropy model are important.

3.4.1 Particle-particle interaction – Packing model

The packaging model is primarily responsible for particle collision and ensuring that the particles are not packed more tightly than it is possible in reality. The packing model applies non-linear inter-particle stress to particles (particle pressure). For the inter-particle stress model, the Harris-Crighton model is chosen and is described in detail [88]. In this work, the `explicit` method is used to calculate the force by considering the volume fraction at the old timestep. The explicit method results in realistic motion of the particle bed but does not guarantee that the bulk material is not overpacked under every circumstance [74].

Andrews and O'Rourke introduced the MP-PIC model, in which the equation for particle motion (introduced in Equation 2.4) includes the effect of particle-particle interaction. This effect incorporates the gradient of the solid stress as a force to particles in dense flows with volume fractions above 5% [89][90]. In other words, a normal force vector is applied to prevent particles

48

from being collapsed into each other. The so-called packing-force is a grid-based property and substitutes the physical impact of particle collision. Therefore, the packing model needs to map the discrete phase to the Eulerian scheme in order to calculate the collision force. The force related to the particle interaction – a critical term in the right-hand side of Equation 2.4 – can be written as

$$\mathbf{F_c} = -\frac{m_p}{\alpha_{pvf}\,\rho_p}\nabla\tau_p \;.$$

(3.6)

Knowing the particle collision force $\mathbf{F_c}$, the velocity of particle ($\mathbf{v}_p^{orig}$) in the domain can be obtained from Equation 2.4 by implementing other known forces such as gravity, etc. In Equation 3.6 $m_p\nabla\tau_p$ represents the gradient of the particle pressure and α_{pvf} is the particle volume fraction of the cell that the particle(s) belong(s) to it and calculated as

$$\alpha_{pvf} = \frac{1}{V_{cell}}\sum_i^{n_{pcell}} V_{p_i}\,,$$

(3.7)

with n_{pcell} as the number of particles existing in the cell. The particle pressure τ_p is obtained from an empirical equation developed by Harris and Crighton [88]

$$\tau_p = \frac{P_s\,\alpha_{pvf}^{\beta}}{\alpha_{cp} - \alpha_{pvf}},$$

(3.8)

where P_s is an empirical constant called solid pressure coefficient and has units of pressure. β is also an empirical constant and is recommended to be between 2 and 5 [91]. α_{cp} represents the particle volume fraction at the close-packing limit. Equation 3.8 concludes that particle pressure is a decreasing function of the voidage and as $\alpha_{pvf} \to 0$ it is imposing the condition that the particle pressure must vanish, which is the pure fluid limit [88]. Additionally, control volumes require the particle pressure to prevent that the particle fraction does not exceed the close-packing limit. Snider [84] suggested the numerically modified expression of Equation 3.8

$$\tau_p^{corr} = \frac{P_s * \alpha_{pvf}^{\beta}}{\max\left\{(\alpha_{cp} - \alpha_{pvf}),(\epsilon * (1 - \alpha_{pvf})\right\}},$$

(3.9)

ϵ is a small constant number on the order of 10^{-7} to remove the singularity at close packing [84].

After calculating τ_p^{corr}, the velocity is corrected by the following equation

$$\mathbf{v}_p^{corr} = \frac{-\Delta t}{\alpha_{pvf}\,\rho_p}\nabla\tau_p^{corr}\;.$$

(3.10)

Since the correction speed is timestep dependent and might become unfeasibly large, OpenFOAM®
provides a further submodel to the packing model. It is called `CorrectionLimitingMethods`
and is supposed to limit the corrected velocity. This restriction dictates that the velocity change of
a particle should not exceed the velocity change in a partially elastic collision. This higher limit is
represented as

$$\left|\mathbf{v}_p^{corr}\right|_{max} = (1 + e)\left|\mathbf{v}_p^{ref}\right|, \tag{3.11}$$

where e is the restitution coefficient of the particles and reference velocity $\mathbf{v}_p^{ref}$ can be either the
absolute velocity of each particle or the relative velocity from the local weight average of particle
velocity in the respective cell. In this work, the absolute velocity is chosen to be compared and
limited for each particle calculation individually.

After the particle velocity is corrected, the position of the particle will be calculated from Equation
2.5. Then, the new velocity for each particle from the packing model is the sum of the original and
corrected velocities

$$\mathbf{v}_p^{new} = \mathbf{v}_p^{orig} + \mathbf{v}_p^{corr}. \tag{3.12}$$

3.4.2 Particle-particle interaction – Isotropy model

The isotropy model represents the collisional effect of scattering that physically occurs as a result
of particle-interaction using statistical methods analogous to those used in the kinetic theory of
gases [92]. The code includes a `stochastic` model that uses a time-scale to calculate the probability
of a particle undergoing a collision. The model changes only the particle velocity in a randomized
way and has no impact on the position of particles in the same timestep. Besides that, momentum
and energy are explicitly conserved in a second step. This approach also helps to spread the particles
uniformly across cells and ease computational averaging of cell-based values [74].

The further effect of particle collisions, i.e., the scattering effect, utilizes an isotropic Gaussian
distribution for the particle velocity [92]. In OpenFOAM®, this is numerically realized with the
available isotropy model `Stochastic`. First, a time constant has to be defined

$$\frac{1}{\tau_G} = \frac{2\sqrt{2}}{5\pi} f_p \, g_0 (1 + e)(3 - e) \tag{3.13}$$

where f_p is a measure of the frequency of particle collisions where its calculation formula is given by O'Rourke et al. [86], e is the restitution coefficient of the particles and g_0 is the radial distribution function and written as

$$g_0 = \frac{\alpha_{cp}}{\max\left\{(\alpha_{cp} - \alpha_{pvf}), (\epsilon * (1 - \alpha_{pvf}))\right\}}. \tag{3.14}$$

In Equation 3.13 the time constant τ_G is defined that the expression $\exp\left(-\frac{t}{\tau_G}\right)$ indicates the probability that a particle will not collide with any other particles in the time interval of $[0, t]$. For instance, as the time interval is one-tenth of τ_G, the probability of having no collision during this time span is around 90%, however, as the time span grows to a value equal to τ_G the probability of no-collision drops to around 36%. In the time spans ten times higher than the time constant, the "no-collision probability" is almost zero. The calculation of τ_G in OpenFOAM® is performed in the submodel `TimeScaleModel` using the option `isotropic`.

Numerically, a number between 0 and 1 is randomly generated for each particle and compared with $\exp\left(-\frac{t}{\tau_G}\right)$. If the particle random number is smaller, there is no collision and therefore, the particle velocity remains unchanged. Otherwise, a random velocity from a Gaussian distribution curve will be assigned to each particle where the local average velocity $\overline{\mathbf{v}_i}$ is the expected value. In this case, the velocity will be linearly transformed to obtain a normally distributed and random velocity

$$\mathbf{v}_p^{temp} = \overline{\mathbf{v}_i} + \mathbf{r}\frac{\sigma}{\sqrt{3}}, \tag{3.15}$$

where $\mathbf{r}$ is a vector generated with standard and normally distributed random numbers from the Box-Muller transform [93] and σ is a scalar and random variation of particle velocities around the mean velocity and it is completely independent of the direction.

Since the number of particles in each control volume is known, a correction step is required to ensure that the mean and variance of particle velocities ($\overline{\mathbf{v}_i}$ and σ) remain constant. For this purpose, the new distribution of particle velocities, as well as average value and variance, has to be calculated locally. The particle velocities are corrected in the isotropy model according to

$$\mathbf{v}_p^{new} = \overline{\mathbf{v}_i} + \left(\mathbf{v}_p^{temp} - \overline{\mathbf{v}_i^{temp}}\right)\frac{\sigma}{\sigma^{temp}}, \tag{3.16}$$

where σ^{temp} is the temporary σ during the correction in the isotropy model. The mentioned equation handles the particle collision statistically in a way that the new velocity for particles with the probability of collision is calculated based on the mean velocity from a local Gaussian

distribution, randomly temporary relative velocity and the ratio of random variation of particle velocities before and after correction. The statistical correction considers the conservation of momentum implicitly. In the isotropy model, the physical properties of particles affect only τ_G. Detailed description and verification of the mathematical model can be found in [94].

3.4.3 Particle-wall interaction

The particle-wall interaction model is actually not part of the MP-PIC method, but a component of every Eulerian-Lagrangian solver in OpenFOAM®. As mentioned in section 3.3, in the DPM collision model, the particle-wall collision is considered by the soft-sphere model from section 2.8.1. In contrast, in the MP-PIC model, the collision is assumed to be based on the hard-sphere model that is explained in section 2.8.2 due to its importance for particle and bed behavior in the simulation of a rotary reactor. OpenFOAM® provides various approaches for the modeling of the particle wall interaction. The `localInteraction` model is the most comprehensive model for this purpose and therefore used in this study.

The `localInteraction` library models the collisions particle-wall using three different scenarios for boundary surfaces such as inlet, outlet and walls.

- `escape` allows the particles to leave the computational domain through the respective boundary. It is, therefore, to be chosen for the outlet.

- `rebound` is the model for elastic contact between particles and the wall as well as the inlet patch. The `rebound` model in MP-PIC is a hard-sphere interaction model for the particle-wall interaction regarding the relative motion to wall velocity.

- `stick` does not apply to this work. By using this option, the particle sticks to the wall after the first collision and does not move anymore.

It should be noted that the `localInteraction` is primarily intended for a short contact between particles and walls and not for long and permanent contacts, as is the case in a rotary kiln. Permanent contacts lead to certain problems as already observed during this study, for example, a dependency of the residence time on the time step. The identified reason for this problem is that in the equation 2.18b, the particle velocity is reduced by a constant coefficient (e) and using smaller time steps, the equation is called more often than in larger time steps. As a result, the larger the time step, the shorter the residence time of individual particles. This study has attempted to develop a new model

for particle boundary conditions based on Coulomb's law of friction, which is independent of the time step. In single-particle case studies, physical results independent of the timestep is achieved (to be discussed in section 4.3.2). However, this achievement could not be verified in case studies with particle beds due to unknown and varying weight force of the top layer(s).

Therefore, the experimentally measured friction coefficient has been used as a user-defined input to obtain an optimum range of timestep. The principle is to achieve an identical average residence time for the particle bed between experiments and simulations. This range of timestep is compatible with the *CFL* number (see Equation 3.1) and fulfills its criterion for the entire simulations in different conditions and scales. Hence, it is important to consider the effects of the particle-wall interaction model while investigating the behavior of the particle-bed in the rotating tube reactor using the MP-PIC method.

To take the rotation of the reactor into account, there are at least three options theoretically possible in OpenFOAM®. The first method is generating a dynamic mesh; i.e., the entire domain rotates around the axis of the cylinder. This method is computationally intensive because of the remapping process of the entire component of each computation cell including the gas phase and lagrangian in each timestep. This method has been tested at the beginning of this work and assessed as a nonfeasible method for large reactors. Another method is using multiple rotating frames, by employing and coupling two sections of the domain analogously as rotor and stator. This method could save the expensive remapping effort from dynamic mesh, however, this is not yet employed in OpenFOAM® for MP-PIC solvers.

The most computationally affordable method is utilizing a rotating velocity to the boundary conditions of the wall so that in case of the contact with particles, the velocity can be applied to the calculation of the hard-sphere model. The boundary condition is available in OpenFOAM® and it is called `rotatingWallVelocity` for boundary type wall. The rotatingwallvelocity can be used only for the rotating wall (patch) that have all faces parallel with the rotation trajectory, for example, a cylinder rotating around its axis. The axis and rotational speed in $\frac{\text{rad}}{\text{s}}$ have to be implemented as a user-defined parameter.

3.4.4 Parcel motion in MP-PIC

In the MP-PIC model, the particle pressure τ_p in the collision force (Equations 3.6 and 3.8) depends only on the particle volume fraction. Instead of calculating the τ_p - as well as other properties - for

all particles, the concept of parcels comes into focus to reduce the computation effort as discussed in section 3.2.3. MP-PIC is able to use this concept efficiently in contrast to DPM, which necessitates the modeling of only one particle per parcel due to the physical background of the model. Regarding the particle properties such as size, density, temperature, component, etc. the parcel concept is used for a certain number of identical particles at the same position. For this purpose, one important prerequisite has to be checked

$$N_{\text{pp}} \sum_{i=1}^{n_{\text{pcell}}} V_{\text{p}_i} \ll (\alpha_{\text{cp}} \cdot V_{\text{cell}}),\qquad(3.17)$$

where N_{pp} is the number of particles per parcel. The condition means that the total volume of parcels has to be much less than the total volume of the computational cell considering the close-pack limit. If the required condition is fulfilled, the model has identical behavior in the case of using parcel and particle concept with a feasible change in computation time. This aspect has been tested and verified for the average residence time of particles in the rotary kiln during this work. In large-scale simulations, it is a usual case to have control volumes much larger than particle size and therefore it is uncomplicated to fulfill this condition.

For the particle interaction, the only Lagrangian value maintained at the parcel location and indirectly required by the Eulerian grid, is the parcel center location. The location should be mapped into the grid and it translates to the solids volume fraction by an evaluation of the number of parcels in any given cell using $\frac{N_{\text{pp}}}{V_{\text{cell}}} \sum_{i}^{n_{\text{pcell}}} V_{\text{p}_i}$. Mapping the parcel position on the Eulerian grid is not only crucial for the calculation of collision force but also should be known for the interphase heat and mass transfer. Therefore, one should note that the concept of parceling is nothing but an algebraic multiplication of particles grouped into a parcel.

The physical interpretation of the parcel interaction model used in MP-PIC can be explained as shown in Figure 3.4 assuming gravity is applied to the parcels downwards with a certain angle of inclination toward the right. Looking at the cell located on the bottom left side, it is assumed that it reached its close-packing limit, so the new parcel cannot fall in the cell due to the result of forces applied reciprocally. So either the forces are balanced and the parcel stays in the cell or because of the gravity and inclination the particle has to fall to the bottom middle cell. In the middle, since the bottom cell is not fully packed, the parcel can fall from the top cell.

From the packing model, the horizontal component of the collision force can be gained and added to the horizontal vector of the gravity force. Hence, the resultant of forces may move some parcels

from the fully packed cell towards the right. In other words, the diffusion-based influence of parcels volume fraction (Equation 3.8) interprets the gradient of τ_{p} (Equation 3.6) in the occupied cells.
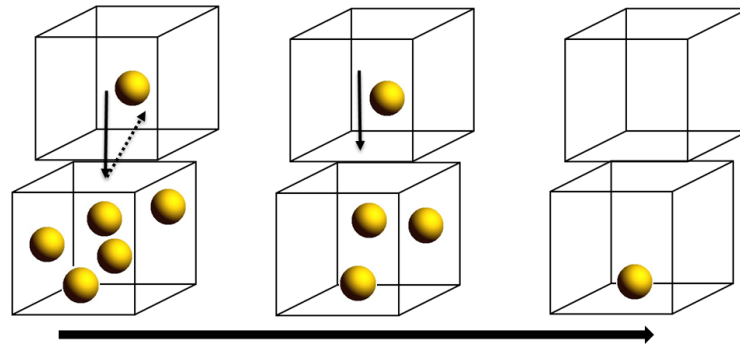
Figure 3.4 Schematic time interpretation of the empirical model used for particle interaction.

Like the DPM model, MP-PIC is a hybrid numerical method, where the Eulerian computational grid is considered for the fluid phase and the Lagrangian computational method calculates the discrete solid-phase motion [86]. MP-PIC is also known as computational particle fluid dynamics (CPFD) and can have an almost identical algorithm to DPM models except the calculation for contact force for inter-particle and particle-wall collisions. The substitution of these two submodels makes the MP-PIC model computationally much more efficient than DPM in industrial-scale simulations. MP-PIC has various parameters that either are calculated by Eulerian methodology or have to be transferred to the Eulerian scheme for further computations. This brings the necessity to investigate the coupling of Eulerian-Lagrangian methodologies.

3.5 Coupling two phases

The conservation of mass, momentum, energy and species has been discussed in the previous chapter for the Eulerian and Lagrangian phases separately. The coupling of these two phases needs a proper mathematical approach for interphase exchange. For this purpose, the source terms in governing equations of continuous and discrete phases play a major role. The gas phase is modeled as a compressible continuum and the flow regime depends on the gas velocity within the reactor. In the laboratory-scale reactor, calculations show that the gas phase exhibits laminar flow. For higher Reynolds numbers of the gas phase and/or high disturbance between the solid and the freeboard gas, turbulence should be considered. Initial calculations for the industrial-scale reactor states noticeably lower average gas velocity within the reactor, but the turbulence model is additionally applied to ensure the consideration of localized turbulent flow induced by the particle bed as well as the consideration of higher rotational Reynolds numbers. To this end, the standard Large Eddy

turbulence model from Smagorinsky will be chosen for the flows beside the laminar model simulations [95]. For the coupling of the two phases, instantaneous density-weighted values from the continuous phase are used. Although one may think the utilizing of time-average values would be reasonable, however, due to the nature of the slow movement of particles in the rotary kilns and very low gas velocity, the fluctuations of values over time are very small and thus the instantaneous values can be used for coupling in this specific application. Unlike fluidized bed systems and other systems where the dispersion of particles due to turbulence in the fluid phase is considerable (e.g. when the drag force on particles is dominant), in this study, the influence of particle dispersion can be neglected.

For simplicity, all equations from here on are explained based on particle principle unless it is explicitly declared. One has to consider the application of applying the number of particles in parcels N_{pp} based on the nature of considered quantity (being intensive or extensive).

Interphase exchange source term for mass $S_{\text{p},m}$ noted in Equation 2.10 is the total mass release from all particles to the continuum, which is calculated from the mass governing equation of the Lagrangian phase (Equation 2.1) as follows

$$S_{\text{p},m} = -\frac{\sum_{i=1}^{n_{\text{pcell}}} \dot{m}_{\text{dry},i} + \dot{m}_{\text{devol},i}}{V_{\text{cell}}}. \tag{3.18}$$

The equation can be interpreted as particle mass release by drying and devolatilization processes.

Interphase exchange source term for species S_{p,Y_i} of the discrete phase arises from devolatilization and evaporation. This term is calculated explicitly from Equation 3.18 using the evaporation rate of the liquid phase and devolatilization rate of volatiles in which the composition of each component is known

$$S_{\text{p},Y_k} = \frac{\sum_{i=1}^{n_{\text{pcell}}} \dot{m}_{\text{dry},i,Y_k} + \dot{m}_{\text{devol},i,Y_k}}{V_{\text{cell}}}, \quad k = 1,2, \dots N_{\text{species}}. \tag{3.19}$$

Where $\dot{m}_{\text{dry},i,Y_k}$ and $\dot{m}_{\text{devol},i,Y_k}$ are the source terms of mass conversion for species k.

Similarly, the interphase exchange source term for momentum $S_{\text{p},mom}$ between the discrete and the gas phase mentioned in the Navier-Stokes (Equation 2.11) is described as

$$S_{\text{p},mom} = -\sum_{i=1}^{n_{\text{pcell}}} \frac{\mathbf{F}_{\text{d}}}{V_{\text{cell}}} \tag{3.20}$$

where $\mathbf{F_d}$ is the drag force.

The energy exchange from the discrete phase to the fluid phase $S_{p,h}$ is

$$S_{p,h} = - \sum_{i=i}^{n_{\text{pcell}}} \frac{\dot{Q}_{\text{conv}}}{V_{\text{cell}}} \qquad (3.21)$$

Therefore, the explicit energy exchange between the two phases is calculated based on the enthalpy of existing particles in the cell as well as temperature change. Analogous to the energy equation for the disperse phase, the energy equation for the continuum consists of source terms for convective heat transfer between gas and particles as well as the radiative heat transfer. Source terms due to convection and radiation heat transport are discussed in section 2.9.1 and 2.9.2, respectively.

3.6 Heat transfer to discrete phase

The physical model of heat transfer to the solid-phase over two mechanisms of convection and radiation has been explained in the previous chapter. Convective heat transfer deals with particles and the surrounding gas in the belonging computational cell. Radiative heat transfer from walls to gas and particles is calculated through an adjusted discrete ordinates model (DOM), which uses the gray gas assumption for the continuous phase. The energy coupling between continuum and discrete phase is expressed by Equations 2.3 and 2.12 as well as Equation 3.21 for the source terms.

It is worth reminding that the particles are assumed as spheres, which makes the calculation of the contact surfaces between neighboring particles impossible. An additional reason for neglecting the contact heat transfer is because of the restriction from the MP-PIC methodology, in which no physical contact between particles is determined (discussed in 2.9). In each computational cell, the convective heat transfer between neighboring particles and the surrounding gas compensates for the absence of contact heat transfer. In addition to that, the radiation model distributes the incoming radiative heat among particles belonging to the same cell with respect to their weighted surface area.

The layout of the developed Eulerian-Lagrangian solver is depicted in Figure 3.2 and the numerical flowchart of the solver for one timestep is to be shown in section 3.9. The heat transfer block emphasizes how the convective and radiative modules require various source terms from both phases and boundary conditions. This indicates that the heat transport calculation cannot be performed for each phase individually, but due to the coupling of the two phases, the heat exchanges have to be solved simultaneously.

3.6.1 Convective heat transfer

The formulation of the convective heat transfer is already discussed in the previous chapter in detail. The Ranz-Marshall correlation based on the Reynolds and Prandtl numbers is used to calculate the Nusselt number for every particle. The convective heat has to be calculated for each parcel and its surrounding gas and then it can be multiplied by the number of particles that belong to the parcel. So the interphase convection occurs in each computational cell based on each parcel properties and the gas phase in the cell.

From Equation 2.19 the heat flux to each parcel can be obtained through the Nusselt number and other known parameters of particles and gas. The Nusselt number is the dimensionless property in heat transfer representing the convective to conductive heat transfer at a boundary in a fluid. The Ranz-Marshall correlation is employed to calculate the Nusselt number (Equation 2.21). On the other hand, for this calculation, the parcel Reynolds number and fluid Prandtl number have to be determined, first (Equations 2.8 and 2.22). Obtaining the Nusselt number yields to the convective heat transfer coefficient through Equation 2.20 and thereafter delivered heat to each parcel (and particles) is obtained for each timestep.

3.6.2 Radiative heat transfer

The mathematical model for the Radiative Transport Equation (RTE) is described in section 2.9.2. In this study, the finite volume method (FVM) is utilized to solve the RTE as the entire continuous-disperse system. In this section, the numerical modeling of the RTE will be introduced. Afterward, the advantages and disadvantages of the two available solutions will be discussed and the suitable methodology for the two-phase flow will be described. Finally, the modified model will be suggested as an extension to the existing solution.

Disperse phase

For a control volume V_c with n_{pcell} parcels, each containing N_{pp} particles, Equations 3.22 and 3.23 are contributed to the calculation of absorption/emission and scattering coefficient of particles, respectively

$$\kappa_{\text{p}} = \frac{1}{V_{\text{c}}} \sum_{i=1}^{n_{\text{pcell}}} (N_{\text{pp}} \cdot A_{p_i}) \, \epsilon_{\text{p}_i} \, , \qquad (3.22)$$

$$\sigma_{s_p} = \frac{1}{V_c} \sum_{i=1}^{n_{pcell}} \left(N_{pp} \cdot A_{p_i} \right) \left(1 - \epsilon_{p_i} \right). \tag{3.23}$$

These equations are simplified so that the diffraction and refraction can be neglected, which is an acceptable and common assumption. These equations are implemented in OpenFOAM® and reviewed in different literature as well [49], [96].

The radiation emission of the discrete phase, on the other hand, is described separately for each particle. To obtain the particle emission, the particle surface A_{s_i} and its temperature T_{p_i} have to be identified. The total volumetric heat flux emitted by particles located in the control volume V_c is calculated by the following equation from Stefan-Boltzmann law

$$E_{disperse} = \sigma \frac{\epsilon_p}{V_c} \sum_{i=1}^{n_{pcell}} N_{pp} \, A_{s_i} \, T_{p_i}^4. \tag{3.24}$$

Employing Equation 3.22 and 2.26 in 2.23 contributes to the calculation of the incoming incident radiation G, where the radiation heat flow for each particle within a specified cell can be calculated by the area-weighted fraction via $G_p = G \cdot \frac{A_{p_i}}{\sum_{i=1}^{n_{pcell}}(A_{p_i})}$. The difference between absorbed and emitted radiation (numerically defined in Equation 3.24) can be gained in a cell through Equation 2.24 for all particles, theoretically. The result can be implemented in Equation 2.3 as the radiation source term for the discrete phase energy equation.

So far it can be outlined that the radiation source term for each particle is obtainable by knowing the particle size and temperature and the incoming incident radiation. However, the calculation of incident radiation needs a comprehensive radiation model with a numerical discretization and coupling of two-phase interaction. To do so, some critical parameters from the continuous phase should be identified, firstly. Then, a methodology for consideration of radiation intensity in the computational cell can be defined.

Continuous phase

The calculation of absorption/emission in the continuous phase is performed by using the gray-gas model from Equation 2.26. This model is available in OpenFOAM® called `greyMeanAbsorptionEmission`. The coefficients are calculated depending on the temperature and composition of the continuous phase.

The model for calculation of the absorption/emission coefficient of the gas phase is modified to prevent overestimation in the values of κ_{g} in the discretized method. The gray-gas radiation model in DOM implemented in OpenFOAM® does not consider the contribution of the volume fraction of particles in a cell, as it assumes the concentration of the disperse phase to be diluted. However, if the volume fraction of particles for arbitrary cells is dominant, this should be taken into account by calculating the reduced absorption coefficient for the gas phase. The total absorption coefficient κ_{total} for a cell in OpenFOAM® is the sum of the coefficients for gas and particle phases $\kappa_{\mathrm{total}} = \kappa_{\mathrm{g}} + \kappa_{p}$. Therefore, an updated variant of `greyMeanAbsorptionEmission` is created for the consideration of volume fraction of the particles `volFractionAbsorptionEmission` with the following equation

$$\kappa_{\mathrm{g}}^{*} = \kappa_{\mathrm{g}}\big(1 - \alpha_{\mathrm{pvf}}\big), \tag{3.25}$$

where κ_{g} is from the original absorption model and α_{pvf} is particle volume fraction in the cell. The modified absorption coefficient κ_{g}^{*} does not vary from κ_{g} where no particles exist in a cell but differ for domains occupied with particles. For an unphysical or artificial packed bed with higher particle volume fraction, the model is adjusted and prevents artifact values of κ_{g} which leads to the negative or zero values of radiative energy balance in a cell. Thus, the modified coefficient considers the effect of dense flow in the calculation of radiative heat transfer in the rotary kiln.

Similar to the discrete phase, the radiation source term for the energy equation of the continuous phase is calculated as the difference between absorbed and emitted radiation in Equation 2.27 where $\dot{Q}_{\mathrm{R_{gas}}}$ is the volumetric heat flux.

The solution of the RTE in OpenFOAM®

So far the proportion of absorbed/emitted radiative heat transfer for each phase in a cell is known. Now, incoming incident radiation can be calculated to obtain the radiation field in the computational domain. The analytical and exact solution of the RTE is yet extremely expensive despite the assumption of wavelength independence. To deal with this, different models suggest numerical solutions to solve the RTE equation. Among the existing radiation transport models, only two models are implemented and verified in OpenFOAM®, that can interact with radiation-active continuous and dispersed phases. They are the P-1 model and the finite volume discrete ordinates model (fvDOM).

P-1 model

The solution of the RTE equation (Equation 2.23) can be approximated by a series of associated Legendre polynomials [90]. In the simplest case, only the first term of the series is involved, which leads to the P-1 model for radiation transport [90]. This approximation is only valid for optically thick media [96]. The transported variable in the P-1 model is the incident radiation G, as an integrated value of intensity over all directions (see Equation 2.25).

The main assumption of this model is that the radiative intensity I is integrated over all directions in a way that G is isotropically resulting in a diffusion-based equation for incident radiation and thus, the P-1 model tends to overpredict dissipation [97].

However, since the radiative heat transfer equation is easy to solve without high CPU demand, many studies use the P-1 model regardless of satisfaction and validation. Another advantage of the P-1 model is that the simplified diffusion equation includes the effects of scattering from other directions in the RTE equation. This is not the case in the discrete ordinates models due to the necessity of an unfeasible iterative solution.

Overall, the P-1 model compromises the computational efficiency and the loss of accuracy (e.g., for media with noticeable optical thickness) although it tends to overestimate the radiative fluxes from local heat sources. After the investigation of its performance (to be discussed in section 4.5.2), it is concluded that the P-1 model is not appropriate for the case study of this work due to significant overestimation of the radiative fluxes to the discrete phase.

Finite volume discrete ordinates model (fvDOM)

Lui et al. developed an accurate and efficient radiation model applicable to generalized 3D geometries using an unstructured finite volume method [98]. For the first time, they combined the discretization strategies to solve the RTE for 3D problems with structured, unstructured or hybrid grids. The combination of the discretization associated with the DOM and FVM brought a new solution to modify the CFD methods for radiation which is already implemented in OpenFOAM® [99]. The finite volume variant of the DOM method is called fvDOM.

With the fvDOM, the RTE is solved by discretizing the direction in addition to the local discretization. Each of the discretized directions fills a solid angle Ω_i, over which the radiation intensity is assumed constant. These solid angles are equidistant without overlap but cover all directions [37]. Two transport equations are solved for each direction, one with positive and one with negative orientation. The result is the solution of discretization

$$\int_{4\pi} d\Omega = 4\pi = \sum_{i=1}^{N} \Omega_i, \tag{3.26}$$

where N is the number of discrete directions. The RTE, therefore, will be transformed into a solved equation with the basis of the fvDOM method as

$$\hat{S}_i \cdot \nabla I_i = \kappa I_{\mathrm{b}} - \kappa I_i - \sigma I_i + \frac{\sigma_s}{4\pi} \sum_{i,j=1}^{N} \Omega_j I_j \, \Phi\left(\hat{S}_i, \hat{S}_j\right), \tag{3.27}$$

where $\hat{S}_i$ is the location variable in the considered direction and $\Phi\left(\hat{S}_i, \hat{S}_j\right)$ is the probability function that a scattered beam from another direction $\hat{S}_j$ is deflected into the considered direction $\hat{S}_i$. So, the integral term for scattering from other directions in the considered direction becomes a finite sum.

This system of differential equations is numerically solvable but the equations for all directions i are coupled to each other through the last term on the right-hand side, which makes an iterative solution necessary. The set of equations has to be solved for every cell in the computational grid, therefore, double summation over cell surfaces and directions of delivered heat to each cell is necessary.

By reforming the equation and applying the Gaussian integral theorem described in [96], [100], the final equation can be obtained with the assumption that the radiation intensity is constant over the cell surface.

Additional simplification considered in the fvDOM of OpenFOAM® omits the scattering terms including the outgoing/incoming scattering to/from other directions to the path length. The reason for this simplification is saving computational time by decoupling the set of differential equations, which results in avoiding the iterative calculation. This is common in radiation models. Thus, the two last terms on the right-hand side of Equation 3.27 will be eliminated. This leads to the following differential equation for each discrete direction in a cell

$$\frac{1}{V} \sum_{i}^{N} \sum_{k} I_{k_i} (S_i \cdot \hat{n}_k) A_k = -\kappa_{\mathrm{total}} I_{V_i} \Omega_i + \Omega_i \left(\kappa_{\mathrm{g}}^* I_{\mathrm{bp_g}} + \frac{E_{\mathrm{disperse}}}{4\pi} \right)_V \tag{3.28}$$

the term on the left side represents the sum of values on the cell surfaces indexed with k. The sums express the total amount of incoming radiation from all directions to the specified cell. The right-hand side of Equation 3.28 consists of two terms; one for absorption and another for emission. The former expresses the total absorption of the cell and the latter represents the emission which is divided into two parts for the continuous and dispersed phases.

Modifications to fvDOM model

In order to solve Equation 3.28, not only the absorption/emission coefficients of the disperse and gas phase has to be determined but also the emission intensity should be quantified. By assuming the cell emission as a known value, the intensity for each discrete direction can be solved with a system of equations for all cell surfaces and boundary conditions. As the system of equations has to be solved independently for each global direction, the structure of the code will be a loop for all cells inside another loop for all directions.

Equations 3.22 and 3.24 are valid to calculate the absorption/emission coefficient and emission intensity for the dispersed phase only if the particle volume fraction is low or in other words, the sum of the projected area of particles is much smaller than the cell surface. The highlighted restriction in 3D models is that the shading effect in the direction-dependent projected area of particles cannot be considered in control volumes. Therefore, by highly packed cells, the sum of the projected surface of spheres can exceed the real projected area of the cell.

A method for the determination of the absorption/emission coefficient for the dense disperse flows is developed and implemented in OpenFOAM$^{®}$ in the framework of this project. In this method, the ratio of the cell projected surface to the projected area of all particles within that cell is considered for any arbitrary ray direction Ω_i.

The calculation of κ_p and E_disperse should fulfill both usual possibilities related to the projected area of a cell and its containing particles:

- cells with low particle volume fraction, where $\sum_{i=1}^{n_\mathrm{pcell}} (N_\mathrm{pp} \cdot A_{\mathrm{p}_i}) < A_\mathrm{pc}$,

- cells with high particle volume fraction, where $\sum_{i=1}^{n_\mathrm{pcell}} (N_\mathrm{pp} \cdot A_{\mathrm{p}_i}) \geq A_\mathrm{pc}$.

A_pc is the direction-dependent projected area of the cell and A_{p_i} declares the projected area of each spherical particle by $A_{\mathrm{p}_i} = \frac{\pi d_{\mathrm{p}_i}^2}{4}$.
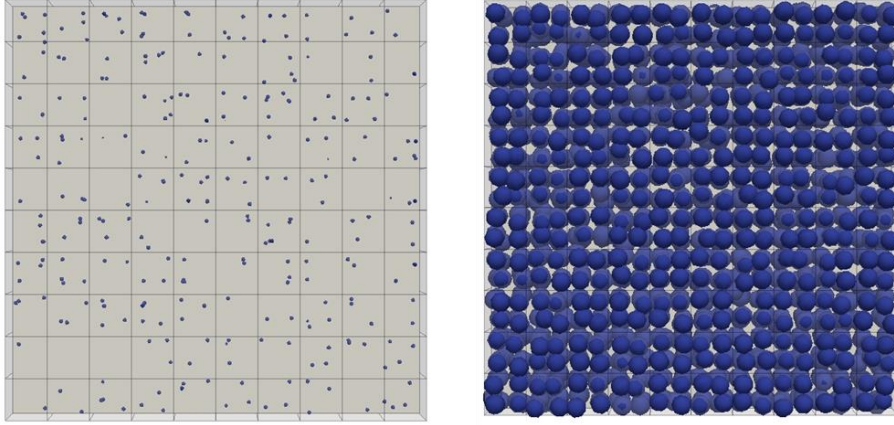
Figure 3.5 Comparison of cells and particles' projected area in the low and high particle volume fraction in cells.

The left-hand side image in Figure 3.5 represents a case study with a low ratio of the particles-to-cell projected area where the default equations of OpenFOAM® for absorption/emission coefficient and emission intensity are valid. The image in the right-hand frame of Figure 3.5 shows an example case of fully packed particles in multilayers consecutively, in which the sum of the projected area of particles is larger than the cell projected area.

The modified equation of the absorption/emission coefficient uses the minimum and maximum functions to return a value with the smaller and larger quantities from the two arguments, respectively.

$$\kappa_{\mathrm{p}}^{*} = \frac{A_{\mathrm{pc}}}{V} \frac{\min(A_{\mathrm{pc}}, \sum A_{\mathrm{p}_i})}{\max\{(A_{\mathrm{pc}} - \sum A_{\mathrm{p}_i}), A_{\mathrm{small}}\}} \epsilon_{\mathrm{p}} \qquad (3.29)$$

The min function in the nominator is responsible for the overlapping effect of particle projected area and ensures that the maximum limit of surface projection (cell projected surface) is not exceeded. This function applies the physical interpretation of shadowing and keeps the intensity balance of cells. The max function in the denominator, on the other hand, ensures the numerical stability and the correct sign of the absorption/emission coefficient for the circumstance of dense/packed disperse phase. The function prevents division by zero or negative values for κ_{p}^{*} through A_{small} as a constant small value. The good compromise between accuracy and stability is found by the value of $A_{\mathrm{small}} = 2.5 \times 10^{-4} A_{\mathrm{pc}}$. The physical interpretation of very large κ_{p}^{*} means the entire absorption of the incoming radiation intensity.

A similar principle has to be applied to Equation 3.24 for the modification of radiative emission from particles in cells.

$$E_{\text{disperse}}^{*} = \min\left(1, \frac{A_{\text{pc}}}{\sum A_{\text{p}_i}}\right) \cdot \sigma \frac{\epsilon_{\text{p}}}{V} \sum_{i=1}^{n_{\text{pcell}}} N_{\text{pp}} \, A_{\text{s}_i} \, T_{\text{p}_i}^4 \qquad (3.30)$$

The min function in Equation 3.30 takes the shading effect of particles into account so that the emitted value will be correlated to the projected area of the cell. As long as the sum of the projected area of particles is less than the cell surface, the function applies unity values and acts neutrally. If the cell is fully packed, the ratio $\frac{A_{\text{pc}}}{\sum A_{\text{p}_i}}$ applies a factor less than one to fulfill the total emission. The factor basically considers a part of the emission that finds no way to leave the cell and it is absorbed by neighboring particles.

The code implicitly anticipates the attenuation of radiation emitted from the disperse phase due to absorption in the continuous phase using κ_{g}^{*} (see Equation 3.25) before it leaves the cell. Therefore, mathematical modification is not directly taken into consideration in Equation 3.30.

One of the simplifications in this model is that the cells are filled with particles isotropically, so-called isotropic packing behavior of particles. Since the upwind scheme is used for the numerical solution of fvDOM, the values are accumulated at the center corresponding to each cell. These parameters are, however, in reality, anisotropic and they depend on the location of each particle. As an example, a stagnant half-filled cell with many particles under the effect of gravity is almost entirely opaque in the direction of gravity but not necessarily in other directions. However, this assumption has a minor influence on the attenuation of radiation due to absorption in the continuous phase in a specific direction. The emission depletion for an arbitrary direction from a particle in the middle of the cell is equal to the emission depletion of another particle near one of the surfaces of the cell. The attenuation deviation due to the location might have a small influence locally but it is negligible since values are obtained by volume integral over the entire domain.

So far, coefficients and terms from Equation 3.28 are identified. By a discretization scheme, and finally, for the numerical solution, the systems of equations for intensities can be solved and the integrated values of incident radiation for the entire computational grid can be obtained.
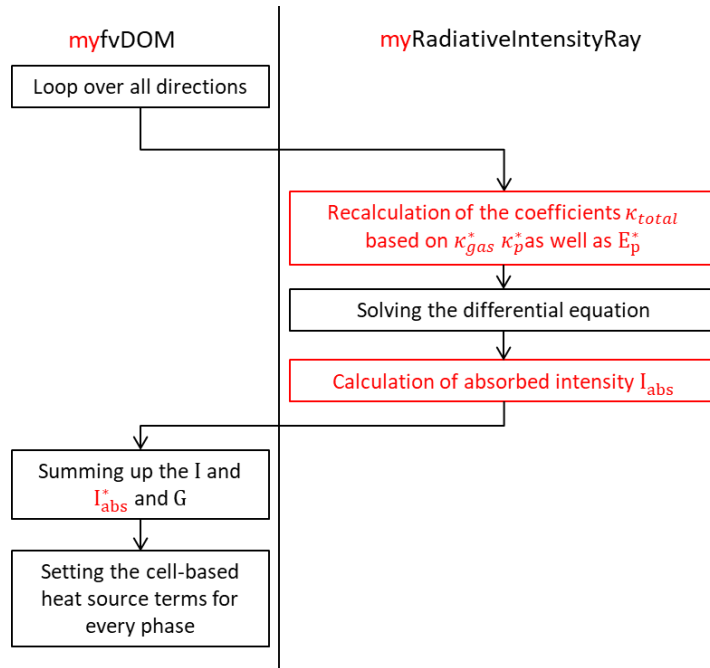
Figure 3.6 Schematic chart of the radiation field calculation for the modified fvDOM model.

Figure 3.6 illustrates the schematic flow chart of the radiation with fvDOM and its submodel `RadiativeIntensityRay` in OpenFOAM®. The default model is shown as `fvDOM` and the modified model is `myfvDOM`. Modifications added to the default model are marked in red. As illustrated, the major part of the modifications is related to the submodel because the fvDOM algorithm is mostly responsible for discretization and integration of the values over directions and location.

For `fvDOM`, the user must specify the number of directions, where in 3D cases two values are necessary. n_φ indicates the number of discrete azimuth angles in a quarter sphere. n_θ specifies the number of discrete polar angles. The distances of two discrete angles are given by

$$\Delta\varphi = \frac{\pi}{2n_\varphi},\tag{3.31}$$

$$\Delta\theta = \frac{\pi}{n_\theta}.\tag{3.32}$$

Therefore, by defining $2\,n_\varphi = n_\theta$ the distance will be identical as $\Delta\varphi = \Delta\theta$. The total number of discrete directions is $N_{\text{directions}} = 4\,n_\varphi\,n_\theta$.

As a further user-input setting, `solverFreq` specifies how frequently the radiation field is solved. Adjusting the `solverFreq` to two, for instance, reduces the computational time related to the

radiation module by half. This adjustment setting and the total number of directions affect calculation time and accuracy mutually.

Neither the default `fvDOM` nor the modified model `myfvDOM` allows considering the scattering of the radiation from particles. Therefore, all particles are considered as black bodies, i.e., the emissivity of particles is therefore $\epsilon_p = 1$ which can lead to some deviations, since this assumption does not perfectly match the physical properties of biomass particles or even charcoal [96]. To overcome this deficiency, a global approach is chosen for a rotary reactor. An equivalent emissivity is calculated and implemented in the boundary condition for the radiation. To simplify the operation, a new boundary condition based on `GreyDiffusiveRadiation` is created, which considers an empirical value for the emissivity of particles. With the new boundary condition, the user specifies the mean particle emissivity, the wall emissivity and an expected mean filling degree along the reactor. The equivalent wall emissivity is thereafter calculated automatically for non-black body particles. Since the modification is applied to the boundary conditions, the emissivity below 1 can be considered for the incoming radiation to the disperse phase. On the other hand, the heat interaction between particles within the reactor is recognized using properties of the black body as no scattering in the RTE is solved.

`fvDOM` radiation model is based on the idea of the finite volume discretized version of the RTE from [98], in which the dilute disperse phase can be considered. The modified `myfvDOM` model is developed for the dense disperse phase up to fully packed and even overpacked to model physically suitable radiation. Analogous to the DPM model for particle-interaction, the ray-tracing method for radiation is computationally expensive and infeasible for large scale calculations. The `fvDOM` model is suitable for the particle-laden with low particle volume fraction. The `myfvDOM` model is, on the other hand, proper for particle interaction with any packing degree.

3.7 Drying model

In the previous chapter, the proper physical model for the drying of biomass particles in an indirectly heated rotary kiln has been explained where no input gas is assumed to be injected into the reactor. The average moisture content of around 50% (wet basis) is assumed in the simulation to meet the average condition of input material.

In OpenFOAM®, two phase-change models are implemented. `liquidEvaporation` handles only evaporation in an unsaturated atmosphere below boiling temperature. It applies the solution of

Fick's law for moisture concentration difference at the particle surface and surrounding gas in the same cell. This model is meant only for surface evaporation and not for constant-temperature vaporization, i.e., boiling. The second available model `liquidEvaporationBoil` handles evaporation in an unsaturated atmosphere via Stefan-Maxwell diffusion. The model is suitable for phase change in a multi-component system and calculates the vaporization of superheated sprays called flash boiling [101]. Unfortunately, this model is also not suitable for the drying of wet particles in a saturated atmosphere via boiling. A solution to this problem is an extension of the former model with an additional thermal model for the vaporization state.

Over time, more particles enter the reactor whereby the water vapor concentration in the gas phase grows and the wet-bulb temperature raises as well. Consequently, either some particles will be entirely dried or the concentration difference of moisture between their surface and surrounding gas will be so small that no evaporation takes place anymore. In this case, the temperature rises until the moisture within the particle reaches its boiling point. The modified drying model switches to the second term in Equation 3.33 and particles reach the boiling state by consuming the input heat to vaporize moisture at $T_{\text{boil.}}$ as far as the water content exists within the particles.

To cover a wide range of applicability like saturated and unsaturated conditions in the reactor, a new drying model is implemented in the code. The drying model switches between a thermal drying model [51] and a linearized diffusion-based model [101]. The thermal model is the most often used drying model in the literature [51] assuming an arbitrary constant temperature as a drying temperature. Any amount of heat delivered to the particle above this temperature vaporizes the moisture. The modified thermal model in this work assumes that drying occurs at the pressure-dependent boiling temperature $T_{\text{boil.}}$, in this case in a saturated atmosphere. $T_{\text{boil.}}$ originates from the semi-empirical Antoine correlation [102]. The modified drying model additionally considers the evaporation below $T_{\text{boil.}}$ based on diffusion described in section 2.10. The moisture removal rate from the particle is written as

$$\frac{dm_{\text{drying}}}{dt} = \begin{cases} N_{\text{p}}\, A_{\text{s}}\, \widetilde{M}_{\text{H}_2\text{O}}, & T_{\text{p}} < T_{\text{boil.}} \\ \dfrac{\dot{Q}}{h_{\text{fg}}}, & T_{\text{p}} \geq T_{\text{boil.}} \end{cases}, \qquad (3.33)$$

where $\dot{Q}$ represents the total heat delivered to the particle, h_{fg} in the denominator is the enthalpy of vaporization. The developed model, therefore, is a supplement to the existing `liquidEvaporation` model considering the boiling temperature calculated based on the pressure of the bulk gas in the Eulerian cell. This introduces the criterion to switch to the thermal

submodel of the drying model. From the dynamic state point of view, two case scenarios may occur in the process:

- The particle enters the reactor at the beginning of the simulation while the concentration of water vapor in the gas phase is negligible. In this case, the evaporation model acts through the default drying model based on diffusion law.

- The heating rate to the particle and evaporation rate to the gas phase come to an equilibrium state when the particle approaches its wet-bulb temperature. In the case of a fully saturated ambient, this is the boiling temperature.

This model is suitable for one active species undergoing phase change, for instance, in this study the moisture. The effect of hygroscopicity of biomass on the enthalpy of phase change is considered and modeling of this phenomenon is discussed in section 2.10. During the drying process, there is no other active heat and mass source term within the particle such as reactions. The same as for the original drying models, intrinsic transport limitation within the particle is neglected.

To recapitulate, the drying model is a combination of already implemented diffusion-based evaporation model and a newly modified thermal model (based on the heat sink method) for vaporization in equilibrium. The drying model is extended because the existing models cannot support the vaporization of liquid in a fully saturated ambient. The combined model stated in Equation 3.33 covers different thermodynamic conditions that wet solid can be subjected to inside the reactor.

3.8 Devolatilization model

The entire thermochemical reaction occurring in biomass particles is assumed in this study as the devolatilization process (see section 2.11.2). In section 2, a suitable reaction mechanism is introduced and fitted via suggested experimental work to the model. Additional effort to use the results from the experiment and keep the mechanism in a single step reaction is expressed as well. The existing model for devolatilization in OpenFOAM® is written only for first-order reactions. However, as experimental results showed the non-elementary effect in the reaction kinetics [14], [55], [57], it is impractical to assume a complex reaction such as devolatilization or pyrolysis under the elementary state. Appropriately, it is necessary to extend the code to an nth order reaction for the devolatilization model.

3.8.1 Implementation of nth order kinetic reaction

The developed model can capture the effect of thermal degradation very well and cover any range of reaction orders. Implementation can be explained by rearranging Equation 2.37 to

$$\alpha_{\text{rxn}} = 1 - \frac{m_{\text{v}}}{m_{\text{v}_0}}, \tag{3.34}$$

by using balance equations: $m = m_{\infty} + m_{\text{v}}$ and $m_0 = m_{\infty} + m_{\text{v}_0}$ for each particle, where m_{v} is the volatile mass in the particle and m_{v_0} the total amount of volatiles and m_{∞} the final mass of char. Rearranging and differentiating of α_{rxn} from the previous equation gives

$$\mathrm{d}\alpha_{\text{rxn}} = -\frac{\mathrm{d}m_{\text{v}}}{m_{\text{v}_0}}. \tag{3.35}$$

Substituting Equations 3.34 and 3.35 into Equation 2.36 results in

$$-\frac{1}{m_{\text{v}_0}}\frac{\mathrm{d}m_{\text{v}}}{\mathrm{d}t} = k_{\text{rxn}} \left(\frac{m_{\text{v}}}{m_{\text{v}_0}}\right)^n, \tag{3.36}$$

where $\mathrm{d}m_{\text{v}} = -\mathrm{d}m_{\text{devol.}}$. Rewriting the aforementioned equation provides the non-elementary devolatilization model applied to each particle as

$$\mathrm{d}m_{\text{devol.}} = k_{\text{rxn}}\, m_{\text{v}}{}^n\, m_{\text{v}_0}{}^{1-n}\, \mathrm{d}t\,. \tag{3.37}$$

By rearranging this equation to the form of devolatilization mass rate ($\frac{\mathrm{d}m_{\text{devol.}}}{\mathrm{d}t}$), the second term on the right-hand side of Equation 2.1 (mass governing equation for discrete phase) can be obtained.

Equation 3.37 is implemented in the related devolatilization submodel in OpenFOAM® and will be validated in the next chapter.

Biomass degradation is a highly complex chemical process and thus it is not possible to define a concrete reaction pathway as well as product yields [2]. Therefore, a particular criterion for biomass conversion has to be defined. The definition concerning the full conversion of biomass in pyrolysis widely depends on material and research focus. In this work, carbon recovery regarding the carbon yield and total mass of the product is used as the quantified criteria for the final conversion. Carbon recovery (CR) has been widely studied in the previous works of the research group and can be found in [11], [12], [24]. Through experimental analysis, it is assumed that the desired product is achieved when around 50 wt.% of the dry biomass is devolatilized.

3.9 Overview of numerical methods

So far the necessary submodels are introduced and discussed from physical, mathematical and numerical aspects. The presented solver in section 3.2.3 is based on the described submodels in this chapter. A simplified numerical scheme in the developed solver during one timestep is shown in Figure 3.7. Calculations for each phase are sketched in the separate blocks. Mass, momentum and energy exchange between phases are handled through source terms.
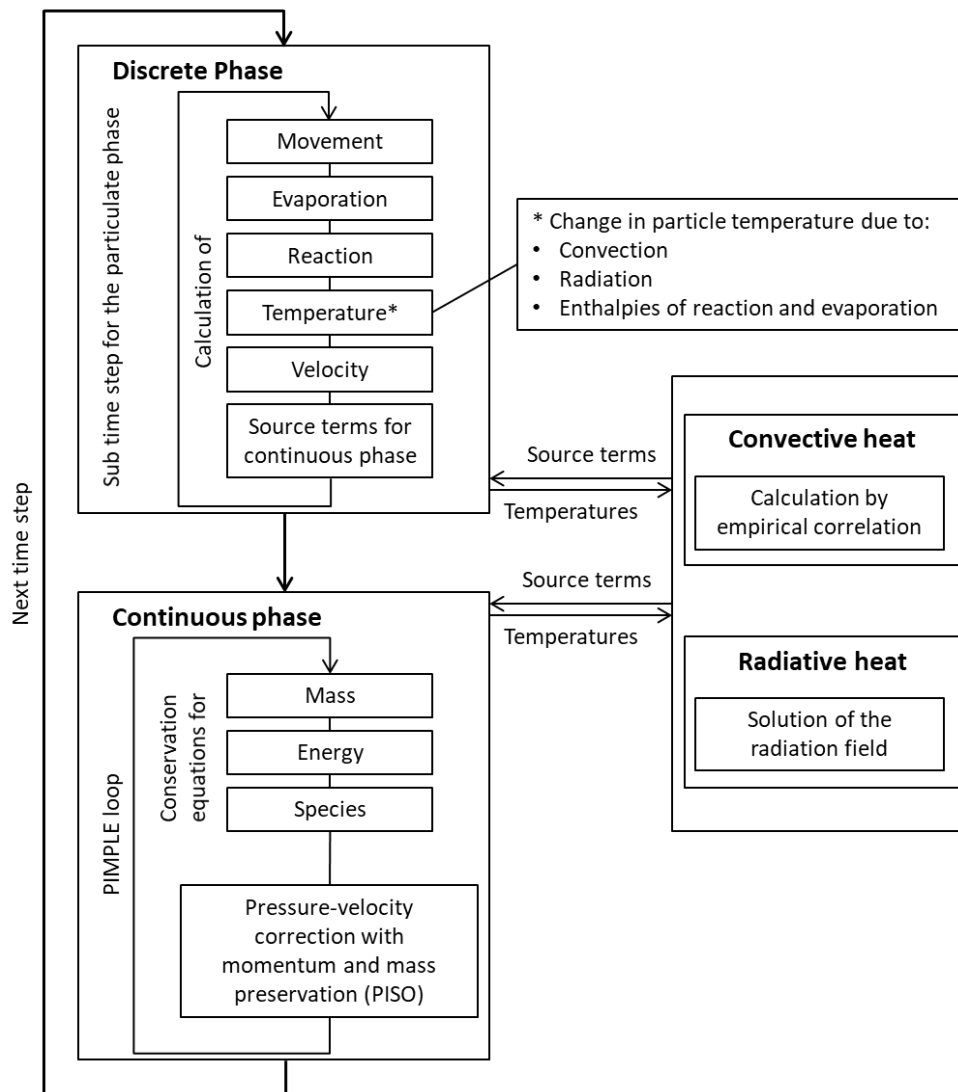
Figure 3.7 Simplified numerical flowchart of the solver for one timestep.

Regarding the discrete phase, parcel properties are natural extensions of particle properties since the MP-PIC assumes that parcels are made up of uniform groupings of particles, where all share the same physical properties. The particle molecular weight is either specified as constant or calculated as a mixture based on the weighted average from the mass fraction of components. The same principle is valid for the heat capacity of particles. For systems with low *CFL* numbers, the sub

timestep for the particulate phase calculation can be neglected, i.e. the global timestep can be applied for all calculations. For every parcel, movement, as well as heat and mass transfer, is calculated through submodels introduced in sections 3.4 to 3.8. To do so, it is necessary to map the location of parcels on the Eulerian grid for interphase exchange of source terms. Therefore, it is crucial to specify for all parcels to which computational cell they belong.

The 3D simulation based on the Eulerian method uses a transient pressure-velocity algorithm (PIMPLE) considering buoyancy force and variable-density properties for the components [103]. No transonic model is included in the algorithm and the nCorrector, i.e., the number of times the algorithm solves the pressure equation and momentum corrector in each step is set on 3. The total number of times the continuous system is solved within one timestep is set to the typical value of one, i.e, applying the algorithm with pressure-implicit split-operator (PISO), for the sake of reducing the computational effort.

The thermodynamic properties of the gas mixture are calculated using the JANAF thermodynamic coefficients [104]. The transport properties of the continuous phase are calculated using the Sutherland model [105]. The continuous phase transport equations are discretized in the Eulerian coordinate with the finite volume method, which is the default solution method of OpenFOAM® [74]. The discretization of the transient term is solved by the Euler scheme and gradient terms by central difference or upwind schemes. The list of solvers for highlighted variables is tabulated in the table Table 3.2.

Table 3.2 Method of solving and numerical tolerance for highlighted variables.

Variable	Solver	Tolerance	Relative tolerance
Cell volume fraction	GAMG	10^{-6}	0
Density	PCG	10^{-5}	0.1
Pressure	GMG	10^{-5}	0.01
Turbulence parameters	smoothSolver	10^{-5}	0.1
Species	smoothSolver	10^{-6}	0
Global ray tracing (radiation)	GAMG	10^{-4}	0

4 Experimental Setup and Validation of Simulation

In the previous chapter, the numerical concepts behind the development of the model are introduced and the adjustment and improvement of the numerical model are discussed. Finally, the submodels are merged and simulations can be performed. In the first part of this chapter, the experimental setup used to validate the simulation will be explained. Thereafter different modules of the simulation will be validated against experimental evaluations or analytical solutions.

4.1 Experimental Setup

A laboratory-scale rotary-drum reactor originally made by Carbolite Gero Ltd. (UK) is used in the experimental study. The reactor has been further developed to meet the reaction conditions for the purpose of the thermochemical conversion of biomass. In the cold run, a quartz glass tube has been used in order to assess the results visually. Nevertheless, in the warm experiment, the glass has been replaced by a metal tube to avoid the danger of glass breakage due to the thermal stress and related problems caused by the axial expansion of the metal rings, which hold the rotating tube.

Figure 4.1 Rotary-drum reactor used in the experimental procedure

The length of the tube is approximately 1.4 m with an outer diameter of about 8.5 cm. The reactor consists of a 1-meter heated electrical furnace, which covers the middle of the rotating tube. Thus, two sides of the tube remain unheated and are kept cooled down by two small blowers. The cooling effect is seen to keep the sealings and bearings of both sides durable in high-temperature conditions. The rotation of the reactor can be adjusted between 3-12 rpm and the inclination can be set from 0.5 to 5 °. In addition, the device offers a vibration system with regulating intensity to modify the feed flow to the reactor, which enters through a hopper (on the left side below the hopper, seen in Figure 4.2).
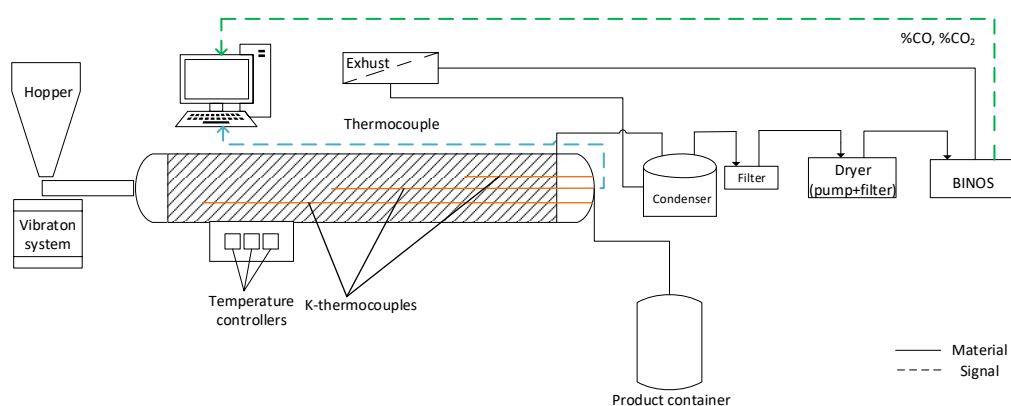
Figure 4.2 Schematic diagram of the rotary-kiln reactor and auxiliary devices.

As shown in the layout of the plant, Figure 4.2, the virgin biomass enters the reactor through a sealed hopper placed above a vibration system. Three thermocouples of different lengths are located in the heated tube measuring the gas temperature in the first quarter, middle and last quarter of the reactor.

A container is connected to the outlet of the rotary tube to collect the products. Additionally, at the end of the reactor, an outlet for the gas phase product has been designed, which links the reactor to the condenser. Condensable by-products remain in the condenser while the condenser has two outlets for non-condensable gases. The main outlet is to the ventilation system while the second stream goes to the pre-treatment devices before the gas analysis system. The schematic flow diagram of the process in the rotary-kiln reactor is shown in Figure 4.2.

The gas stream to the analysis device has to pass a pre-filtration and enters the dryer device in which a second filter and the pump are integrated. The outlet of the dryer is connected to a Non-Dispersive Infrared Absorption (NDIR) gas analyzer BINOS® (Leybold-Heraeus, Germany) that measures CO and CO_2 concentration of the gas, which can be used to evaluate the start and end time of the reaction. The outlet of the BINOS® is then redirected to the exhausting system. Online signals from

thermocouples and BINOS® will be shown on the computer using National Instrument™ visualizer LabVIEW [106].

4.2   Implemented Geometry

The rotary reactor apparatus is modeled and imported to the simulation. The laboratory-scale geometry is modeled as a horizontal cylinder and the entire reactor tube is modeled as the computational domain. The default mesh generator of OpenFOAM® "blockMesh" has made the implemented geometry of the rotating tube consisting of hexahedral cells. Details of the Laboratory-scale geometry are tabulated in Table 4.1 and shown in Figure 4.3.

Table 4.1 details of laboratory-scale geometry

Length of the reactor	$1.40\ m$
Diameter of the reactor	$0.085\ m$
Overall number of cells (hexahedra)	11200
Length of cells (along the tube)	Constant $0.01\ m$
Max aspect ratio	2.55
Max skewness	0.95
Minimum volume	$3.9 \times 10^{-7}\ m^3$
Maximum volume	$8.9 \times 10^{-7}\ m^3$
Total volume	$0.00686\ m^3$
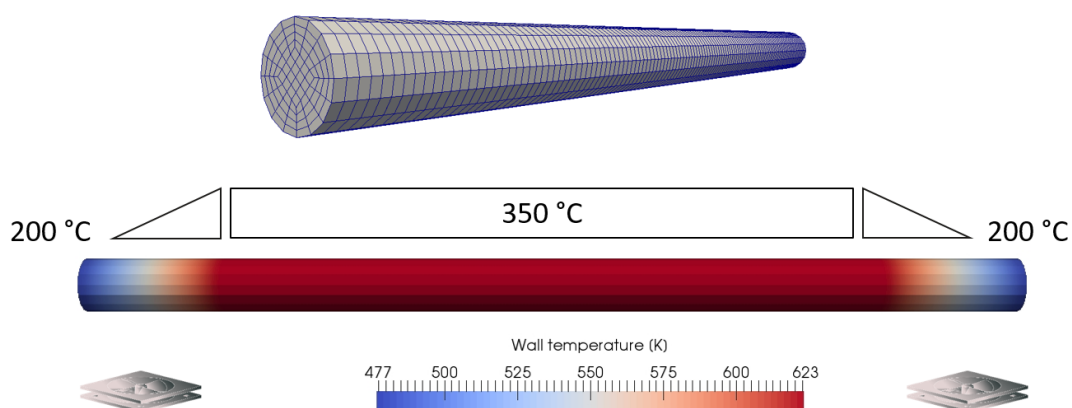
Figure 4.3 View of the geometry of the laboratory-scale rotary reactor model for specific wall temperature.

75

Cells have variable width and height due to the grid shape but the value is below 0.01 m for each case as the min and max volume of the cells show it as well. The pattern shown in Figure 4.4 has been implemented in order to keep the aspect ratio and skewness of cells in an acceptable range for the sake of accuracy in discretization especially for those cells that are closer to the center of the tube. The cross-sectional view shows that the x-y computational domain is divided into 5 different merged blocks. Four different slices of inner circle surround the rotated square in the middle. In total, 16 vertices on both sides of the tube make full geometry.
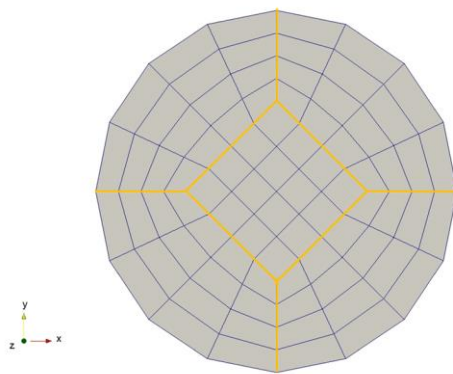
Figure 4.4 Cross-sectional view of the tubular reactor.

Due to the restrictions regarding the unresolved Eulerian-Lagrangian method (expressed in section 3.2.2), finer mesh generation is not possible for the Laboratory scale geometry while handling particles with a diameter of 6 mm. Moreover, due to the laminar regime within the gas phase and the slow movement of the discrete phase, there are no concerns regarding the accuracy. In the large-scale simulation, this restriction is negligible since the fact that the size ratio of particle-to-reactor is much smaller. Additionally, in large-scale simulations, grids have to be studied and optimized to compensate for computational performance.

4.3   Movement of spherical particles

In the series of cold run validation, various experiments have been performed at room temperature and it is attempted to verify whether the developed solver responses physically. To increase the precision of the validation of numerical simulation with experimental data, monodisperse particles are considered. Wooden spherical particles with a diameter of 6 mm, with particle and bulk density of 713 and 442 kg/m^3 are used in the experiment and simulation. The reactor is at ambient pressure and there is no gas flow input to the inlet boundary.

Additionally, qualitative evaluation of bed shape and bed height in a cubic box is studied for better conclusions in the modification of physical parameters. The visualization of the results for different restitution coefficient and timestep as determinative parameters is given and explained here.

Firstly, the behavior of the particle bed as a function of the calculation grid and the restitution coefficient is investigated. It should be noted that the restitution coefficient for particles is used in different models and submodels; here the focus is on the `explicit` packing model and `correctionLimitingMethod` submodel because only with this combination a realistic bed height could be achieved. Details of numerical models and submodels can be found in section 3.4.

The tuning of the restitution coefficient is a decisive task to reproduce a physical bed shape, for instance, if the restitution coefficient is fixed at too small values, unphysical overpacking of the bulk is the result and if it is set to larger coefficients, the particles fly around arbitrarily and even in extreme cases, they fill the whole box uniformly.

Figure 4.5 exhibits a designed simulation with 4000 particles of 1 cm diameter in a cubic box with an edge length of 20 cm. The Simulation timestep is 1 ms. Figure 4.5 shows that the lower restitution coefficient causes the unphysical overpacking of the bed especially in the case of using finer mesh. Moreover, for similar restitution coefficient, the different bed heights are clear for varied mesh sizes. The difference indicates how important it is to have a feasible size ratio between grid cells and particles particularly in lower values of restitution coefficient such as simulation of wet bulk.

So, it can be stated that the size of the grid has a considerable influence on bed behavior. For case studies involving dense flows and packed beds, the coarser grid can be used to achieve a more realistic behavior. In the case of a finer grid, on the other hand, the bed collapses more strongly. One possible explanation for unrealistic behavior in the case of lower cell-to-particle size ratios is that a single particle already has a very large influence on the particle volume fraction in a cell. For example, with one particle in a cell, particle volume fraction α_p might be between 0.3 and 0.4 and for this volume fraction, the packing force is still quite low. But if a second particle enters the cell, α_p already exceeds the closed pack limit of particle volume fraction α_{cp} and enormous particle pressure force applies to the particles located in the cell. On the other hand, the same impact can be imposed on the neighboring cells and consequently higher pressure forces from the next cells can be balanced mutually while the overpacking is stabilized in the domain. This suggests that the particles should not be as big as the cells. The minimum cell-to-particle size ratio of 2.2 is recommended for this application.
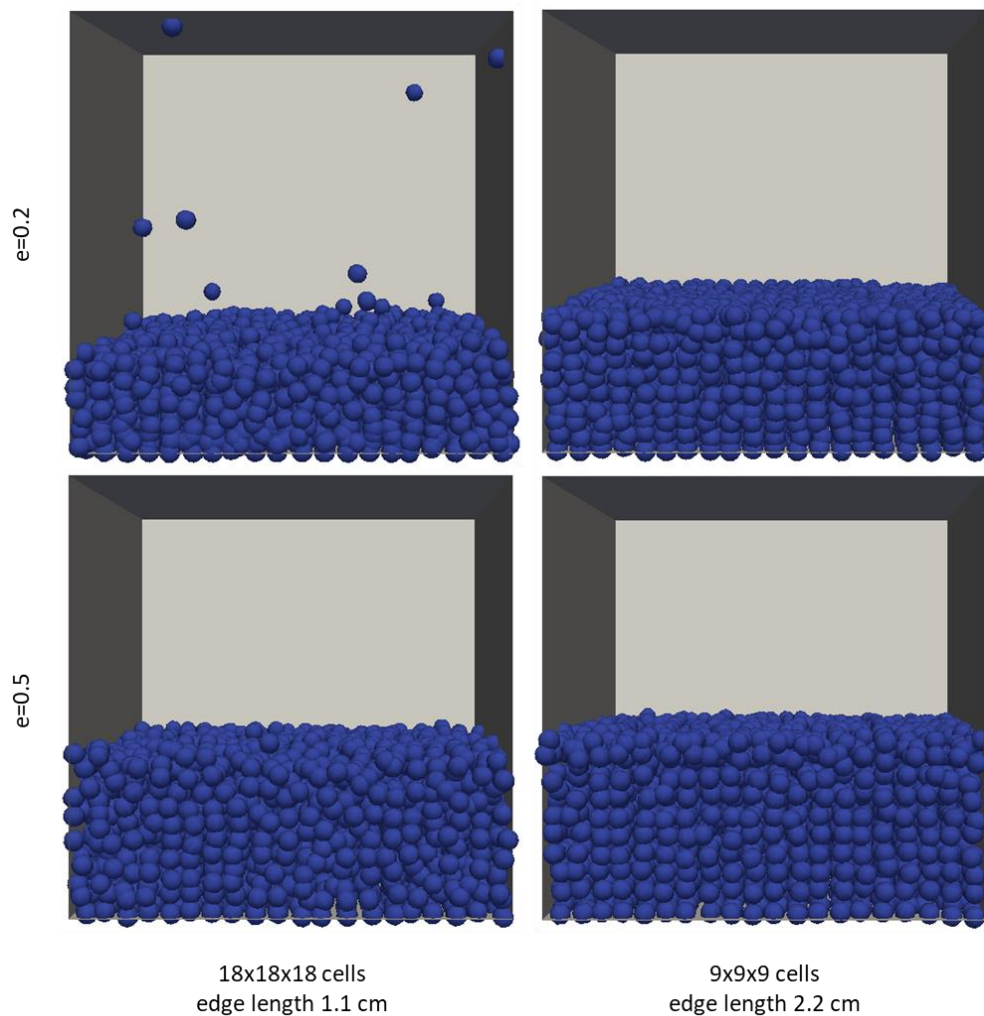
Figure 4.5 Behavior of the particle bed as a function of the computational grid and the restitution coefficient with timestep of 1 ms.

The second analysis is about timestep variation and its impact on the particle bed behavior. As it is mentioned previously, the timestep has a great effect on computational performance and calculation precision. For this case study, the coarser mesh with the restitution coefficient of 0.5 is chosen. Results are shown in Figure 4.6 for the lower and higher limits of time steps; namely 1 and 10 ms respectively. To visualize the impact, the upper layer of particles, approximately 1200 particles, are colored in red.

With smaller time steps, the particle bed behavior is already known as a physically suitable, example from Figure 4.5. By increasing the timestep to 10 ms, it can be seen that the particle bed is slightly over packed. The mixing degree of red particles in the bed of blue particles displays an unrealistic diffusion effect for stagnant bed and therefore faster particle movement comparing to the physical model. However, on the contrary, in the rotary drum, the bulk has already a radial mixing in the reactor, so this factor does not play an important role in the bulk behavior. This issue must be

investigated more in-depth for stagnant applications and case studies in which diffusion of granular flow is determining.

As a comparison between both cases, the latter simulation is 10 times faster than its associate model, which is the determining factor in large-scale simulation with long run times. In this study, the timestep is kept always in the range of below 10 ms, especially for large-scale simulation it is on average about 6 ms.

$\Delta t = 1$ ms $\Delta t = 10$ ms
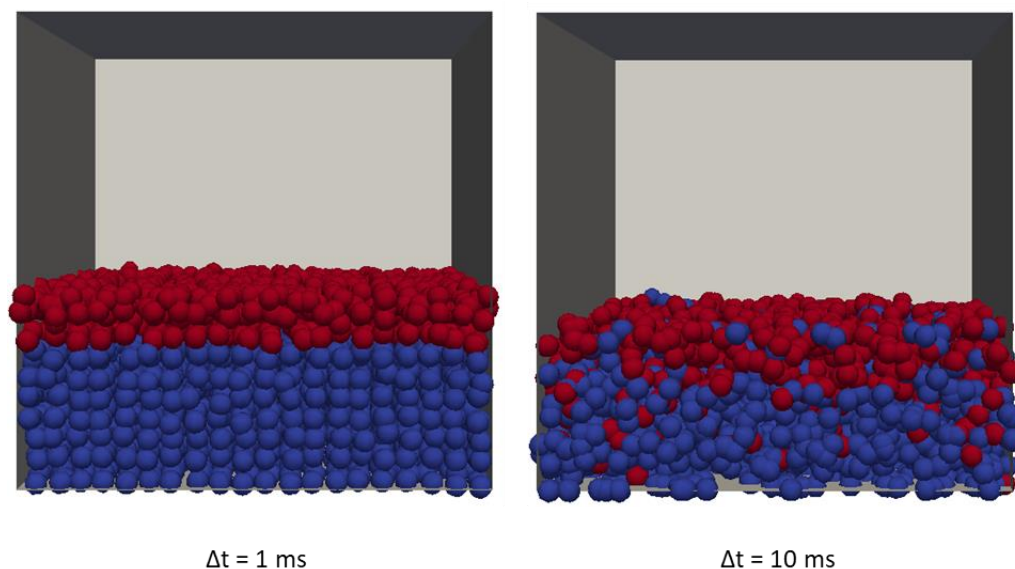
Figure 4.6 Behavior of the particle bed as a function of the time step.

4.3.1 Movement of spherical particles in tubular reactors

As was discussed in section 2.7 transverse motion of particles in the rotary kiln, mixing and motion of solid materials in rotary kilns are highly dependent on the transversal type of movement of the bed. The Froude number is calculated for the lab-scale reactor and based on that, we determine the type of movement of particles in the reactor. For the lab-scale reactor, the Froude number is obtained to be about $Fr = 1.2 \times 10^{-4}$ representing a transition process between sliding and mixing motion based on Table 2.1.

During the experiment with spherical particles, it is observed that while using the glass tube, the sliding motion occurs in which the process ensures that the particle-wall friction is smaller than critical friction. On the other hand, the substitution of the metal tube for the warm operation exhibits a different motion as the spherical particles surge transversally. This suggests that in the case of the metal tube, where the surface is considerably rougher, the wall friction is equal to or larger than critical friction.

4.3.2 Validation of residence time in tubular reactors

The residence time of spherical single-particle and particles in the bulk are the first measurements in the rotating tubular reactor that are performed for the verification of the simulation. Verification of residence time of the solid phase in the reactor is one of the highlighted parameters of the cold run since it covers other important parameters related to the movement of particles during the process. Physical simulation is achievable only if the correct residence time of the solid phase is determined.

The residence time of a single particle

In the absence of collision interaction, dominant forces to a single particle in a rotating tubular-shape reactor are gravity and forces due to particle-wall interaction. Particle-wall interaction in axial and radial direction introduces friction force, which mainly influences the residence time and shows how the particle might oscillate in the tube.

For the residence time of the single-particle, sets of experiments are carried out in 3 different rotation speeds (3, 7 and 12 rpm) for 8 different inclination angles (0.5, 0.75, 1, 1.5, 2, 3, 4 and 5 °). Twelve repetitive measurements for each case have been done in order to reduce error and calculate the standard deviation. The coefficient of rolling friction has been calculated from those experiments as well. Two different Lagrangian models, DPM and MP-PIC, have been used for particle movement in the simulation for the comparison and to validate the experimental results.

Figure 4.7 shows the result of measurement and simulation for a specific rotation speed of 12 rpm. Variation of residence time from the experiment due to imperfect sphericity of wooden particles has been calculated as standard deviation. The deviation is higher for the lower angle of inclination, which is reasonable because for the lower inclinations the component of gravity force along the tube length is less dominant for the particle. However, on the higher angle of inclinations where the particle acceleration mostly depends on gravity, the impact of non-sphericity is diminished and the deviation in residence time is negligible.
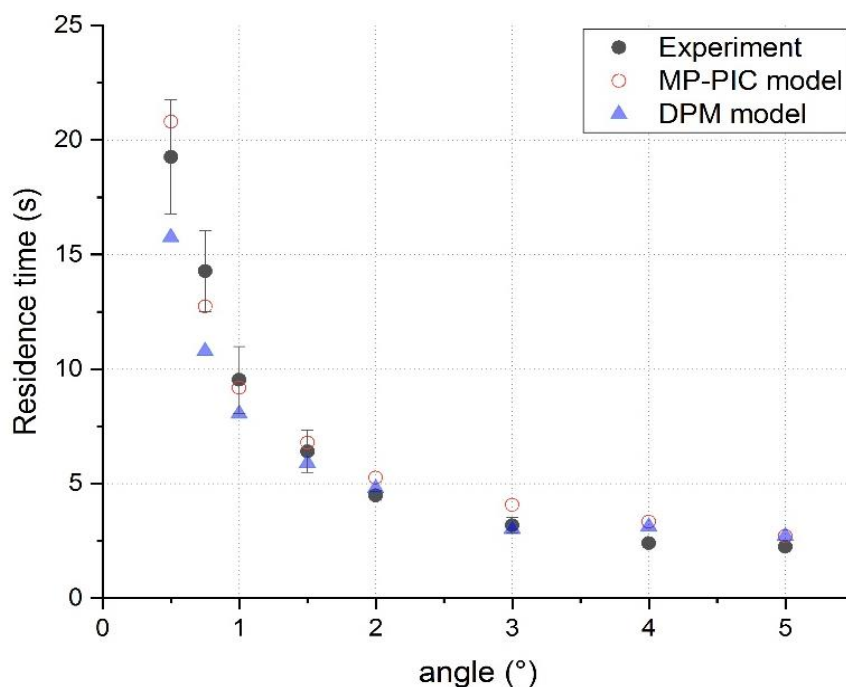
Figure 4.7 Experimental and simulation result of single particle residence time for the various angle of inclination with a specified rotation speed of 12 rpm.

The result of the simulation obtained from MP-PIC and DPM models have been illustrated separately for the sake of comparison. As the results of Figure 4.7 show, simulation from the MP-PIC method is in good agreement with experimental data. The DPM model has an unexpectedly higher deviation in the lower limit of inclination. This might be due to the large number of physical constants that the DPM model needs accurately as inputs in contrast to its competitor model. It has to be noted that in this study the reduced particle stiffness (RPS) model is used to decrease the calculation cost as the approach is widely accepted for coarse particles where contact force is dominant [78]. This approach could presumably increase the inaccuracy of the calculation.

Due to the low relative velocity between particle and gas in the tube, no considerable influence of the drag model has been observed in the simulation. Additionally, for the single-particle, in experiment and simulation, the effect of variation of the rotation speed of the tube was studied and it can be considered as negligible in inclinations higher than 2°. However, the angle of inclination of the tube has an impact on the oscillation of the particle while rolling.

Figure 4.8 compares the result of particle tracking simulation for single-particle movement using the MP-PIC method for different angles of inclinations. The result shows that the span of particle oscillation is larger when the acceleration force along the reactor is larger and thus residence time is shorter. The residence time of each simulation can be evaluated in Figure 4.7.
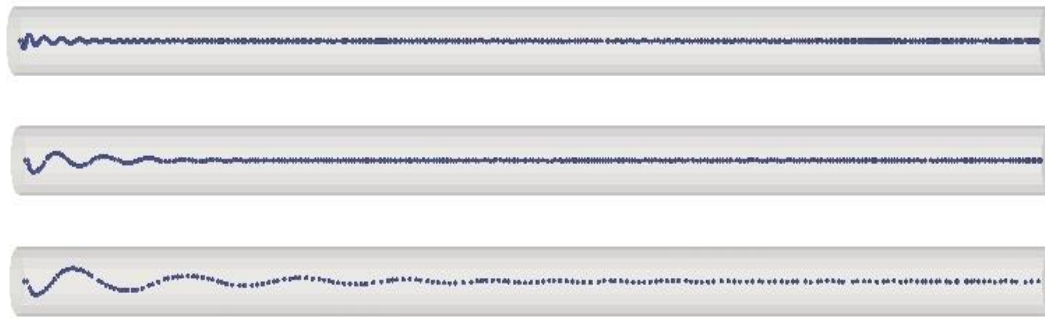
Figure 4.8 Comparison (top view) of the particle oscillation in the tube by different angles of inclination with a specified rotation speed of 12 rpm; at the top: simulation with the 1 °, in the middle with 2 ° and bottom with 5 ° of inclination.

The residence time of bulk

After the validation of single-particle residence time for various angles of inclination, the same experiment has been done for the bulk of particles. Particle-in-bed residence time for 5 different inclination angles (1° – 5°) and 3 different rotation speeds (3, 7 and 12 rpm) with 1000 particles input is evaluated.

Residence time in the reactor depends on different parameters such as inclination and rotation of the unit. Material throughput to the reactor can be measured by adjusting the inclination and vibration intensity. This parameter has also a slight impact on the residence time of the bulk material. Therefore, for the bulk residence time it is important to measure the input mass flow and implement it in the simulation. The measured mass flow for each case for different inclination at a constant vibration intensity is listed in Table 4.2.

Table 4.2 Measured mass flow of particles at various inclinations with a constant vibration intensity.

Inclination (°)	Input particles (1/s)	Mass flow (kg/h)
1	16.64	4.89
2	19.61	5.76
3	24.39	7.16
4	43.15	12.68
5	53.39	15.68

With a marked particle, the average residence time of particle-in-bed is evaluated in twelve repetitive measurements. Figure 4.9 shows the formation of bed in the experimental procedure as well as the related simulation.
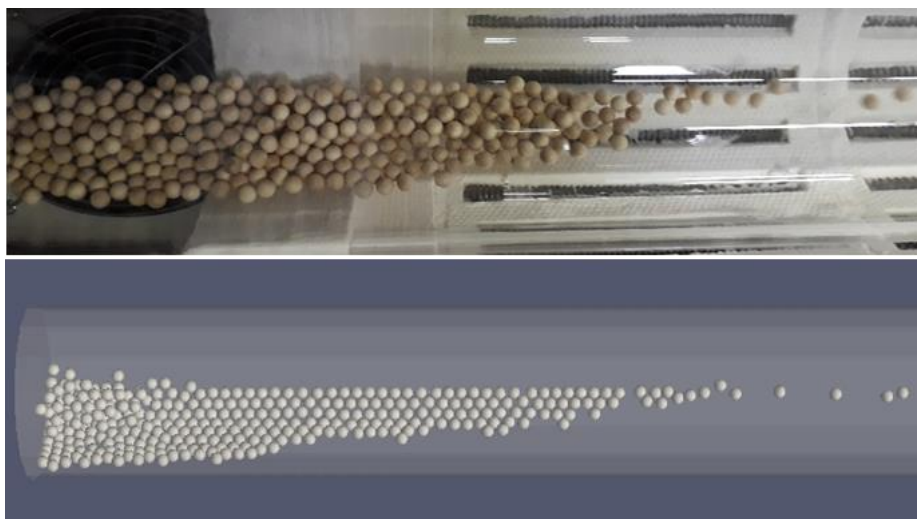
Figure 4.9 Visualization of experimental setup and modeling of particle residence time in the rotary reactor.

Figure 4.10 shows the experimental and simulation results of the average residence time of bulk containing 1000 particles with input flow from Table 4.2. High deviation in the experimental measurements are expected and connected with the position and injection-time of the marked particle. For example, particles, in the beginning, have less interaction with each other, they can roll more freely, and thus they have shorter residence time. On the other hand, at a later time, due to pile formation at the inlet of the reactor, some particles might roll or jump reversely toward the inlet patch and get trapped in the corner, which increases their residence time considerably. Therefore, the average residence time from repetitive experiments is a good approximation of steady-state residence time of bulk in the reactor.

The MP-PIC model gives closer results to the average obtained from experimental work. The DPM model has also acceptable values in the relatively smaller angle of inclinations but the range of deviation matches the experimental data better. It was expected to observe more accurate results from the DPM model. The model is more detailed and consequently computationally more expensive. It might be the case that the model computes the resolved interaction inaccurately due to insufficient experimental parameters, which are numerous and difficult to obtain in most cases. An alternative explanation could be the usage of reduced particle stiffness (RPS) model due to computational effectivity. Although the approach is widely accepted for coarse particles where contact force is dominant, the influence should be studied in more detail.

On the other hand, by implementing the measured rolling coefficient of particles it seems that the inter-particle interaction used in the packing model of the MP-PIC model works accurately enough.
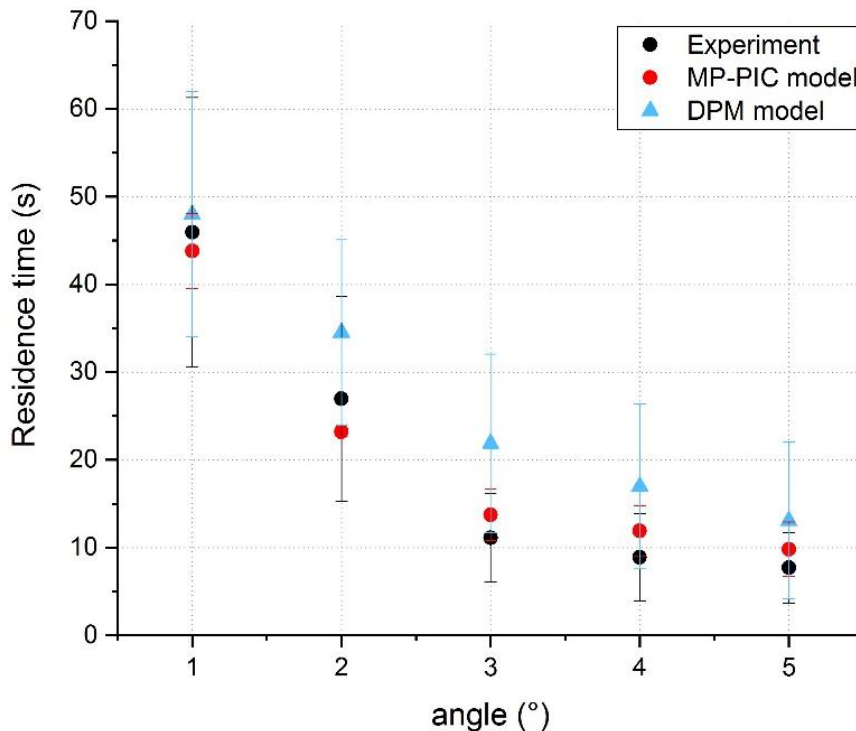
Figure 4.10 Experimental and simulation result of the residence time of bulk containing 1000 particles for various angles of inclinations with a specified rotation speed of 12 rpm.

In conclusion, the MP-PIC model has a good agreement with experimental data although it is computationally less expensive compared to DPM and it is in favor of large-scale simulations. Regardless of the smaller deviation to experimental data, the average residence time from MP-PIC simulations fit to mean residence time in steady-state experimental evaluations.

4.3.3 Validation of mixing behavior

The mixing of materials in the rotary reactor is one of the influencing parameters on the conversion of biomass particles. The degree of mixing of monodisperse spherical particles with 6 mm diameter in the rotary reactor is studied and it has been compared with results from simulation from both studied methods.

Radial and axial mixing are two different mixing opportunities that particles could have where particle-to-reactor diameter, particle-wall friction coefficient, rotation, and inclination are the relevant parameters. The axial mixing provides good information about the bed movement in the reactor and it gives a generally good overview of the profile distribution of residence time of the particle. The lower the axial mixing is, the lower the residence time deviation will be. A lower axial mixing index guarantees a homogenous quality of the product at steady-state operation. However,

axial mixing is to some extent inevitable and it is not in favor of the quality. High axial mixing can cause large variations in residence time of bulk material and therefore less homogeneity might appear in the quality.

On the other hand, radial mixing is important for uniform heat and mass transfer in rotary drum and therefore homogenous product properties. To ensure sufficient radial mixing, the degree of filling and particle diameter have to be kept below a limit as a function of reactor diameter and rotational speed.

Quantifying the degree of mixing with the mixing index is a challenging case study. In practice, measuring the mixing index is highly sensitive to the experimental parameters such as time span between injections of two sets of particles, the mixing area in the reactor, and assuming a comparable area in which particles will be positioned and counted for calculation of mixing index. For granular flows, visual qualification and quantification and for non-spherical particle flows with unspecified geometry, dispersion analysis are meant to refer to the axial mixing index.

To quantify the mixing behavior of spherical particles, the Generalized Mean Mixing Index (GMMI) developed by Asmar et al. was proposed and used to quantify mixing by means of a simple mixing index in its x-y-z components [107]. The Authors have stated that the index illustrates the usefulness of the discrete element method (DEM) simulations in studying mixing and segregation in bulk solids subject to movement. The mixing index for axial coordinates can be calculated as

$$GMMI_{x_i} = \left[\frac{\sum_{j=1}^{n}(x_j - x_{ref})}{n} \right] \bigg/ \left[\frac{\sum_{k=1}^{N}(x_k - x_{ref})}{N} \right] \qquad (4.1)$$

Where the index i represents a specific type of particles, n is the total number of particles of type i and N is the total number of particles. The formula is simply the mean of the x-coordinate of particle centers of type i divided by the mean of the identical coordinate of all particles. x_{ref} is the reference x-coordinate which is calculated relative to a reference x-coordinate such as one of the corners [107]. $GMMI_{y_i}$ and $GMMI_{z_i}$ are calculated similarly by replacing the coordinate-related variables in the abovementioned formula. The Generalized Mean Mixing Index for type i can be defined as

$$GMMI_i = \frac{(GMMI_x + GMMI_y + GMMI_z)}{3} \qquad (4.2)$$

GMMI is a coordinate-related mixing index and thus can be larger than unity. For a better assessment of the mixing index in this study, the center of the coordinate system is set at the bottom left corner and the normalization is applied to the calculated indices.

Results from experimental evaluations are compared with simulation only by top view captures and therefore the *y*-coordinate is eliminated from calculations. An example of experimental capture is shown in Figure 4.11 for the calculation of GMMI. Marked points on the blue spheres are the coordinate of the center of particles for calculation of the nominator of Equation 4.1. The open-source software WebPlotDigitizer has been used for the estimation of the coordinates of particles [108].
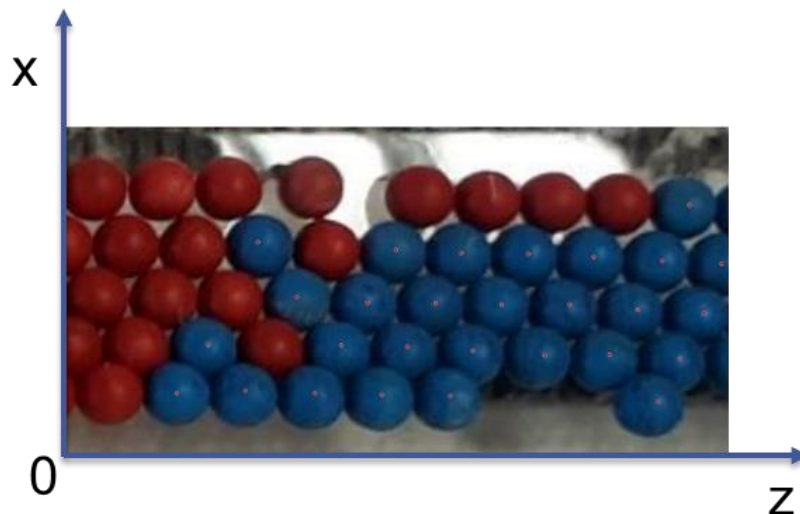
Figure 4.11 Top view image captured from the glass tube reactor for calculation of mixing index.

Axial mixing of spherical particles

To assess the axial mixing, two sets of 1000 identical particles, with different colors are injected in the reactor consecutively. In this experiment, the input flow, as well as the time gap between finishing one set and starting another set, is kept constant. Figure 4.12 shows a comparison among measurement, DPM and MP-PIC model for an example case study with 1° of inclination and 12 rpm rotation. The input flow and duration of particle injection for the simulation are calculated from Table 4.2.

Results show that, as the inclination increases, the mixing area becomes narrower and the degree of mixing becomes lower as well. Above 3 degrees of inclination, no axial mixing is observed as particles rolling fast and the interaction between sets of particles is minimized. Table 4.3 quantifies the normalized mixing indexes for the studied cases up to 3°.

Table 4.3 Comparison of Generalized Mean Mixing index for 1-3 ° inclination.

Inclination (°)	Normalized GMMI experimental	Normalized GMMI DPM	Normalized GMMI MPPIC
1	0.49	0.40	0.43
2	0.47	0.38	0.40
3	0.46	0.38	0.40
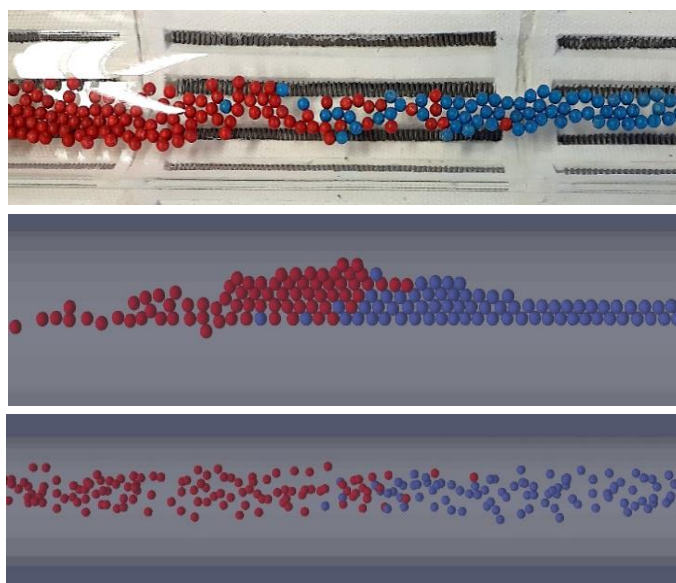
Figure 4.12 Visual assessment of mixing intensity for the experimental case, DPM and MP-PIC model (respectively from top to bottom), the case study of 1° inclination and 12 rpm rotation.

As can be seen in Figure 4.12 and Table 4.3, the result from the MP-PIC model has a qualitatively acceptable result compared to the experiment and the normalized mixing index is in good agreement with the evaluated data. Although particles are distanced from each other more than in reality, the shape of the bed and axial mixing is acceptable. The DPM model formed a bed closer to reality however due to the overdense bed formation the mixing index deviates from experimental data.

The simulation methods show the axial mixing behavior of spherical particles with an acceptable match to the experimental trials. The adjusted MP-PIC model has less deviation from the measured data although the bed spreads higher than in reality. It can be concluded that both models are validated and functioning in an acceptable spectrum.

Radial mixing of spherical particles

Separate experimental pieces of equipment are designed including a hopper and injection tube that are vertically divided into two halves to inject non-mixed sets of particles to the reactor. After the injection, particles were positioned in the bed and there was almost no radial mixing although the degree of filling of the tube was in the range of 10%. Observations show that up to the maximum rotation of the device (12 rpm) spherical particles roll in the bed and keep their position.

Due to the relatively small particle-to-reactor diameter ratio, sphericity of the particles and low rolling coefficient no radial mixing has been observed for spherical particles in the laboratory testbench. Practical observations show that at the operation conditions only a rolling flow regime existed and no cascading occurs during the bed movement.

For the simulation, a similar procedure is made to analyze the results of radial mixing. The inlet patch for the particle injection in the simulation computational mesh is split into two disjointed sections. A series of simulations with identical physical parameters is carried out to match the experimental conditions. The results from DPM agrees well with the test runs and no radial mixing in the reactor is observed as long as the bed is formed at the bottom of the reactor. However, the MP-PIC exhibits some degrees of radial mixing which is due to the principle of the particle interaction method. The restriction is due to the absence of direct mutual contact of neighboring particles. More specifically, the way that the MP-PIC method deals with all particles that belong to a computational cell does not allow any direct collision between them and thus radial mixing is inevitable for this computation methodology. This restriction does not influence the case studies with non-spherical particles due to the dominant radial mixing within the bed.

4.4   Movement of non-spherical Particles

One of the highlighted restrictions of the Lagrangian methods implemented in the open-source and commercial packages is that they consider particles only as spherical shapes. Thus, no geometrical variety can be chosen for the particles. This restriction, in fact, brings noticeable deviation for bed shape and mean residence time in the reactor.

For the simulations with wet biomass as the reactant, there are hardly any data available for the target values. Therefore own experimental tests are carried out. Previous and ongoing experimental tests in the continuous lab-scale tubular reactor show an optimum residence time for the steam-assisted carbonization of biomass with certain conditions to be between 30 to 60 minutes for a wide range of mass flow and particle thickness. The conclusion from previous researches focuses on 45

minutes of the solid residence time for a wide range of biomass products. Accordingly, the same residence time is used to be adjusted as the initial residence time for the numerical simulation in this work.

Experimental tests with various biomass materials show the same conclusion for the lab-scale reactor. Using the metal tube for the process, slumping bed motion is clearly confirmed for all test cases which is the sign of larger particle-wall friction than the critical friction (see Table 2.1). Hence, an acceptable radial mixing is expected in the rector which is experimentally observed.

To adapt the MP-PIC model for non-spherical particles, an additional resistance force is introduced that prohibits the quick rollout of particles from the inclined reactor. The approach represents the real biomass particles with unspecified geometries and comparable thickness to diameter ratio and helps to adjust the bed motion and the residence time of non-spherical biomass based on measured residence time. The enhanced friction method models the effect of non-sphericity and has proven to predict the correct particle behavior in experiments with prescribed residence time as well as the experimentally observed mixing of the processed biomass without increasing the complexity of the simulation. The simulated residence time of real biomass particles with enhanced friction and arbitrary inclination angle shows good agreement with measured residence times in the lab-scale rotary kiln. However, further study to adapt the MP-PIC model for non-spherical particles is necessary for a precise prediction without tuning.

For the main purpose of this study, important parameters are the mean axial and radial velocity of particles, which is adjusted to the test case by evaluation of average residence time, axial dispersion behavior and shape of the bed. These parameters determine the homogeneity of product properties under the influence of heat and mass transfer.

4.4.1 Mixing of non-spherical particles

In the case of using biomass as the input feed, it is not straightforward to assume an equivalent shape for the bulk. Therefore, the geometry of the solid bulk remains random and undefined although some physical parameters have to be utilized to quantify the overall properties. One practical suggestion is to enhance the friction coefficient of granular particles to emulate the bulk behavior. In addition to that, switching the isotropy model (discussed in section 3.4.2) can contribute to building up the interparticle friction in the simulation.

In these preliminary investigations, for the bed shape, the setting parameter μ (see chapter 3.4.4) in the particle boundary condition was identified as decisive variable. μ is defined as a restitution coefficient for the tangential component of velocity relative to the wall and physically interpreted as a tangential friction coefficient.

The first attempt of modification was carried out by adjusting the μ for the reactor wall. Figure 4.14 shows that at μ =0.1 the particles stack mainly in the lower part of the rotating tube and hardly cover the walls. With $\mu = 0.2$ on the other hand, some particles already move unrealistically high up the walls. With the higher value of μ, this phenomenon is intensified. Since the desired intermediate state cannot be achieved with the normal particle boundary condition, a new position-based boundary condition for particle-wall interaction has been defined.

In the new boundary condition, the $\mu = 0.2$ is used for the bed-wall contact zone and it is zero from a certain height of the wall where no particle is assumed to be. This position-based conditional boundary condition is designed so that the particles do not move up unrealistically high at the walls. To determine the maximum height, the user has to specify two bulk-related parameters: dynamic angle of repose θ and the expected bed height h_s in the rotating tube.

- The dynamic angle of repose is a bulk-related characteristic and can be defined as the steepest angle of descent relative to the horizontal plane to which a material can be piled without slumping. The dynamic angle of repose is proportional to the bulk angle in a rotating drum while monitoring the bed perpendicular to the cross-sectional plane of the tube. This parameter can be measured by different methods. In this work, the tilting box method has been used to evaluate the dynamic angle of repose for the used bulk.

- Bed height can be calculated from the ratio of bulk and reactor volume or more straightforward from the occupied cross-sectional area of the reactor. The volume of the bulk can be calculated based on bulk density and an optimized input mass flow to the reactor. A range of filling degree is usually known for rotary drum reactors. The filling degree of the reactor can also determine the bed height.

The geometrical correlation of bed height h_s, angle of repose θ and the maximum height of the bulk in the drum y_{max} is presented in Figure 4.13. With angle γ and two triangles containing γ it can be proven that θ is equal to ε.

The maximum height y_{max} can be calculated from the following equation:

$$y_{max} = -\frac{d_R}{2}\cos(\gamma_{max})$$ (4.3)

where d_R is the inner diameter of the reactor and the negative sign is because the zero-point is on the central axis of the cylinder and y-direction is defined parallel to gravity. $\gamma_{max} = \varepsilon + \beta/2$ is the sum of the dynamic angle of repose and half of the center angle of the bed which can be calculated from the bed height and angle of repose as
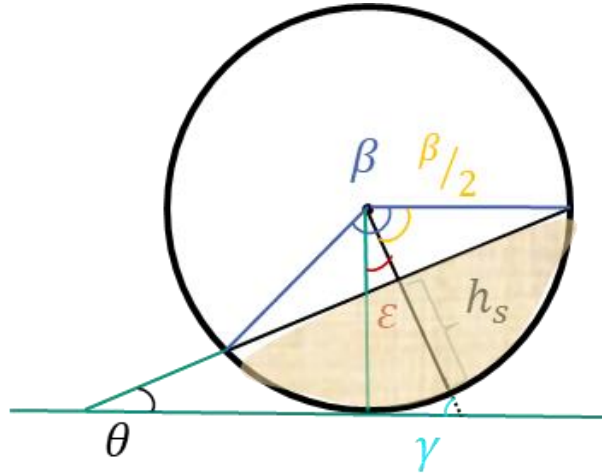
Figure 4.13 Mathematical correlation of bed height h_s, angle of repose θ and the maximum height of the bulk in the drum y_{max}.

$$\gamma_{max} = \theta + \cos^{-1}\left(1 - \frac{h_s}{d_R}\right),$$ (4.4)

γ_{max} is reformed to use the term $\frac{h_s}{d_R}$ which is the filling degree of the reactor. For the case shown in Figure 4.13, y_{max} is exceptionally zero (e.g. the bulk has the same height as the center of the drum) because of the $\gamma_{max} = 90°$.

In the right image of Figure 4.14, the bed behavior with the modified boundary condition is shown, where up to the defined height $\mu = 0.2$ is valid. For the bulk material used in this experiment dynamic angle of repose is measured around $\theta = 30°$ and a filling degree equal to 14% is estimated. It can be seen that with the new boundary condition a realistic behavior can be achieved. The x-component velocity scale is represented only for the particles belonging to the right side image.

With the modified boundary condition, the shape of the bed appears much more realistic and is similar to what one would expect with a rolling bed behavior. The distribution of the x velocities fits roughly to this bed behavior as well. The right side image of Figure 4.14 presents the scale for x velocities, in which the lower particle layer has to move up the wall and generally from left to

right (presented with lighter colors in the positive direction). The upper layer should roll from right to left and fill the vacancies at the bottom (presented with darker colors in a negative direction). The x velocities can depict an approximate physical bed motion, however, an exact pattern of individual particle movement is not obtained. This is due to the known restrictions of particle interaction of the MP-PIC solver. In general, bed shape and proportion of particle velocity show a good agreement with experimental data and uniform mixing behavior of the bulk is observed which is as expected from the results of various tests.
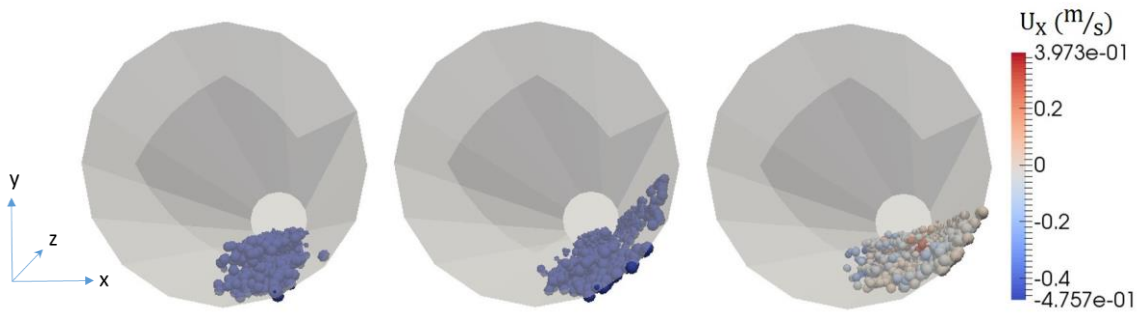
Figure 4.14 Bulk formation and behavior in the rotary drum with μ =0.1 (left), with μ =0.2 (middle) and with modified boundary conditions (right).

Another important parameter for verification of the bulk behavior of non-spherical particles is axial dispersion. Often the axial dispersion models are used to verify the axial mixing of the bulk [109], [110]. Therefore an axial dispersion coefficient D_{ax} is introduced, which has the same function and unit as the diffusion coefficient analogous to the mixture of gases.

$$Pe = \frac{\overline{v_p}\, l}{D_{ax}} \tag{4.5}$$

Equation 4.5 is the dimensionless Peclet number, which is used for the axial dispersion analysis where $\overline{v_p}$ is the mean axial velocity and l is the characteristic length. For sufficiently high Peclet number i.e. $Pe > 100$, consistent to cases of this study, it can be approximated as a function of the dimensionless variance of the residence time [111]:

$$Pe \approx \frac{2}{\sigma_\Theta^2} \tag{4.6}$$

The dimensionless variance σ_Θ^2 is often used in the literature to characterize the distribution of the residence time which on the other hand gives the axial dispersion [109], [110]. It can be defined as

$$\sigma_\Theta^2 = \frac{\frac{1}{N}\sum_{i=1}^{N}(t_i - \bar{t})^2}{\bar{t}^2} \tag{4.7}$$

The nominator of the equation 4.7 is the dimensional variance σ^2 for N particles with the average residence time of $\bar{t}$ and the denominator is squared average residence time.

For each simulation test case, it is possible to identify the residence time of every particle therefore all of the variables of equation 4.7 are known and the Peclet number (Equation 4.6) is calculable. $\overline{v_p}$ the mean axial velocity and l the characteristic length are also known. Rearranging the equation 4.5 the axial dispersion coefficient D_{ax} can be obtained.

In order to investigate the longitudinal mixing and later on the residence time behavior of the bulk material, several long-term simulations in the laboratory-scale geometry were performed. The simulation time was 6000 s for each case. The residence time of each particle leaving the reactor is recorded at the outlet cross-section, to provide detailed information on axial dispersion as formulated formerly. The number of particles that left the reactor and contributed to the analysis exceeds 5600.

The values for the axial dispersion coefficient in the simulations generally lie between $10^{-6}\,\frac{m^2}{s}$ and $10^{-5}\,\frac{m^2}{s}$. This is also a very common range of values in the literature [110]. To investigate the influence of the angle of inclination on the axial dispersion coefficient, identical simulations were carried out with different angles. Figure 4.15 shows the dependence of the residence time and the axial dispersion coefficient on the inclination angle. The axial dispersion coefficient tends to increase with increasing angle of inclination (or with decreasing residence time). According to the empirical equation from Sherritt et. al [112] this corresponds to the real behavior since the axial dispersion coefficient is reciprocally proportional to the filling degree of the reactor and residence time.

Good agreement between the value of axial dispersion from simulation and data from literature has been observed. The results from the simulation proved a physical trend of dispersion against variation of the angle of inclination. It can be concluded that the axial dispersion of the particles assuming the effect of non-sphericity is in the expected range from bulk materials. More details on residence time adjustment and distribution are given in the next section.
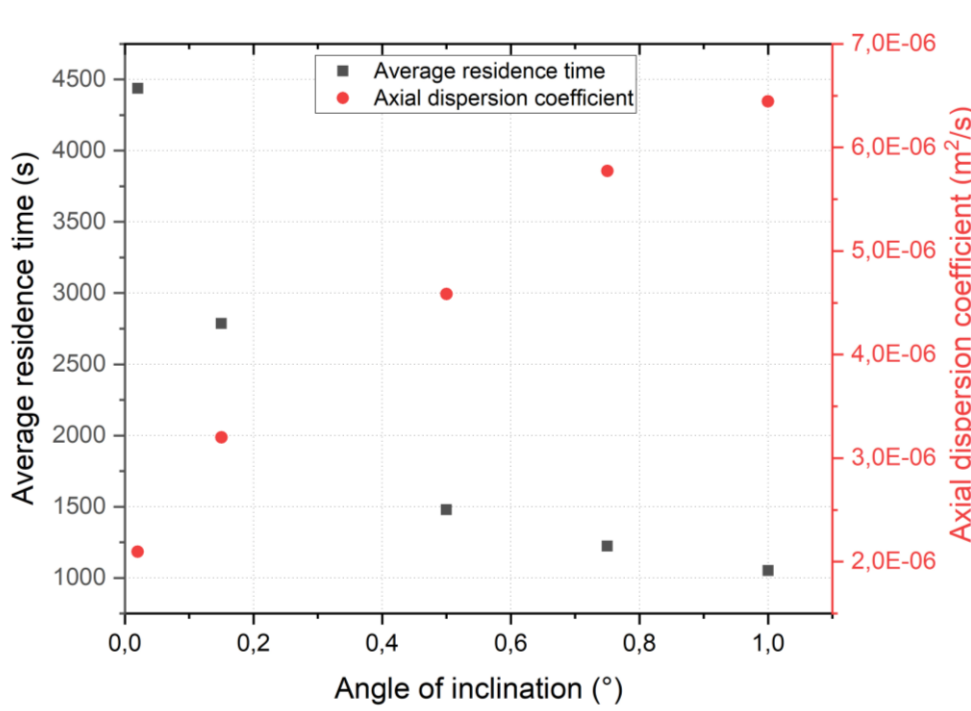
Figure 4.15 Mean residence time and axial dispersion coefficient as a function of inclination.

4.4.2 Residence time of non-spherical particles

Implementation of the operating parameters for the desired residence time of bulk material in the reactor is investigated in this section. The aim is to obtain a match with experiments and consequently to achieve acceptable homogeneous product properties. The verification of dispersion along the reactor with data from literature must lead to a realistic residence time distribution for bulk material, which follows a Gaussian curve.

Despite the success of developing a new model and boundary condition to simulate the bed shape and the motion based on the measured dynamic angle of repose (explained in section 4.4.1), this model has not been used in the long run simulations, due to the need for applying very small timesteps. The realistic shape of the bed was the outcome of the enhanced friction coefficient between spherical particles and the rotating wall but functional with timestep below 2 ms which is unapplicable for this scale. The model with operative timestep needs an artificially tuned angle of inclination to achieve a valid residence time for the discrete phase. By adjusting the angle of inclination in the model, the residence time obtained from experimental work is verified in the simulation and the normal distribution and axial dispersion matches the literature very well. No discrepancy has been found between the two models concerning mixing effect, dispersion and heat and mass transfer.

In the experimental work, for the constant rotational speed of around 10 rpm, the degree of inclination is set to approximately 0.75° for a mixed and non-homogeneous type of biomass. Sets of simulations with a specified timestep resulted in an equivalent average residence time only in case of changing the component of gravity force applied to particles along the reactor. The circumstance is due to the noticeably higher interparticle friction of non-spherical bulk material when it comes to a comparison to granular flows. Higher friction between particles with various geometry can consequently influence the random direction of contact force. In most cases, it weakens the passage force and therefore the average residence time will be much higher in the case of having non-spherical particles in the bulk [113].

An equivalent angle of inclination was obtained at around 0.15 ° to assure an average residence time of about 2700 seconds. Figure 4.16 exhibits the average residence time of an example from the simulation results of monodispersed particles, in which the effect of non-sphericity is applied. Results show that 50% of particles leave the reactor with the residence time of 2700 ± 100 seconds and almost 85% of the bulk remain in the reactor for a duration of 2700 ± 10% seconds.
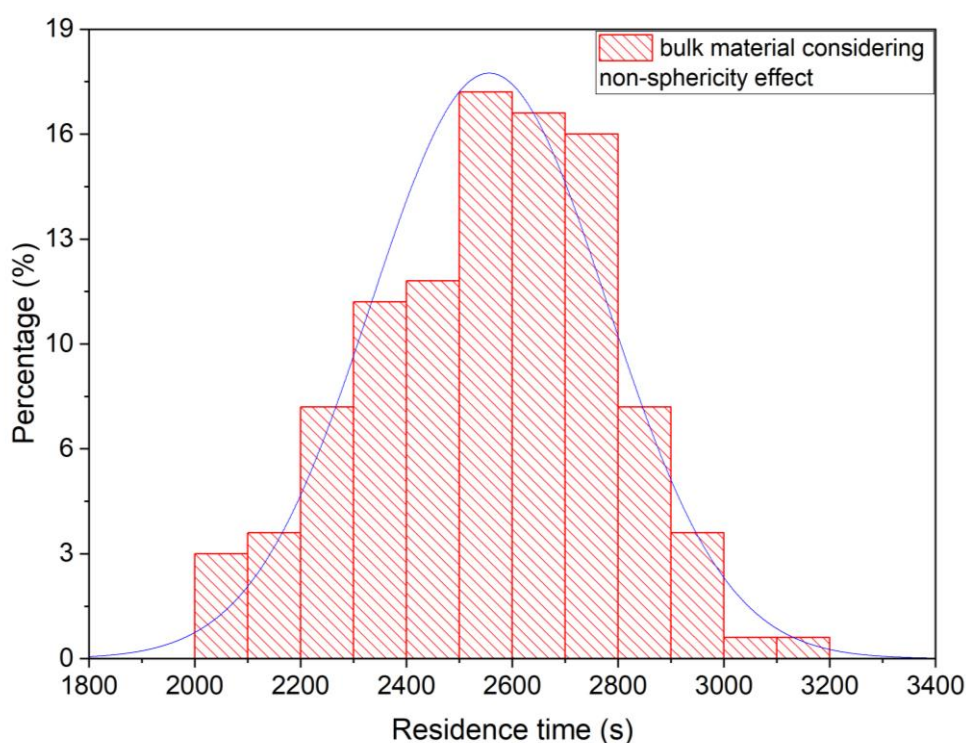
Figure 4.16 Adjusted parameters in the simulation: histogram of the residence time of particles leaving the reactor.

In the entire simulation with the laboratory-scale geometry, the mechanical parameters are kept constant to preserve a similar residence time for the bulk material. Nevertheless, minor deviation due to different rates of mass and size change is inevitable, however, no noticeable variation has

been observed in the series of simulations. The final observation is that the average residence time of the particles converges after almost 3600 seconds of simulation run to a mean value of around 2700 seconds. Therefore, the result for long-run simulations should be obtained and processed in the stationary state after 3600 seconds of simulation run time.

4.5   Heat Transport to Solid Phase

4.5.1 Validation of convective heat transport

Validation of convective heat transfer delivered to particles via verification of heat transfer coefficients is a significant step in the validation of the entire thermal process. This section aims to design an applicable method to estimate the heat transfer coefficients from experiments and compare it with calculated values from simulation.

Figure 4.17 shows a simplified sketch of an experiment that is designed and carried out based on the conservation equation of energy for particles. The experiment has been performed for a batch of five similar particles at least 10 times for three different gas temperatures of 100, 200 and 300 °C. The average residence time of each batch has been measured carefully and applied to those five particles.

The goal is to measure the input heat to each particle and estimate the share of convective heat transport and therefore evaluate the heat transfer coefficient. In every practical test, five wet particles with an average moisture content of approximately 50% enter the reactor. The residence time is adjusted in a way that particles leave the reactor while their moisture content is still above 25%. This procedure helps to eliminate the measurement error due to the additional heat of sorption to the latent heat of evaporation called the hygroscopicity effect (see section 2.10).
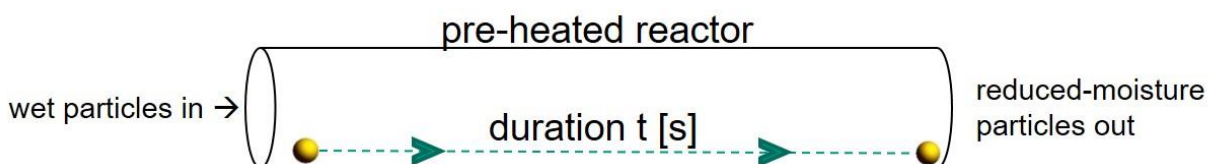
Figure 4.17 Sketch of the experiment for evaluation of heat transfer coefficient.

Considering the conservation of energy applied to each particle with the assumption that there is no accumulation in the system, the overall energy equation is

$$Q_{convection} + Q_{radiation} - Q_{latent} - Q_{sensible} = 0 \qquad (4.8)$$

The first two terms are the source terms of heat transfer to the particle and the latter ones are sink terms or heat stored within the particle.

$$Q_{convection} = h_p \cdot A_p \cdot (T_\infty - T_p) \cdot t \qquad (4.9)$$

Equation 4.9 is an accumulative form of Newton's cooling law where $Q_{convection}$ can be calculated per Joule if the other three source and sink terms are known. In this equation, it is assumed that in the first stage of drying, specifically above fiber saturated point, the particle area stays constant. The pre-heated reactor has a constant wall temperature and therefore the gas temperature T_g is constant. T_p is the temperature of the particle during the residence time in the reactor. Due to the transient state of the particle, the initial and final temperature of particles differs considerably. Therefore, to estimate the heat transfer coefficient there are uncertainties for an accurate solution. An average temperature will be considered for the particle and the limits of uncertainties will be evaluated by the initial and final temperature of the particle. Consequently, the evaluated heat transfer coefficient has to be in the expected range.

$Q_{sensible}$ is the amount of energy stored within a particle to heat up to the final temperature $T_{p_{final}}$

$$Q_{sensible} = m_p \cdot \bar{c}_p \cdot (T_{p_0} - T_{p_{final}}) \qquad (4.10)$$

In this equation, the initial mass of the particle is used to calculate sensible energy. The heat capacity of the particle is estimated based on the average heat capacity of the initial and final state of the particle. The effect of the heat capacity of the water content has to be evaluated by interpolation from

$$\bar{c}_p = x_{dry} \cdot c_{p\,wood} + x_{water} \cdot c_{p\,water} \qquad (4.11)$$

where x_{dry} is the mass fraction of the dried particle, x_{water} is the mass fraction of water content and c_p terms represent the specific heat capacity of the wood and water within the particle. In order to estimate the final temperature of a particle in the equilibrium state of evaporation $T_{p_{final}}$ wet-bulb temperature calculation has been used. The relative humidity of hot air in the reactor is negligible even in case of assuming 100% relative humidity of the ambient air at room temperature (before heating the reactor). This hypothesis is taken for the calculation of the particle temperature. For a certain gas temperature and relative humidity at atmospheric pressure, the final temperature of the particle can be estimated by using the wet-bulb temperature curves with acceptable precision. Thus, $Q_{sensible}$ can be determined straightforwardly and also using $T_{p_{final}}$, it is now possible to calculate the average temperature $\overline{T_p}$ for Equation 4.9 as well.

Q_{latent} is determined experimentally by measuring the evaporated water content from particles by multiplying the weight reduction of particles by the evaporation enthalpy.

The radiation energy source term $Q_{radiation}$ has to be calculated analytically by the Stefan-Boltzmann law

$$Q_{radiation} = \sigma \cdot \epsilon \cdot A \cdot (T_g^4 - \bar{T}_p^4) \cdot t \qquad (4.12)$$

As σ is the Stefan-Boltzmann constant and ϵ is the emissivity of the particle taken 0.85, which is a usual assumption for such an application [114]. The view factor for each particle can be supposed as unity under the assumption that there is no bed formation in the reactor, which is the case of this experiment. The same as convective source term, the residence time of the particle has to be taken into consideration.

So far, for Equation 4.8 three of four terms are known and therefore the total amount of the convective source term can be calculated. From Equation 4.9 the average, lower and higher range of heat transfer coefficient of the particles h_p can be evaluated. Figure 4.18 compares the experimentally evaluated htc with calculated values by OpenFOAM® with the Ranz-Marshall correlation. As can be seen, the values from the simulation are between the lower and higher range of estimation for each of the measured points and therefore agree well with experimental data.

Restrictions in the assessment of htc are the main source of uncertainties and differences between correlation and experiment. Parameters such as particle temperature, specific heat capacity, emissivity, etc. are among the parameters that provoke the error in the calculation. However, the definition of a range for the higher and lower possible coefficients is a helpful technique to verify the applicable range of measured values. Figure 4.18 shows a better agreement in the higher reactor temperature at 300 °C. Although the tests with lower temperatures exhibit less precision, the measured values are between average and higher range of htc and therefore acceptable.

The result of this evaluation shows that the radiation heat source to the discrete phase is not negligible in the range of reaction temperature. In Table 4.4 a summary of the share of sink and source terms for a single particle has been gathered as an approximation. It is pointed out that the effect of radiation increases as the temperature rises, for instance, it delivers a contribution of energy to the single-particles from one-third of source term energy at 100 °C to about 57% at 300 °C test case. Additionally, it is emphasized that the share of energy consumed for phase change Q_{latent} was considerably higher than the share of energy consumed for temperature change $Q_{sensible}$. This is an advantage for this experiment because Q_{latent} is calculated directly by the mass deduction and

therefore the precision of the measurement is higher than the calculation of sensible heat sink term which is estimated by the wet-bulb temperature technique.
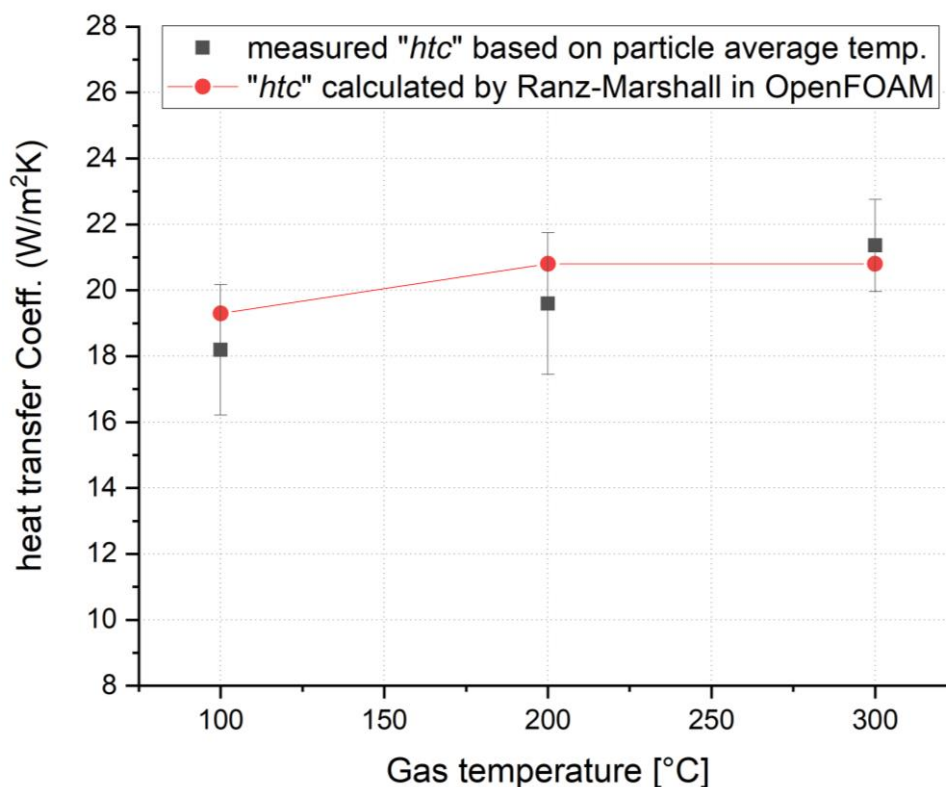
Figure 4.18 Comparison of calculated and experimentally evaluated heat transfer coefficient for spherical particles in a tubular reactor.

Table 4.4 Approximated share of source and sink terms to/within a 6mm particle.

Condition	Total energy (J)	Share of sink terms		Share of source terms	
		% $Q_{sensible}$	% Q_{latent}	% $Q_{convection}$	% $Q_{radiation}$
100 °C	78.4	11	89	64	36
200 °C	94.0	16	84	53	47
300 °C	102.5	16	84	43	57

From Table 4.4 it can be concluded that the share of sensible energy for experiments with 200 °C and 300 °C was almost identical although the total amount of delivered heat is around 10% higher in the latter case. Between the 100 °C and 200 °C test cases, the delivered energy shows around 20% raise and an obvious increase in the share of sensible energy. From the trend, it can be deduced that the growth in the final temperature of the particle should be smaller between higher temperature

tests compared to the two first trials. For a detailed examination, a comparison of the particle temperature in the equilibrium state of evaporation between wet-bulb temperature calculation and the value obtained from simulation has been compared in Table 4.5.

Table 4.5 Comparison of particle temperature in the equilibrium state of evaporation.

Condition	Wet-bulb temperature (°C)	Simulation temperature (°C)
100 °C	42	42
200 °C	53	59
300 °C	57	62

The outcome shows a good agreement between evaluation and simulation and it matches the expectation as well. The higher estimated temperature in the simulation can be due to the transport limitation in the surrounding gas and the influence of evaporated moisture in the cells or neighboring cells in which the particle moves. This phenomenon results in higher humidity in the surrounding ambient of the particle and therefore higher wet-bulb temperature. This effect is not considered in the simplified calculation of wet-bulb temperature in Table 4.5 thus is it possible that the values from simulation could be closer to reality. Nevertheless, both sets of results show an acceptable trend about the particle temperature change in different conditions as it is interpreted.

4.5.2 Validation of radiative heat transport

Validation of radiative heat transport in a cubic box

The radiative heat transfer model as significant for the heat transfer to the disperse phase has to be validated. As it is explained in the previous chapter, the default finite volume method of the discrete ordinate model, `fvDOM`, is adjusted to consider conditions involving highly dense phase flow. The new model so-called "`myfvDOM`" can evaluate the radiation heat transport for the entire geometry of multiphase flow even for overpacked computational cells.

In this section, radiation models P1, fvDOM, and myfvDOM are to be tested and checked for their precision in simple cases where an analytical solution is available. Thereby the strengths and weaknesses of the respective models can be worked out. Test cases were performed in a cubic box with a 20 cm edge length consisting of cubic cells with 1 cm edge length. Spherical particles have a diameter of 1 cm as well. The focus is especially on the interaction of radiation and particulate

phase. Therefore, convective heat transfer, as well as mass transfer (e.g. by evaporation) between particle and gas phase, were deactivated and the gases are assumed to be non-radiative.

To investigate the behavior of radiation models with a large number of particles, tests were carried out with 1800 particles in the mentioned box. The diameter of particles has been intentionally chosen equal to cell length to check the performance of models in extreme cases. As Figure 4.19 shows, the upper wall (above the particle bed) is warmer than the sidewalls. The temperature of the warm wall is 673 K and the temperature of the cold walls is equal to the initial temperature of the particles at 373 K. This means that there should be no net heat flow between the particles and the cold walls at the bottom in the beginning.

For particle-particle interaction, the DEM model was chosen in which reduced particle stiffness (RPS) model is used and additionally the modulus of elasticity of the particles was set unphysically low. This will result in overpacked cells. Although this is not realistic, it can occur at least temporarily in simulations and should, therefore, be considered in the simulation. The physical time of the simulations is set to 11 s, of which only the last 10 s were considered since there is a lot of particle movement in the first second so that the results can hardly be evaluated.
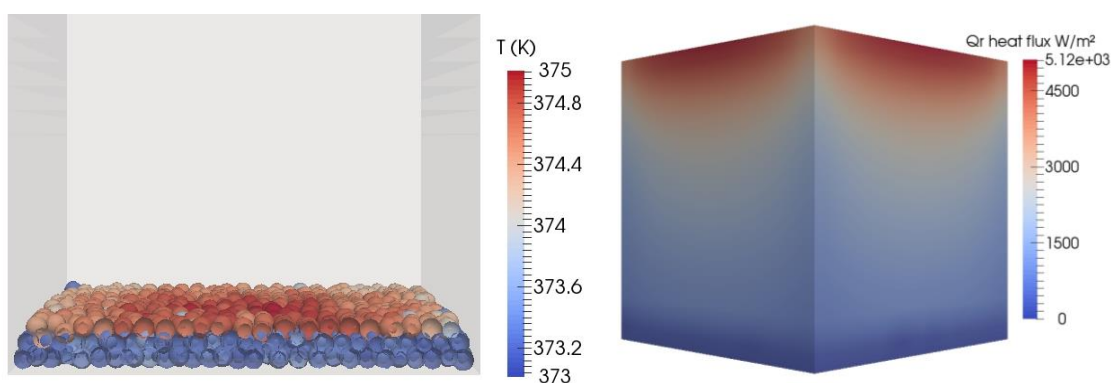
Figure 4.19 Distribution of particle temperatures (left) and distribution of Heat flux density on the side walls (right) during the box test with 1800 particles.

Figure 4.19 depicts the qualitative validation of the developed model for packed and overpacked particulate phase. The right image presents the distribution of heat flux density and shows how the particles in the lower part of the box are shielded from the radiation emitted from the ceiling and therefore the heat flux density caused by the radiation becomes almost zero. This shading effect becomes even more apparent when looking at the particle temperatures in the left-side image. As it is observable, the uppermost layer of particles receives the radiation heat from the upper wall, as the lower layers stay unheated. This effect is examined on the original fvDOM and P-1 model via

the identical test case. None of the models matches the obtained results from modified myfvDOM qualitatively or quantitatively.

For the evaluation, the total heat flow to the particles was calculated from the difference of initial and final temperature of particles in the bed based on

$$\dot{Q}_{p_{total}} = \frac{1}{\Delta t} \sum_i m_i c_{p_i} \Delta T_i \qquad (4.13)$$

This was then compared with the time-averaged, radiation-related heat flow at the walls, which was summed over all walls, in order to approve the conservation of the radiation energy. The conservation of the radiation energy was observed to be held suitably for all models at all times.

For the quantitative validation, the heat flow from the warm wall to the particles is estimated towards a view factor calculation. It is assumed that the uppermost particle layer represents a flat plane. As can be seen in Figure 4.19, since the 1800 particles fill approximately the lower 2 cm of the box, a visibility factor was calculated between two parallel plates with a as edge lengths of 20 cm and a distance of 18 cm. The formula for this calculation can be looked up in the appendix of view factor calculation from [96]. The view factor is calculated as $F_{1\rightarrow2} = 0.2286$ and it can be used to calculate the heat flux in

$$\dot{Q}_{SF} = \sigma F_{1\rightarrow2} a_{box}^2 \left(T_{wall}^4 - T_{layer}^4\right) \qquad (4.14)$$

where the T_{wall} and T_{layer} are the temperatures of the upper wall and uppermost particle layer respectively and a^2 represents the radiation surface.

A comparison of the evaluated radiative heat transfer to particles between radiation models in OpenFOAM® and the calculation based on the view factor is tabulated in Table 4.6. As the second and third rows in the table exhibit, it should be noted again that all models ensure the conservation of radiant energy. However, large deviations from the expected heat flow between the hot wall and the particles can be observed.

Table 4.6 Radiation heat flow in a box with 1800 particles: comparison of different models with view factor calculation.

Heat flow (W)	View factor	myfvDOM	DOM	P-1
To particles	96.31	97.36	82.58	288.92
From all walls	96.31	96.71	82.42	289.45

Obviously, with the P-1 model, the radiation heat from the hot wall to the particles is overestimated by a factor of about 3. In the case of the P-1 model, the deviation of wall heat flow from the analytical solution is even greater than the test case of an empty box. This can be interpreted as the P-1 model is not suitable for anisotropic radiative intensities and the miscalculation is escalated in case of having fully packed cells with large particles due to an increase of anisotropic properties such as the shading effect.

On the opposite side, the original DOM model underestimates the absorbed radiant energy by the particles. The relative deviation is about 15% and therefore the model is much more suitable than the P-1 model to be used as the basis of further development. Besides that, during the analysis of the results of the heat flow at the lower wall, it has been observed that almost 12.6 W radiation heat reached the surface despite the fact that the surface is completely covered with several layers of particles. Overall, it can be seen that the radiation intensity is not sufficiently attenuated in the original DOM model and therefore the particles do not absorb enough heat either.

The mentioned errors and deficiencies were the reason for the further development of the DOM model to myfvDOM model. Examining the results between view factor calculation and the modified model shows that with the new model the calculations can be reproduced very well. Table 4.6 distinguishes the results of the latter model from the other radiation models with a relative error of approximately 1 % to the reference calculation while the conservation of energy is in an acceptable range of relative error well below 1%.

Validation of radiative heat transport in the rotating tube

In the further steps of validation, the modified radiative heat transfer model is applied to the geometry of the rotary drum. The simulation is performed with the Carbolite Gero reactor geometry explained in section 4.2. For a filling with 1700 spherical particles of 6 mm diameter, the heat flow to the particles, energy conservation, computing time and the distribution of the heat flow density at the tube wall is considered. The tube walls have a uniform, constant temperature of 673 K, the particles have a temperature of 320 K at the beginning.

In the verification of the developed model, the three radiation models are compared to each other for a certain simulation time, same as previous test cases. Table 4.7 expresses some of the highlighted parameters of the simulation.

Table 4.7 Comparison of the three basic radiation models in a simulation with rotary drum geometry.

Model	Required computation time (s)	$\dot{Q}_{wall}$ (W)	$\dot{Q}_{p_{total}}$ (W)	$T_{p\,min}$ (K)	$T_{p\,max}$ (K)
myfvDOM	2199	929.7	934.2	331.3	349.7
fvDOM	1990	671.0	678.2	328.8	345.7
P-1	502	1625.4	1629.7	352.1	354.1

In the first blink, it is worth noticing that the simulation with the myfvDOM takes more than 4 times longer than the case of using the P-1 model, however, the results remained incomparable and inconsistent as before. Table 4.7 shows the temperature distribution of all particles in the results by $T_{p\,min}$ and $T_{p\,max}$. It can be seen that with the P1 model all particles have approximately the same temperature due to insufficiently calculated shielding of the radiation. The distributions are calculated in fvDOM and myfvDOM more realistic and consistent with each other.

The total absorbed radiation heat by particle-phase $\dot{Q}_{p_{total}}$ is conforming with total heat emitted from the hot wall $\dot{Q}_{wall}$. Thus for energy conservation, it can be seen that all three models have a negligible deviation in the range of below 1% by comparing $\dot{Q}_{p_{total}}$ with $\dot{Q}_{wall}$. Furthermore, the trend of values from models is in agreement with values in the above validation procedure for the cubic box. Both trends state the underestimation of the amount of heat that particles absorb when the fvDOM model is used and the overestimation of absorbed heat in case of using the P1 model.

Unlike the previous test case, there is no straightforward analytical solution for the test cases in the rotary drum reactor filled with particles. But the distributions of the heat flux densities on the walls can indicate the accuracy of the calculations with the three different models which are shown in Figure 4.20. Therefore, the verification is carried out by reference to the maximum possible radiative heat flux using the Stefan-Boltzmann law as an indication of the correctness. The maximum possible heat flux density can be calculated:

$$\dot{q}_{p,max} = \sigma\left(T_w^4 - T_{p_{min}}^4\right) = 10949\,\frac{W}{m^2} \tag{4.15}$$

A comparison between models in Figure 4.20 depicts that the P-1 model gives an almost uniform distribution of radiation heat flux in the reactor (note the scaling in each case) by neglecting of the shading effect in the reactor. However, both fvDOM and myfvDOM models give a more realistic distribution where the emitted heat flux is significantly increased in the area where the particles laid at the bottom of the reactor. Qualitatively, the distributions with the two latter models are similar,

but quantitatively there are significant differences and the mentioned underestimation of the default model is to be seen once again.
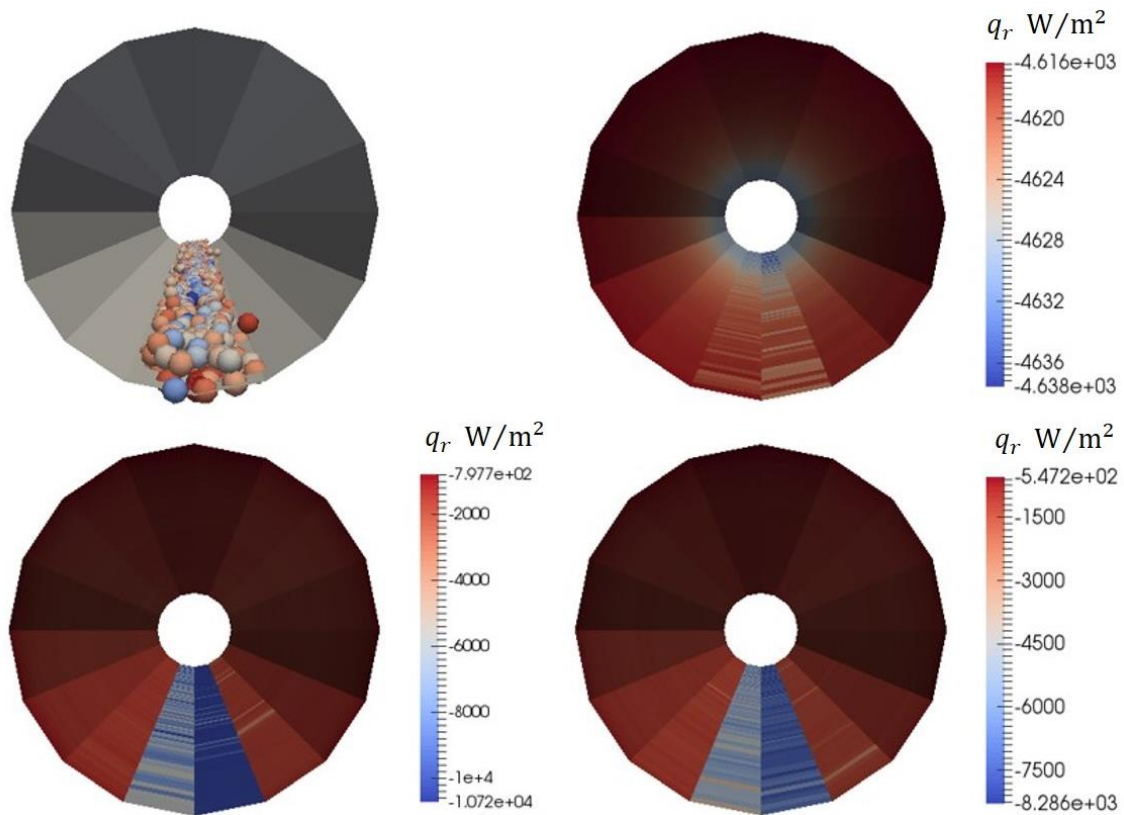
Figure 4.20 Particle bed model in the rotary drum reactor (top left), distribution of the radiation-related heat flux density q_r with P-1 (top right), myfvDOM (bottom left) and fvDOM (bottom right).

According to Figure 4.20, the absolute maximum heat flux density obtained in the simulation using the myfvDOM model is $10720 \frac{W}{m^2}$ (shown by negative sign, i.e. heat absorption, on the scale of Figure 4.20 at the bottom left) which is in a good agreement with the value calculated by Stefan-Boltzmann law in 4.15. So, the verification of the test case from a rotating tube approves the outcome from the box test case and it can be concluded that the adjusted radiation model represents the reality best among the three models.

4.6   Verification of Drying Model

After the validation of heat sources, it is clear that the amount of energy delivered to the particles can be calculated. In the next step, the verification of the developed drying model implemented in OpenFOAM® is to be investigated. Verification of the drying model for a single particle is performed by considering the convective heat source as the only energy source term to particles to keep the setup as simple as possible. The drying model is verified against the transient solution with

the convective heat transfer coefficient as an input which is called here the analytical solution. Therefore, the heat transfer coefficient obtained from the Ranz-Marshall correlation with experimental validation and analytical solution can be used in this model to compare the self-developed constant-temperature drying model with the implemented model in OpenFOAM®.

The simulation for the verification purpose is designed so that a single particle is injected with an initial temperature of 30 °C into the reactor filled with 100% water vapor at a superheated temperature of 400 °C at atmospheric pressure. This is the condition that can be developed at the steady-state condition in the reactor. In practice, however, the gas phase temperature probably fluctuates and it is below wall temperature at the beginning of the drying zone. It is expected that the particle will be heated up to its boiling temperature without any prior phase change while the ambient is fully saturated and no evaporation can occur. Thereafter the vaporization could start in the constant temperature until the particle is fully dried.

Figure 4.21 shows the comparison between the implemented model in OpenFOAM® and the analytical solution for the heating and drying of a spherical particle considering a small Biot number (uniform temperature). As can be seen, the particle temperature stays constant as long as the particle contains moisture. This is in accordance with the thermal model concept and verifies that the implemented model for drying is suitable for the proposed condition.
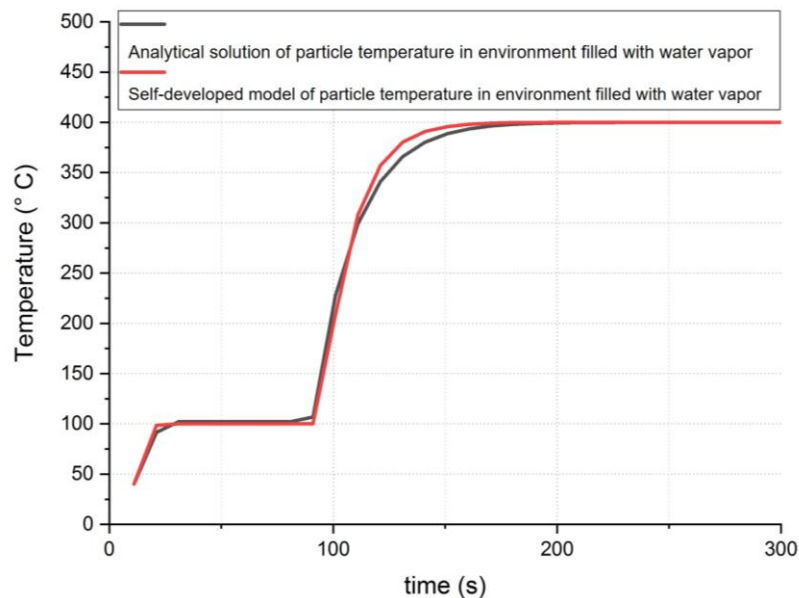
Figure 4.21 Comparison of analytical solution and OpenFOAM® model for drying a particle in a reactor with pre-heated pure steam as freeboard gas.

Next, the function of the model is studied for the case that the ambient of the reactor is not saturated with humidity. This might have a wider application in other studies where moisture content is

relatively low or inlet gas is introduced to the reactor for example for inertization or application of gasifiers. However, in this application, it can happen less often, for example at the beginning of the operation as the volume of the reactor is not yet filled with steam and inert gas or air exist in the freeboard gas. In this case, the evaporation model discussed in section 2.10 and Equation 2.28 is used.

For a better overview, Figure 4.22 shows two scenarios of drying particularly in a dry air atmosphere and in a 100 % water vapor condition. In the case of the reactor with dry air, the concentration difference between the particle surface and the freeboard gas causes the evaporation at relatively low temperature and therefore thermodynamic equilibrium keeps the temperature of the particle close to the wet-bulb temperature. Consequently, the particle is kept below boiling temperature as long as it contains moisture. In contrast, having steam as the freeboard gas prevents any evaporation below the boiling point and thus the temperature of the particle will be elevated to boiling temperature and thereafter vaporization starts.
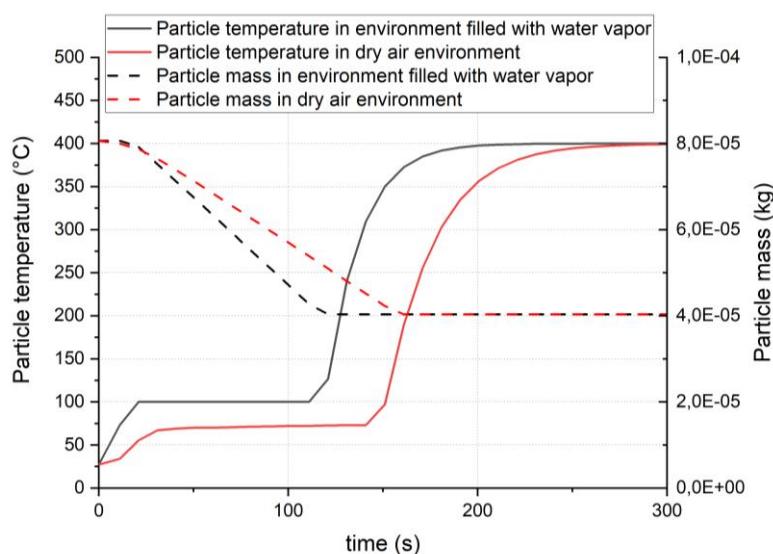
Figure 4.22 Comparison of drying a particle in dry air and environment filled with water vapor.

Therefore, it can be concluded that the phase change rate $\frac{dm_{\text{drying}}}{dt}$ and generally, the heating rate in superheated steam is higher compared to drying in an unsaturated environment. As the figure proves, a lower residence time for the drying of the identical material is needed in case of using superheated steam as the drying medium. The reason can be found in the thermophysical properties of steam, which remarkably differ from dry air. The results are in agreement with the general conclusion from the application of superheated steam drying technology by comparison with air-drying systems [115].

The functionality of the implemented drying model in saturated ambient is tested against a transient-mode self-written code with the analytical solution of the constant-temperature boiling model. Very good agreement between the two models is observed. In non-saturated ambient, the results of the model are compared with the existing drying models in OpenFOAM® and identical results are obtained. It is concluded that the drying model is suitable for the proposed application.

4.7   Verification of the Reaction Model

The kinetic model used for the carbonization of biomass is a multi species single-step n^{th} order Arrhenius equation, in which experimentally estimated kinetic rates of biomass is implemented. The assumption of a single-step reaction for the low-temperature conversion of lignocellulosic biomass in low heating rates such as torrefaction, slow pyrolysis, and carbonization is generally accepted [29], [33], [116]. Furthermore, since the produced tar from biomass and altogether the entire gas phase does not reach high temperatures, the impact of secondary reactions such as tar cracking is negligible. Usually above the reaction temperature range of 500 - 550 °C tar cracking kinetics has a considerable effect [3], [16], [117], [118].

Kinetics of lignocellulosic biomass have been determined by thermogravimetric analysis to predict mass loss evolution in the work of Müller-Hagedorn [57] (see section 2.11.1). The experiment is conducted at low heating rates to ensure the absence of heat and mass transport limitations. Thus, a kinetically controlled regime at the temperatures of 300, 325 and 350 °C are chosen intentionally for this comparison because the experimental conditions match this range very well. Additionally, due to the nature of the exponential dependency on temperature, the conversion degree is very sensitive in this operational temperature and the variation reacts suddenly and significantly to temperature changes. So, below the validated range, the negligible reaction occurs and above the range, this specific conversion terminates quickly and other reactions with various and undefined kinetics start.

Series of continuous experimental tests for walnut shells with 30 wt.% moisture content at different temperatures is performed to validate the model. Repetitive and continuous tests with average mass input of around 0.58 kg/h with 40 – 45 minutes of residence time are used to analyze the effect of the reactor temperature on the final mass of the product.

The result from these sets of experiments clarifies the mass loss from solid during the reaction. Therefore, the final mass of the remaining char m_∞ can be assessed for each set of the experiment in accordance with the final temperature. The correctness of this assumption is tested via longer

reaction time for each reaction condition while proving that no further change in the final yield is observable. This parameter is an input to the simulation for evaluation of the ratio of final char and volatiles to the virgin biomass.

For modeling, an overall global kinetic is estimated and implemented while the simulation is adjusted to the experimental parameters. The normalized mass of volatiles is calculated as the assessment quantity for termination of the reaction. Normalized values, in this case, are equivalent to the degree of conversion as well. As it is stated in Section 3.8.1, based on experimental analysis of previous works, it is concluded that the normalized mass of volatiles is around 50 wt.% of the dry input.

Figure 4.23 illustrates the result of justification of the final state of the product for experimental and simulation in different reaction temperatures. The evaluated values in experimental measurements are the accumulative total mass of remaining solid after about two hours of a continuous process. For the simulation cases, the average values are obtained from the char yield of particles that are leaving the reactor after one hour of simulation, in which the operational steady-state is already reached.
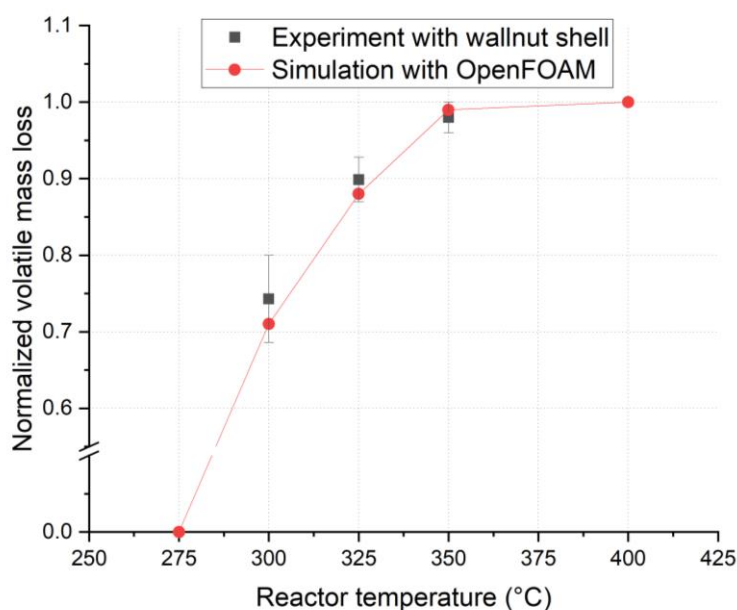
Figure 4.23 Final normalized mass loss equivalent to the degree of conversion for different reaction temperature in experiment and simulation.

The simulation has a mono-sized particle of 6 mm but in the experimental work, the size of the biomass was different and particle thicknesses were qualitatively inequivalent. The match between simulation and experiment shows that the reaction is in the kinetically controlled regime regardless

of the difference in particle size and heat or mass transport limitation has a negligible effect on the operational condition and yield of the final product.

Overall, the simulated results for the conversion of biomass using implemented kinetics are in good agreement with experimental work in the focused temperature. Additionally, the trend proves that the material under conversion is in the kinetically controlled stage in the final zone of the reactor. It can be concluded that for this input mass flow, a wall temperature of 350 °C for the reactor is suitable and optimized to be operated continuously, while higher temperatures of the reactor lead to faster conversion and further mass loss due to reaction kinetics above this temperature range.

4.8   Validation of the Entire Process

The final step of the validation focuses on the overall thermal conversion of biomass, which is performed by the heating, drying, and carbonization of a certain mass of wooden spheres. For this purpose, dry particles were soaked in liquid water to provide wet wood as the input for the experiment. An average of 42 wt.% ±4 moisture content has been absorbed for different sets of prepared samples. For each residence time, a fresh and identical batch of particles is used and each test is performed at least two times to reduce the uncertainties of the measurement.

The test is designed as a series of batch-wise experiments, in which the residence time of particles is varied in the reactor. The final mass of particles is then measured to evaluate the state of the conversion. In order to keep the residence time precise, the function of the continuous reactor is partially converted to a semi-batch operational plug flow reactor. An extension tool with a round metal net two millimeters smaller than the inner diameter of the reactor is built individually, which can be inserted into the reactor. The tool functions as a closed outlet for solid material while the produced gaseous by-products can pass through. Since the extension is movable, there is the possibility to evacuate the particles from the reactor at a certain applied residence time. The product collector is purged with inert gas in order to quench the hot particles and avoid further conversion (see Figure 4.2). This additionally helps to avoid condensation of the evaporated moisture in the collector, which can be a source of measurement uncertainties.

The experiment is carried out in the steady-state operational condition at stable freeboard gas temperature where there is no gas input introduced to the reactor. The rotation of the reactor has been set to a constant value of 10 rpm during the entire test. For each batch of the experiment 1000 wet particles have been injected to the reactor within the first 40 seconds. Highlighted properties of

the input including conditions of the reactor are summarized in Table 4.8. Measured and calculated values are used as input in the simulation as well.

Table 4.8 Summary of the operational condition for the validation test.

Biomass input		Reactor	
Input mass (g)	138 ± 8	Gas temperature (°C)	350 °C
Initial temperature (°C)	25	Pressure	atmospheric
Moisture content wt.%	42 ± 4	Length (m)	1.4
Dry mass (g)	80.0 ± 0.2	Diameter (cm)	8.0 cm
Volatile fraction (wt.%)	75	Rotation (rpm)	10 rpm
Particle diameter (mm)	6.0	Inclination (°)	3
Heat of reaction (kJ/kg*)	-400	Gas input	none
particle density (kg/m^3)	1224.7	Gas output	to the condenser
Dry mass c_p (J/kg.K)	2000	Coal-collector	purged with N_2

* Heat of reaction in this study is considered based on the mass of volatiles

An interval of 10 minutes is chosen to evaluate the result of the test. The final residence time of 60 minutes is operated for the longest batch test. Regarding the fact that the initial and dry masses are known, physical and chemical processes can be observed distinctly during the mass loss. A comparison of the measured results with the simulation is shown in Figure 4.24. The drying zone is shown in blue representing the mass loss of the solid due to moisture evaporation/vaporization. The mass loss due to devolatilization/carbonization is shown in the yellow zone.

The comparison between experiment and simulation shows excellent agreement regarding the prediction of the reaction end time. However, in the first interval, the measured mass loss shows a considerable deviation from the simulation result. As it is seen, at 10 minutes of residence time, particles are completely dried and the mass loss due to the reaction is already about 30 grams. Although in the simulation with optimized parameters the drying process is terminated as well, the reaction is just at the beginning stage and shows only around 5 grams of mass loss. A possible reason for this disagreement could be that the evaporation and devolatilization are decoupled submodels. Due to the uniform temperature of each particle, these two processes cannot occur simultaneously. This means in the simulation the drying has to be terminated firstly, then the particle temperature can rise and the reaction can start. However, if the proportion of delivered heat by radiation is significant (or dominates for some particles) which might be the case of this work, the radiation model for the packed bed would distribute the heat flux between all particles in the

specified control volume. This would moderate the local effect of radiation on some particles, which in reality might heat up and lose mass faster than the average of bulk. Additionally, some particles may stick to the wall of the reactor during the drying and devolatilization stages due to the stickiness of the wall (because of the tar formed at their surface or the tar that remained at the wall). This is an observed phenomenon in the experiment during the validation. Occasional sticking of particles to the hot wall increases the delivered heat to those particles due to the elevated radiation and contact heat transfer, which is considered in the simulation only based on averaging methods for control volumes.
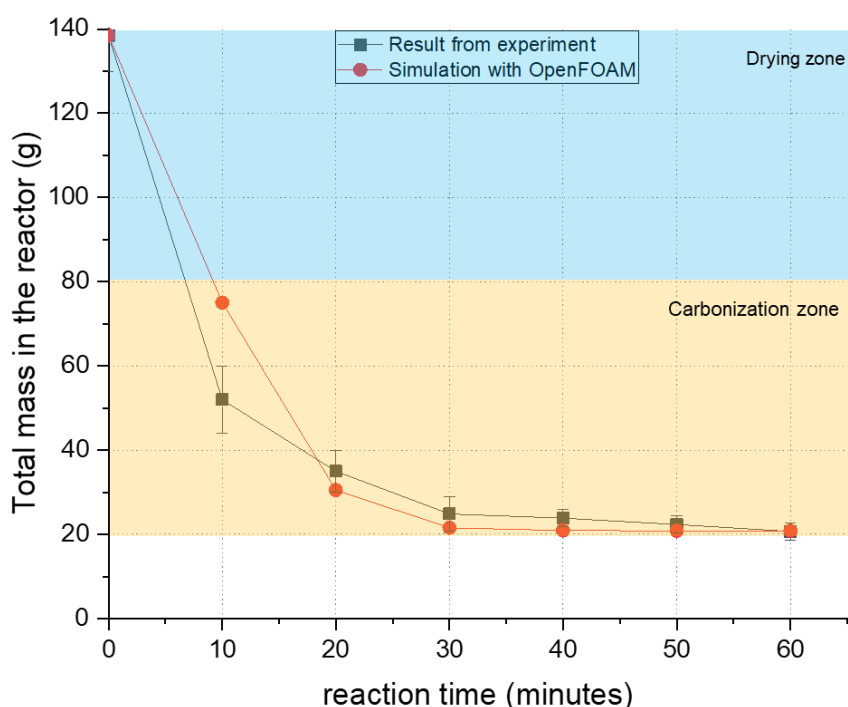
Figure 4.24 Validation of the entire process with wooden spherical particles. Comparison of own experimental work with self-developed solver in OpenFOAM®.

The deviation between the outcome from the experiment and simulation might explain this hypothesis. Additionally, it may be probable that, while the drying in the core of particles is ongoing, the devolatilization is propagating in the surface layers. A suggestion for future work in this framework could be a definition of surface temperature (for instance from the one-third rule) while the thermally thin assumption remains valid within the particle. In this case, if the surface temperature rises higher than a certain ratio compared to the temperature of the particle, the devolatilization model can be activated for a tuned thickness of particle surface to adjust the mass loss rate to experimental data.

One important adjusting parameter in the simulation is the overall emissivity of radiative heat transfer to particles, which is the product of particle emissivity and wall emissivity. The best overall agreement is obtained with particle emissivity $\epsilon_p = 0.70$ and the wall of emissivity $\epsilon_w = 0.85$, which are taken into account via the adjusted boundary condition for the reactor wall. These parameters will be implemented in the simulation as adjusted values and will be used in further case studies as well. Another important thermophysical parameter is the starting temperature for the reaction. In this case, the temperature of 227 °C is given which is realistic for the devolatilization of wood [33]. Lower values might lead to better data-fitting for simulation because the gap between the drying and devolatilization process might be covered as a compromise, however, it might not be realistic.

Except for the first point, Figure 4.24 exhibits an overall acceptable agreement of overall mass loss between experiment and simulation. Results above 20 minutes of residence time exhibit a relative deviation of below 5%. The results specifically show that the simulation is a reliable tool to predict the termination time of the reaction. It can be claimed that the analysis of the degree of conversion is an answer to the question "when does the biomass approach to fully converted products?"

It can be concluded that the developed model is a useful and applicable tool for the optimization of the reactor conditions based on input material to reach the final conversion of biomass particles.

5   Results and discussion

In this chapter, the extended numerical tool is used for the simulation of the laboratory-scale rotary kiln and a large-scale rotary kiln. The numerical results of the laboratory-scale reactor will be given first. The simulation setups are based on the validated and concluded parameters discussed in the previous chapter. In the second section, the numerical improvements are presented which are required to run the simulation on the large-scale reactor. The motivation is to make the long run of numerous test cases possible as the parameterization for various conditions is necessary. This section is specifically tailored for this study as an attempt to explore the target of computation efficiency on long-run large-scale simulations.

In the final section, a comprehensive parameter study for the industrial-scale design is performed to help the optimization of the process in terms of the final biomass conversion. The parameter studies regarding the wall temperature, mass flow rate and moisture content of the biomass particles for both scales are tabulated in Table 5.1. The test cases are performed to find the optimal operating conditions for wet biomass carbonization in each scale.

Table 5.1 Parameter study of lab-scale and large-scale rotary kiln for wet biomass carbonization.

Size	Wall Temp. (K)	Mass flow rate (kg/h)	Moisture content (%)	Particle size (mm)
Lab-scale	573	0.580	50	6
	598	0.580	50	6
		1.160	0, 10, 20, 30, 50	
		1.760	50	
	623	0.580	50	6
	673	0.580	50	6
Large-scale	673	350	50	Normal distribution expected: 6 variance: 2 range: 1-9
	723			
	773			
	873			

5.1 Laboratory-scale results

The laboratory kiln reactor rotates with a speed of 1-10 rpm and an inclination angle of 0.5° - 5.0°. For every type of biomass, the angle of inclination is tuned to obtain a mean residence time of 2700 s with the predefined rotation speed of 10 rpm. In the beginning, biomass as wooden bulk with specified size ranges is inserted into the empty reactor, which has a constant wall temperature. The simulations are performed until steady-state conditions are reached. The results presented in the following refer to steady-state conditions and the geometry sketched in Figure 2.1.

The average gas velocity originating due to evaporation and devolatilization within the lab-scale reactor applying the highest mass flow rate is around $0.1 \frac{m}{s}$ which corresponds to Reynolds numbers of $Re < 200$. So the laminar model is used for the calculation of the flow regime. The parceling concept is not used in the laboratory-scale model including all simulations of section 5.1, i.e., each parcel represents one particle. This is due to the low number of particles in the domain and thus acceptable computational effort. At the steady-state condition, for the input flow of 0.58 kg/h, more than 5100 particles exist in the computational domain, while for the highest flow by 1.74 kg/h around 13100 particles remain in the reactor. During the laboratory-scale simulations monodispersed spherical particles with a diameter of 6 mm are used.

5.1.1 Influence of the reactor's wall temperature

The overall process in the reactor is divided into four stages, namely, heating-up, drying, reaction and overburning. The mass fractions of the components within the particles are used to classify these stages. With this method, the state of the bulk along the reactor is investigated on particles that are in the reactor 3600 s after the start of the simulation.
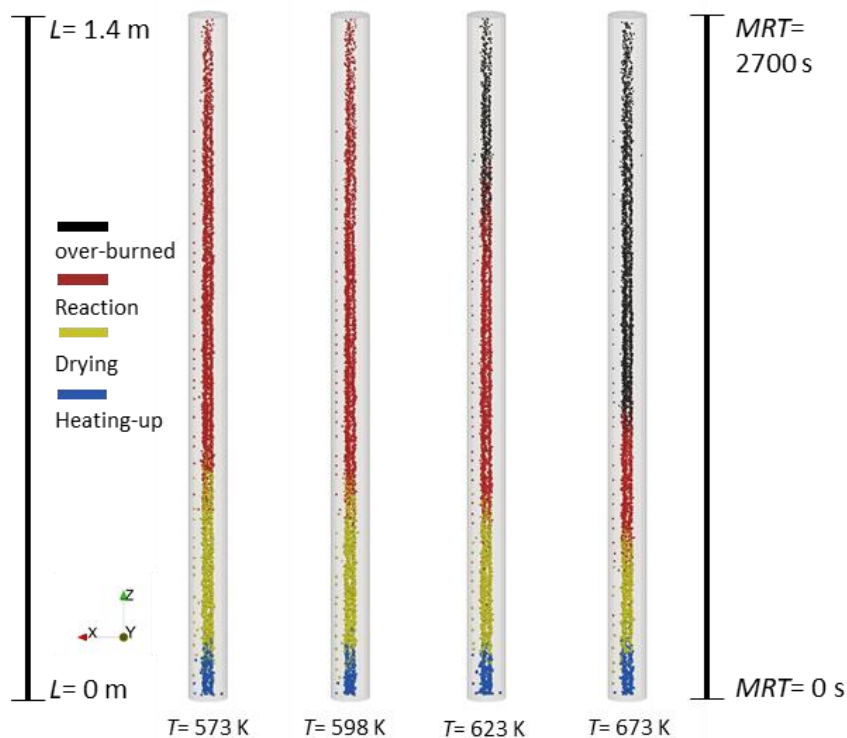
Figure 5.1 Four stages of the process in the rotary kiln at different wall temperatures (top view).

The different stages of the carbonization process undergone by the discrete phase are shown in Figure 5.1 at steady-state conditions (physical time of 3600 s). The left indicator represents the length of the reactor (z-direction) and the right-hand side indicator shows the Mean Residence Time (MRT≈2700 s) of the particles in the reactor. In the heating up zone (blue region), the mass of the particles does not change while their temperature increases. In the drying zone (yellow region), the moisture content (MS) of particles is decreased to zero by evaporation/vaporization. After the drying is completed, the devolatilization starts (red region), where particles release volatiles (Tar, H_2O, CO_2 and CO) and lose further mass. Reaching the final mass of the particles, the over-burned stage (black region) shows a further increase in temperature. Other possible changes in product properties, such as secondary reactions along the over-burned zone, are neglected due to the uncritical final temperature.

The heating-up zone is relatively short compared to the other zones. The carbonization is kinetically limited and therefore the reaction zone is comparatively long. At a wall temperature of 573 K, a final conversion of 71 % is attained and reaches 88 % and 99 % at wall temperatures of 598 K and 623 K, respectively. On the other hand, at the highest temperature, less than half of the reactor length is required to complete the product's conversion.

From the previous statements as well as analyzing Figure 5.1 and Figure 5.2, it can be concluded that the most appropriate wall temperature for the lab-scale reactor is 623 K, where the reaction is

116

completed at the end of the kiln, and only a short over-burned zone exists. The comparison of these four case studies shows that the conversion is very sensitive to the wall temperature. For each case, the final conversion of the particles is also given at the right-hand side of each case in Figure 5.2.
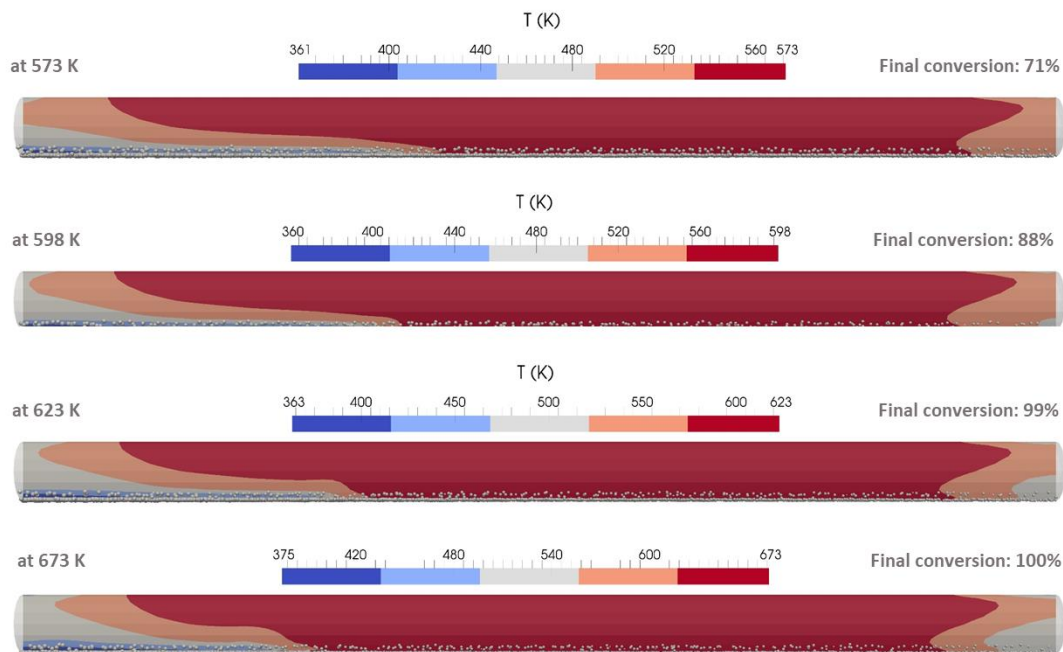
Figure 5.2 Gas temperature on a cutting plane, passing through the center of the rotary kiln for different wall temperatures (side view). Here and in all consequent figures, the bulk and gas move from left to right.

In completion of Figure 5.2, Figure 5.3 depicts the gas-phase moisture content (MS) Y_{H_2O} in the freeboard gas of the reaction at the final time. The blue zone refers to the low moisture content as devolatilization occurs. Interesting to see is the backward shift of the blue zone by an increase in wall temperature. The reason is connected to the elevated rate of evaporation showing that at higher temperatures the reaction starts in the earlier stage of the reactor. Another consequence of the growth in wall temperature is the drop in the lowest MS concentration in the freeboard gas. At 573 K, the lowest MS is about 0.80 representing a slow rate of devolatilization while in the other cases it drops to about 0.5 which is another proof for the elevated rate of evaporation.
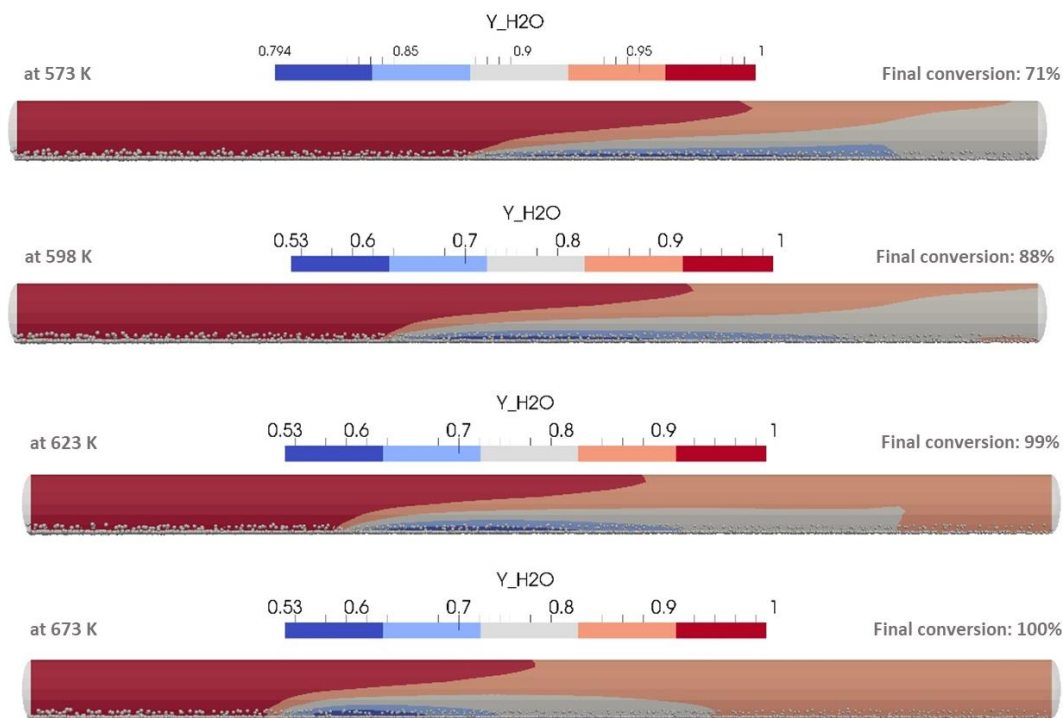
Figure 5.3 Gas-phase MS (Y_{H_2O}) on a cutting plane, passing through the center of the rotary kiln for different wall temperatures (side view).

Figure 5.4 additionally exhibits the particle temperature in the rotating tube for the mentioned conditions showing that particles in the bed in all case studies have reached the wall temperature. The small difference comes from the last 20 cm of the tube that is not heated (see Figure 4.3). This result makes sense specifically considering the long residence time of the solid phase in the reactor. Here it can be once again emphasized that the process is kinetically limited and not limited by heat transfer.
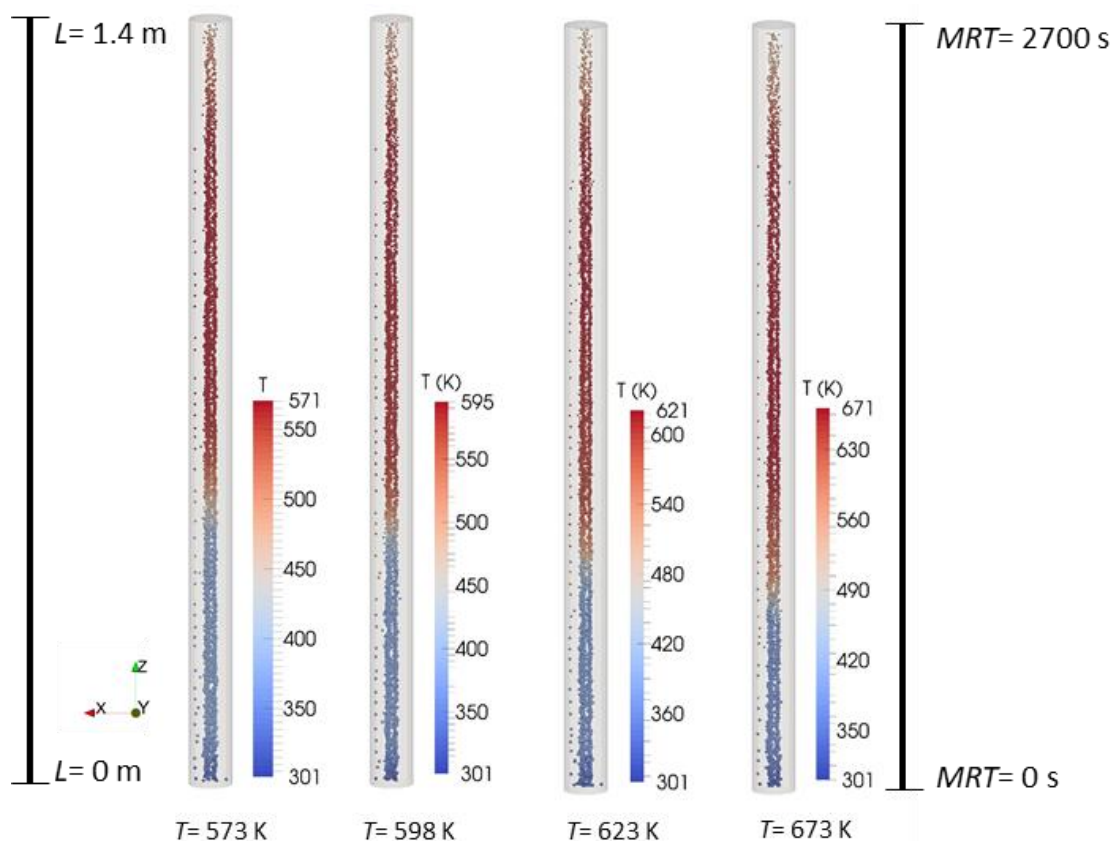
Figure 5.4 Particle temperature analysis at different wall temperatures (top view).

5.1.2 Influence of mass flow rate

In Figure 5.5, the influence of the biomass mass flow rate is illustrated for the reactor with the wall temperature of 598 K and the initial particle moisture content of 50% (see also Table 5.1). The final conversion strongly depends on the length of the contact between the bulk and the hottest layer of freeboard gas. Due to this energy-intensive process, a larger mass flow rate sharply increases the required heat and consequently limits the overall conversion.
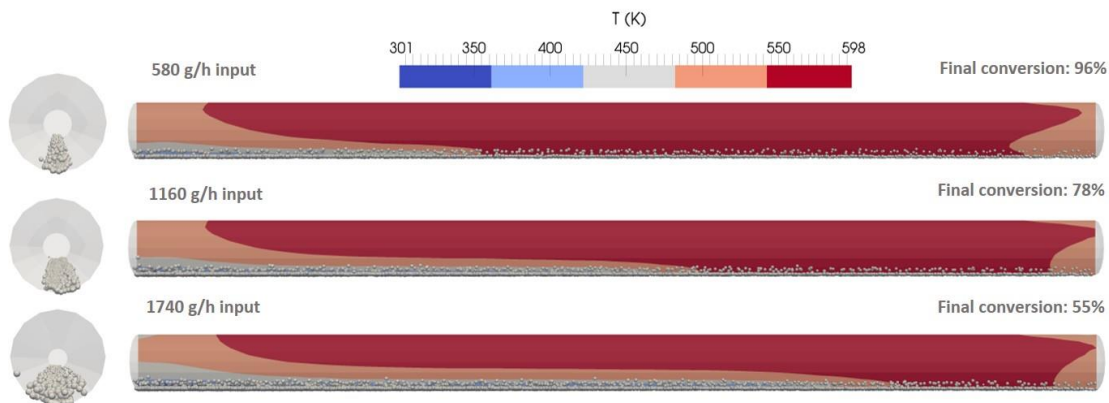
Figure 5.5 Gas temperature on a cutting plane, passing through the center of the rotary kiln at different mass flow rates (side view).
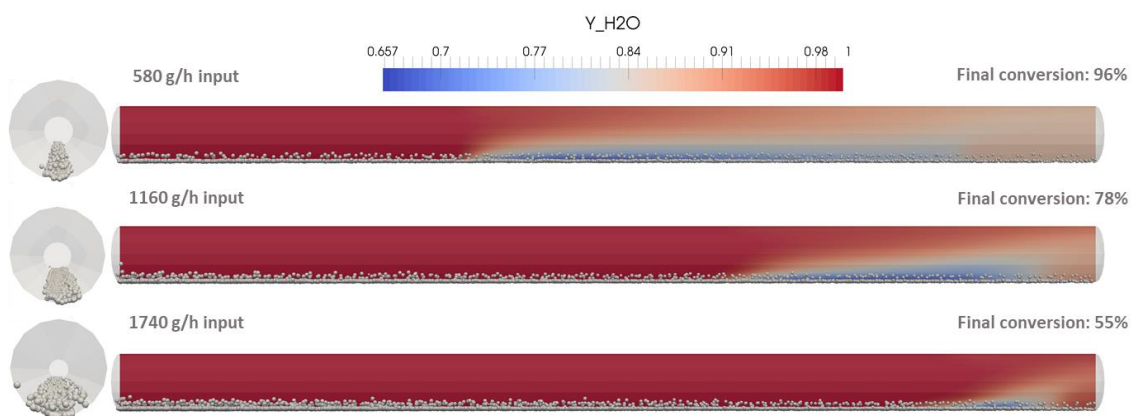
Figure 5.6 Moisture mass fraction Y_{H_2O} on a cutting plane, passing through the center of the rotary kiln at different mass flow rates (side view).

Initially, the gas phase in the reactor consists of dry air. During the drying phase, the air is gradually displaced by moisture and later partly by volatiles. Under steady-state conditions, only water vapor and volatiles are present in the gas phase and the mass fraction of non-condensable volatiles is $1 - Y_{H_2O}$. With the lowest particle mass flow rate in Figure 5.6 (top), the carbonization reaction starts within the first half of the reactor and the mass fraction of volatiles grows suddenly near the bulk and is then diluted gradually by the moisture flow coming from the drying zone. By raising the mass flow rate, the moisture released from the bulk displaces a larger volume in the reactor. Due to the same wall temperature in all cases, the volatile release is postponed and the reaction zone is shifted towards the end of the reactor. With mass flow rates above 2 kg/h, the devolatilization does not start at the presence of biomass in the reactor.

5.1.3 Influence of moisture content

Figure 5.7 depicts the influence of the initial moisture content (MS) of biomass particles on the gas temperature at a constant reactor wall temperature of 598 K and a mass flow rate of 1.160 kg/h. Raising the MS from 0% to 50% at a constant mass flow rate shows a similar effect on the gas temperature as raising the mass flow rate at the constant moisture content (compare with Figure 5.6). However, while raising the MS, the final conversion is first slightly increased although one may think about the downtrend.
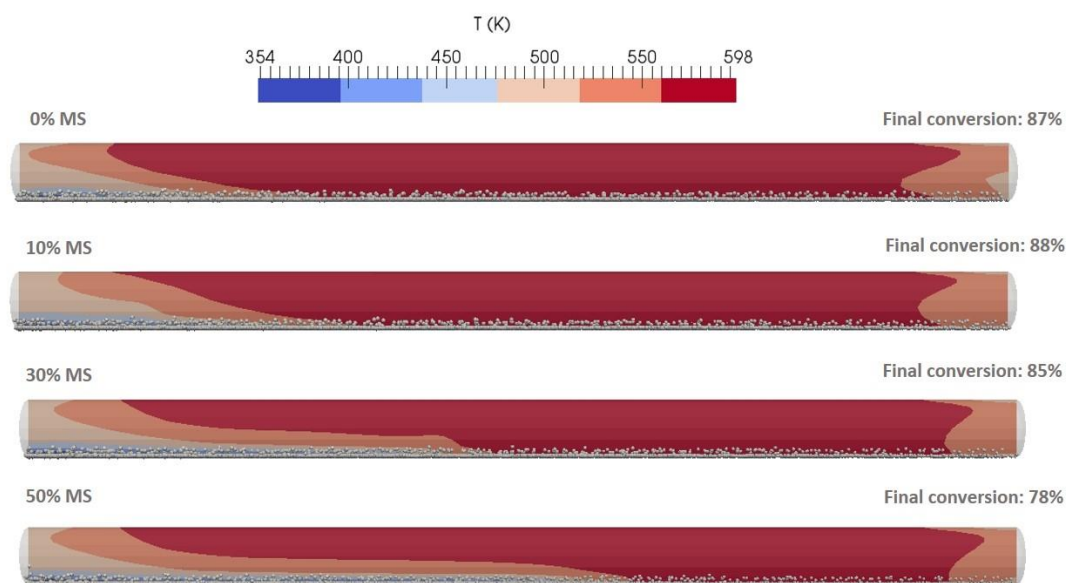
Figure 5.7 Gas temperature on a cutting plane through the center of the rotary kiln at the different MS (side view).

The effect on the final conversion is due to the elevation of the heat transfer coefficient in the presence of higher MS in the freeboard gas. In this case, the larger c_{p_g} of steam leads to a higher Prandtl number. Consequently, the Nusselt number increases, i.e., raises the heat transfer coefficient of the particles. Additionally, the larger heat capacity of the gas keeps its temperature higher, during the heating of cold/wet bulk which leads to an increase in the overall heat transfer to the bulk. The author investigated this effect in a simulation for a single particle and different ambients specifically [119] (see section 4.6).

The overall conversion rate of the cases with MS 0% and 10%, from Figure 5.8, proves that despite the increase in the total of required heat, the gain in the interphase heat transfer dominates. The difference between the final conversion of the cases with MS 0 % and 30 % is unexpectedly small, as shown in Figure 5.8. This can be explained by the gas MS in the former case staying nearly

around $Y_{H_2O} = 0.50$, while in the latter case, a large zone of the reactor (heating-up and drying zones) is entirely filled with the super-heated steam $Y_{H_2O} = 1.0$.
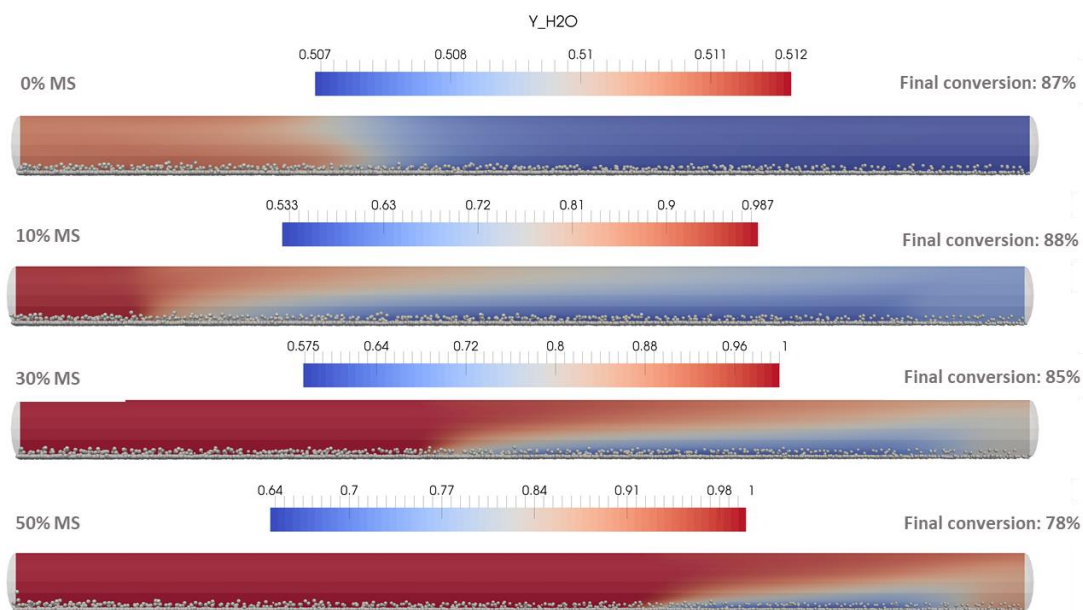
Figure 5.8 Gas MS on a cutting plane through the center of the rotary kiln at the different initial MS of particles (side view).

5.2   Scale-up calculation & numerical improvement

So far, results for the laboratory-scale rotary kiln have been presented. They allow guiding the design of the industrial-scale reactor. For this purpose, the residence time of the bulk is taken from the lab-scale simulation, based on the experimental study of kinetically limited carbonization reaction [14], [55], [56]. Although most parameters such as the particle composition, the MS, the initial temperature, the reaction mechanism, etc. are taken from the former, the filling degree in the lab-scale is around 14% which is considerably larger than the one of large-scale as of 4.4 %. This large difference is because the fact that the biomass particles in the lab-scale and the large-scale reactor have the same MRT, but the mass flow rate in the large-scale reactor is higher by a factor of 350, thus requiring a larger area to transfer heat to the particles, however, the surface area effective for the heat transfer cannot be enlarged proportionally, therefore a decrease in the filling degree is inevitable.

The large-scale simulations of the reactor at an industrial scale require considerably larger computational resources. The long physical time of the simulation, e.g. 3600 s, leads to a large number of timesteps which is an additional reason for the computational expensive simulation and extremely long computation time. To find an optimal setup, a study on grid independence is carried

out. The finest computational mesh consists of 2,700,000 hexahedral control volumes, with an average edge size of 2×2×2 cm for the total 12-m length of the reactor. This is the finest possible mesh resolution, due to the restriction from particle volume fractions in a cell. To compensate the computational cost, the first thought was to make the mesh coarse in the axial direction along the reactor and therefore two additional meshes with an average cell size of 2×2×5 cm and 2×2×10 cm are generated where each contains 1,080,000 and 540,000 cells.
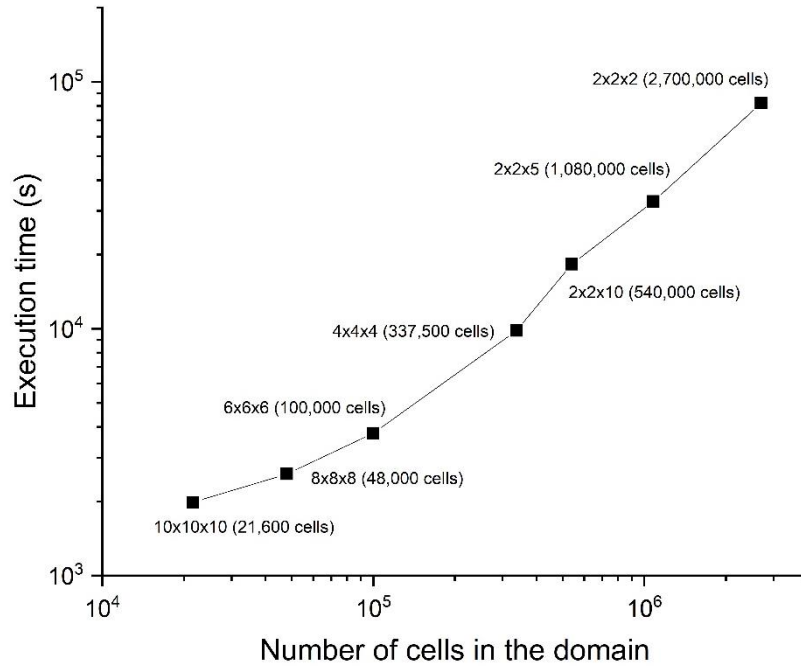
Figure 5.9 Overall performance of the simulation using different grid sizes.

Further investigations reveal that meshes with an aspect ratio closer to unity, have better numerical stability in the calculation of temperature along the centerline of the reactor as compared. To perform so, several meshes with average edge size of 4×4×4 cm, 6×6×6 cm, 8×8×8 cm and 10×10×10 cm are generated where they are composed of 375,000, 100,000, 48,000 and 21,600 cells. The performance of these simulations is shown in Figure 5.9 as an index of execution time where all cases included particles up to 10,000 and run until 230 s physical time with an identical timestep of 6 ms.

The grid with an edge size of 4×4×4 cm is chosen for the large-scale simulation due to the compromise between precision and performance which accelerates the simulation by 8.45 times. In comparison with the finest mesh, the relative deviation in the time-averaged gas temperature, at the centerline of the reactor is only about 0.30% after 230 s which is shown in Figure 5.10.

Mesh resolution with average edge sizes of 2×2×5 cm is not chosen despite slightly better accuracy due to the inefficient computational performance. Mesh resolution with an average edge size of 2×2×10 cm is avoided to be consistent with the aspect ratio of cells closer to unity as a decisive factor for numerical precision and stability regardless of the overall aspect ratio.
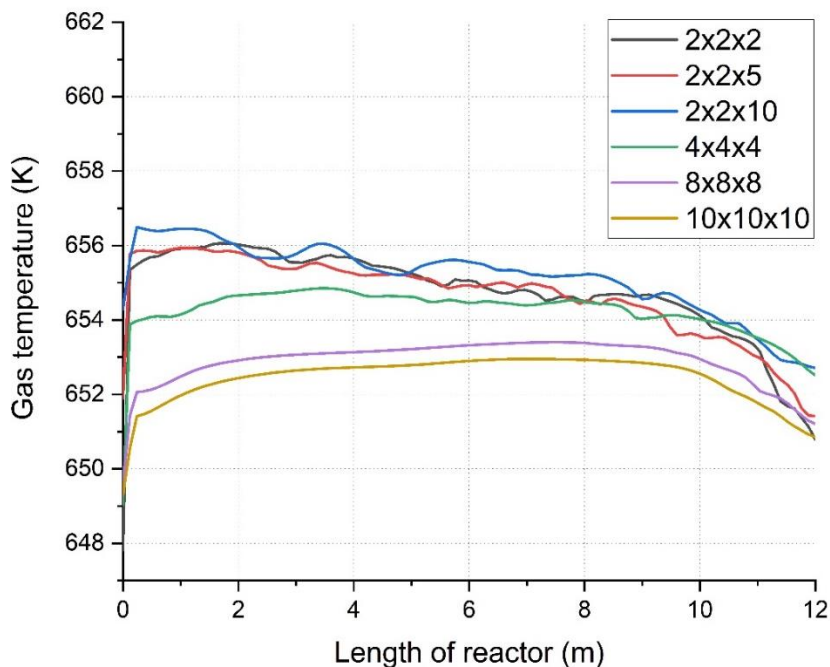
Figure 5.10 Gas temperature on the centreline along the reactor for different grid sizes.

The CPU performance for the computation of the disperse phase, using the MP-PIC method is studied next. For a short simulation with only 2 s of physical time, the number of particles is varied from 5,000 to 450,000 in 11 steps. The computational effort increases linearly with the number of particles in the domain. For a single CPU, the average execution time per timestep grows from 5.1 s to 31.2 s, for the smallest and largest number of particles, respectively. In contrast to the lab-scale simulations, where each parcel represents one particle, in the large scale simulations, parcels with 10 particles are modeled for a feasible computational performance. In the steady-state condition, there are more than 3,330,000 particles in the domain at the same time. It was found that, on the other hand, the computation time of the DEM-based model in the lab-scale grows exponentially with the number of particles. Even when applying the reduced particle stiffness model suggested by [78], to the DEM, it is still computationally expensive for large-scale simulations. The result of CPU performance against the growth of the particle amount in the domain is shown in Figure 5.11.
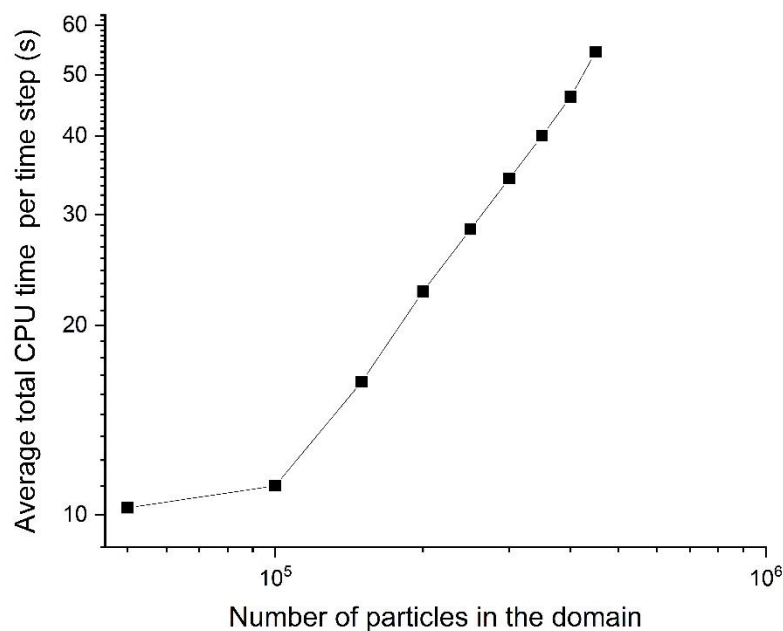
Figure 5.11 Performance of a single CPU core by varying the number of particles in the domain.

5.2.1 Computational performance of the radiation model

The resolved radiation models based on the discrete ordinate methods are computationally very intensive and therefore they have a direct impact on the computation efficiency of simulations. This effect can be high enough to turn the large-scale simulation into an infeasible case in terms of computational cost even on parallel runs with several hundreds of processors. Therefore, investigation to reduce the computational effort with an acceptable precision is necessary. Table 5.2 summarizes the results of a series of simulations that were carried out on the realistic physical time scale for the Carbolite Gero geometry in which, submodels and parameters are adjusted and finalized.

As it was explained in section 3.6.2, the total number of discrete directions, as well as the setting solver frequency (i.e. the setting that determines how many time steps elapse between the solutions of the radiation field) have a decisive influence on the computing time. Various trials and case studies are carried out on the enlargement of solver frequency and reduction of the number of discrete directions. The results suggest that the solver frequency is a more effective tuning setting rather than the number of directions on the computational effectivity. This means, higher solver frequencies lead to a better agreement with the reference case than those with a lower number of directions. However, this is only true to a limited extent and this must always be considered for each specific case by checking the trend of the sensitivity analysis.

In the same manner, the number of discrete directions is kept as high as possible and for the displayed results only 128 and 72 directions are tabulated. The results for lower numbers of directions are ignored since the computation time is not distinctly lower for a comparable solver frequency whereas the accuracy is remarkably diminished. In Table 5.2, the highlighted variation of the computation time for simulation on the parallel run with 16 processors is shown. The table compares the time-averaged radiation heat flows of the reactor's wall $\dot{Q}_{wall}$ by variation of the number of discrete directions and radiation solver frequency. Furthermore, a mean deviation from the reference case with 128 directions and radiation solver frequency for each timestep (`solverFreq=1`) was calculated. The relative deviation was calculated for each of the data points and then averaged over time.

Table 5.2 Computing time and mean wall heat flow during a one-hour simulation in a laboratory-scale reactor.

Discrete directions	Solver freq.	Computation time (s)	$\dot{Q}_{wall}$ (W)	Relative deviation (%)
128	1	62100	211.97	0
72	1	37543	215.53	2.69
72	10	10111	216.69	2.39
72	20	8775	216.84	2.50
-	deactivated	6671	0	Not defined

In the modified fvDOM radiation model, 72 global spatial directions for ray-tracing are used to calculate the radiation field in each 20th timestep. The results are compared to the refined case with 128 directions and the solver frequency of 1. The computation time decreases immensely due to the increase of the solver frequency and the reduction of the total number of directions. In particle temperatures, only an average deviation of 2.5% is observed compared to the reference case, while the computation time is reduced by a factor of 1/7. The optimized setting with discrete directions of 72 and a solver frequency of 20 has only an increase of computation effort around one third compared to the case with the deactivated radiation model.

The computing time required by radiation model myfvDOM could be reduced to an acceptable level without leading to significant changes in the simulation results. This was achieved by reducing the total number of discrete directions to 72 and increasing the radiation field solver frequency to 20. Further simulations have been carried out with these adjustments.

5.2.2 Computational performance of the parallel run

Another significant parameter that influences the simulation performance is the domain decomposition. Domain decomposition refers to the parallel computation on distributed processors. For a parallel run, the geometry and associated fields have to be broken into pieces and allocated to separate processors for a solution [74]. In the simulations including a large number of Lagrangian particles, the decomposition method has to be chosen carefully to minimize the computational effort.

The Scotch decomposition method decomposes the domain based on minimizing the interconnection between sub-domains and therefore number of processor boundaries. This helps to reduce the data exchange between processes but ignores the effect of particles leading possibly to an imbalance of the number of Lagrangian particles per sub-domain. Among all available decomposition methods, it is found that uniform decomposition in axial direction yields the best performance in the case of long-run and steady-state simulations.

The worst-case decomposition is based on uniform decomposition based on the direction of the reactor height. The different approaches are shown in Figure 5.12. In image A, the worst-case approach is illustrated as all particles are located at the lower part of the reactor where only one processor node is responsible for the bottom sub-domain and has to compute all Lagrangian particles. This load increases over time as the number of particles increases in the domain. Figure 5.12B shows the uniform decomposition in the axial direction, which yields the best results and C shows the decomposition with the Scotch method, which performs between the worst-case A and best case B. In Figure 5.12 each color represents a group of sub-domains.
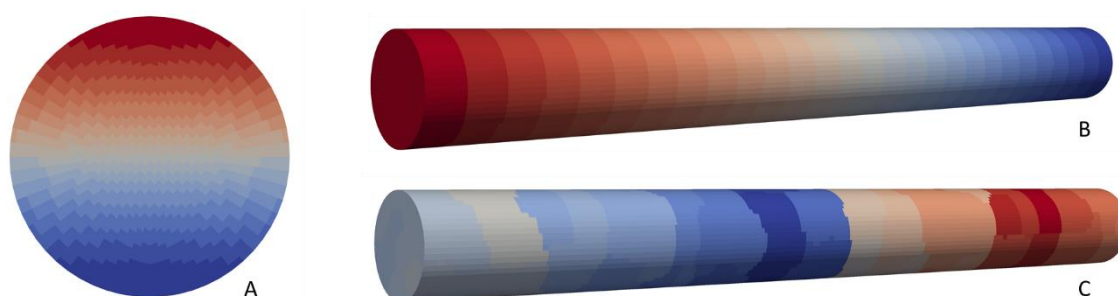
Figure 5.12 Different methods of decomposing the computational domain for parallel runs. Colors show the sub-domains.

Because the full simulation of the large scale reactor is only possible on massively parallel hardware, the parallel performance is tested with 2 up to 1120 CPU cores on the high-performance computer "bwUniCluster 1.0" at the Karlsruhe Institute of Technology, Germany. Reasonable

parallel scaling is observed up to 560 CPU cores, however, queue time has to be considered as an influencing factor in parallel performance. The average total amount of CPU-hours for each simulated case is around 40,000. Figure 5.13 represents the performance of the runs with different numbers of parallel CPU cores. 280 CPU cores parallelization was tested and used as an acceptable trade-off between simulation performance and queue time.
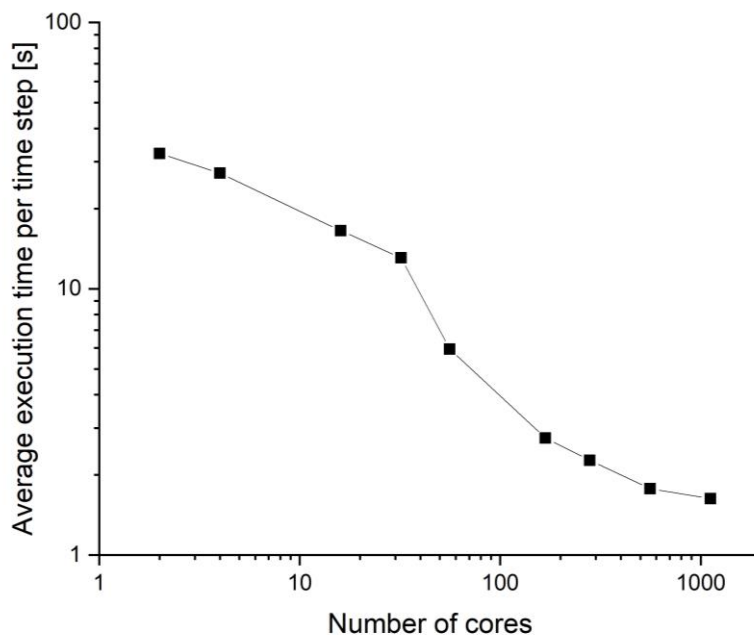
Figure 5.13 Execution time of the simulation, based on the number of parallel CPU cores.

5.3 Large-scale results

The industrial-scale reactor has a length of 12 m and a diameter of 1.2 m and rotates with the speed of 10 rpm. The numerical mesh consists of 4×4×4 cm cells, described in section 5.2. These parameters are defined by a real application. The rotation below 5 rpm is common for industrial-scale rotary kilns with built-in installations [120]. Since the large-scale reactor does not have a shovel or internal flights but instead is in the simulation a cylinder, the larger rotational speed is applied for comparable mixing in the numerical setup. However, based on the bed behavior diagram from Henein et al. [37] (see Figure 2.1), the bed motion is still in the same regime as for rotation below 5 rpm, where the Froude number lies in the range of $10^{-5} < Fr < 10^{-3}$ and therefore associates an analogous bed motion to the lab-scale reactor.

Like the procedure for the small-scale setup, the goal is to find operating condition for producing fully converted biochar at a minimal energy expense. In the large-scale study, a polydisperse distribution is considered for particles in the kiln (see Table 5.1 and Figure 5.19) and at the

128

stationary state, an average of approximately 3.35 million particles reside within the computational domain. Therefore, for a feasible computational performance parcels with 10 particles are modeled. The wall temperature of the kiln is varied for the parameter study. Unlike the lab-scale simulations, a uniform wall temperature is considered for the entire wall of the reactor. The average gas velocity in the industrial-scale kiln (for an averaged wall temperature) with a 15 times larger reactor diameter compared to the latter case is in the range of $0.12\frac{m}{s}$ to $0.15\frac{m}{s}$. This corresponds to a Reynolds number $Re \approx 3050$ and therefore different flow regimes may appear in the two scales. However, the industrial-scale reactor is only weakly turbulent. The displayed results in this section are based on instantaneous values. As already discussed in section 3.5 due to the negligible effect of fluctuation and generally low gas and particle velocity snapshot values are used for coupling of the two phases.

The results are shown for different wall temperatures at the steady-state. They determine the temperature for the reactor wall in terms of fully converted biochar at minimal energy expense. Transient results for a specified case with the wall temperature of 773 K are illustrated, in order to show how the steady-state is reached.
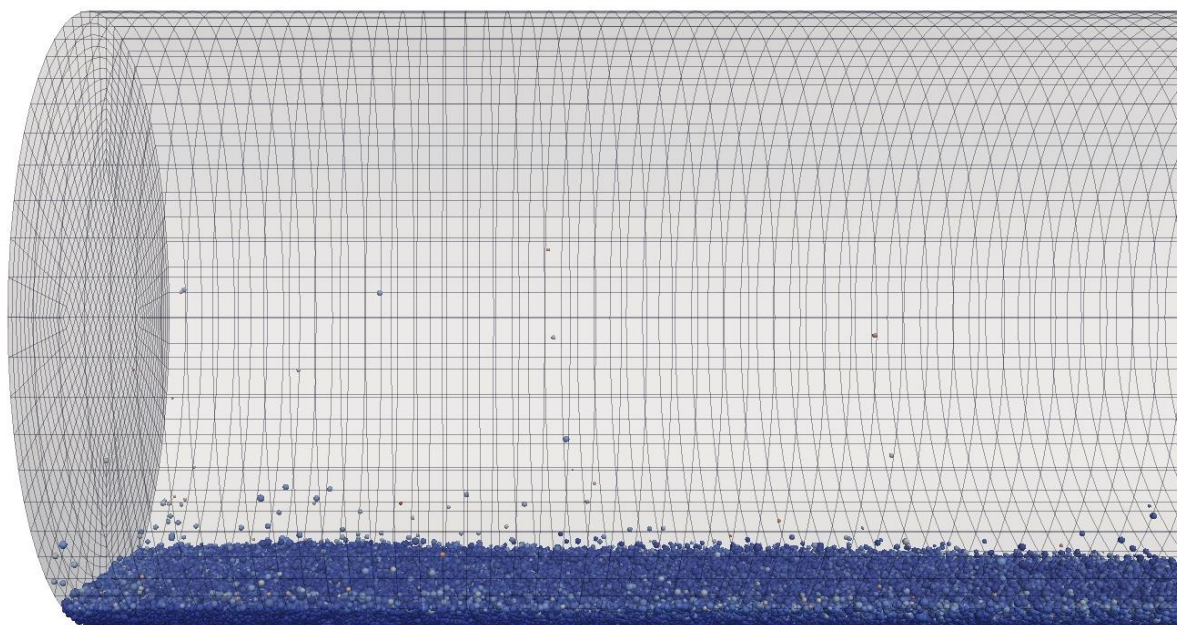
Figure 5.14 The large-scale rotating reactor with the visible computational grid filled with polydisperse particles.

5.3.1 Transient study of gas-phase parameters

Gas-phase temperature

Figures in the transient section show a rectangular cutting plane of the tubular kiln reactor, as well as seven cross-sectional planes, which are 2 m apart. Figure 5.15 presents the gas temperature at different simulation times for constant wall temperature of 773 K. A homogenous temperature profile can be seen in locations far from the bulk. However, after the drying zone, the gas temperature near particles shows a uniform profile as well. It can be concluded that the radial homogeneity of the temperature field in the reactor is enhanced compared to the lab-scale (cf. Figure 5.2). Although the freeboard gas has the room temperature at the initial time, the simulation with the constant wall temperature in Figure 5.15 shows that the gas is already heated up after 100 s.

After 1800 s, the temperature profile approaches the steady-state and there are no significant variations in the gas temperature distribution except that the low-temperature region (blue range, due to wet particles) expands towards the exit. Uniform gas temperature profile identical to the corresponding wall temperature is observed near the reactor outlet among all timesteps after 100 s.

Initial composition of the freeboard gas

Figure 5.16 shows that at the beginning of the simulation, the O_2 and N_2 contents in the freeboard gas are 0.21 and 0.79, respectively, which is the defined initial condition of the reactor. During the process, moisture and volatiles substitute the initial gas, while the atmospheric pressure pushes the gas out of the reactor, through the outlet patch. After approximately 1800 s, there is almost no air/oxidizing agent in the reactor anymore. In other words, oxygen and nitrogen content have no further variation after around 1800 s and only other gas compositions will be available in the domain. The result is especially highlighted for the case that the influence of the presence of air is considerable due to safety issues, for example, fire and explosion hazards or due to reaction with oxygen leading to lower carbon recovery in the solid product and consequently higher CO_2 emission.
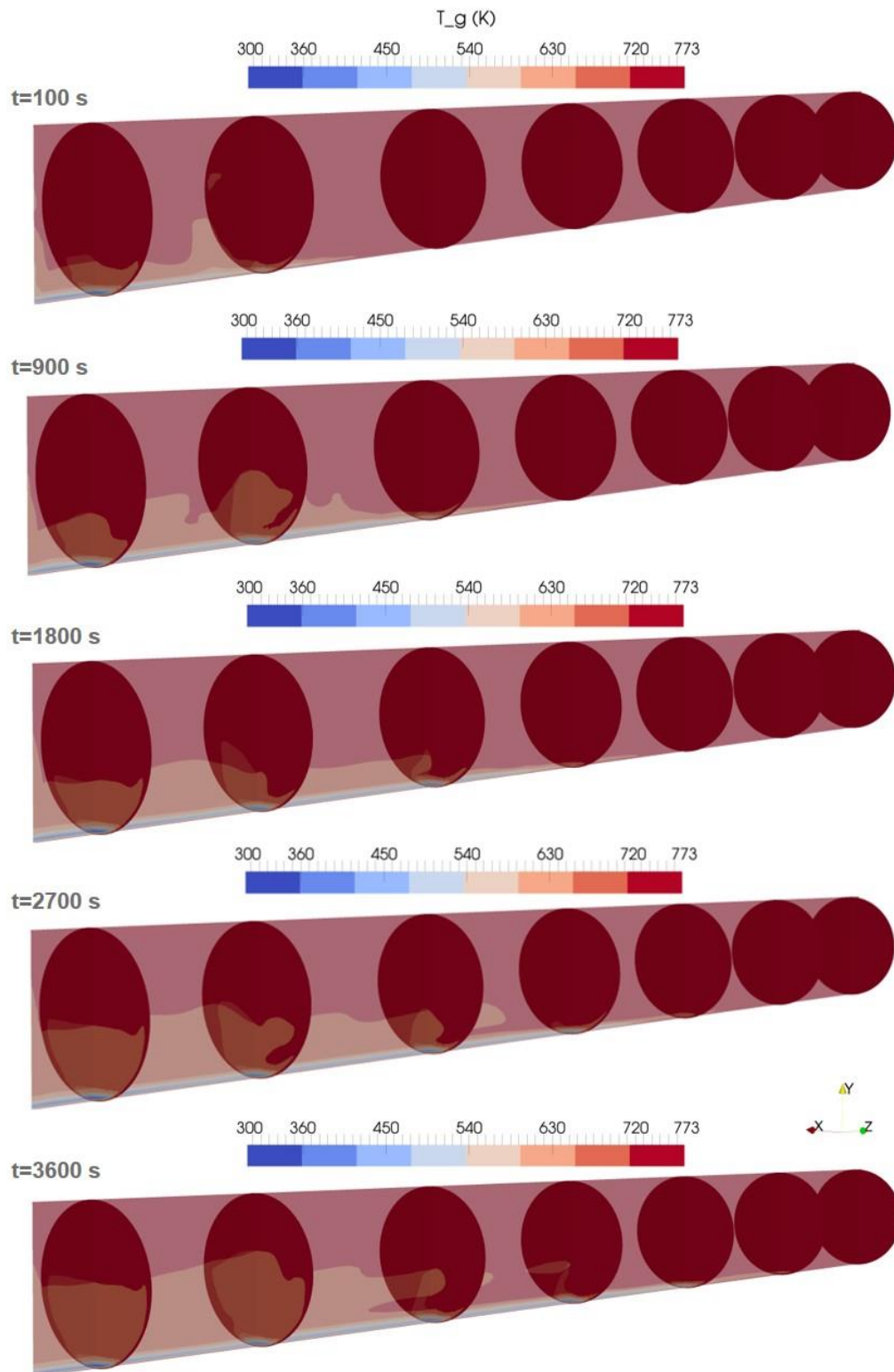
Figure 5.15 Gas temperature in the large-scale rotary kiln. The axial cutting plane, passing through the center and cross-sectional planes at different times (isometric view).
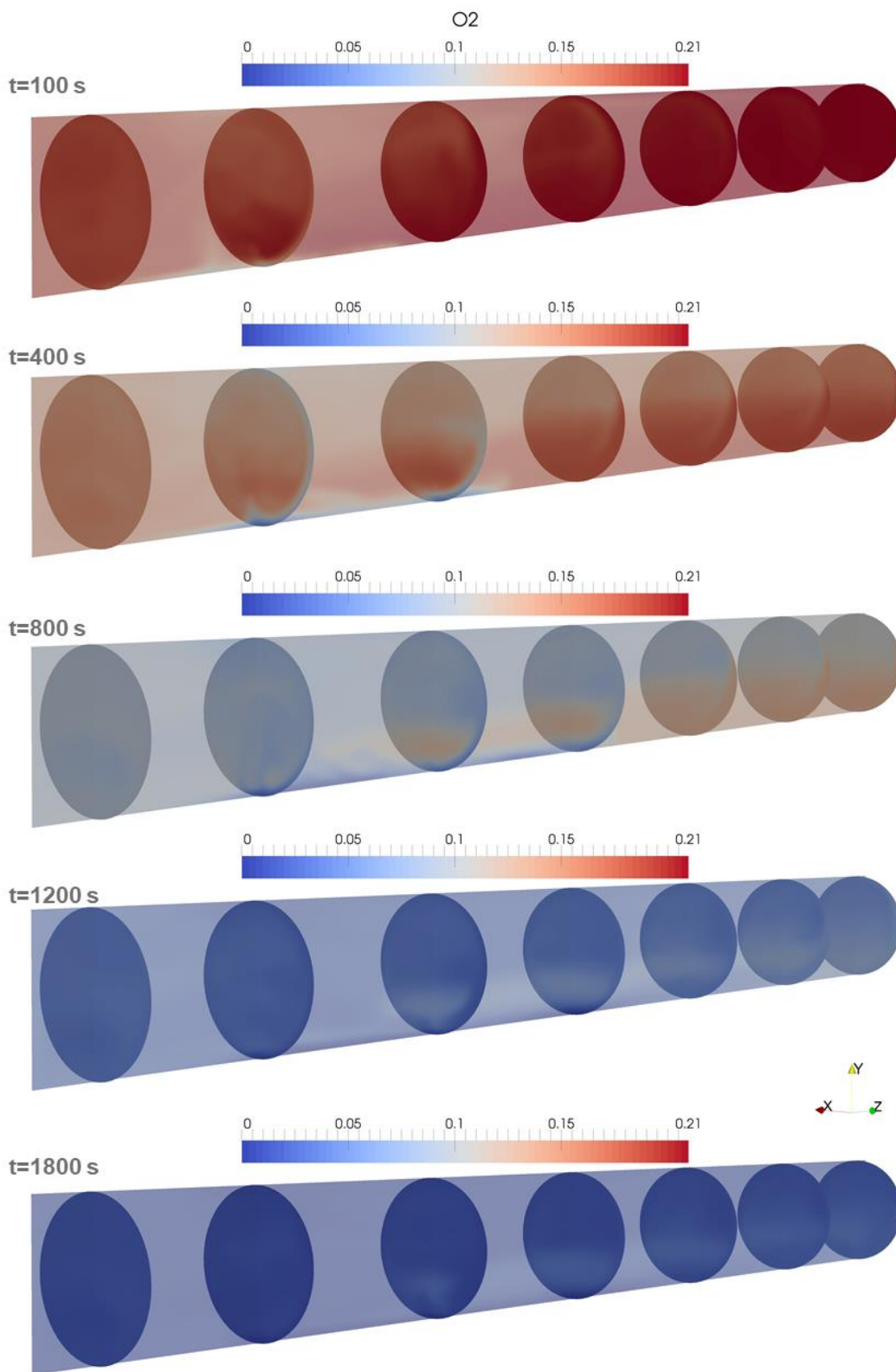
Figure 5.16 Oxygen mass fraction in the large-scale rotary kiln. The axial cutting plane, passing through the center and cross-sectional planes at different times (isometric view).

Volatiles mass fractions

In Figure 5.17, the time evolution of the tar mass fraction Y_{Tar} of the gas phase is illustrated for the case study with the wall temperature of 773 K. At the beginning of the process, there are no volatiles present in the gas phase. After 400 s, the early devolatilization is observed between 6 to 8 m (3rd and 4th planes) which is because of the first particles moving down in the reactor and get into the contact with the hottest gas. However, at later times while more biomass flows in the reactor, the heat exchange load and cold gas release are increased. For instance, at 800 s the devolatilization only begins after 8 m and will shift more to 10 meter toward the end of the reactor at 1200 s, while a higher volume is filled with volatiles. This is consistent with the results from Figure 5.15 as well. After around 1800 s, the tar mass fraction reaches the stationary state. The distribution of CO and CO_2 is the same as with tar and only their magnitudes differ. This is because the mass release from the particles follows the global reaction rate from the devolatilization kinetic.

Accumulated mass of by-products

Figure 5.18 shows the moisture release while drying (left) and the volatile release during the reaction (right) from the solid phase at different temperatures. From the figure, it can be concluded that the economically reasonable range of release based on the accumulated by-product is between wall temperatures of 673 and 873 K. At higher wall temperatures, for example, above 873 K, the higher release rate from the solid is observable on a shorter length of the reactor.

The rate of moisture released from the bulk (left of Figure 5.18) shows an expected increase by an elevation of the wall temperature of the reactor. At 773 K, a small decrease is visible in the drying rate at around 3000 s, as the bulk mass constantly increases in the reactor. The trend in the first half of the simulation is closer to that of 837 K. However, by increasing the mass input, the colder gas moves more rapidly in the reactor and consequently, the heat transfer limitation in the drying zone slows down the drying rate.

Figure 5.18 on the right-hand side shows the development of the evolution of volatiles. The cases 673 K, 723 K and 773 K reach their stationary states while the rate at 873 K is still on a slight non-linear rise. The accumulated volatile release in the reactor at 673 K after approximately 1500 s, remains constant, due to the heat transfer limitation, i.e. the transferred heat is not sufficient to bring the biomass into the reaction stage. At this temperature, the total amount of supplied heat is used for the heating-up and the drying processes. The released volatiles in the first 1500 s are related to the early reaction of the first inlet particles as explained in Figure 5.17.
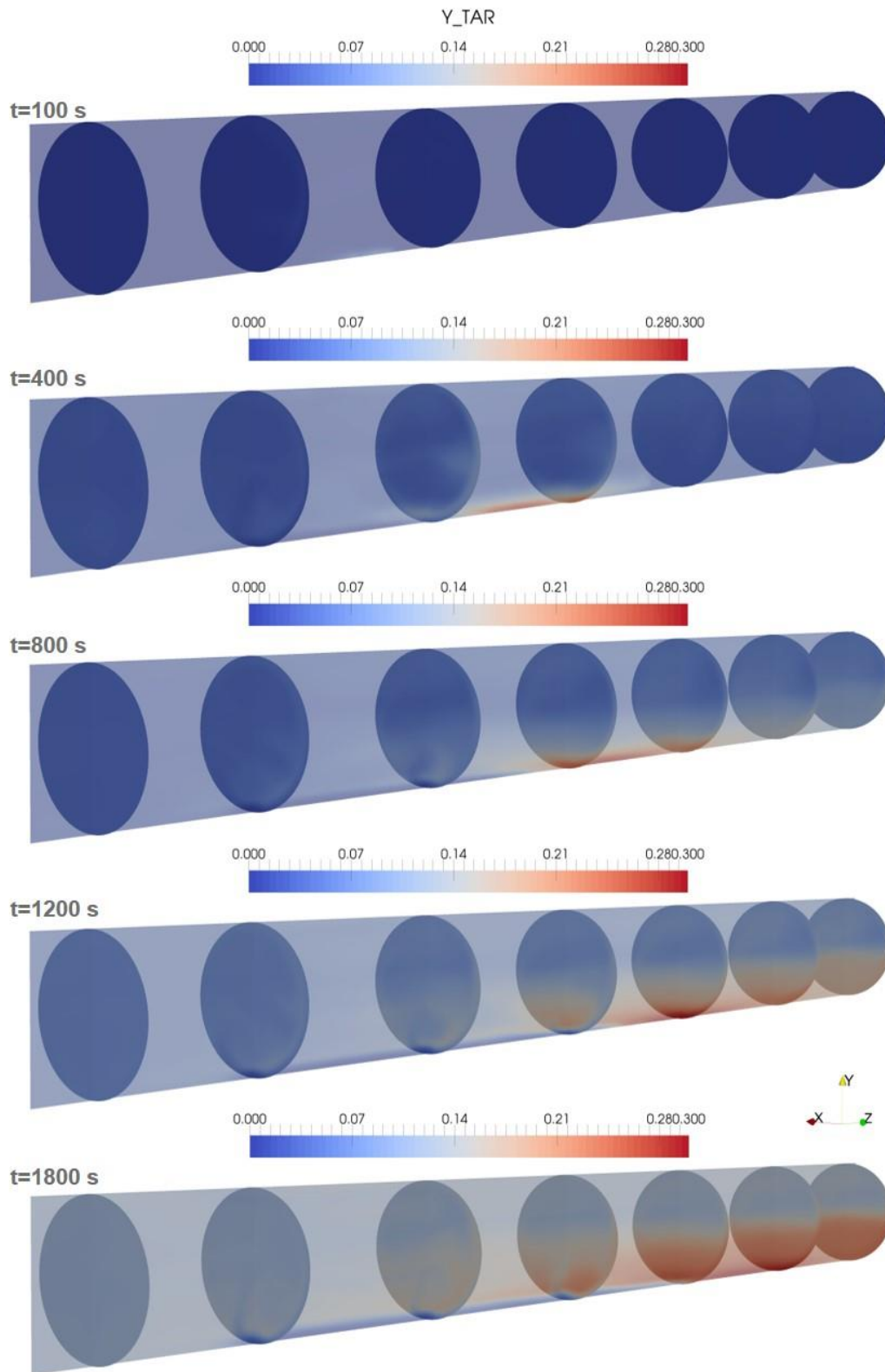
Figure 5.17 Axial cutting plane, passing through the center and cross-sectional slices of tar mass fraction in the gas with the wall temperature of 773 K (isometric view).
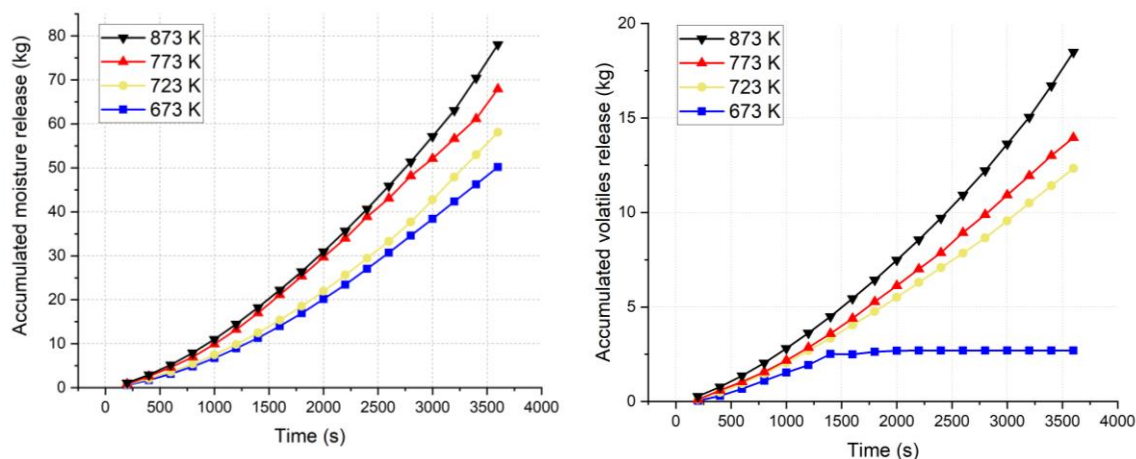
Figure 5.18 Accumulative release of moisture while drying (left) and volatiles (right) from the biomass, during the thermal conversion.

In the next section, the steady-state analysis of these four case studies will be explained in detail and the simulations with parameters fulfilling the full conversion of the solid with the lowest energy effort will be highlighted.

5.3.2 Steady-state results for large-scale simulations

Influence of the wall temperature on the biomass conversion

The wall temperature of the large-scale reactor is varied intuitively to find the most favorable trade-off for processing the biomass in the kiln in terms of full conversion and energy effective wall temperature. Results of the steady-state simulation are shown in Figure 5.19, after a physical time of 3600 s.

In order to find a favorable wall temperature, the mass fraction of char Y_{char} present in the product is studied. A particle initially contains the mass fraction of moisture, $Y_{moist} = 0.50$, volatiles, $Y_{vol.} = 0.25$ and fixed carbon and ash $Y_{char} = 0.25$. Ideally, the char mass fraction of particles leaving the reactor should be $Y_{char} = 1.0$, which can be observed for the cases at the wall temperature above 723 K, in Figure 5.19 on the left.

In contrast, the conversion degree for the wall temperature of 673 K is not satisfying, as the graph shows that more than 50% of the particles leaving the reactor are not even completely dried since their Y_{char} is below 0.5. Therefore, it can be concluded that in contrast to the lab-scale geometry, where the wall temperature of 673 K is an overdesigned case, the large-scale reactor with 673 K is underdesigned for biomass carbonization. This is consistent with the interpretation of the transient results from Figure 5.18. By increasing the reactor temperature to 723 K, the degree of conversion

of biomass is improved. Around 92% of the leaving particles already reach the desired $Y_{char} \geq 0.90$. Further increase of the temperature completes the devolatilization reaction for the same residence time where the char mass fraction of all particles is equal to 1.0.
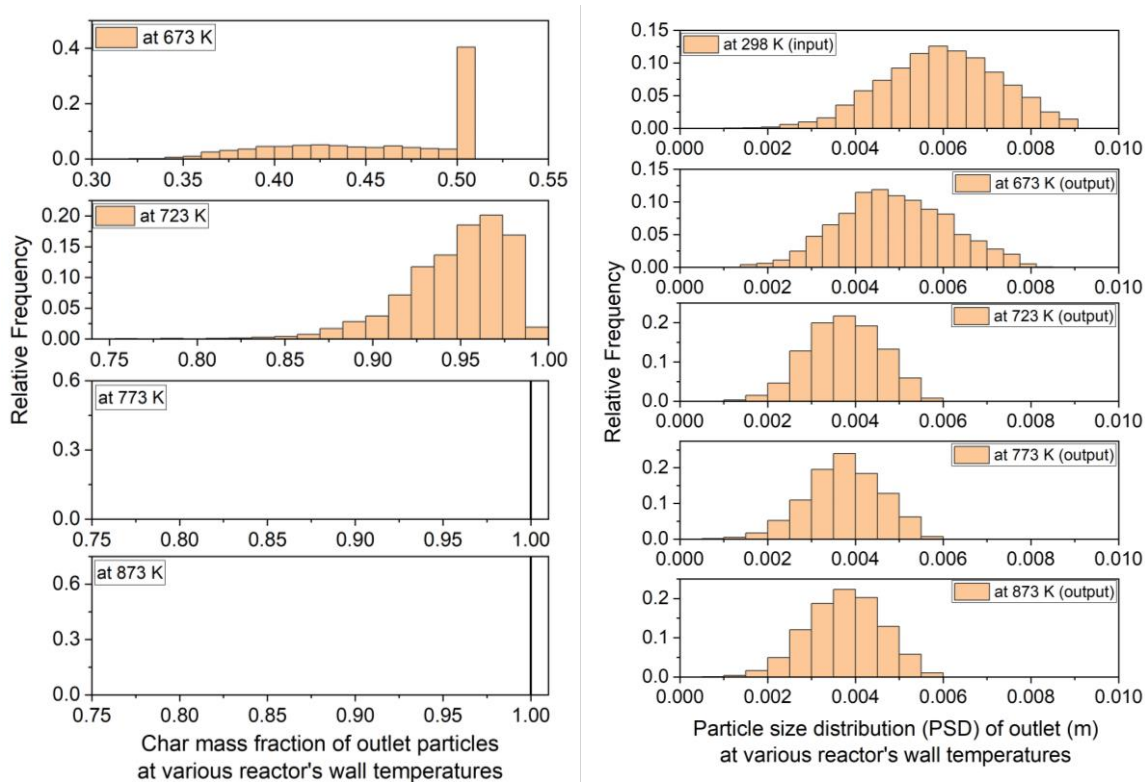
Figure 5.19 Distribution of particles leaving the reactor based on their char mass fraction (left) and particle size of input and products (right) at different reactor wall temperatures.

Figure 5.19 left suggests that the suitable wall temperature of a simulation case concerning the final conversion of particles should be between 723 K and 773 K. Therefore, these two cases are further referred to as "the optimal wall temperature cases". Fluctuations of the feed parameters for instance seasonal or material-related variable parameters such as MS and input temperature of the biomass would require further adjustments of the wall temperature.

Influence of the particle size on the final product

The particle size distribution (PSD) and its variation during the thermal processing of particles have been studied in the reactor. The uppermost graph in Figure 5.19 on the right corresponds to the particle size distribution of the feed as the values are mentioned in Table 5.1. Other graphs in the figure are related to particles leaving the reactor between 3500 s and 3600 s reaction time for various reactor wall temperature. As already discussed in section 2.5, the constant density model is used for the particle shrinkage.

The increase of the wall temperature of the reactor directly influences the heat flux to the bulk. Consequently, the temperature of particles increases and therefore there will be enhancing the reaction rate. The shrinkage of the particles is due to the release of moisture and volatiles. Figure 5.19 detects that by increasing the wall temperature the particle size distribution shifts to the left. This particle shrinkage can be observed by comparing the PSD graph at 298 K with cases at 673,723 and 773 K. No considerable change is noticed between the case at 773 K and 873 K. This once again demonstrates that the carbonization is entirely over by the wall temperature of 773 K and the higher temperature does not contribute to further conversion in terms of the specified reaction under study. In reality, the increase of the reactor temperature while the degree of conversion reached 1.0 has rather a negative impact on char yield and overall efficiency. In these simulations, further reactions related to higher temperatures, e.g., exothermic decompositions are not considered. These results are in agreement with the char fraction of particles from the left-hand side graphs at corresponding temperatures in Figure 5.19.

The effect of particle sizes on their temperature distributions along the reactor is shown in Figure 5.20. The PSD is divided into two fractions namely a small fraction for particles with a diameter of smaller than 5 mm and the large fraction for particles larger than 5 mm. In this figure, only the two case studies with favorable wall temperature with regard to their particle conversion are demonstrated.
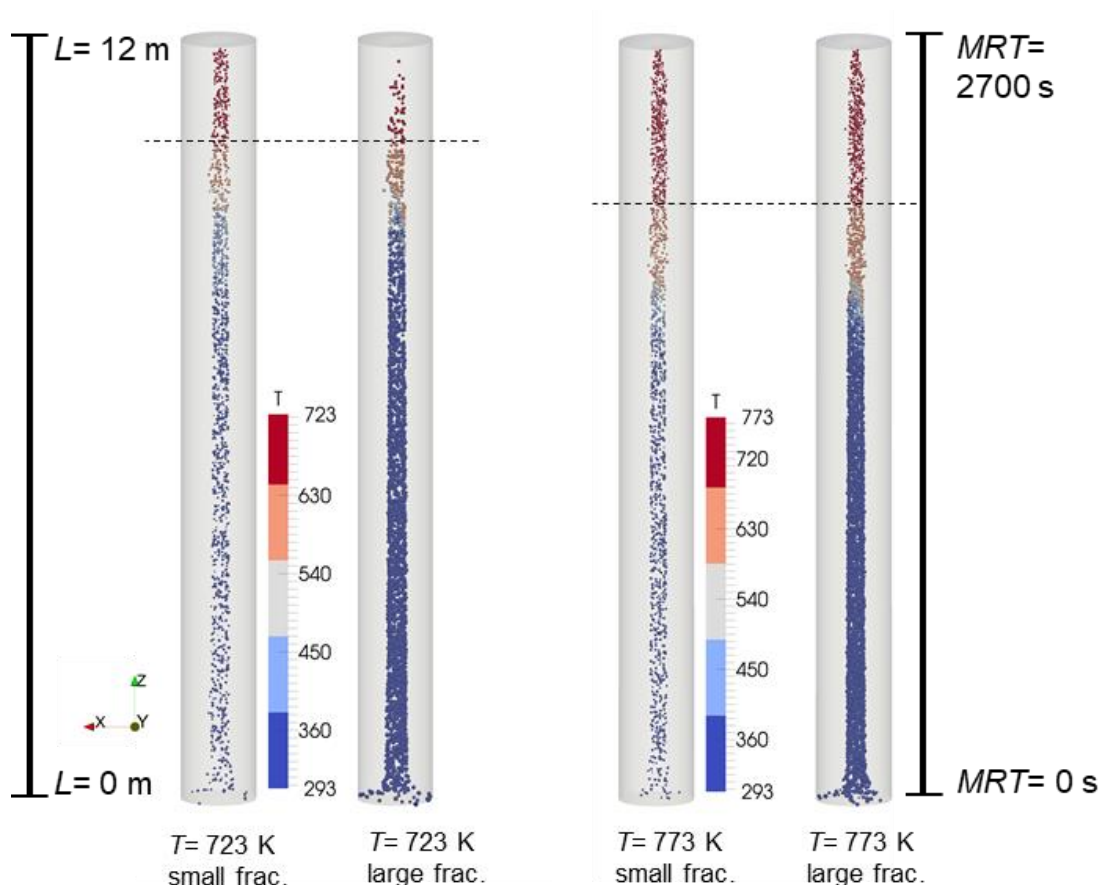
Figure 5.20 The effect of particle sizes on their temperature distributions along the reactor
(top view).

As the results show, the final temperature and composition of particles are not dependent on their size. This means the particle size in this study has no influence on the conversion of the bulk in different lengths of the reactor.

It can be due to the good mixing in the bulk, which causes a homogenous heat transfer within all particles with different sizes. This results in a similar temperature range in each longitudinal section of the reactor as is shown in Figure 5.20. It is worth mentioning that a decisive parameter for this phenomenon is the long residence time of the bulk in the reactor as the process is not under heat transfer control and rather it is kinetically limited. In the experimental work on the laboratory-scale, similar behavior is also observed during the conversion of biomass with comparable particle size distribution [121]. Based on own experiment and measurements in the laboratory-scale reactor, the elemental analysis measurements of the carbon content of the produced char by the standard deviation being less than 2.7%, confirmed the product homogeneity.

Analysis of the process stages along the reactor

For the investigation on the state of the bulk along the reactor again a quantitatively defined state of particles is used. This is based on the mass fraction of components within the particles at the latest simulation time of 3600 s.

For the investigated temperatures, similar to the lab scale, four zones/stages are introduced (compare with Figure 5.1). To compare the two scales, it is worth mentioning that the range of wall temperatures in the large-scale simulations in Figure 5.21 (673 – 873 K) is considerably higher than the range in the lab-scale simulations in Figure 5.1 (573 – 673 K). At the same wall temperature (673 K) and the same MRT (2700 s), the laboratory and industrial-scale reactors show different behaviors: while the biomass in the lab-scale reactor reaches the over-burned state at the end of the reactor, the reaction has not even started in the industrial-scale reactor even with a significantly smaller degree of filling. This demonstrates, that the scaling-up behavior cannot be predicted directly from the laboratory-scale results and full simulations of the large-scale reactor are necessary.
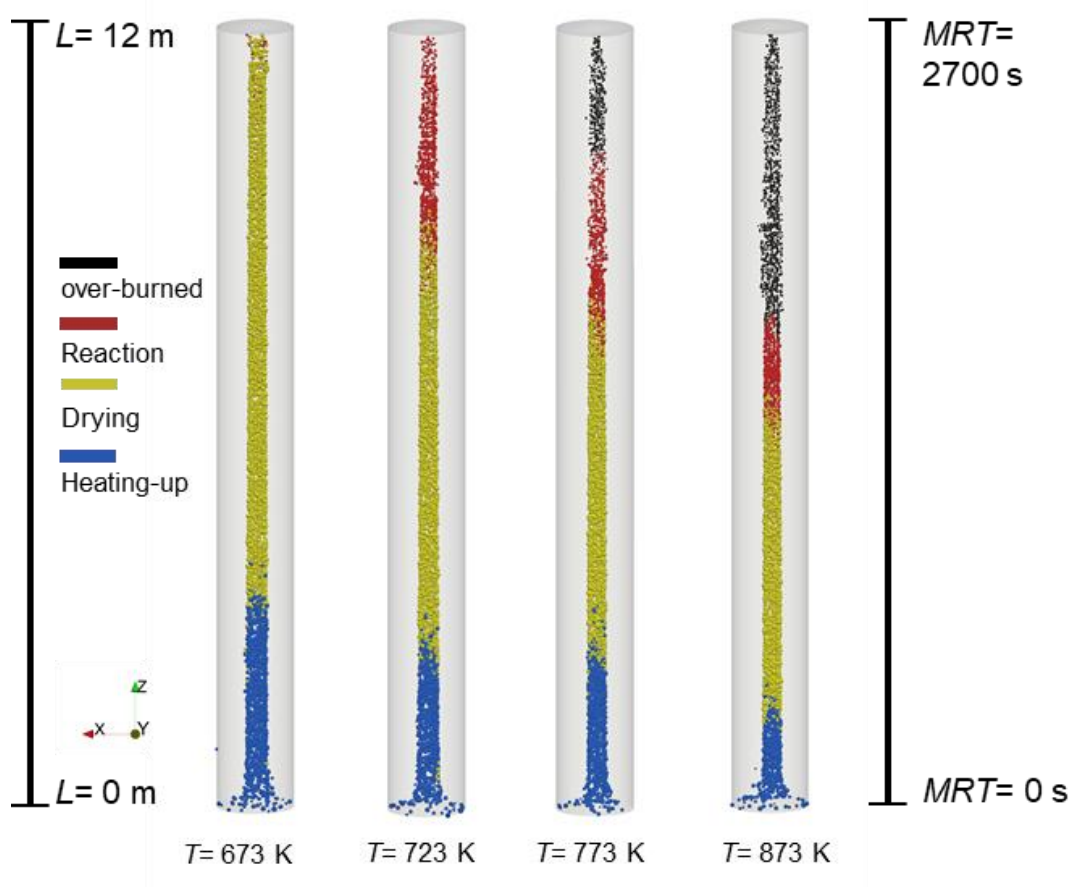
Figure 5.21 Stages of the process along the reactor after reaching the steady-state (top view).

At the wall temperature of 873 K, only 7 meters of the reactor are used to complete the conversion of the particles, see Figure 5.21. This has a negative impact on the desired state of the product and, additionally, decreases the energy efficiency of the reactor drastically. Further reactions related to this temperature, e.g., secondary cracking are neglected. No further model development is performed for the overburned char as it is unwanted and the high-temperature cases are only part of the sensitivity analysis.

The favorable wall temperature in terms of particle conversion and energy consumption lies between 723 K and 773 K, where the reaction is completed and no over-burned zone exists at the end of the rotary kiln. Such a case is commonly treated in the literature without consideration of secondary reactions [2], [18]. The overall comparison of these four cases shows that the conversion is quite sensitive to the wall temperature.

Gas temperature in the rotary kiln

The wet bulk cools down the surrounding gas and as a result, the coldest zone tracks the non-dried bulk in the reactor. The gas-phase temperatures at the bottom of the reactor in Figure 5.22 are correlated to the stages of the process seen in Figure 5.21. The end of the blue zone in Figure 5.22 can be compared with the different stages of the process in Figure 5.21 where it proves the end of the drying zone for each case.

In the legend of Figure 5.22, the upper-temperature limit is set to the corresponding wall temperature. At higher temperatures, the release rates of moisture and volatiles become higher which consequently causes higher average velocities in the reactor. The final time in Figure 5.18 declares that the accumulative mass release at 873 K is around 15 kg higher than that of at 773 K. This amount corresponds to a higher velocity, and consequently to a lower gas residence time in the reactor. It explains why the gas in the hottest reactor, unlike other cases, does not have enough time to reach the homogenous and final temperature at the last stage of the reactor. On the other hand, the case with the lowest temperature, the stratification phenomenon is clear in the radial temperature distribution in the reactor. For the 873 K, the outflow velocity of the gas is 0.15 m/s on average with local maxima of 0.45 m/s. The highest velocity magnitude in the entire domain is common in all cases, due to the rotation of the kiln, and has a value of 0.627 m/s (10 rpm rotation).
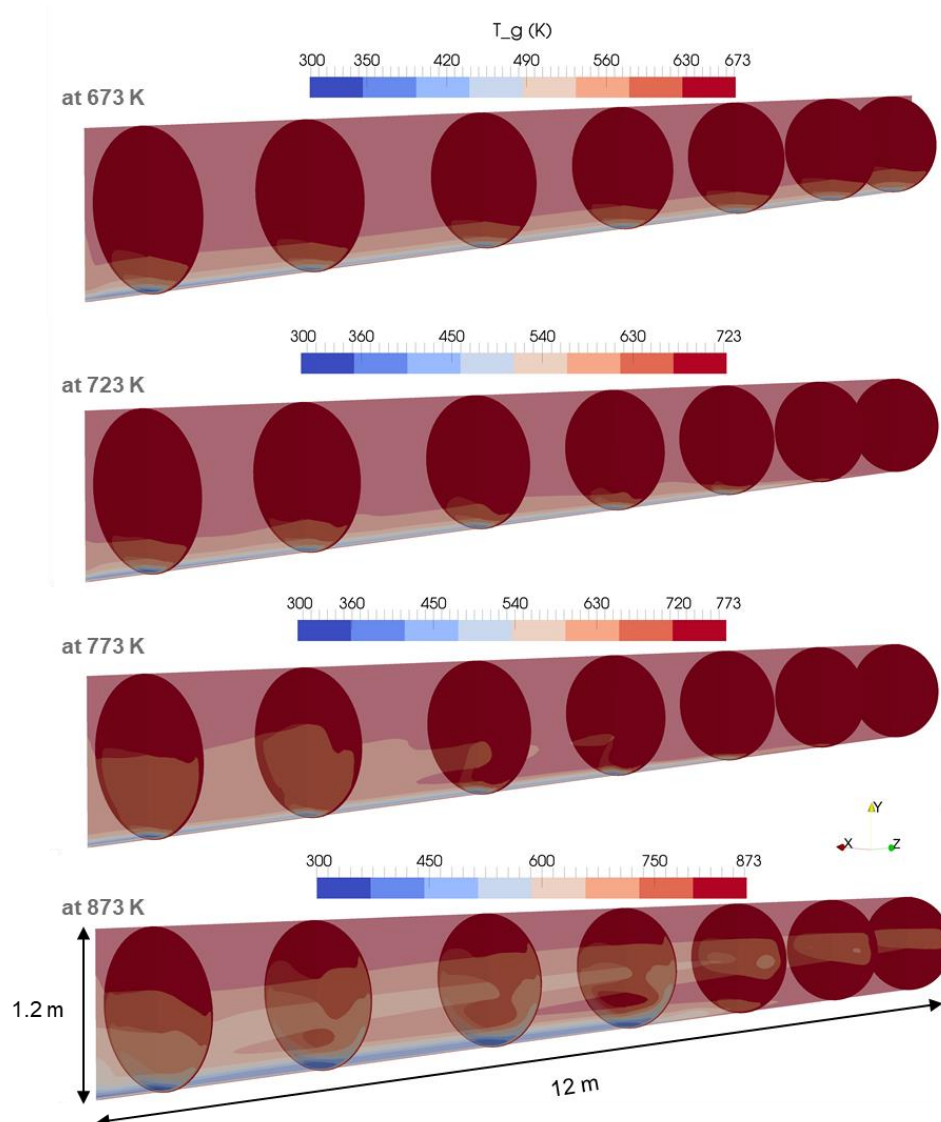
Figure 5.22 Gas-phase temperature in the rotary kiln at different wall temperatures (isometric view).

Moisture and volatiles in the gas phase

At the steady-state condition, the initial air is completely displaced by the produced steam and volatiles. As it was shown in Figure 5.16, after approximately half an hour of continuous process neither nitrogen and nor oxygen is present in the reactor. On the other hand, the mass release from evaporation and reaction fills the reactor with steam and volatiles. Figure 5.23 depicts the mass fraction of moisture within the reactor, where the rest of the gas is non-condensable volatiles (tar, CO_2 and CO). Therefore, the blue zone in the figure represents the mass fraction of volatiles.

At 673 K at the beginning of the reactor, the negligible amount of volatiles comes from the early devolatilization of biomass up to the time 1500 s when it occurs before reaching the steady-state. The volatiles are then gradually pushed out and diluted over time. This scenario can be followed by looking at Figure 5.18 on the right for the mentioned operating temperature.

Looking at the rest of the cases in Figure 5.23, the amount of moisture in the first half of the reactor increases with temperature. At the highest temperature, almost only water vapor exists up the second cross-sectional planes. This means that the enhanced drying rate and consequently higher velocity counteracts the penetration of the produced volatiles to this region.

The volatiles are produced in the second half of the reactor, where further increase in the wall temperature leads to a shift of the reaction zone to the left side. Likewise, the mass fraction of the volatiles in the freeboard gas is reduced due to the dilution with a comparatively larger amount of moisture coming from the drying zone. The comparison of the amount of moisture and volatiles release at the latest points from Figure 5.18 confirms the domination of the vapor release over the volatiles generation. As a consequence, gas with a relatively higher moisture mass fraction is present at the outlet.
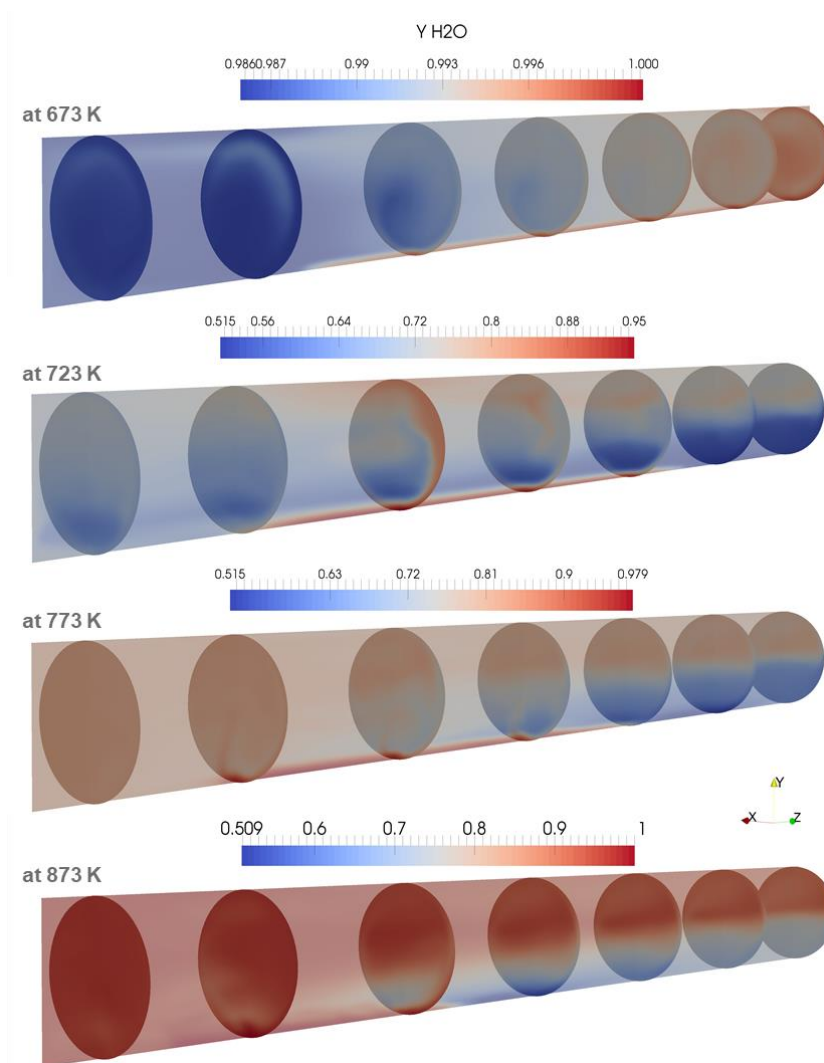
Figure 5.23 MS of the gas in the rotary kiln at different wall temperatures (isometric view).

142

5.3.3 Overall process design

Thermal power of the process

Based on the steady-state conditions, the thermal power transferred to the bulk material in the rotary kiln is evaluated at the suitable wall temperature of 773 K. For the estimation of the overall thermal power of the process, several parameters such as the inlet boundary conditions and process parameters have to be identified and measured first. Table 5.3 tabularizes the highlighted assumptions for the simulation, based on given geometry and experimental measurement in the setup.

Table 5.3 Highlighted assumptions and thermophysical constants used for the large-scale simulation.

Biomass input		Reactor	
Input mass (g)	350 kg/h	Wall temperature (K)	773
Initial temperature (K)	293	Gas temperature (K)	300
Moisture content wt.%	50	Pressure	atmospheric
Volatile fraction (dry wt.%)	50	Gas input	none
Particle diameter (mm)	see Table 5.1	Residence time (min)	51
Particle density (kg/m^3)	713	Angle of inclination (°)	0.25
Moisture c_p (J/(kg.K))	4180	Rotation (rpm)	10
Volatiles c_p (J/(kg.K))	2000	Biomass hygroscopiciy	considered
Char c_p (J/(kg.K))	800	Heat of reaction (kJ/kg*)	- 400

* Heat of reaction is considered based on the mass of volatiles

The established CFD-MPPIC large-scale simulation at the steady-state condition helps to have a reliable calculation for process design and overall calculations when the results can be coupled with a process simulation software. The final temperature of the gas phase leaving the reactor can be evaluated from Figure 5.22 and the results depict the final temperature at 773 K for the entire outlet patch.

Other important parameters are the overall degree of conversion and the temperature of the solid phase. The outcome from Figure 5.19 concluded that the devolatilization process of discharging particles is finished and the mean temperature of particles is 770 K. This temperature is calculated from the average temperature of the particles discharging from the outlet patch. So far, the inlet and outlet boundary conditions are identified and calculated. Using the thermophysical properties from Table 5.3 a design for the total required energy per unit of time can be calculated.

The thermal power is regarded for the heat transferred from the inner wall to the bulk. The balance calculated in Table 5.4, is the integration of overall thermal demand for different steps including sensible heat, and latent heat and reaction enthalpy. The inner thermal power of the carbonization reactor with 350 kg/h input is tabulated. Assuming an overall efficiency of $\eta = 0.6$, the total power of the unit, including the afterburner, is estimated to be at about 300 kW$_{th}$.

Table 5.4 Inner thermal power of the rotary kiln reactor.

Process stages	Thermal power (kW)	Thermal power in %
Thermal power to heat-up (blue zone)	22.6	12.5
Thermal power to dry the bulk (yellow zone)	109.7	61
Thermal power for the reaction (red zone)	48.3	26.5
Total heat transferred	180.6	100

The demanded thermal power for drying of the input bulk with 50 % MS (yellow zone) in Figure 5.21, dominates the sum of the other stages. The portion of the heat flux in each zone approximately corresponds to the length of the stage in the reactor. The thermal power for the reaction contains the necessary power to heat the dried bulk and gas components as well as the enthalpy of devolatilization where their shares are 21 % and 5.5 %, respectively.

Importance of transient simulation using CFD approach

The process simulation software Aspen Plus [122] (Aspentech version 10) is a design package based on the direct calculation of mass and energy balances based on solely time-resolved differential equations for homogeneous elements which numerically coverages to steady-state operational conditions. Using this software, the inputs and experimental results from the laboratory-scale unit are integrated to design an overall process simulation for the scale-up of the wet biomass carbonization plant. In the simulation, the unit is designed as energy-efficient and ecological-friendly as possible using the concept of industrial economizer and afterburners as an integration to the flue gas treatment unit.

Figure 5.24 depicts a simplified sketch of a process flow diagram that is designed during this work for a wet biomass carbonization unit using a single reactor concept with an indirect heating mechanism. On the left-hand side below all inputs, the pure burner is placed which operates with natural gas and provides the required energy of the reactor. The two red contours in the diagram

represent the carbonization reactor and the economizer /afterburner unit on the middle and upright respectively.

Figure 5.24 is a typical example of basic engineering for thermal conversion plant design by reliable simulation software such as Aspen Plus. However, the data for the scale-up is based on experimental results from laboratory research. Hence, in this case, several disadvantages of the steady-steady simulation tools like Aspen Plus play a decisive role. One of the general cons - as the name shows - is that the simulation tools converge for the steady-state solution and there is no transient solution mechanism considered in the model. Another underlined disadvantage is the thermal equilibrium between two phases in the reactor. That means in every specified length of the reactor as well as the outlet, the solid and gas have an identical temperature. It is in a while that in this section for instance from Figure 5.22 it is concluded that the energy equation of phases is independent of each other and it should be coupled properly.

Results from Figure 5.24 suggest a final temperature of about 350 °C (623 K) as for the outlet of the reactors which is based on the data from lab-scale experimental work. However, it has been shown that the reactor with a wall temperature of 773 K is proper for this scale. This implicitly means that there is a considerable discrepancy in heat transfer and its interphase limitations between two scales although it is stated that the entire process is under kinetic control due to the slow kinetic rate of the carbonization. Additional information related to the process flow diagram presented in Figure 5.24 is tabulated.

The comparison of the steady-state process simulation and the Eulerian-Lagrangian numerical simulation affirm the importance of transient state simulations with coupled interphase heat transfer for scale-up calculations and it shows that scale-up calculations relying on lab-scale data and steady-state simulations can result in a significant underestimation of the reactor. However, it is a helpful tool specifically for energy and mass balance calculations. The calculations belonging to the economizer unit show that 325 kW harvestable power is available in the flue gas leaving the unit. Harvestable power has been estimated based on cooling down to 160 °C which is still above the dew point of moisture in the flue gas for safety reasons related to corrosion. By taking the thermal load of the afterburner (i.e. the burner that decomposes the non-solid byproducts of the reaction) into account this carbonization unit has the capacity of approximately 500 kW_{th} power turnover for 350 kg/h input with 50 wt.% moisture.

Stream	16	17	20	25	26	27	27-2	28	29-30	30	34-38	40	41	42	43	44	X
Mass Flow kg/hr																	
H2O	175,00	175,00	0,00	38,20	0,00	0,00	0,00	175,00	224,43	238,87	43,79	0,00	0,00	43,79	0,00	238,87	282,67
N2	0,00	0,0001	0,00	0,00	0,00	79,00	79,00	0,0001	79,00	424,18	690,37	0,00	690,37	690,37	345,18	424,19	1114,56
CO2	0,00	0,0003	15,67	0,00	15,67	0,00	0,00	0,005	29,38	99,94	53,49	0,00	690,37	53,49	0,00	99,95	153,44
O2	0,00	0,0001	0,00	0,00	0,00	21,00	21,00	0,00	1,05	54,56	131,84	0,00	209,63	131,84	104,81	54,57	186,40
H2	0,00	0,00	0,00	0,00	0,00	0,00	0,00	0,00	0,00	0,00	0,00	19,50	0,00	0,00	0,00	0,00	0,00
CH4	0,00	0,00	0,00	0,00	5,00	0,00	0,00	0,00	0,00	0,00	0,00	0,00	0,00	0,00	0,00	0,00	0,00
HMF	0,00	0,00	0,00	33,70	0,00	0,00	0,00	0,00	33,70	0,00	0,00	0,00	0,00	0,00	0,00	0,00	0,20
BIOMASS	175,00	0,00	0,00	0,00	0,00	0,00	0,00	0,00	0,00	0,00	0,00	0,00	0,00	0,00	0,00	0,00	0,00
CHAR	0,00	87,57	87,57	0,00	0,00	0,00	0,00	0,00	0,00	0,00	0,00	0,00	0,00	0,00	0,00	0,00	0,00
Total Flow kg/hr	350,00	262,5	87,57	87,57	5,00	100,00	100,00	175,00	367,57	817,15	919,50	19,50	900,00	919,50	450,00	817,57	1737,07
Temperature C	25,00	348,00	348,00	364,00	15,00	15,00	864,12	348,00	791,02	1083,22	325,14	15,00	15,00	937,73	15,00	1012,63	160,00

Process flow diagram labels: BE4-ALT · Q = 185 kW · BE2-300/350 · BE2001 · BE4000 · BE4001 · ECO-AIR · ECONOMIZ · QHarvestable* = 325 kW · 87,5 kg/h charcoal

Legend: Temperature (C) / Mass Flow Rate (kg/hr)

Figure 5.24 process flow diagram of the designed integrated plant for wet biomass carbonization.

6   Summary

Many conventional approaches to processing lignocellulosic biomass, wet municipal and biogenic wastes are abandoned nowadays due to ecological hazards and negative long-term impacts on the environment. Thermal treatments of wet biomass have been reintroduced recently as a solution to issues regarding the handling and recycling of biodegradable wastes. These treatments have a wide range of applications concerning the inial and desired states. Operational temperature, pressure and residence time as well as the type of reactor are influencing parameters for the process design. Low-temperature pyrolysis, e.g. carbonization, in overheated steam ambient, the so-called steam-assisted carbonization is the process considered in this work for the conversion of the inputs.

In this work, a simulation tool is presented which can simulate the transient, two-phase and multidimensional carbonization of wet biomass in rotary reactors. It is based on the development of the open-source framework OpenFOAM® and combines the Lagrangian method to simulate the motion and conversion of biomass in a particle bed with its Eulerian method to simulate the gas phase. Both the discrete biomass particles and the multicomponent gas phase are fully coupled. New models for drying, chemical carbonization kinetics and radiation have been developed for the conditions in the rotary kilns and have been implemented into OpenFOAM®.

Initial cold-runs tests indicate that both available interparticle models are proper for spherical particles in the tubular reactor. However, due to the lack of related physical models, none of them is applicable for non-spherical particles and particles with ill-defined geometries. The perspective of further development for both models demands intensive experimental and theoretical effort. In the case of applying the direct numerical solution, i.e. DEM-based solver, the computational effort would unreasonably increase as well, however, a precise approach can be assured. On the other hand, in the case of applying statistical-based numerical models, for instance, solvers based on the MP-PIC model, extensive experimental work is required to prepare a complementary model for adjusting the numerical constants and variables, however, the success and precision cannot be guaranteed. Hence, further achievements in particle simulation such as bed motion and residence time with the measured angle of inclination are in perspective for this research field to answer remained uncertainties.

Various submodels have been further developed and adjusted to the application of the thermal conversion of biomass in the indirectly heated kiln reactor and validated in the context of this work. The model includes a shrinkage model for solid particles. The adaptable drying model for every

moisture concentrations in the ambient gas is extended. The new drying model can switch between the existing evaporation model for situations with concentration differences and a newly implemented boiling model that is based on the thermal model. An extension of the nth-order reaction rate with the Arrhenius-like reaction rate coefficient has been derived and implemented in the code. The newly multi-species single step n-th order reaction submodel can consider complex reactions such as carbonization and the reaction scheme is utilized to release by-products regarding their masses within the particles. The thermophysical properties are subject to change with time and vary based on the transient composition within each particle. Moreover, the direction-based radiation model is adjusted for a computational cell with arbitrary particle volume fractions. The original fvDOM radiation model is thought for the dilute phase of particles, where the effect of local opacity due to the existence of particles can be neglected. However, in this application, the packed bed of the particulate phase exists in the reactor. Therefore, the radiation model is extended for applications in the packed bed with high particle volume fractions.

A series of validation cases are designed and applied to the laboratory-scale studies and the results from the experiment are used to tune the numerical models. Finally, the results are compared and the models are found to be in good agreement with experimental results. The validations show that the new models can accurately simulate the complex physical processes that govern the heating, drying and carbonization inside the reactor. The new tool is used to perform a series of simulations for wet biomass carbonization in a rotary kiln reactor at the laboratory scale. Parameter studies regarding the influence of biomass mass flow rate, moisture content and the wall temperatures reveal the sensitivity of biomass conversion to those parameters and help to choose operating conditions for specified char yield or carbon content.

The laboratory-scale simulation is then scaled up to an industrial scale plant with a given geometry, with a biomass throughput of 350 kg/h. Scale-up challenges were large-scale modeling and their requirements for at least 3600 seconds of physical time simulation including up to 4 million physical particles. This concluded the demands of about 40 thousand CPU-hours per simulation for a total of up to 1 million timesteps. Grid independence studies, mesh optimization and parallelization performance tests were applied to enhance the simulation performance. 8 times faster simulations are recorded by using a coarser mesh with negligible inaccuracy. The optimized decomposition method of the computational domain is highlighted as an important setscrew during the long-run simulations. The preferred decomposition method boosted the performance of simulations at least by 100%, comparing to other practical decomposition methods. Additionally, for the Lagrangian phase, the parcel concept is tested and successfully applied to reduce the computational effort of

the particulate phase. Last but not least, the radiation submodel, as one of the most computation expensive modules, is regulated by utilizing reduced solver frequency and ray-tracing directions. The computation reduction of factor $1/7$ is achieved by the optimization of the radiation model while keeping results within 2.5% accuracy. All in all, it can be stated that the optimization has helped to upgrade the performance by a factor of at least 100 times.

Given the real reactor dimensions and biomass input characteristics, the transient and steady-state conditions are analyzed and the solid-gas flow behavior within the reactor is analyzed. A suitable operating condition is determined by analyzing several lagrangian properties for all particles during the process including, temperature, composition, degree of conversion, size and shrinkage of the particles near the reactor outlet. This condition with regard to the specified biomass conversion can be summarized by a reactor wall temperature between 723 K and 773 K. The calculation considers the probable local turbulence via the Large-Eddy approach for the large-scale reactor as well. At the lower temperature, the conversion of the wet biomass to char lies at about 95%. The results also show that the final conversion state of the particles cannot be directly extrapolated from the simulation results of the laboratory scale reactor to the industrial-scale. Therefore, full simulation of the large-scale reactor on supercomputers is necessary. It has been shown, that the new tool can efficiently simulate the full process on up to 560 CPU cores. Therefore, it is suitable for the design of reactors where the dense particulate phase has a dominant contribution.

Finally, results are compared with solutions from steady-state process simulation software based on only time-resolved differential equations which emphasize the necessity of using a transient CFD-based model, e.g., Eulerian-Lagrangian method. It can be concluded that a reliable and more efficient plant design is the outcome of fully resolved simulation of the reacting two-phase flow in addition to the overall calculations and balances.

7 Zusammenfassung

Viele konventionelle Verfahren zur Behandlung von lignozellulosehaltiger Biomasse, nassen Siedlungsabfällen und Biomüll werden heutzutage aufgrund ökologischer Gefahren und negativer Langzeitwirkungen auf die Umwelt aufgegeben. Die thermische Behandlung von feuchter Biomasse wurde vor kurzem als Lösung für Probleme bei der Entsorgung und dem Recycling von Abfällen wieder eingeführt. Diese Behandlungen haben ein breites Anwendungsspektrum hinsichtlich der Anfangs- und Zielzustände. Betriebstemperatur, Druck und Verweilzeit sowie die Gestaltung des Reaktortyps sind entscheidende Parameter für die Prozessauslegung. Niedertemperatur-Pyrolyse, z.B. Karbonisierung, in überhitztem Dampf, die sogenannte „Steam-Assisted Carbonisation", ist das in dieser Arbeit untersuchte Verfahren zur Umwandlung der Einsatzstoffe.

In dieser Arbeit wird ein mehrdimensionales Simulationswerkzeug vorgestellt, mit dem die transiente, zweiphasige Karbonisierung von feuchter Biomasse in Drehrohrreaktoren simuliert werden kann. Es basiert auf dem Open-Source-Framework OpenFOAM® und kombiniert die Lagrange-Methode zur Simulation der Bewegung und Umwandlung des Biomasse-Partikelbetts mit der Eulerschen Methode zur Simulation der Gasphase. Die diskreten Biomasse-Partikel und die Mehrkomponenten-Gasphase sind vollständig gekoppelt. Neue Modelle für Trocknung, chemische Karbonisierung und Strahlung wurden für die Bedingungen in Drehrohröfen entwickelt und in OpenFOAM® implementiert.

Kaltlaufversuche zur Bewegung von Partikeln im Drehrohrofen deuten darauf hin, dass beide in der Software verfügbaren Interpartikelmodelle für kugelförmige Partikel im Rohrreaktor geeignet sind. Jedoch ist keines von beiden für nicht-sphärische Partikel und Partikel mit schlecht definierten Geometrien anwendbar. Die Weiterentwicklung beider Modelle erfordert intensive experimentelle und theoretische Untersuchungen, die über den Rahmen dieser Arbeit hinausgehen. Im Falle der Anwendung der direkten numerischen Lösung, d.h. eines DEM-basierten Lösers, würde sich der Rechenaufwand ebenfalls unangemessen erhöhen, wobei ein exakter Ansatz nicht gewährleistet werden kann. Im Falle der Anwendung statistisch basierter numerischer Modelle, z.B. Solver auf Basis des MP-PIC-Modells, sind dagegen umfangreiche experimentelle Arbeiten zur Anpassung der numerischen Konstanten und Variablen erforderlich, wobei der Erfolg und die Genauigkeit nicht garantiert werden können. Zur Klärung solcher Problemstellungen sind umfangreiche

Untersuchungen zur Partikelsimulation sowie Bettbewegung und Verweilzeit mit dem gemessenen Neigungswinkel notwendig.

Für die Anwendung der thermischen Umwandlung von Biomasse im indirekt beheizten Drehrohrreaktor wurden verschiedene Teilmodelle weiterentwickelt und angepasst und im Rahmen dieser Arbeit validiert. Die verschiedenen Teilmodelle beinhalten ein Schrumpfungsmodell für Feststoffpartikel. Sowie ein anpassbares Trocknungsmodell für jede Feuchtekonzentration im Umgebungsgas. Das Trocknungsmodell kann zwischen dem bestehenden Evaporationsmodell für Situationen mit Konzentrationsunterschieden und einem neu implementierten Siedemodell, das auf dem thermischen Modell basiert, umschalten. Ein Reaktionsmodell für globale Reaktionen n-ter Ordnung kann komplexe Reaktionen wie z.B. Karbonisierung berücksichtigen, und ein Reaktionsschema für die Freisetzung von Nebenprodukten, das aus Experimenten zur Karbonisierung abgeleitet ist, wird in den Code implementiert. Die thermophysikalischen Eigenschaften ändern sich mit der Zeit und variieren auf der Grundlage der transienten Zusammensetzung innerhalb jedes Partikels. Außerdem wird das richtungsbasierte Strahlungsmodell für eine Rechenzelle mit willkürlichen Partikelvolumenanteilen angepasst. Das ursprüngliche fvDOM-Strahlungsmodell ist für verdünnte Partikel-Phasen gedacht, wo der Effekt der lokalen partikelbedingten Opazität vernachlässigt werden kann. Bei dem betrachteten Drehrohrreaktor besteht jedoch die partikuläre Phase aus einem dichten Festbett, so dass das Strahlungsmodell für Anwendungen im Festbett mit hohen Partikelvolumenanteilen erweitert wird.

Das entwicklelte Modell wird auf Ergebnisse aus Untersuchungen an einem Drehrohrreaktor im Labormaßstab angewandt, wobei die experimentellen Ergebnisse zur Abstimmung der Modellparameter verwendet werden. Die Validierungen zeigen, dass die neuen Modelle die komplexen physikalischen Prozesse, die die Erwärmung, Trocknung und Karbonisierung im Reaktor steuern, zuverlässig simulieren können. Das entwickelte Werkzeug wird verwendet, um eine Reihe von Simulationen für die Karbonisierung feuchter Biomasse in einem Drehrohrreaktor im Labormaßstab durchzuführen. Parameterstudien zum Einfluss von Biomasse-Massenstrom, Feuchtigkeitsgehalt und Wandtemperaturen zeigen die Sensitivität der Biomasse-Konversion auf diese Parameter und helfen bei der Wahl der Betriebsbedingungen für eine bestimmte Kohleausbeute beziehungsweise einen bestimmten Kohlenstoffgehalt.

Die Simulation im Labormaßstab wird dann auf eine Anlage im industriellen Maßstab mit einer gegebenen Geometrie und einem Biomassedurchsatz von 350 kg/h hochskaliert. Die Herausforderungen beim Scale-up waren die Modellierung im Großmaßstab und die Simulation für

mindestens 3600 Sekunden physikalische Zeit unter Einbeziehung von bis zu 4 Millionen physikalischen Partikeln. Daraus ergaben sich die Anforderungen von etwa 40 Tausend CPU-Stunden pro Simulation für insgesamt bis zu 1 Million Zeitschritte. Studien zur Gitterunabhängigkeit, Gitteroptimierung und Parallelisierungsleistung wurden durchgeführt, um die Simulationsleistung zu verbessern. Durch die Verwendung eines gröberen Gitters mit noch vertretbarer Genauigkeit werden 8-mal schnellere Simulationen aufgezeichnet. Die optimierte Dekompositionsmethode der Berechnungsdomäne ist bei den Langzeitsimulationen eine wichtige Stellschraube. Die bevorzugte Dekompositionsmethode steigerte die Leistung der Simulationen im Vergleich zu anderen praktischen Dekompositionsmethoden um mindestens 100 %. Zusätzlich wird für die Lagrange-Phase das Parcel-konzept getestet und erfolgreich angewendet, um den Rechenaufwand der Partikelphase zu reduzieren.

Schließlich wird das Strahlungs-Submodell als eines der berechnungsintensivsten Module durch die Verwendung reduzierter Solver-Frequenz und Raytracing-Richtungen reguliert. Durch die Optimierung des Strahlungsmodells wird eine Rechenzeitreduktion um den Faktor 1/7 erreicht, wobei die Ergebnisse innerhalb einer Genauigkeit von 2,5 % bleiben. Insgesamt kann festgestellt werden, dass die Optimierung zu einer Leistungssteigerung um einen Faktor von mindestens 100 geführt hat.

Unter Berücksichtigung der Abmessungen des realen Reaktors und der Eingangsdaten, der Biomasse werden die instationären und stationären Bedingungen analysiert und das Feststoff-Gas-Strömungsverhalten innerhalb des Reaktors untersucht. Durch die Analyse verschiedener Eigenschaften für die Partikel, einschließlich Temperatur, Zusammensetzung, Umwandlungsgrad, Größe und Schrumpfung der Partikel am Reaktorauslass, werden günstige Betriebsbedingungen für den Betrieb des Drehrohrreaktors festgelegt. Diese Bedingungen für einen möglichst vollständigen Umwandlungsgrad der Biomasse lässt sich durch die Reaktorwandtemperatur zusammenfassen, die zwischen 723 K und 773 K liegt. Die Berechnung berücksichtigt die auftretende lokale Turbulenz über den Large-Eddy-Ansatz für den Großreaktor. Bei der niedrigeren Temperatur (723 K) liegt die Umwandlung der feuchten Biomasse zu Biokohle bei etwa 95%. Die Ergebnisse zeigen auch, dass der endgültige Umwandlungszustand der Partikel nicht vom Reaktor im Labormaßstab auf den industriellen Maßstab extrapoliert werden kann. Daher ist eine vollständige Simulation des industriellen Reaktors auf Supercomputern erforderlich. Es hat sich gezeigt, dass das entwickelte Tool den gesamten Prozess auf bis zu 560 CPU-Kernen effizient simulieren kann. Daher ist es für die Auslegung von Reaktoren geeignet, bei denen die dichte partikuläre Phase einen dominanten Beitrag leistet.

Schließlich werden die Ergebnisse mit Lösungen aus einer Prozesssimulationssoftware verglichen, die auf nur zeitabhängigen Differentialgleichungen basiert. Dieser Vergleich zeigt die Notwendigkeit der Verwendung eines transienten CFD-basierten Modells, z.B. der Euler-Lagrange-Methode. Es kann festgestellt werden, dass eine zuverlässige und effiziente Anlagenauslegung das Ergebnis einer vollständig aufgelösten Simulation der reagierenden Zweiphasenströmung zusätzlich zu den Gesamtberechnungen und -bilanzen ist.

Bibliography

[1] A. Demirbas, *Biofuels - Securing the Planet's Future Energy Needs*. Springer London, 2009.

[2] P. Basu, *Biomass Gasification and Pyrolysis*. Academic Press (Elsevier), 2010.

[3] X. Shi, F. Ronsse, and J. G. Pieters, "Finite element modeling of intraparticle heterogeneous tar conversion during pyrolysis of woody biomass particles," *Fuel Process. Technol.*, vol. 148, no. 2, pp. 302–316, Jul. 2016, doi: 10.1016/j.fuproc.2016.03.010.

[4] J. Steinbrück, S. Tavakkol, G. Francis, and H. Bockhorn, "Jatropha – Potential of biomass steam processing to convert crop residues to bio-coal and thus triple the marketable energy output per unit plantation area," *Ind. Crops Prod.*, vol. 136, no. January, pp. 59–65, 2019, doi: 10.1016/j.indcrop.2019.04.065.

[5] V. Scherer, S. Wirtz, B. Krause, and F. Wissing, "Simulation of Reacting Moving Granular Material in Furnaces and Boilers An Overview on the Capabilities Of the Discrete Element Method," *Energy Procedia*, vol. 120, pp. 41–61, Aug. 2017, doi: 10.1016/j.egypro.2017.07.154.

[6] A. K. Sadhukhan, P. Gupta, and R. K. Saha, "Modelling of pyrolysis of large wood particles," *Bioresour. Technol.*, vol. 100, no. 12, pp. 3134–3139, Jun. 2009, doi: 10.1016/j.biortech.2009.01.007.

[7] H. P. Zhu, Z. Y. Zhou, R. Y. Yang, and A. B. Yu, "Discrete particle simulation of particulate systems: Theoretical developments," *Chem. Eng. Sci.*, vol. 62, no. 13, pp. 3378–3396, 2007, doi: 10.1016/j.ces.2006.12.089.

[8] H. P. Zhu, Z. Y. Zhou, R. Y. Yang, and A. B. Yu, "Discrete particle simulation of particulate systems: A review of major applications and findings," *Chem. Eng. Sci.*, vol. 63, no. 23, pp. 5728–5770, 2008, doi: 10.1016/j.ces.2008.08.006.

[9] Q. Xiong, S. Aramideh, A. Passalacqua, and S. C. Kong, "BIOTC: An open-source CFD code for simulating biomass fast pyrolysis," *Comput. Phys. Commun.*, vol. 185, no. 6, pp. 1739–1746, 2014, doi: 10.1016/j.cpc.2014.02.012.

[10] W. Chen, J. Peng, and X. T. Bi, "A state-of-the-art review of biomass torrefaction,

densification and applications," *Renew. Sustain. Energy Rev.*, vol. 44, pp. 847–866, Apr. 2015, doi: 10.1016/j.rser.2014.12.039.

[11]   D. Reichert, B. Genova, J. Steinbrueck, M. Rossbach, L. Walz, and H. Bockhorn, "Biomass steam processing of barley straw towards biocoal – A carbonisation alternative," in *19th European Biomass Conference & Exhibition*, 2011, pp. 2027–2031.

[12]   J. Steinbrueck, D. Reichert, B. Genova, M. Roßbach, L. Walz, and H. Bockhorn, "Biocoal in Minutes – Biomass Steam Processing on the Pilot Plan Scale," in *20th European Biomass Conference and Exhibition*, 2012, pp. 2–5.

[13]   J. Steinbrueck, L. Walz, and H. Bockhorn, "Biocoal in minutes - Quick and easy source for carbon materials," in *6th International Conference on Carbon for Energy storage/conversion and environment protection*, 2015, p. 45.

[14]   M. Müller-Hagedorn and H. Bockhorn, "Pyrolytic behaviour of different biomasses (angiosperms) (maize plants, straws, and wood) in low temperature pyrolysis," *J. Anal. Appl. Pyrolysis*, vol. 79, no. 1-2 SPEC. ISS., pp. 136–146, 2007, doi: 10.1016/j.jaap.2006.12.008.

[15]   M. Sasaki, Z. Fang, Y. Fukushima, T. Adschiri, and K. Arai, "Dissolution and Hydrolysis of Cellulose in Subcritical and Supercritical Water," *Ind. Eng. Chem. Res.*, vol. 39, no. 8, pp. 2883–2890, 2000, doi: 10.1021/ie990690j.

[16]   A. Anca-Couce, "Reaction mechanisms and multi-scale modelling of lignocellulosic biomass pyrolysis," *Prog. Energy Combust. Sci.*, vol. 53, no. 2016, pp. 41–79, Mar. 2016, doi: 10.1016/j.pecs.2015.10.002.

[17]   M. J. C. Van Der Stelt, "Chemistry and reaction kinetics of biowaste torrefaction-PhD Thesis," Technische Universiteit Eindhoven, PhD Thesis, 2010.

[18]   F. Ronsse, R. W. Nachenius, and W. Prins, "Carbonization of Biomass," in *Recent Advances in Thermo-Chemical Conversion of Biomass*, Elsevier, 2015, pp. 293–324.

[19]   P. N. Ciesielski, M. B. Pecha, A. M. Lattanzi, V. S. Bharadwaj, M. F. Crowley, L. Bu, J. V. Vermaas, K. X. Steirer, and M. F. Crowley, "Advances in Multiscale Modeling of Lignocellulosic Biomass," *ACS Sustain. Chem. Eng.*, vol. 8, no. 9, pp. 3512–3531, Mar. 2020, doi: 10.1021/acssuschemeng.9b07415.

[20] M. A. Romero Valle, "Numerical Modelling of Granular Beds in Rotary Kilns," Delft University of Technology, Master Thesis, 2012.

[21] A. A. Boateng, *Rotary Kilns Transport Phenomena and Transport Processes*, vol. 53, no. 9. Burlington, MA, USA: Butterworth-Heinemann (Elsevier Inc.), 2008.

[22] S. Tavakkol, "Modeling and Simulation of Biomass Carbonization via Biomass Steam Processing (BSP)," Karlsruhe Institute of Technology, Master thesis, 2016.

[23] D. Reichert, V. Boll, B. Genova, J. Steinbrueck, M. Rossbach, L. Walz, and H. Bockhorn, "Biocoal through Biomass Steam Processing - An experimental and Aspen Plus modeling study," 2014.

[24] J. Steinbrück, "Biomass Steam Processing Konzeption und Entwicklung eines Verfahrens zur Karbonisierung von Biomasse," Kalrsruhe Institute of Technology, PhD Thesis, 2019.

[25] H. R. Norouzi, R. Zarghami, and N. Mostoufi, "Insights into the granular flow in rotating drums," *Chem. Eng. Res. Des.*, vol. 102, pp. 12–25, Oct. 2015, doi: 10.1016/j.cherd.2015.06.010.

[26] X. Shi, "Heat and mass transfer modelling of auger reactors," 2016, [Online]. Available: http://lib.ugent.be/catalog/rug01:002275059.

[27] D. M. Christ, "The Effect of Char Kinetics on the Combustion of Pulverized Coal under Oxyfuel Conditions," RWTH Aachen, PhD Thesis, 2013.

[28] M. J. Hagge, "A numerical model for biomass pyrolysis," Iowa State University, PhD Thesis, 2005.

[29] J. L. Klinger, "Modeling of Biomass Torrefaction and Pyrolysis and Its Applications," Michigan Technological University, PhD thesis, 2015.

[30] I. H. Hwan, "Heat Transfer Mechanisms in an Indirectly Heated Rotary Kiln with Lifters and Its Role in Scaling," Curtin University of Technology, Western Australia, PhD Thesis, 2009.

[31] B. N. A. Stephane, "Experimental study and modeling of hydrodynamic and heating characteristics of flighted rotary kilns," University of Toulouse, PhD thesis, 2015.

[32] X. Ku, T. Li, and T. Løvås, "CFD-DEM simulation of biomass gasification with steam in a

fluidized bed reactor," *Chem. Eng. Sci.*, vol. 122, pp. 270–283, 2015, doi: 10.1016/j.ces.2014.08.045.

[33] C. Di Blasi, "Modeling chemical and physical processes of wood and biomass pyrolysis," *Prog. Energy Combust. Sci.*, vol. 34, no. 1, pp. 47–90, Feb. 2008, doi: 10.1016/j.pecs.2006.12.001.

[34] N. Wakao and S. Kaguei, *Heat and Mass Transfer in Packed Beds*, vol. 1. 1982.

[35] C. T. Crower, J. D. Schwarzkopf, M. Sommerfeld, and Y. Tsuji, *Multiphase with Droplets Flows wnd Particles*. CRC Press Taylor & Francis Group, 2012.

[36] L. De Lorenzis and A. Düster, *Modeling in Engineering Using Innovative Numerical Methods for Solids and Fluids*, vol. 599. Cham: Springer International Publishing, 2020.

[37] H. Henein, J. K. Brimacombe, and A. P. Watkinson, "The modeling of transverse solids motion in rotary kilns," *Metall. Trans. B*, vol. 14, no. 2, pp. 207–220, Jun. 1983, doi: 10.1007/BF02661017.

[38] J. Mellmann, "The transverse motion of solids in rotating cylinders-forms of motion and transition behavior," *Powder Technol.*, vol. 118, no. 3, pp. 251–270, 2001, doi: 10.1016/S0032-5910(00)00402-2.

[39] P. A. Cundall and O. D. L. Strack, "A discrete numerical model for granular assemblies," *Géotechnique*, vol. 29, no. 1, pp. 47–65, Mar. 1979, doi: 10.1680/geot.1979.29.1.47.

[40] W. Zhong, A. Yu, G. Zhou, J. Xie, and H. Zhang, "CFD simulation of dense particulate reaction system: Approaches, recent advances and applications," *Chem. Eng. Sci.*, vol. 140, pp. 16–43, 2016, doi: 10.1016/j.ces.2015.09.035.

[41] Y. Tsuji, T. Tanaka, and T. Ishida, "Lagrangian numerical simulation of plug flow of cohesionless particles in a horizontal pipe," *Powder Technol.*, vol. 71, no. 3, pp. 239–250, 1992, doi: 10.1016/0032-5910(92)88030-L.

[42] K. Yamane, M. Nakagawa, S. A. Altobelli, T. Tanaka, and Y. Tsuji, "Steady particulate flows in a horizontal rotating cylinder," *Phys. Fluids*, vol. 10, no. 6, pp. 1419–1427, Jun. 1998, doi: 10.1063/1.869858.

[43] M. J. Hagge and K. M. Bryden, "Modeling the impact of shrinkage on the pyrolysis of dry biomass," *Chem. Eng. Sci.*, vol. 57, no. 14, pp. 2811–2823, 2002, doi: 10.1016/S0009-2509(02)00167-7.

[44] K. M. Bryden, K. W. Ragland, and C. J. Rutland, "Modeling thermally thick pyrolysis of wood," *Biomass and Bioenergy*, vol. 22, no. 1, pp. 41–53, Jan. 2002, doi: 10.1016/S0961-9534(01)00060-5.

[45] D. Shi, W. L. Vargas, and J. J. McCarthy, "Heat transfer in rotary kilns with interstitial gases," *Chem. Eng. Sci.*, vol. 63, no. 18, pp. 4506–4516, 2008, doi: 10.1016/j.ces.2008.06.006.

[46] Y. Cengel, *Heat and Mass Transfer - A Practical Approach*. Mc Graw Hill, 2006.

[47] N. Wakao, S. Kaguei, and T. Funazkri, "Effect of fluid dispersion coefficients on particle-to-fluid heat transfer coefficients in packed beds. Correlation of Nusselt numbers," *Chem. Eng. Sci.*, vol. 34, no. 3, pp. 325–336, 1979, doi: 10.1016/0009-2509(79)85064-2.

[48] D. Kunii and T. Chisaki, *Rotary Reactor Engineering*, First ed. Tokyo: Elsevier, 2008.

[49] R. Siegel and J. R. Howell, *Thermal radiation heat transfer*. New York: Taylor&Francis, 2002.

[50] M. Chmielewski and M. Gieras, "Planck Mean Absorption Coefficients of H2O, CO2, CO and NO for radiation numerical modeling in combusting flows," *J. Power Technol.*, vol. 95, no. 2, pp. 97–104, 2015.

[51] R. Mehrabian, S. Zahirovic, R. Scharler, I. Obernberger, S. Kleditzsch, S. Wirtz, V. Scherer, H. Lu, and L. L. Baxter, "A CFD model for thermal conversion of thermally thick biomass particles," *Fuel Process. Technol.*, vol. 95, no. March, pp. 96–108, Mar. 2012, doi: 10.1016/j.fuproc.2011.11.021.

[52] Forest Products Laboratory, *Wood Handbook: Wood as an Engineering Material Agricultural Handbook*. U.S. Department of Agriculture, Washington, DC, 1987.

[53] M. A. Stanish, G. S. Schajer, and F. Kayihan, "A mathematical model of drying for hygroscopic porous media," *AIChE J.*, vol. 32, no. 8, pp. 1301–1311, Aug. 1986, doi: 10.1002/aic.690320808.

[54] H. Bockhorn, A. Hornung, U. Hornung, S. Teepe, and J. Weichmann, "Investigation of the Kinetics of Thermal Degradation of Commodity Plastics," *Combust. Sci. Technol.*, vol. 116–117, no. 1–6, pp. 129–151, Aug. 1996, doi: 10.1080/00102209608935546.

[55] M. Müller-Hagedorn, H. Bockhorn, L. Krebs, and U. Müller, "Investigation of thermal degradation of three wood species as initial step in combustion of biomass," *Proc. Combust. Inst.*, vol. 29, no. 1, pp. 399–406, Jan. 2002, doi: 10.1016/S1540-7489(02)80053-0.

[56] M. Müller-Hagedorn, H. Bockhorn, L. Krebs, and U. Müller, "A comparative kinetic study on the pyrolysis of three different wood species," *J. Anal. Appl. Pyrolysis*, vol. 68–69, pp. 231–249, 2003, doi: 10.1016/S0165-2370(03)00065-2.

[57] M. B. Müller-hagedorn, "Charakterisierung der Pyrolyse von Biomasse am Beispiel von Nadel- und Laubbaumholz," Universität Karlsruhe, PhD Thesis, 2004.

[58] F. Shafizadeh and P. P. S. Chin, "Thermal Deterioration of Wood," in *Wood Technology: Chemical Aspects*, 1977, pp. 57–81.

[59] C. Di Blasi, "The state of the art of transport models for charring solid degradation," *Polym. Int.*, vol. 49, no. 10, pp. 1133–1146, 2000, doi: 10.1002/1097-0126(200010)49:10<1133::AID-PI519>3.0.CO;2-E.

[60] J. M. Johansen, P. A. Jensen, P. Glarborg, M. Mancini, R. Weber, and R. E. Mitchell, "Extension of apparent devolatilization kinetics from thermally thin to thermally thick particles in zero dimensions for woody biomass," *Energy*, vol. 95, pp. 279–290, 2016, doi: 10.1016/j.energy.2015.11.025.

[61] D. L. Pyle and C. A. Zaror, "Heat transfer and kinetics in the low temperature pyrolysis of solids," *Chem. Eng. Sci.*, vol. 39, no. 1, pp. 147–158, 1984, doi: 10.1016/0009-2509(84)80140-2.

[62] M. Corbetta, A. Frassoldati, H. Bennadji, K. Smith, M. J. Serapiglia, G. Gauthier, T. Melkior, E. Ranzi, and E. M. Fisher, "Pyrolysis of Centimeter-Scale Woody Biomass Particles: Kinetic Modeling and Experimental Validation," *Energy & Fuels*, vol. 28, no. 6, pp. 3884–3898, Jun. 2014, doi: 10.1021/ef500525v.

[63] A. D. Paulsen, M. S. Mettler, and P. J. Dauenhauer, "The Role of Sample Dimension and

Temperature in Cellulose Pyrolysis," *Energy & Fuels*, vol. 27, no. 4, pp. 2126–2134, Apr. 2013, doi: 10.1021/ef302117j.

[64]   H. R. Norouzi, R. Zarghami, R. Sotudeh-Gharebagh, and N. Mostoufi, *Coupled CFD-DEM Modeling*, vol. 91. Chichester, UK: John Wiley & Sons, Ltd, 2016.

[65]   D. Gidaspow, *Multiphase flow and fluidization: continuum and kinetic theory descriptions*. Academic press, 1994.

[66]   S. Elgobashi, "An Updated Classification Map of Particle-Laden Turbulent Flows," in *IUTAM Symposium on Computational Approaches to Multiphase Flow*, Dordrecht: Springer Netherlands, 2006, pp. 3–10.

[67]   A. Hager, "CFD-DEM on Multiple Scales - An Extensive Investigation of Particle-Fluid Interactions," Johannes Kepler Universität Linz, PhD Thesis, 2014.

[68]   B. Peters, E. Schröder, C. Bruch, and T. Nussbaumer, "Measurements and particle resolved modelling of heat-up and drying of a packed bed," *Biomass and Bioenergy*, vol. 23, no. 4, pp. 291–306, 2002, doi: 10.1016/S0961-9534(02)00052-1.

[69]   S. Schulze, P. Nikrityuk, F. Compart, A. Richter, and B. Meyer, "Particle-resolved numerical study of char conversion processes in packed beds," *Fuel*, vol. 207, pp. 655–662, 2017, doi: 10.1016/j.fuel.2017.05.071.

[70]   CPFD Software LLC, "Barracuda Computational Particle Fluid Dynamics." [Online]. Available: https://cpfd-software.com/.

[71]   CD-adapco Inc., "STAR CCM+ Users Manual." Melville, NY, USA.

[72]   ANSYS Inc., "ANSYS CFX 18.0 Documentation." 2018, [Online]. Available: https://www.ansys.com/products/fluids/ansys-cfx.

[73]   ANSYS Inc., "ANSYS Fluent User's Guide." 2018, [Online]. Available: https://www.ansys.com/products/fluids/ansys-fluent.

[74]   C. Greenshields and The OpenFOAM Foundation, "OpenFOAM User Guide," *OpenFOAM Foundation*, 2019. https://cfd.direct/openfoam/user-guide/.

[75]   S. Tomasch, "Numerical Investigation of the Interaction between Dust Explosions and Inert

Particulate Additives Using an Euler-Lagrangian Approach in OpenFOAM ®," Montan Universität, Master thesis, 2016.

[76] S. V. Patankar, *Numerical heat transfer and fluid flow*. New York: Mc Graw Hill, 1980.

[77] K. L. Johnson and K. L. Johnson, *Contact mechanics*. Cambridge university press., 1987.

[78] K. Washino, E. L. Chan, and T. Tanaka, "DEM with attraction forces using reduced particle stiffness," *Powder Technol.*, vol. 325, pp. 202–208, Feb. 2018, doi: 10.1016/j.powtec.2017.11.024.

[79] J. Hærvig, U. Kleinhans, C. Wieland, H. Spliethoff, A. L. Jensen, K. Sørensen, and T. J. Condra, "On the adhesive JKR contact and rolling models for reduced particle stiffness discrete element simulations," *Powder Technol.*, vol. 319, pp. 472–482, Sep. 2017, doi: 10.1016/j.powtec.2017.07.006.

[80] C. H. Ibsen, E. Helland, B. H. Hjertager, T. Solberg, L. Tadrist, and R. Occelli, "Comparison of multifluid and discrete particle modelling in numerical predictions of gas particle flow in circulating fluidised beds," *Powder Technol.*, vol. 149, no. 1, pp. 29–41, 2004, doi: 10.1016/j.powtec.2004.09.042.

[81] M. Chiesa, V. Mathiesen, J. A. Melheim, and B. Halvorsen, "Numerical simulation of particulate flow by the Eulerian-Lagrangian and the Eulerian-Eulerian approach with application to a fluidized bed," *Comput. Chem. Eng.*, vol. 29, no. 2, pp. 291–304, 2005, doi: 10.1016/j.compchemeng.2004.09.002.

[82] D. M. Snider, P. J. O'Rourke, and M. J. Andrews, "An Incompressible Two-Dimensional Multiphase Particle-In-Cell Model for Dense Particle Flows," Los Alamos National Laboratory, 1997.

[83] J. R. Travis, F. H. Harlow, and A. A. Amsden, "Numerical Calculation of Two-Phase Flows," *Nucl. Sci. Eng.*, vol. 61, no. 1, pp. 1–10, Sep. 1976, doi: 10.13182/NSE76-A28455.

[84] D. M. Snider, "An Incompressible Three-Dimensional Multiphase Particle-in-Cell Model for Dense Particle Flows," *J. Comput. Phys.*, vol. 170, no. 2, pp. 523–549, Jul. 2001, doi: 10.1006/jcph.2001.6747.

[85] X. Shi, R. Sun, X. Lan, F. Liu, Y. Zhang, and J. Gao, "CPFD simulation of solids residence

time and back-mixing in CFB risers," *Powder Technol.*, vol. 271, pp. 16–25, 2015, doi: 10.1016/j.powtec.2014.11.011.

[86] P. J. O'Rourke and D. M. Snider, "An improved collision damping time for MP-PIC calculations of dense particle flows with applications to polydisperse sedimenting beds and colliding particle jets," *Chem. Eng. Sci.*, vol. 65, no. 22, pp. 6014–6028, Nov. 2010, doi: 10.1016/j.ces.2010.08.032.

[87] M. J. Andrews and P.J. O'Rourke, "The Multiphase Particle-In-Cell (MP-PIC) Method For Dense Particulate Flows," *Int. J. Multiph. Flow*, vol. 22, no. 2, pp. 379–402, 1996.

[88] S. E. Harris and D. G. Crighton, "Solitons, solitary waves, and voidage disturbances in gas-fluidized beds," *J. Fluid Mech.*, vol. 266, no. 1, p. 243, May 1994, doi: 10.1017/S0022112094000996.

[89] D. M. Snider, S. M. Clark, and P. J. O'Rourke, "Eulerian-Lagrangian method for three-dimensional thermal reacting flow with application to coal gasifiers," *Chem. Eng. Sci.*, vol. 66, no. 6, pp. 1285–1295, 2011, doi: 10.1016/j.ces.2010.12.042.

[90] S. S. Sazhin, E. M. Sazhina, O. Faltsi-Saravelou, and P. Wild, "The p-1 model for thermal radiation transfer: Advantages and limitations," *Fuel*, vol. 75, no. 3, pp. 289–294, 1996, doi: 10.1016/0016-2361(95)00269-3.

[91] F. M. Auzerais, R. Jackson, and W. B. Russel, "The resolution of shocks and the effects of compressible sediments in transient settling," *J. Fluid Mech.*, vol. 195, no. 1, p. 437, Oct. 1988, doi: 10.1017/S0022112088002472.

[92] C. K. K. Lun, S. B. Savage, D. J. Jeffrey, and N. Chepurniy, "Kinetic theories for granular flow: inelastic particles in Couette flow and slightly inelastic particles in a general flowfield," *J. Fluid Mech.*, vol. 140, pp. 223–256, Mar. 1984, doi: 10.1017/S0022112084000586.

[93] G. E. P. Box and M. E. Muller, "A Note on the Generation of Random Normal Deviates," *Ann. Math. Stat.*, vol. 29, no. 2, pp. 610–611, Jun. 1958, doi: 10.1214/aoms/1177706645.

[94] P. J. O'Rourke and D. M. Snider, "Inclusion of collisional return-to-isotropy in the MP-PIC method," *Chem. Eng. Sci.*, vol. 80, pp. 39–54, 2012, doi: 10.1016/j.ces.2012.05.047.

[95] J. Smagorinsky, "General Circulation Experiments with the Primitive Equations," *Mon.*

Weather Rev., vol. 91, no. 3, pp. 99–164, Mar. 1963, doi: 10.1175/1520-0493(1963)091<0099:GCEWTP>2.3.CO;2.

[96] M. F. Modest, *Radiative heat transfer*, Second ed. San Diego: Academic Press (Elsevier), 1993.

[97] A. Oliver González and A. Vdovin, "Radiation heat transfer in OpenFOAM," Göteborg, 2009. [Online]. Available: http://www.tfd.chalmers.se/~hani/kurser/OS_CFD_2009/AlexeyVdovin/Radiation_in_OpenFoam_final.pdf.

[98] J. Liu, H. Shang, and Y. Chen, "Development of an unstructured radiation model applicable for two-dimensional planar, axisymmetric, and three-dimensional geometries," *J. Quant. Spectrosc. Radiat. Transf.*, vol. 66, pp. 17–33, 2000, doi: 10.2514/6.1999-974.

[99] K. Jensen, J. Ripoll, A. Wray, D. Joseph, and M. Elhafi, "On various modeling approaches to radiative heat transfer in pool fires," *Combust. Flame*, vol. 148, no. 4, pp. 263–279, Mar. 2007, doi: 10.1016/j.combustflame.2006.09.008.

[100] N. Weber, "Weiterentwicklung eines Lagrange-Modells für Drehrohrreaktoren mit OpenFOAM," Karlsruher Institut für Technologie, Master Thesis, 2019.

[101] B. Zou, A. M. Gomes, and R. C.J., "Studies of Superheated Fuel Spray Structures and Vaporization in GDI Engines," *Int. J. Engine Res.*, vol. 1(4), pp. 321–336, 2000.

[102] P. Atkins and J. de Paula, *Atkins' Physical Chemistry*, 10th ed. Oxford: Oxford University Press, 2014.

[103] H. K. Versteeg and W. Malalasekera, *Introduction to Computational Fluid Dynamics*, Second Edi., vol. M. Edinburgh, England, 2007.

[104] M. W. Chase, J. L. Curnutt, J. R. Downey, R. A. McDonald, A. N. Syverud, and E. A. Valenzuela, "JANAF Thermochemical Tables, 1982 Supplement," *J. Phys. Chem. Ref. Data*, vol. 11, no. 3, pp. 695–940, Jul. 1982, doi: 10.1063/1.555666.

[105] W. Sutherland, "LXXV. A dynamical theory of diffusion for non-electrolytes and the molecular mass of albumin," *London, Edinburgh, Dublin Philos. Mag. J. Sci.*, vol. 9, no. 54, pp. 781–785, Jun. 1905, doi: 10.1080/14786440509463331.

[106] C. Elliott, V. Vijayakumar, W. Zink, and R. Hansen, "National Instruments LabVIEW: A Programming Environment for Laboratory Automation and Measurement," *J. Assoc. Lab. Autom.*, vol. 12, no. 1, pp. 17–24, Feb. 2007, doi: 10.1016/j.jala.2006.07.012.

[107] B. N. Asmar, P. A. Langston, and A. J. Matchett, "A generalised mixing index in distinct element method simulation of vibrated particulate beds," *Granul. Matter*, vol. 4, no. 3, pp. 129–138, Dec. 2002, doi: 10.1007/s10035-002-0112-8.

[108] A. Rohatgi, "WebPlotDigitizer." Pacifica, California, USA, 2019.

[109] P. S. T. Sai, G. D. Surender, A. D. Damodaran, V. Suresh, Z. G. Philip, and K. Sankaran, "Residence time distribution and material flow studies in a rotary kiln," *Metall. Trans. B*, vol. 21, no. 6, pp. 1005–1011, 1990, doi: 10.1007/BF02670271.

[110] R. G. Sherritt, "Three-Dimensional Particle Diffusion in a Rotating Drum Reactor," University of Calgary in Alberta, PhD Thesis, 2001.

[111] O. Levenspiel, *Chemical Reaction Engineering*, no. 3rd edition. John Wiley & Sons, 1999.

[112] R. G. Sherritt, J. Chaouki, A. K. Mehrotra, and L. A. Behie, "Axial dispersion in the three-dimensional mixing of particles in a rotating drum reactor," *Chem. Eng. Sci.*, vol. 58, no. 2, pp. 401–415, 2003, doi: 10.1016/S0009-2509(02)00551-1.

[113] J. D. Sullivan, C. G. Maier, and O. C. Ralston, "Passage of Solid particles through rotary cylindercal kilns," Washington, 1927.

[114] P. Graeser and M. Schiemann, "Emissivity of burning bituminous coal char particles – Burnout effects," *Fuel*, vol. 196, pp. 336–343, 2017, doi: 10.1016/j.fuel.2017.01.110.

[115] H. Romdhana, C. Bonazzi, and M. Esteban-Decloux, "Superheated Steam Drying: An Overview of Pilot and Industrial Dryers with a Focus on Energy Efficiency," *Dry. Technol.*, vol. 33, no. 10, pp. 1255–1274, Jul. 2015, doi: 10.1080/07373937.2015.1025139.

[116] C. Branca and C. Di Blasi, "Global Kinetics of Wood Char Devolatilization and Combustion," *Energy and Fuels*, vol. 17, no. 6, pp. 1609–1615, 2003, doi: 10.1021/ef030033a.

[117] Y. Haseli, J. A. Van Oijen, and L. P. H. De Goey, "Modeling biomass particle pyrolysis with temperature-dependent heat of reactions," *J. Anal. Appl. Pyrolysis*, vol. 90, no. 2, pp. 140–

154, 2011, doi: 10.1016/j.jaap.2010.11.006.

[118] W. C. Park, A. Atreya, and H. R. Baum, "Experimental and theoretical investigation of heat and mass transfer processes during wood pyrolysis," *Combust. Flame*, vol. 157, no. 3, pp. 481–494, Mar. 2010, doi: 10.1016/j.combustflame.2009.10.006.

[119] S. Tavakkol, T. Zirwes, J. A. Denev, N. Weber, and H. Bockhorn, "Development and validation of an Euler-Lagrange method for the numerical simulation of wet-biomass carbonization in a rotary kiln reactor," *29. Dtsch. Flammentag*, 2019.

[120] W. L. McCabe, J. C. Smith, and P. Harriott, *Unit Operation of Chemical Engineering*, Seventh Ed. McGraw-Hill, 2005.

[121] A. Izquierdo Espinosa, "Study of the production and analysis of bio-charcoal and bio-activated carbon from waste materials," Karlsruhe Institute of Technology, M.Sc. Thesis, 2019.

[122] Aspen Technology Inc., "Aspen Plus® - User Guide." Cambridge, MA, USA, 2016, [Online]. Available: http://www.aspentech.com.

[123] S. Tavakkol, T. Zirwes, J. A. Denev, F. Jamshidi, N. Weber, H. Bockhorn, and D. Trimis, "An Eulerian-Lagrangian method for wet biomass carbonization in rotary kiln reactors," *Renew. Sustain. Energy Rev.*, vol. 139, p. 110582, Apr. 2021, doi: 10.1016/j.rser.2020.110582.

[124] S. Tavakkol, T. Zirwes, J. A. Denev, F. Jamshidi, and H. Bockhorn, "Development of an Openfoam Solver for Numerical Simulation of Carbonization of Biomasses In Rotary Kilns," in *15th OpenFOAM Workshop*, 2020, pp. 1–8.

[125] S. Tavakkol, N. Weber, T. Zirwes, and J. Denev, "Performance of Large Scale Eulerian-Lagrangian Numerical Simulation for Particulate Flow in Rotating Reactors," in *6th Symposium of Baden-Württemberg High-Performance Computing*, 2019, pp. 1–4.